Synthesis and Structure of Group I and II Nitrides as Potential Hydrogen Stores

Thesis submitted to the University of Glasgow for the Degree of Doctor of Philosophy

By

Natalie Sorbie

School of Chemistry

University of Glasgow

September 2011

Abstract

This thesis describes the synthesis and characterisation of group I and group II nitride materials as potential hydrogen stores. New synthetic routes as well as the development of conventional methods were employed to synthesise binary and ternary nitrides.

Ball milling of single phase α-Li_3N and of commercial Li_3N was performed to induce a phase transformation in order to synthesise β-Li_3N which adopts a hexagonal crystal structure (space group *P6₃/mmc*). The beta polymorph was initially characterised by PXD and subsequently by a variable temperature PND experiment, which demonstrated that the phase transformation to α-Li_3N began at 600 K. Due to the fact that β-Li_3N exhibits the same magnitude of Li^+ conductivity as α-Li_3N and that lithium ion diffusion is thought to be an important factor in the hydrogen storage potential of the solid, a further PND investigation to study the interaction of D_2 gas with β-Li_3N was performed. At lower temperatures, negative thermal expansion can be observed; this expands following similar trends known for α-Li_3N and commercial Li_3N. In agreement with the behaviour of Li_3N reported in the literature, Li_3N reacts with D_2 at higher temperatures resulting in the formation of $LiND_2$ and LiD.

The phase behaviour in the complex Li-N-H system is still being debated despite significant research in this area. This work has focussed on lithium nitride hydride, which has been reported as a minority phase during the hydrogenation of Li_3N. Li_4ND was prepared by both conventional means and by a novel synthesis using microwaves; the product was characterised by PXD and PND. During both conventional and microwave syntheses, tetragonal Li_4ND (space group *I-4*) and a new high temperature cubic polymorph formed (space group *Fm-3m*) where N^{3-}, D^- and $(ND)^{2-}$ are disordered across the *anti*-fluorite anion sites. With regard to providing further evidence for the proposition of a new reaction pathway upon hydrogenation of Li_3N, Li_4ND and Li_2ND were reacted *in-situ* during a PND investigation forming a solid solution and resulting in synthesis of a cubic 'quasi-imide' phase. The 'quasi-imide' phase was refined against a modified cubic Li_2ND starting model. The presence of D^+ and D^- ensured that charge balance was maintained. As the stoichiometry increases, the anion distribution changes; the occupancy of N^{3-} and N from $(ND)^{2-}$ on the 4a site increases as does the occupancy of protonic D from $(ND)^{2-}$ on the 192l site.

A ternary nitride, LiCaN (space group *Pnma*), was prepared by both conventional and novel (via microwaves) means. Optimization of the reaction parameters was the initial

focus of the investigation in order to synthesise single phase LiCaN. Firstly, a PND study was performed in order to ascertain accurate Li positions and ensure the material was perfectly stoichiometric as made. In order to compare the Li-Ca-N system with reports on the Li-Mg-N system in which both Mg-rich and Li-rich phases as well as stoichiometric LiMgN have been synthesised, attempts were made to synthesise non-stoichiometric Li-Ca-N compounds. This system was investigated by PND.

List of Figures

List of Tables

1 Introduction

After much pioneering work in the 1920s and 1930s and in subsequent decades by Juza and colleagues, [1 2 3] the nitride chemistry of binary and ternary systems has progressed markedly over the last decade. Extensive research into many binary compounds from most regions of the periodic table has been carried out resulting in such nitrides now being well characterised. This is becoming increasingly true for ternary and higher nitrides too. [4]

Although this area of solid state chemistry has progressed significantly, there are still many synthesis barriers to overcome in regards to the preparation of nitrides; notably thermodynamics. Synthetic challenges within nitride chemistry occur due to the strength of the N_2 triple bond (941 kJ mol^{-1}). [5] In comparison to nitrides, oxides are by far the most comprehensively studied and characterised group of compounds known to solid state chemists; there are tens of thousands of oxide compounds known in comparison to only several hundred nitrides. [6] Since the bond strength of the O_2 double bond is lower (499 kJ mol^{-1}), this gives a solid explanation as to why nitrides are generally less stable than oxides. The thermodynamics of nitride formation is primarily to blame for the earlier lack of success in making these compounds. During the synthesis of nitrides, it is necessary to break the N_2 bond subsequently lowering the overall free energy of formation (ΔG_f^o). Since ΔG_f^o for nitrides is low, decomposition of nitride materials occurs at lower temperatures which is thermodynamically favourable due to the loss of N_2. The relative instability of ionic nitrides can be explained by the challenges faced in forming the N^{3-} anion from atomic N (2300 kJ mol^{-1}); [7] the same cannot be said for oxides as the formation of O_2 occurs from atomic O at + 700 kJ mol^{-1}. This accounts for the fact that nitrogen is reluctant to form predominantly ionic bonds with all but the most electropositive elements. The concept of the inductive effect, described by Etourneau *et al*, is demonstrated by the most electropositive of metals and it is this effect that enables metal-nitrogen bonds in ternary and higher compounds to be stable. [8] It should be noted that when nitrogen bonds with binary and higher compounds of the electropositive s-block element, the resultant compounds are not necessarily classic ionic compounds which one might expect. Instead, these compounds demonstrate varied valence and bonding behaviour which in turn leads to a great variation in the structural and reaction chemistry expected.

The reactivity of nitrides towards air and moisture is another problem faced by solid state chemists. Preparation and analysis has to be carried out under an inert atmosphere as reactions with water are usually thermodynamically favourable resulting in the formation of hydroxides and ammonia.

The interest in nitrides results from their ability to form often unique structures and also the fact that they exhibit a variety of unusual or unexpected physical properties. Even though only a small number of nitrides are known, many of them are useful materials with new found applications. For example, Si_3N_4 is used as an insulating material for coatings on semiconductor circuits, and AlN and TaN have uses as refractory ceramics.[6] The marked development in nitride chemistry over the last decade has meant that it is now more practical to refer to nitrides in their sub-groups; oxynitrides, nitride halides, subnitrides and nitride clusters as well as non-metal and nitridosilicates. In addition to this, ternary and higher order nitrides have also been studied. [9]

1.1 Nitride Chemistry

Evolution of nitride chemistry over the past decade and the growing interest within the field has resulted in the characterisation of many binary nitride compounds from regions throughout the periodic table, many of which were initially synthesised over 50 years ago. Numerous in-depth reviews have been published in the area of nitride chemistry focusing on synthetic methods, structures and related properties (such as conductivity potential). [10, 11, 12] The chemistry of binary metal nitrides has been well studied, with the most common chemical formulae being MN or M_3N_2 (where M denotes the metal atom). Excluding Li_3N, no other stable binary group 1 nitrides are known since the stabilities of the alkali metal binary nitrides are thought to be low (this prediction is based on the lattice energies which is a measure of the strength of bonds within a solid). Numerous binary nitrides of the alkaline earth metals are known: Be_3N_2, Mg_3N_2 and Ca_3N_2 with some of these forming subnitrides such as Ca_2N, Sr_2N and Ba_2N. These materials will be discussed further in subsequent sections.

With regards to bonding in nitrides, the contribution of ionic bonding to the stability of nitrides is likely to be low due to the high energy of formation of N^{3-} from atomic N, [4] as previously discussed. It should be noted that although some of the earlier alkali and alkaline earth metal nitrides are known to be ionic, they also exhibit partial covalency. This partial covalency arises from the presence of the cation which polarises the anion, for example, in Li_3N. The partial covalency is due to the fact that Li^+ is a small cation

and therefore has a tendency to draw electrons towards it from the N^{3-} anion which results in distortion of the electron cloud of the anion. With regards to the heavier group 2 metals, such as Sr and Ba, they tend to adopt a subnitride formation and both exhibit a unique combination of both ionic and metallic bonding. Figure 1-1 is an overview of the types of bonding adopted by group 1 and 2 metals.

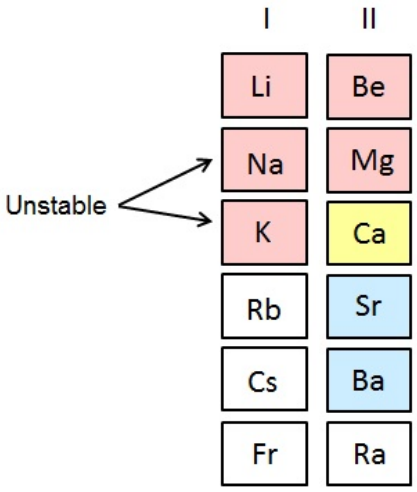

Figure 1-1: An overview of bonding in group 1 and 2 binary nitrides.
Ionic nitrides are highlighted in pink, metallic nitrides are highlighted in blue and those that are currently unknown are shown in white. Calcium is highlighted in yellow since it forms both ionic and metallic nitrides.

1.1.1 Alkali metal binary nitrides

1.1.1.1 Lithium Nitride

Alkali metal nitrides are dominated by lithium nitride, Li_3N. It is the only known stable binary nitride that is readily accessible synthetically (Na_3N and K_3N require extreme conditions to enable synthesis). [13]

Lithium nitride was first characterised by Zintl and Brauer in the 1930s using single crystal diffraction data. [14] Further research and significant advances were made decades later by Rabenau and Schulz using more up-to-date techniques resulting in Li_3N being assigned to space group *P6/mmm*. [15] More recently, research has unveiled the existence of Li_3N in three polymorphs. Alpha-Li_3N is stable at room temperature and pressure, and synthesised from the elements under ambient conditions. Beta–Li_3N, [16] which is structurally related to Na_3As, can be obtained from α-Li_3N via high pressure methods

(4.2 kbar at 300K). [17] The third polymorph, γ-Li_3N, can be fully transformed from β–Li_3N between 35-45 GPa and is stable up to 200 GPa. [18]

The unique structure of the alpha polymorph (Figure 1.2) is composed of two layers; an [Li_2N] layer and a layer of Li atoms only. [15] The graphite-like hexagonal layers of planar lithium hexagons are centred by a nitrogen atom. Each NLi_6 hexagon in the [Li_2N] layer is capped above and below the *ab* plane by a further lithium ion which connects the layers the third dimension (along the *c*-axis). Nitrogen atoms are packed differently in each phase; in the alpha phase, simple packing of the nitrogen atoms occurs and in the beta phase (Figure 1-3), a close packed motif results, [16] i.e. co-ordination of the nitrogen atoms changes from hexagonal bipyramidal in the alpha structure to trigonal bipyramidal in the beta structure. Although the alpha polymorph is stable at room temperature, the cavities that exist between the Li_2N layers yield a rather loosely packed structure facilitating a reversible transition to the beta phase that occurs under relatively mild pressure conditions. [16]

The crystal structure of the β-form, isotypic with Li_3P, is also composed of planar layers with hexagonal symmetry. Each nitrogen atom is bound by two lithium atoms, at 209.5 pm above and below the plane. β-Li_3N was first detected by ^{7}Li-NMR in a Li_3N single crystal at hydrostatic pressures in which the transition pressure was reported as 4.2 kbar at 300 K. [17] Although the new phase could not be structurally characterised, a variance in the ^{7}Li-NMR spectrum revealed the presence of 2 inequivalent Li sites with different quadrupole coupling constants from the alpha structure; 406 and 164 kHz instead of 582±2 and 285±2 kHz. [18] Least squares calculations determined lattice constants which gave a *c/a* ratio of 1·78 for β-Li_3N (in comparison to a value of 1·03 for that of α-Li_3N)[14] indicative of a Na_3As structure type. [19]

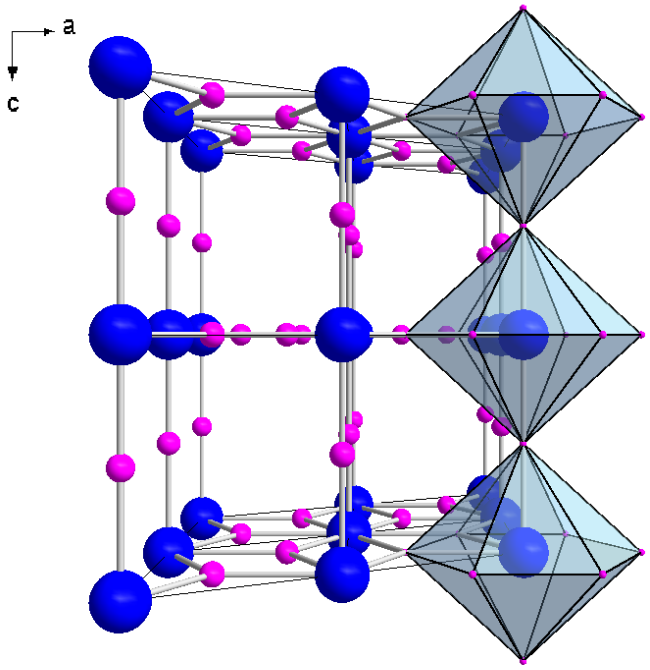

Figure 1-2: Hexagonal structure adopted by α-Li_3N (Li^+ - pink, N^{3-} - blue)

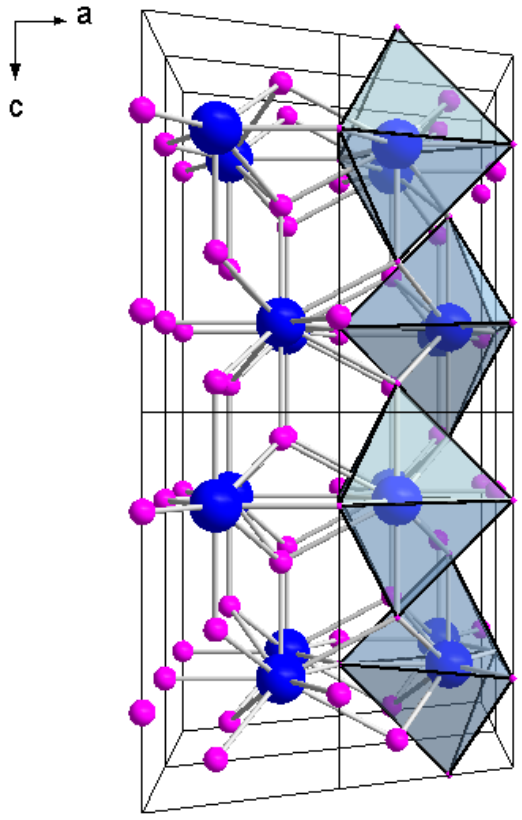

Figure 1-3: Hexagonal structure adopted by β-Li_3N (Li^+ - pink, N^{3-} - blue)

Indication of a third polymorph of Li_3N, γ-Li_3N, was observed in depressurised samples of Li_3N which had been subjected to pressures of more than 10 GPa. [18] X-ray diffraction data showed that this high pressure phase was consistent with a cubic face-centred lattice, and it is isostructural with Li_3Bi.

Polycrystalline Li_3N has a remarkably high Li-ion conductivity, reported by Boukamp and Huggins as being approximately 10^{-4} Ω^{-1} cm^{-1} and this rapid conduction of the Li^+ ions is caused by Li vacancies within the Li_2N layers. [20] Due to this exceptionally high Li-ion conductivity, Li_3N has a potential application as a solid electrolyte in lithium ion batteries. Further investigations using PND were performed much later by Gregory *et al* confirming that α-Li_3N has 3% Li vacancies at room temperature. [21]

Li *et al* investigated Li^+ ion diffusion in both the alpha and beta phases by direct current (DC) and alternating current (AC) impedance measurements. [22] Findings concluded that although both polymorphs exhibit the same order of magnitude (10^{-4} S cm^{-1}) of Li^+ ion conductivity at room temperature, the conductivity mechanism differs in each. Migration of the Li^+ ions occurs along the pure Li planes in β-Li_3N whereas in α-Li_3N, Li^+ diffusion occurs within the Li_2N plane. These results present potential for optimization of the ionic conductivity within Li_3N with regards to lithium in rechargeable batteries. Li_3N also shows promise as a hydrogen storage material and this will be discussed later in this chapter (refer to Section 1.2).

1.1.2 Alkaline earth metal binary nitrides

The chemistry of alkaline earth metal nitrides is rather broad and further understanding in this area of the periodic table can be attributed to new discoveries of new binary, ternary and higher phases. The alkaline earth metals form stable binary nitrides with the general formula M_3N_2. Lighter alkaline earth metals such as beryllium and magnesium form binary nitrides, Be_3N_2 and Mg_3N_2 respectively and are considered as being classically ionic. They show no indication of forming low oxidation state compounds, unlike calcium. On consideration of strontium and barium, both metals form the sub nitrides; Sr_2N [23] and Ba_2N [24] or Ba_3N [25] respectively. Those heavier group 2 metals (e.g. Sr and Ba) that adopt a subnitride formation have a tendency to form metallic bonds unlike the nitrides of beryllium and magnesium which tend to form ionic bonds.

1.1.2.1 Beryllium Nitride

Be_3N_2 forms two known polymorphs; the low temperature α-phase and the higher temperature β-phase, where the phase transition occurs at approximately 1673 K.[26] The alpha polymorph (Figure 1-4) is formed readily by reacting beryllium metal with either nitrogen or ammonia at ambient pressure [27, 28] which results in the formation of a white microcrystalline material. [29] The resulting material adopts a cubic *anti*-bixbyite structure (space group *Ia-3*) with tetrahedral co-ordination of the beryllium to the nitrogen. In turn, the nitrogen atoms are octahedrally bonded to the beryllium atoms. [28] There are two crystallographically different nitrogen atoms in α-Be_3N_2; N(1) exhibits distorted octahedral coordination and N(2) has a more complex hexa-coordination. Therefore the structure of the alpha polymorph has the beryllium atoms located in the tetrahedral sites of an approximately cubic, distorted, deficient, close-packed array of nitrogen atoms. The high temperature beta polymorph (Figure 1-5) adopts a hexagonal structure and the beryllium atoms occupy the interstitial sites within the close packed nitrogen layers. In β-Be_3N_2, there are two fully occupied beryllium atom sites present whilst the third beryllium atom is disordered between two tetrahedral sites. [30]

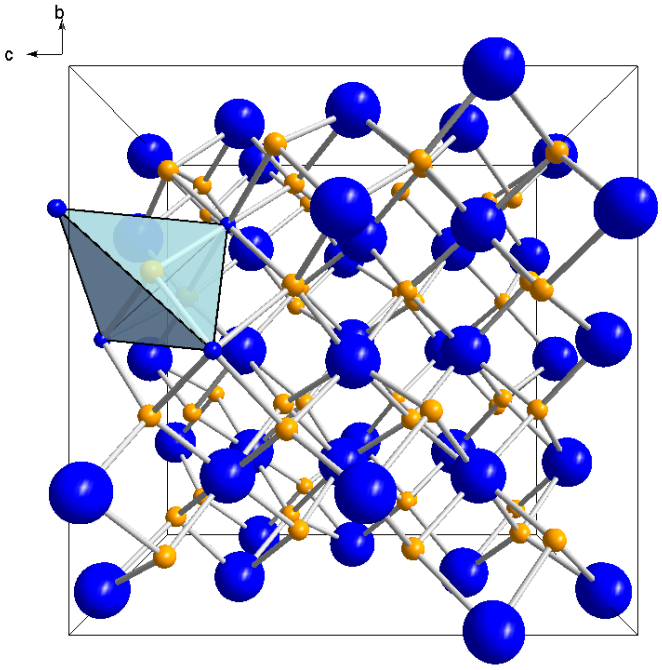

Figure 1-4: Cubic anti-bixbyite structure adopted by α–Be_3N_2 (Be^{2+} - orange, N^{3-} - blue)

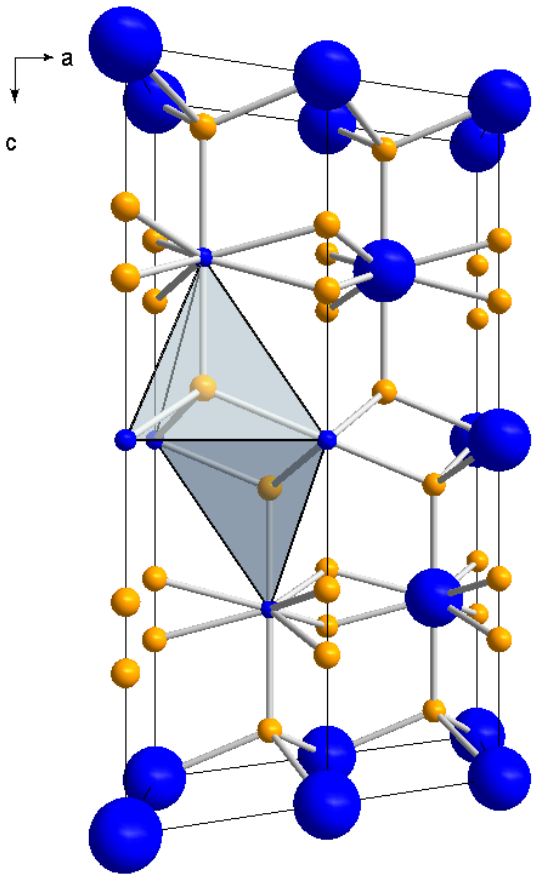

Figure 1-5: Hexagonal structure adopted by β–Be_3N_2 (Be^{2+} - orange, N^{3-} - blue)

1.1.2.2 Magnesium Nitride

Magnesium nitride can be synthesised following the same procedure as outlined for Be_3N_2. [28, 31] Reckeweg and DiSalvo obtained yellow/orange product when placing Mg metal in an alumina crucible under flowing N_2 at 1300 K. [32] Alternatively, it can be synthesised by forming a sodium/magnesium alloy which is reacted with nitrogen followed by vacuum distillation resulting in a highly crystalline product by exploiting the solubility of magnesium metal. [33, 34] Three polymorphs of Mg_3N_2 are known; α, β and γ with phase transitions at 823 K (α→β) and 1053 K (β→γ) [35] however the alpha polymorph is the only form which has been fully characterised. Mg_3N_2 was fully refined from PND data by Partin *et al* confirming that it adopts a cubic *anti*-bixbyite structure analogous with Be_3N_2 (Figure 1-4) [36] and crystallising with the space group, *Ia-3* (*a* = 9.9528 (1) Å). [37]

1.1.2.3 Calcium Nitride

Calcium nitride exists in many forms. Calcium metal occupies a unique position, forming stoichiometric Ca_3N_2 [38] and the subnitride Ca_2N. [39] Calcium nitride can form as α-Ca_3N_2 or β-Ca_3N_2. [40] A third polymorph of Ca_3N_2, the γ phase [41] was initially thought to exist but this has since been reported as cyanamide-nitride, $Ca_4N_2(CN_2)$. [42, 43] $Ca_{11}N_8$ was originally reported as a compound of the Ca-N family by Laurent *et al* [44] however further studies have led to reports that this phase is actually $Ca_{11}N_6(CN_2)_2$. [42, 43] A pernitride, Ca_3N_4 has also been reported to exist within the Ca-N system however information on this material is limited. [45]

The α-polymorph is red-brown in colour and was originally formed by the direct reaction of calcium metal under a nitrogen atmosphere between 923 and 1423 K [28] or by alloy formation with sodium at lower temperature. [46] α-Ca_3N_2 is isostructural with the *anti*-bixbyite structure of Mg_3P_2 and also with beryllium and magnesium nitrides; α-Be_3N_2 and Mg_3N_2 (Figure 1-4). [28] The *anti*-bixbyite structure of α-Ca_3N_2 (as well as α-Be_3N_2 and Mg_3N_2) is often referred to as a C-sesquioxide type which is a defect-type of the fluorite structure. Single crystal and power X-ray diffraction studies describe a tetrahedral coordination around the Ca atoms to nitrogen where the nitrogen atoms are considerably more distorted than was initially reported. The N(1) ions are surrounded by six Ca^{2+} ions in a distorted octahedral configuration and the N(2) ions are surrounded by six Ca^{2+} in a distorted trigonal prismatic configuration. [47]

Initial investigations into β-Ca_3N_2 showed that the material formed at lower temperatures at around 623 K and on heating to higher temperatures of 773 K, a phase transition to cubic α-Ca_3N_2 occurs. [48, 49] Furthermore, like Li_3N, the beta phase could also be synthesised from the alpha form by applying pressure. [50] Recent studies by Höhn *et al* reported that the β-phase of Ca_3N_2, which is a black material, can be synthesised via another two different methods. [40] Firstly, the beta polymorph can be prepared by reacting calcium metal with nitrogen at 700 K. Alternatively, reacting Ca_2N with nitrogen at 500 K also results in the formation of β-Ca_3N_2. Until recently, the beta polymorph of Ca_3N_2 was poorly characterised but further investigation has led to reports stating that β-Ca_3N_2 crystallises in the rhombohedral space group *R-3c* where a = 6.18920 (5) Å and c = 16.61115 (19) Å. [40] Rietveld refinements also gave no indication that β-Ca_3N_2 deviates from stoichiometric Ca_3N_2.

A third polymorph of Ca_3N_2, γ, was originally reported as a high temperature phase and formed by reacting calcium metal and nitrogen at 1323 K. [51] Further studies by Reckeweg and DiSalvo revealed that the compound initially reported as γ-Ca_3N_2 was actually a cyanamide-nitride, $Ca_4N_2(CN_2)$, composed of transparent, yellow needles. In addition to this discovery, $Ca_{11}N_8$ was investigated and found to be another cyanamide-nitride, $Ca_{11}N_6(CN_2)_2$, composed of dark red needles. Both cyanamide-nitrides were prepared using stoichiometric mixtures of $Na_2(CN_2)$, $CaCl_2$ and Ca_3N_2 in Ta ampoules and reacted between 1200 and 1400 K. Initial single crystal X-ray analysis in conjunction with IR and Raman spectroscopy was performed on the proposed cyanamide-nitride structures in 2000 [42] which were then re-determined in 2008. [43] The X-ray diffraction data and subsequent analysis performed on the cyanamide-nitrides revealed that $Ca_4N_2(CN_2)$ crystallises in space group *P4₂/mnm* and $Ca_{11}N_6(CN_2)_2$ in *Pnma*. A further calcium nitride, Ca_3N_4, is a possible product of the decomposition of $Ca(NH_2)_2$ in high vacuum at 673 K. [45]

Via several synthetic routes including the reduction of Ca_3N_2 and reaction of calcium metal in liquid sodium yielded the subnitride, Ca_2N. [52] Reductions of Ca_3N_2 were performed under either an argon atmosphere (at high temperature) or under vacuum (at a comparatively lower temperature). The alternative synthetic method involving the formation of a Ca/Na alloy, took place at 873 K under a positive nitrogen pressure. The resultant subnitride, Ca_2N, was reported to crystallise with a layered hexagonal structure in the space group *R-3m*. The layers are composed of $[NCa]^+$ with edge-sharing NCa_6 octahedra which stack along the *c*-axis and are separated by large 'van der Waals' gaps (Figure 1-6).

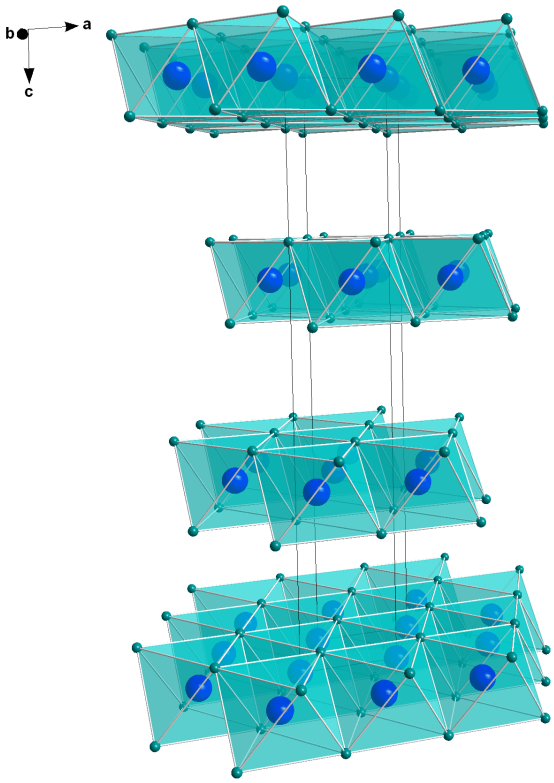

Figure 1-6: Layered hexagonal structure of Ca_2N (Ca^{2+} - teal, N^{3-} - blue)

1.1.2.4 Nitrides of Strontium and Barium

Unlike Ca, which is the only alkaline earth metal that has the ability to form the cubic *anti*-bixybite Ca_3N_2 and the subnitride Ca_2N, neither α-Sr_3N_2 and α-Ba_3N_2 have been isolated as yet [12] and no reliable evidence proving their existence has been reported. It should be noted that at the present time, the reason for the absence of Sr_3N_2 and Ba_3N_2 has not been confirmed although the presence of nearby d-orbitals or the importance of the cation size could provide a basis to the argument for their non-existence. [24] In contrast, the subnitrides, Sr_2N and Ba_2N, have been synthesised and subsequently analysed using X-ray diffraction. [24]

Initially Sr_2N was thought to be non-existent as Brice *et al* claimed that it was a nitride hydride, M_2NH_x [53] however a PND study conducted by Brese and O'Keeffe led to full characterisation of Sr_2N. [23] It should be noted that hydrogen can be incorporated into the structure resulting in the formation of M_2NH_x, for example, Ca_2NH and Sr_2NH. [24] Subsequently, Reckeweg and DiSalvo in 2002 conducted a further study into alkaline earth metal nitride compounds including Sr_2N. [24] The strontium subnitride was prepared by flowing N_2 gas over Sr metal at 1100 K for 24 h (Sr (I)). An alternative synthesis was also reported by Reckeweg and DiSalvo involving reacting Sr metal with NaN_3 at

1000 K and 1300 K, resulting in the formation of two similar Sr_2N products (Sr_2N (II) and Sr_2N (III) respectively) but it should be noted that none of the Sr_2N compounds prepared were identical. [24] The same synthetic method was employed for Ba_2N. The resultant products were described as being black and shiny crystals with red or blue lustrous effects for Sr_2N and Ba_2N respectively. It was reported that Ba_2N had an extremely strong affinity towards any moisture or oxygen as decomposition of the product was observed after only a few hours. Decomposition even occurred within a recirculating glove box where the levels of moisture were closely monitored. Single crystal X-ray investigations and subsequent data analysis showed that the subnitrides of the alkaline earth metals crystallise in the rhombohedral *anti*-$CdCl_2$ structure type. A previous PND study on Sr_2N reported a layered $CdCl_2$ type structure where different Sr-Sr distances indicate the irregularity of the octahedron.

With regards to the bonding in Sr_2N and Ba_2N and as mentioned previously, these subnitrides exhibit both ionic and metallic bonding. Ionic bonding between M^{2+} (e.g. Sr or Ba) and N^{3-} is responsible for holding the M_2N layers together whilst metallic bonding is responsible for *inter*-layer bonding.

A further subnitride of barium was reported as Ba_3N by Steinbrenner and Simon. [25] This nitride was synthesised by reacting Ba with nitrogen in a 6:1 ratio at a temperature of 670 K. Homogenization of the product was performed at 570 K in the presence of Na which was subsequently distilled off forming Ba_3N. Subsequent heating to 830 K results in the decomposition of Ba_3N to Ba_2N and Ba. The structure of Ba_3N is an *anti*-TiI_3 type crystallising in space group $P6_3/mcm$.

1.1.3 Ternary Nitrides

Ternary nitrides, composed of only alkali and alkaline earth metals, are a relatively small group of compounds. No ternary nitrides composed of only group 1 elements are known and only a few containing group 2 elements and nitrogen are known. The majority of purely s block metal ternary nitrides that have been discovered are composed of both group 1 and group 2 metals and tend to be ionic in nature. However, even in ternary compounds where there are a high proportion of electropositive elements present, the metal-nitrogen bonds exhibit significant covalent character.

Ternary nitrides tend to crystallise in the (*anti*) fluorite structure when the ionic radius $r(Li^+)/r(M^{n+}) \geq 1$. [54] The basic structure of a fluorite is that of CaF_2 from the mineral

which lends its name to the structure (Figure 1-7) and is a very common material which is found in nature.

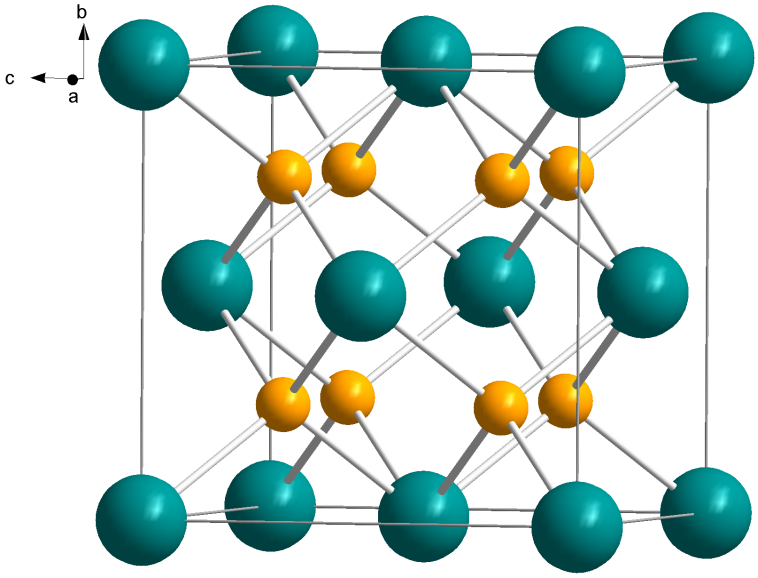

Figure 1-7: A basic fluorite structure (Ca^{2+} - teal, F^- - orange)

A fluorite can be described as face centred cubic packing of cations; the anions occupy all of the tetrahedral holes. The unit cell of the fluorite structure is composed of 8 tetrahedra which form a three-dimensional edge-sharing network, with cations at the corners and an anion in the centre of each tetrahedron. In order to maintain the ideal fluorite structure, the cation:anion radius ratio must be 4.38. If this is not the case and the radius ratio is smaller, the cations would be pushed apart and therefore closest packing would not prevail. In comparison, a larger ratio would mean that the anions would not be in contact with the four co-ordinating cations at once therefore this scenario does not fulfil the requirements either. In ternary nitrides, the tetrahedral holes of the approximately cubic close packed matrix of nitride anions are occupied by cations hence the *anti*-fluorite structure.

1.1.3.1 Lithium Beryllium Nitride

Of the alkali metals, only lithium is known to form ternary nitrides with the elements of group 2. In 1969, Brice *et al*, reported that reacting Li_3N and Be_3N_2 (or beryllium metal) under a nitrogen atmosphere at a temperature of 853 K results in the formation of LiBeN. [55] A PXD study and subsequent analysis revealed that the structure is orthorhombic with lattice parameters, a = 8.75 Å, b = 8.16 Å and c = 7.65 Å. Although

this study completed initial structural studies into the first of the group 2 elements (Be, Mg and Ca) which forms ternary nitrides with lithium, little is known regarding the properties of LiBeN. Decades later, Somer *et al* reported the formation of single crystals at a temperature of 1275 K [56] and the structure was solved in a monoclinic space group ($P2_1/c$) with lattice parameters a = 4.540(1) Å, b = 4.760(1) Å, c = 5.807(1) Å, which differs from that reported previously. [55] The structure reported by Somer *et al* is composed of layered $^{2}_{\infty}[BeN_{3/3}]^{-}$ anions which are held together by Li atoms. [56]

1.1.3.2 Lithium Magnesium Nitride

Previous to the discovery of LiBeN, LiMgN was reported by Juza in the 1940s. [57, 58] The synthesis of LiMgN involves reacting Li_3N and Mg_3N_2 via a solid state reaction at temperatures of 1073-1123 K and on cooling to room temperature produces orthorhombic LiMgN (space group *Pnma*) (Figure 1-8 b). [33] Initial investigations in this system by Juza and Hund reported that the 1:1 Li/Mg ternary nitride, LiMgN, was a cubic, cation-disordered *anti*-fluorite structure [58] however subsequent studies decades later by Yamane *et al* reported the structure of LiMgN to be orthorhombic (space group *Pnma*), by employment of PXD and Rietveld analysis. [59] Two other phases present within the Li_3N-Mg_3N_2 system were also reported by Yamane *et al*; a lithium rich phase and a magnesium rich phase. The lithium rich structure was reported as a simple cubic *anti*-fluorite whereas the magnesium rich structure was reported as being a distorted *anti*-bixbyite. Bailey *et al* performed further studies, by means of PND, reporting that LiMgN undergoes a structural transition at temperatures above 673 K resulting in the formation of a cubic *anti*-fluorite structure (space group *Fm-3m*). [33]

A PND investigation into the non-stoichiometric Li-Mg-N compositions were also conducted by Bailey *et al* resulting in a nitrogen-deficient, magnesium-rich phase, $Li_{0.24}Mg_{2.76}N_{1.92}$, (Figure 1-8 a) which is isostructural to the Mg_3N_2 starting material; a cubic *anti*-bixbyite material (space group $I2_13$) over a temperature range of 293 – 873 K. The second non-stoichiometric compound in the system, $Li_{1.11}Mg_{0.89}N_{0.96}$, retains the cubic *anti*-fluorite structure (crystallising in the *Fm-3m* space group) (Figure 1-8 c). The third and final non-stoichiometric Li-Mg-N compound investigated by Bailey *et al* was $Li_{1.09}Mg_{0.91}N_{0.97}$ which crystallises in the orthorhombic *Pnma* space group; isostructural with LiMgN. From the findings, it was reported that both the LiMgN and Mg_3N_2 structure types can accommodate variable metal and nitrogen stoichiometries.

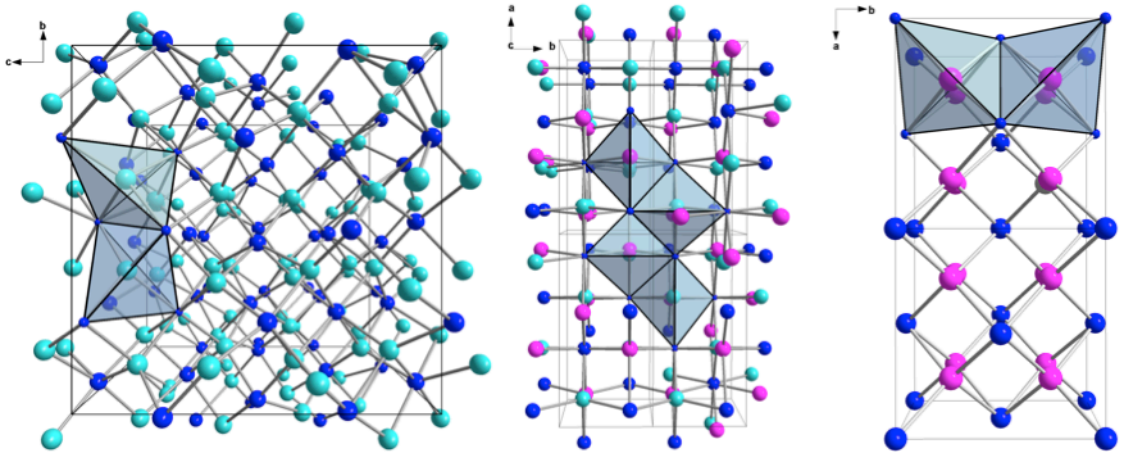

Figure 1-8: Structures within the Li-Mg-N system.
(a) cubic *anti*-bixbyite structure of the Mg-rich phase, (b) orthorhombic stoichiometric LiMgN, (c) cubic *anti*-fluorite structure of the Li-rich phase (Li^+ - pink, Mg^{2+} - aqua, N^{3-} - blue).

1.1.3.3 Lithium Calcium Nitride

Unlike the Li-Mg-N system, to date, only one ternary nitride, LiCaN, is known in the Li-Ca-N system and the structural information on LiCaN is limited to one single crystal X-ray diffraction experiment. [60] LiCaN can be synthesised by reacting Li_3N and Ca_3N_2 (or calcium metal) under a nitrogen atmosphere of 2 bar at 873 K (or 773 K). [61] LiCaN adopts an orthorhombic, distorted *anti*-fluorite structure where half of the tetrahedral holes are occupied by Ca atoms and the Li atoms are displaced from the remaining half of the tetrahedral centre positions of the approximately cubic close-packed nitrogen matrix. The Li atoms are displaced by 0.135 Å from a tetrahedral face but 3.570(8) Å from the fourth nitrogen atom. [60] The Li atoms are coordinated to N in a trigonal planar symmetry (which is similar to that found in Li_3N) and the Ca atoms are tetrahedrally coordinated to N. Coordination of the nitrogen atoms results in the form of a distorted pentagonal bipyramid, connected axially by two calcium atoms and equatorially by two calcium atoms and three lithium atoms (Figure 1-9).

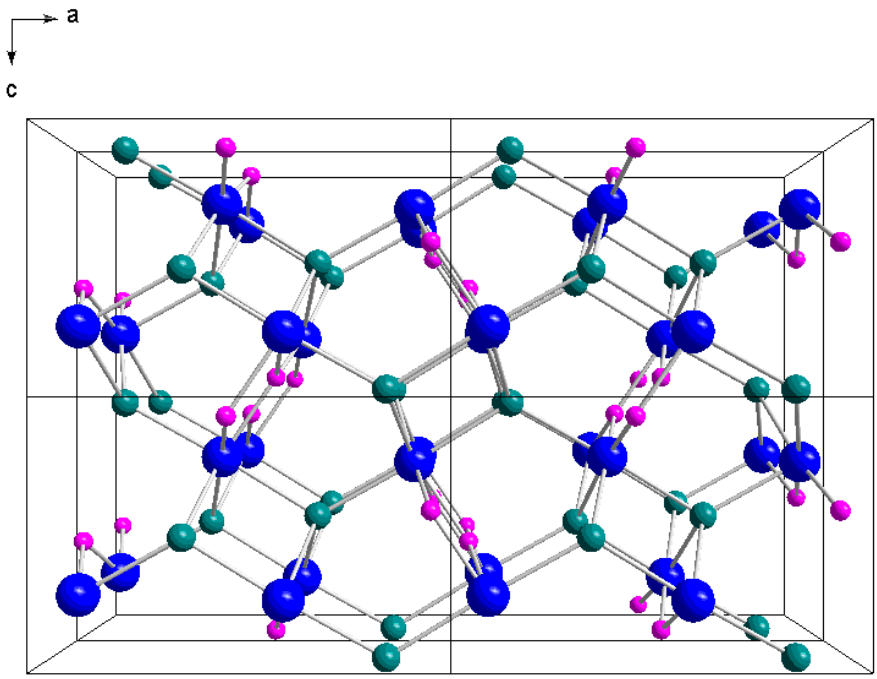

Figure 1-9: Distorted orthorhombic anti-fluorite structure of LiCaN.
(Li^+ - pink, N^{3-} - blue and Ca^{2+} - teal)

1.1.3.4 Lithium Strontium Nitride

In regards to the Li-Sr-N system, there are two known compounds; LiSrN and Li_4SrN_2. [60, 62] The synthesis of the 1:1 product follows the trend of that reported for the other ternary nitrides where Li_3N and Sr_3N_2 (or strontium metal) are reacted under a nitrogen atmosphere at 873 K. Brice *et al* also reported an alternative synthesis for LiSrN by reacting Sr_3N_2 on Li metal at 873 K under a nitrogen atmosphere. Furthermore, LiSrN can be synthesised by nitriding a Li/Sr alloy and increasing the temperature stepwise to 1023 K. Li_4SrN_2 was prepared by reacting Li_3N with Sr metal in a 4:1 molar ratio under a nitrogen atmosphere. [60] The reaction was heated to 973 K and cooled over a 12 h period which yielded Li_4SrN_2.

In the 1:1:1 ternary compound, which is isostructural to YCoC, strontium is tetrahedrally coordinated to nitrogen. These nitrogen atoms are coordinated in a distorted octahedral geometry to Li (axial) and Sr (equatorial). The PXD pattern of LiSrN was indexed on a tetragonal cell with lattice parameters, a = 11.08 Å and c = 13.40 Å. Further work by Brice *et al* reported the formation of a solid solution between LiSrN and Li_2O which results in simplification of the structure; the compounds form cubic *anti*-fluorite structures isostructural to LiMgN.

In great contrast to LiSrN, the crystal structure of Li_4SrN_2 more closely resembles the structure of Li_3N. The N atoms are coordinated in the form of a distorted pentagonal bipyramid as opposed to hexagonal bipyramids (NLi_6 in Li_3N), which are connected axially by two lithium atoms and equatorially by two strontium atoms and three lithium atoms. [60]

1.1.3.5 Lithium Barium Nitride

Concluding the Li/group 2 ternary nitride compounds is the Li-Ba-N system. This system has not been investigated to the extent of the other Li-A-N systems therefore it is the least well defined. [63] LiBaN is synthesised by the reaction of Li_3N and Ba_3N_2 under a nitrogen atmosphere at 873 K. Alternatively, LiBaN can be synthesised by reacting lithium and barium metals under a nitrogen atmosphere also at 873 K yielding a black product. [63] Although the structure has yet to be solved, its powder X-ray diffraction pattern has been indexed on a hexagonal unit cell (a = 6.79 Å and c = 8.05 Å). Brice *et al* also reported that, like LiSrN, LiBaN forms a solid solution with Li_2O resulting in a structure once again isostructural to LiMgN.

1.1.4 History of Microwaves

The first applications of microwaves began in 1920 with the development of the magnetron by Hull. [64] A decade later, during the 1930's, advances in communication using microwaves developed with Marconi installing a 57 cm wavelength radio providing telephone and teleprinter service over the 15 mile path from Vatican City to Castel Gandolfo. [65] Further advances in the development of microwave technology were made during World War II where Southworth focussed efforts on making components for radar systems. [66] It was then not until the 1960s that microwaves were designed to be used domestically. [67]

1.1.4.1 Microwave synthesis

A decade after the domestic exploitation of microwaves, the first report of microwaves for chemical research was reported performed by Lui and Wrightmann. [68] The technology has since proved useful as an alternative to conventional solid-state chemistry synthesis methods. Initially microwave chemistry was used in analytical processes, for example fat analysis and protein hydrolysis but advances in this field have led it to be applied in chemical synthesis including the synthesis of

organometallics, coordination compounds and nanoparticles. [69] Due to the high temperatures and long reaction times required by conventional methods, microwave irradiation offers an alternative source of heating and much quicker reaction times. Microwaves have become increasingly widespread for chemical reactions sparking many scientists to adopt this approach for materials synthesis, for example in the synthesis of metal halides [70] as well as in the synthesis of binary and ternary nitrides. [71] It is believed that microwave techniques promote heating in fine metal particles by using electric currents induced in them from the electromagnetic field of the microwave. There are two types of microwave reactor configurations that can be employed in chemistry; single-mode microwave reactors and multi-mode microwave reactors. Both can be advantageous over conventional methods in terms of efficiency, for example, reduction of reaction times and selective heating, however scalability is problematic for these types of reactions as increasing the mass of material being reacted is likely to have direct effect on the resultant product.

The use of microwaves in synthetic chemistry is becoming increasingly diverse branching into different areas from organic to materials chemistry. Microwave heating involves the oscillation of polar molecules or ions under an electric or magnetic field. In the presence of an oscillating field, particles try to align themselves in phase with the field which may be prevented by electrical resistance for example. As a consequence, the ordered motion of particles is restricted therefore random motion may occurs resulting in the production of heat. Not all materials interact with microwaves and therefore the materials can be categorized into either those that are transparent to microwaves, those that absorb microwaves and those that reflect microwaves (refer to Section 2.2.2 for further details).

Several binary and ternary nitrides have been synthesised via both direct microwave heating and with microwave generated nitrogen plasmas. Houmes and zur Loye synthesised various binary and ternary nitrides such as AlN and Li_3AlN. [71] Using Li_3AlN as an example, this ternary nitride can be synthesised by direct reaction between Li_3N and AlN since the reactants have a sufficient nitrogen content. If it is apparent that the nitrogen content of the starting materials is lower and nitrogen uptake is required for the synthesis of the desired product then reactions can take place under a nitrogen plasma to aid formation. Using Li_3N as a starting material in microwave reactions to synthesise ternary compounds has proven to be successful. [72] Since lithium is an

electronic conductor and its nitride is an ionic conductor, they both have the ability to heat well on exposure to microwaves.

1.2 The Li-N-H System

1.2.1 Hydrogen Storage

Considering the desire for a cleaner environment by reducing harmful emissions and the threat to fossil fuel depletion, the need for alternative energy storage and power generation is now greater than ever therefore one of the main focuses of materials research currently involves finding efficient means of energy conversion and storage. [73] A sustainable and secure energy supply is vital to ensure that the ever increasing energy demands of developed and developing nations can be met. [74] The increasing energy requirements in addition to the depletion of fossil fuels combine to pose a serious lack of sustainable energy sources and therefore the problem must be addressed.

Hydrogen-based energy systems may prove to be a practical solution for problems and hydrogen is currently seen as the main candidate as an energy vector in mobile applications such as vehicles powered by fuel cells, however the fact that hydrogen is difficult to store has limited its use thus far. Conventionally, hydrogen gas is stored and transported as a compressed gas or liquid however both require strict conditions under which they must be stored. With regards to compressed hydrogen gas, the gas must be intensely pressurised and stored in a pressure vessel. Liquid hydrogen has the capability of storing more hydrogen in a given volume in comparison to compressed hydrogen, however when considering the potential use of liquid hydrogen as a store, it too requires specific storage conditions, namely cryogenic conditions. An alternative to the aforementioned hydrogen stores would be to use a material that can sorb large amounts of hydrogen, for example lithium nitride. However, significant improvements are required if hydrogen stores are to become viable in the future; more basic and subsequent in-depth research must be conducted in addition to addressing the problems which may arise when implementing the technology. It should be noted that since hydrogen is not a naturally available source, large-scale processes must be employed to cope with the changeover to a nation which would then be dependent on the hydrogen economy for its energy demands. Considering the hydrogen economy, with regard to meeting and sustaining the demand for an alternative energy carrier the most important factor is obviously that the material must store a considerable amount of hydrogen and

the temperature and cycling times must be suitable. Guidelines on these factors along with other criteria, including safety and cost effectiveness, have been published by the US Department of Energy (DoE). Strict gravimetric targets for a storage system have been outlined; 6.5 wt. % H_2 by 2015 (with an ultimate goal of 7.5 wt. % H_2). [75]

Various chemical storage materials have been proposed including both light, (e.g. MgH_2) [76] and complex (e.g. $LiBH_4$) [77] metal hydrides and nitrides-imides-amides (e.g. Li-N-H). [78, 79, 80] If hydrogen is bound in a compound then chemisorption is required as an initial step before the formation of a chemical bond with hydrogen or the absorption of hydrogen in the bulk material. [74] If hydrogen is present as molecular hydrogen and only adsorbed onto the surface of the solid or present within the internal volume of the material, i.e. framework structures, then this is referred to as physisorption. [74] It should be noted that in compounds where physisorption plays a role, these compounds are less appealing due to the fact that the hydrogen is so weakly bound that strict conditions such as low temperatures or high pressures would be required in order for them to have a practical use.

One material with hydrogen storage potential is lithium nitride and a major breakthrough in 2002 by Chen *et al* reported that Li_3N could reversibly store large amounts of hydrogen. However the pressures at which hydrogen is released were still too high to have any practical use. [81] Nonetheless, the Li-N-H system could provide a promising route to tackling the need for alternative energy storage. Although the Li-N-H system is promising, the understanding of the hydrogen-storage capabilities of these nitride-imide-amide materials still requires much investigation as challenges which have already been met with other complex hydrides, such as kinetics and reversibility, [77] pose similar problems for this proposed system. Although there has been vast progress leading to a greater understanding of the Li-N-H system in a relatively short period of time, the goal of achieving a storage medium for the storage of hydrogen is still very much in its infancy.

As early as the beginning of the 20th century, studies on the hydrogenation and dehydrogenation of Li_3N were being conducted. This resulted in what was believed to be Li_3NH_4 which on decomposition at high temperatures gave Li_3NH_2 and H_2 (or as direct products of $Li_3N + 2H_2$ above 973 K). [82, 83] Further investigation by Ruff and Goeres led to the conclusion that 'Li_3NH_4' was a mixture of $LiNH_2$ and LiH (1:2) and 'Li_3NH_2' which was a mixture of Li_2NH and LiH (1:1). [84, 85]

Lithium nitride absorbs hydrogen forming the amide and the hydride, shown in the reaction mechanism below (Equations 1 and 2). Theoretically, Equation 1 can store 10.4 wt. % of hydrogen however in practice, this value is lower and shown to be 9.3 wt. % [81] and the molar ratio of absorbed hydrogen atoms to the Li_3N starting material is 4:1.

$$Li_3N + 2H_2 \leftrightarrow Li_2NH + LiH + H_2 \leftrightarrow LiNH_2 + 2LiH \quad (1)$$

$$Li_3N + 2H_2 \leftrightarrow LiNH_2 + 2LiH \quad \Delta H = -96.3 \text{ kJ/mol } H_2 \quad (2)$$

As shown in Equation 1, Chen *et al* states that the process follows a clear 2-step reaction pathway.

$$Li_3N + H_2 \leftrightarrow Li_2NH + LiH \quad \Delta H = -165 \text{ kJ/mol } H_2 \quad (3)$$

$$Li_2NH + H_2 \leftrightarrow LiNH_2 + LiH \quad \Delta H = -44.5 \text{ kJ/mol } H_2 \quad (4)$$

The first step of the reaction (Equation 3) leads to the formation of lithium imide (Li_2NH), the structure of which was originally determined by Juza and Opp in 1951, [86] and lithium hydride (LiH). This is followed by the formation of lithium amide ($LiNH_2$) [87] and a further molecule of LiH (Equation 4). It is only the second step of the reaction process (Equation 4) that is readily reversible due to the favourable enthalpy value (-44.5 kJ/mol H_2). It has the capability to absorb/desorb 6.5 wt. % of hydrogen stored in lithium imide at 528 K easily due to the smaller negative enthalpy change (ΔH) upon uptake of hydrogen, in comparison to the reaction described in Equation 3.

On decomposition of pure $LiNH_2$ at elevated temperatures, NH_3 is evolved (Equation 5), however, when $LiNH_2$ is in contact with 1 equivalent of LiH, the pathway changes as shown in Equation 6 with Li_2NH forming and H_2 is released at a lower temperature. [78] It is believed that this dehydrogenation reaction proceeds due to the strong affinity between $H^{\delta+}$ in $LiNH_2$ and H^- in LiH.

$$2LiNH_2 \rightarrow Li_2NH + NH_3 \quad (5)$$

$$LiNH_2 + LiH \rightarrow Li_2NH + H_2 \quad (6)$$

An alternative reaction pathway regarding the decomposition pathway of $LiNH_2$ has been described in Equations 5 and 7. Hu and Ruckenstein [79, 80] and Ichikawa *et al* [88] proposed that the reaction mechanism is ammonia mediated.

$$2LiNH_2 \rightarrow Li_2NH + NH_3 \quad (5)$$

$$NH_3 + LiH \rightarrow LiNH_2 + H_2 \quad (7)$$

The first step (Equation 5) is endothermic and involves the decomposition of lithium amide resulting in the formation of lithium imide and ammonia. Decomposition of $LiNH_2$ is performed under vacuum at a temperature of 673 K resulting in the formation of Li_2NH. [89] *Ab initio* calculations were performed by Miceli *et al* in order to propose a mechanism for the reaction in Equation 5 and findings suggested that the transformation pathway is dependent on the surface-to-volume ratio of the $LiNH_2$ crystallites. [90] Shaw *et al* proposed that Equation 5 proceeds via the schematic presented in Figure 1-10. [91] The decomposition of $LiNH_2$ occurs via the growth of a Li_2NH shell around a shrinking $LiNH_2$ core accompanied by ammonia desorption (Figure 1-10 [A]). The desorbed ammonia gas then reacts with LiH releasing hydrogen gas promoting the formation of $LiNH_2$ (Equation 7, Figure 1-10 [B]).

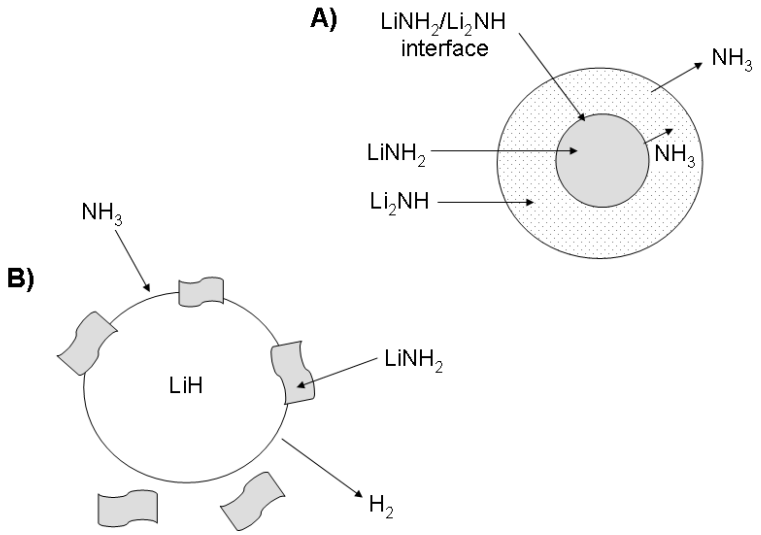

Figure 1-10: Schematic of the decomposition reaction pathway of $LiNH_2$ and LiH. [A] Decomposition of $LiNH_2$. [B] Formation of $LiNH_2 + H_2$ from $NH_3 + LiH$.

Even though the breakthrough by Chen *et al* in 2002 was a great step forward, there are several factors that still require addressing. These challenges are being investigated to improve the performance of the Li-N-H system and to broaden knowledge on the absorption and desorption properties of the system.

Within the Li-N-H system, various paths have been followed to optimise performance. Modifying the microstructure of the material, using catalysts or doping materials (Li-M-N-H) are all areas which have been investigated in the hope that a further understanding and improved performance of the system will be obtained. Kojima *et al* investigated the effects of the microstructure on H_2 storage capability and concluded that mixtures of

metal imide, amide and hydride could be synthesised by using a mechanochemical reaction where a 10 bar H_2 pressure was applied. [92] However, only a small amount of the material was converted to the desired products (i.e. lithium amide and lithium hydride).

Further studies on the effects of the microstructure with regard to hydrogen storage were conducted by Leng *et al*. It was reported that ball milling Li_3N under a pressure of 4 bar of NH_3 for 2 h results in the formation of $LiNH_2$ therefore milling under NH_3 rather than H_2 delivers the desirable product more readily. [93] Moreover, Markmaitree *et al* reported that ball milling reduced the onset temperature for the decomposition of $LiNH_2$, from 393 K to room temperature. However, the temperature must reach 503 K before $LiNH_2$ fully decomposes. It was reported that by the employment of ball milling, the reduction in particle size, the increase of the surface area and the decreased activation energy were the key factors in decomposition of $LiNH_2$. [94] An investigation into the effects of the alpha and beta polymorphs of Li_3N on hydrogen absorption properties were investigated by Minella *et al* [95] in which it was concluded, after milling at 20 bar for 4 h and obtaining $LiNH_2$ and LiH, neither of the polymorphs of Li_3N had an effect on the formation of the products.

Combining modification of the microstructure (for example, by ball milling) with the presence of a catalyst (for example, $TiCl_4$) has improved the absorption/desorption kinetics as well as a noteworthy reduction in desorption temperatures where 5.5 wt. % of hydrogen was released between 423-523 K with no formation of ammonia. [88] It should be noted that although this is another significant advancement, the mechanism by which catalysts affect the reaction is not yet known.

Using high resolution synchrotron X-ray diffraction, the structural and compositional changes in the Li-N-H system were investigated by David *et al* in order to clarify the processes which occur during the absorption/desorption cycling of hydrogen. [96] The transformation of lithium imide to lithium amide during the cycling of hydrogen occurs through non-stoichiometric intermediates which are based on cubic *anti*-fluorite-like Li-N-H structures. David *et al* also describes the generation of Frenkel-type defects which occur due to the movement of a lithium ion (cation) to a nearby, unoccupied site creating a vacancy. These findings were corroborated by Huq *et al* from *in-situ* neutron diffraction studies during deuteration and de-deuteration of Li_3N which also implied the presence of non-stoichiometric intermediates. [97]

1.2.2 The structures of Lithium Amide and Lithium Imide

Lithium amide crystallises in the tetragonal space group *I-4* with lattice parameters of a = 5.0344 (2) Å and c = 10.2556 (5) Å, [98] the structure of which is an ordered fluorite derivative. Within the structure, Li^+ ions occupy the tetrahedral holes with the nitrogen in a cubic close packed arrangement. [99] A representation of the structure is shown in Figure 1-11.

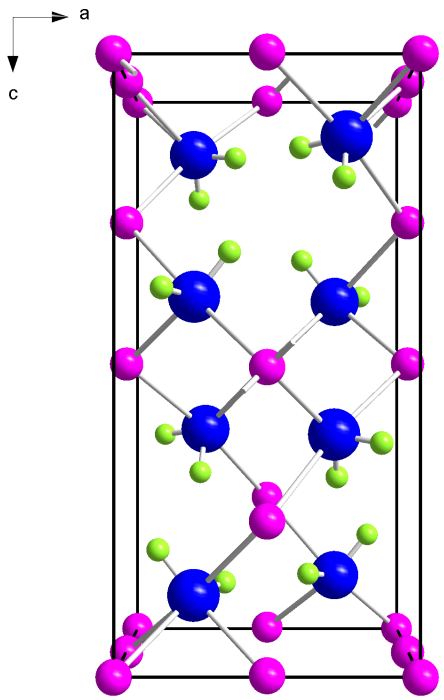

Figure 1-11: Representation of the structure of $LiNH_2$ (Li^+ - pink, N^{3-} - blue, H^+ - green)

The crystal structure of cubic Li_2NH has been studied in-depth by several PXD and PND investigations. Juza and Opp proposed the first crystal model of Li_2NH (space group *Fm-3m*) which adopts an *anti*-fluorite structure consisting of Li^+ and $[NH]^{2-}$, however the sites occupied by hydrogen atoms were not included. [86] A further, more recent study by Ohoyama *et al* was performed by PND which suggested a different crystal model in space group *F-43m* which exhibits face-centred cubic (fcc) symmetry. [100] In 2005, Noritake *et al* conducted a synchrotron X-ray diffraction experiment to determine the crystal structure and charge density analysis of Li_2NH. [101] Findings were in agreement with Juza and Opp where it was concluded that the imide crystallises in the *Fm-3m* space group and proposing that the hydrogen atoms occupy the 48h (Wyckoff notation) sites around the nitrogen atoms. The most recent study was

performed by Balogh *et al* in attempt to understand crystal structures and phase transformations of Li_2NH/D by PXD and PND. [102] The proposed model for the high temperature phase was a disordered cubic structure (space group *Fm-3m*) where deuterium atoms were randomized over the 192l sites. A representation of the high temperature cubic form of Li_2NH is displayed in Figure 1-12; this structure crystallises in the *Fm-3m* space group (a = 5.047 Å). [85]

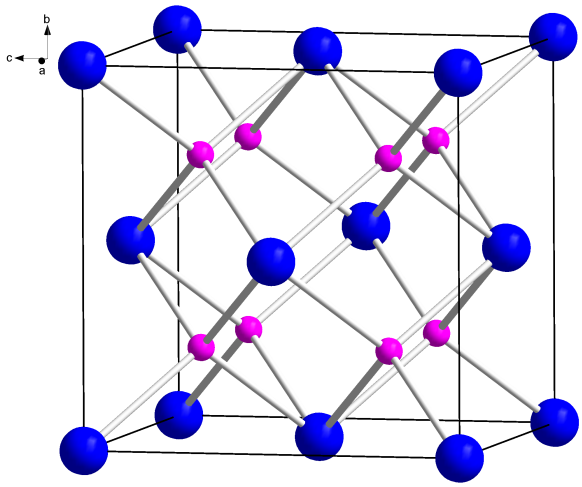

Figure 1-12: Representation of the structure of cubic Li_2NH as a conventional *anti*-fluorite with nitrogen atoms on a face-centred cubic lattice.
(Li^+ - pink, N^{3-} - blue)

1.2.3 Lithium Nitride Hydride, Li_4NH

A further Li-N-H material is known, lithium nitride hydride (Li_4NH), which was reported by Marx in 1997. [103] Li_4NH was synthesised by Marx using a 1:1 ratio of Li_3N:LiH and heating to 673 K for 6 hours under an argon atmosphere. Synthesis was performed under an argon atmosphere to prevent the formation of Li_2NH which would occur if the reaction was performed under nitrogen or hydrogen. Powder X-ray diffraction and powder neutron diffraction analysis of Li_4NH was performed by Marx to determine the structure of the material. The lattice parameters of the tetragonal Li_4NH (space group *I41/a*) structure were reported as a = 4.8868 (1) Å and c = 9.9321 (3) Å (PND). The unit cell of Li_4NH can be thought of in terms of two *anti*-fluorite unit cells; it is a doubled face-centred cubic (FCC) cell. Lithium atoms occupy all tetrahedral holes in the anion close packed lattice making the structure a tetragonal variant of close packing. Nitride and hydride ions are ordered along the axis of the doubled FCC cell as

illustrated in Figure 1-13. Redetermination of the structure was then performed by Niewa and Zherebtsov in 2002. [104]

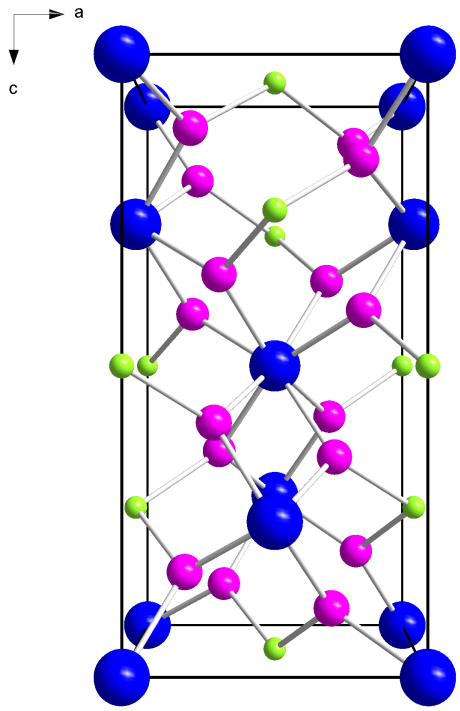

Figure 1-13: Representation of the structure of Li_4NH.
(Li^+ - pink, N^{3-} - blue, H^+ - green).

Marx stated that within the structure of Li_4NH, each atom had four equivalent neighbours sited on the corners of a stretched tetrahedron. [103] A further eight dissimilar neighbours are present and it was reported that this changes the coordination geometry of Li_4NH to a cuboctahedron; a polyhedron consisting of eight triangular faces and six square faces (Figure 1-11). The bond co-ordination of Li_4NH can be more clearly observed in Figure 1-14.

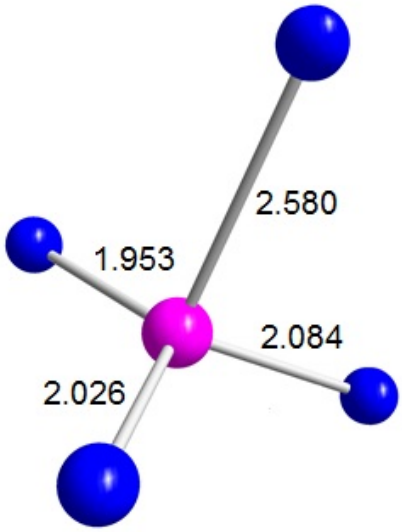

Figure 1-14: Bond coordination environment of the LiN_4 tetrahedron in tetragonal Li_4ND based on the interatomic distances obtained from Rietveld refinement of PND data at 323 K (Li^+ - pink, N^{3-} - blue).

In terms of the reactivity of Li_4NH, Marx proposed that reacting finely ground mixtures of Li_4NH and Li_2NH in different ratios would form non-stoichiometric phases but to-date no further reports have been published by this author. Subsequent to the proposal by Marx, Weidner *et al* and Bull *et al* reported that a non-stoichiometric intermediate occurs between Li_4ND and Li_2ND [102] during deuteration of Li_3N; this phase is known as a 'quasi-imide' which has a composition of $Li_{2+x}ND$ (x = 0 - 0.7). [105, 106] A further study focusing on Li_4NH and $Li_{2-x}NH_{1+x}$ (x = 0, 0.5, 1) has been published by Crivello *et al* [107] which also described the formation of an intermediate phase adding further confirmatory evidence to the fact that the original pathway of hydrogenation of Li_3N described by Chen *et al* is not as simple as was initially reported. [81]

1.3 Scope of this work

The following chapters include further exploration into the synthesis and characterisation of various nitride materials as the basis of solid state hydrogen storage media. Novel and conventional synthetic methods for the preparation of nitride materials were employed and compared throughout this work. This thesis focuses on Li_3N and the significant role it plays in each chapter of this thesis highlights its importance as a potential hydrogen storage medium.

Firstly, a study of the effects of ball milling to encourage a phase transition in Li_3N was performed and structural characterisation of the product was investigated by PXD and

PND. Little structural information has been reported on β-Li_3N however its importance in comparison to α-Li_3N should not be underestimated as in terms of ionic conductivity, both polymorphs exhibit the same order of magnitude of Li^+ conductivity therefore indicative of its potential as a Li_3N-based lithium ionic electrolyte for lithium ion rechargeable batteries. [22]

Although Li-N-H shows great potential as a hydrogen storage system, the pathways involved in the absorption and desorption of hydrogen are not fully understood. Based on beliefs that a minority phase of Li_4NH as well as Li_2NH form on hydrogenation (deuteration) of Li_3N, subsequent studies of reactions involving these two products are investigated in this work to gain an understanding of the reaction conditions under which non-stoichiometric 'quasi-imide' phases form, in addition to studies conducted by Weidner *et al*. [105] Further PND studies were conducted on Li_4ND and Li_2ND to understand their behaviour at variable temperatures.

Further work involving Li_3N and its ability to react with another binary nitride, Ca_3N_2, in attempt to synthesise a ternary nitride, LiCaN was also investigated. Previous studies on the Li-Ca-N system by PXD have suggested that it is a distorted orthorhombic *anti*-fluorite however in order to ascertain a definitive structural model as well as the likelihood of possible defect structures, PND was performed. Information on the Li-Ca-N system is relatively limited in comparison to the Li-Mg-N system for example, therefore PND studies were performed to investigate any similarities between the systems and to lay a foundation for a full systematic study of the process and mechanism of hydrogenation in this system.

Throughout this thesis, the success of novel synthetic methods has been highlighted and a report of full structural analysis on the various materials studied by PXD and PND is reported.

1.4 References

[1] R. Juza and H. Hahn, *Zeitschrift für Anorganische und Allgemeine Chemie*, 1938, **239**, 282

[2] R. Juza and W. Sachsze, *Zeitschrift für Anorganische und Allgemeine Chemie*, 1945, **253**, 95

[3] R. Juza, K. Langer and K. von Brenda, *Angew*andte *Chemie International Edition in English*, 1968, **7**, 360

[4] F. J. DiSalvo and S. J. Clarke, *Current Opinion in Solid State and Materials Science*, 1996, **1**, 241

[5] U. v. Alpen, *Journal of Solid State Chemistry*, 1979, **29**, 379

[6] F. J. DiSalvo, *Science*, 1990, **247**, 649

[7] U. v. Alpen, *Journal of Solid State Chemistry*, 1979, **29**, 379

[8] J. Etourneau, J. Portier and F. Monil, *Journal of Alloys and Compounds*, 1992, **188**, 1

[9] R. Kniep, *Pure and Applied Chemistry*, 1997, **69**, 185

[10] R. Niewa and F. J. DiSalvo, *Chemistry of Materials*, 1998, **10**, 2733

[11] D. H. Gregory, *Journal of the Chemical Society Dalton Transactions*, 1999, 259

[12] D. H. Gregory, *Coordination Chemistry Reviews*, 2001, **215**, 301

[13] D. Fischer and M. Jansen, *Angew*andte *Chemie International Edition in English*, 2002, **41**, 1755

[14] E. Zintl and G. Brauer, *Zeitschrift fü*r *Elektrochemie und Angewandte Physikalische Chemie*, 1935, **41**, 102

[15] A. Rabenau and H. Schulz, *Journal of the Less-Common Metals*, 1976, **50**, 155

[16] H. J. Beister, S. Haag, R. Kniep, K. Strössner and K. Syassen, *Angew*andte *Chemie Int*ernational *Edition in English*, 1988, **27**, 1101

[17] M. Mali, J. Roos and D. Brinkmann, *Physical Review B*, 1987, **36**, 3888

[18] A. Lazicki, B. Maddox, W. J. Evans, C. –S. Yoo, A. K. McMahan, W. E. Pickett, R. T. Scalettar, M. Y. Hu and P. Chow, *Physical Review Letters*, 2005, **95**, 165503

[19] G. Brauer and E. Zintl, *Zeitschrift für Physikalische Chemie*, 1937, **837**, 323

[20] B. A. Boukamp and R. A. Huggins, *Materials Res*earch *Bull*etin, 1978, **13**, 23

[21] D. H. Gregory, P. M. O'Meara, A. G. Gordon, J. P. Hodges, S. Short and J. D. Jorgensen, *Chemistry of Materials*, 2002, **14**, 2063

[22] W. Li, G. Wu, C. Moysés Araújo, R. H. Scheicher, A. Blomqvist, R. Ahuja, Z. Xiong, Y. Feng and P. Chen, *Energy and Environmental Science*, 2010, **3**, 1524

[23] N. E. Brese and M. O'Keeffe, *Journal of Solid State Chemistry*, 1990, **87**, 134

[24] O. Reckeweg and F. J. DiSalvo, *Solid State Sciences*, 2002, **4**, 575

[25] U. Steinbrenner and A. Simon, *Zeitschrift für Anorganische und Allgemeine Chemie*, 1998, **624**, 228

[26] P. Eckerlin and A. Rabenau, *Zeitschrift für Anorganische und Allgemeine Chemie*, 1964, **304**, 218

[27] C. L. Hoenig and A. W. Searcy, *Journal of the American Ceramic Society*, 1967, **50**, 460

[28] M. v. Stackelberg and R. Paulus, *Zeitschrift für Physikalische Chemie*, 1933, **B22**, 305

[29] O. Reckeweg, C. Lind, A. Simon and F. J. DiSalvo, *Zeitschrift für Naturforschung, Teil B. Anorganische Chemie, Organische Chemie*, 2003, **58**, 159

[30] D. Hall, G. E. Gurr and G. A. Jeffrey, *Zeitschrift für Anorganische und Allgemeine Chemie*, 1969, **369**, 108

[31] D. R. Glasson and S. A. A. Jayaweera, *Journal of Applied Chemistry*, 1968, **18**, 77

[32] O. Reckeweg and F. J. DiSalvo, *Zeitschrift für Anorganische und Allgemeine Chemie*, 2001, **627**, 371

[33] A. S. Bailey, P. Hubberstey, R. W. Hughes, C. Ritter and D. H. Gregory, *Chemistry of Materials*, 2010, **22**, 3174

[34] H. Mathewson, *Zeitschrift für Anorganische und Allgemeine Chemie*, 1905, **48**, 191

[35] D. W. Mitchell, *Industrial and Engineering Chemistry*, 1949, **41**, 2027

[36] J. David, Y. Laurent and J. Lang, *Bulletin de la Société Française deMinéralogie et de Cristallographie*, 1977, **72**, 1949

[37] D. E. Partin, D. J. Williams and M. O'Keeffe, *Journal of Solid State Chemistry*, 1997, **132**, 56

[38] Y. Laurent, J. Lang and M. –T. Le Bihan, *Acta Crystallographica B*, 1968, **24**, 494

[39] E. T. Keve and A. C. Skapski, *Inorganic Chemistry*, 1968, **7**, 1757

[40] P. Höhn, S. Hoffman, J. Hunger, S. Leoni, F. Nitsche, W. Schnelle and R. Kniep, *Chemistry – A European Journal*, 2009, **15**, 3419

[41] Y. Laurent, *Revue de Chimie Minérale*, 1968, **5**, 1019

[42] O. Reckeweg and F. J. DiSalvo, *Angewandte Chemie International Edition in English*, 2000, **39**, 412

[43] O. Reckeweg and F. J. DiSalvo, *Zeitschrift für Naturforschung, Teil B. Anorganische Chemie, Organische Chemie*, 2008, **63**, 530

[44] Y. Laurent, J. Lang and M. –T. Le Bihan, *Acta Crystallographica B*, 1969, **25**, 199

[45] V. P. Itkin and C. B. Alcock, *Bulletin of Alloy Phase Diagrams*, 1990, **11**, 497

[46] D. H. Gregory, M. G. Barker, P. P. Edwards and D. J. Siddons, *Inorganic Chemistry*, 1995, **34**, 5195

[47] A. M. Heyns, L. C. Prinsloo, K. –J. Range and M. Stassen, *Journal of Solid State Chemistry*, 1998, **137**, 33

[48] H. H. Franck, M. A. Bredig and G. Hoffmann, *Naturwiss*, 1933, **21**, 330

[49] H. Hartmann and H. J. Fröhlich, *Zeitschrift für Anorganische und Allgemeine Chemie*, 1934, **218**, 190

[50] R. S. Bradley, D. C. Munro and M. Whitfield, *Journal of Inorganic and Nuclear Chemistry*, 1966, **28**, 1803

[51] Y. Laurent, J. David and J. Lang, *Comptes Rendus de L'Académie des Sciences Paris*, 1964, **259**, 1132

[52] D. H. Gregory, A. Bowman, C. F. Baker and D. P. Weston, *Journal of Materials Chemistry*, 2000, **10**, 1635

[53] J. F. Brice, J. P. Motte and J. Aubry, *Revue de Chimie Minérale*, 1975, **12**, 105

[54] R. D. Shannon, *Acta Crystallographica A*, 1976, **32**, 751

[55] J. F. Brice, J. P. Motte and R. Streiff, *Comptes Rendus de L'Académie des Sciences Paris*, 1969, C269, 910

[56] M. Somer, W. Carrillo-Cabrera, E. M. Peters, K. Peters, H. G. von Schnering, *Zeitschrift für Kristallographie*, 1996, **211**, 635

[57] R. Juza and F. Hund, *Zeitschrift für Anorganische und Allgemeine Chemie*, 1948, **257**, 1

[58] R. Juza and F. Hund, *Naturwissenschaften*, 1946, **33**, 121

[59] H. Yamane, T. H. Okabe, O. Ishiyama, Y. Waseda and M. Shimada, *Journal of Alloys and Compounds*, 2001, **319**, 124

[60] G. Cordier, A. Gudat, R. Kniep and A. Rabenau, *Angewandte Chemie International Edition in English*, 1989, **28**, 1702

[61] W. X. Yuan, J. Li, G. Wang, A. G. Cheng and X. Zhao, *Journal of Crystal Growth*, 2006, **290**, 621

[62] J. F. Brice, J. P. Motte and J. Aubry, *Comptes Rendus de L'Académie des Sciences Paris*, 1970, **C270**, 1658

[63] J. F. Brice and J. Aubry, *Comptes Rendus de L'Académie des Sciences Paris*, 1970, **C271**, 825

[64] G. B Collins, *Microwave Magnetrons*, 1948, 6, 1st Edition, McGraw-Hill, New York

[65] H. Sobol and K. Tomiyasu, *IEEE Transactions on Microwave Theory and Techniques*, 2002, **50**, 594

[66] H. Sobol, *IEEE Transactions on Microwave Theory and Techniques*, 1984, **32**, 1170

[67] J. M. Osepchuk, *IEEE Transactions on Microwave Theory and Techniques*, 1984, **32**, 1200

[68] S. W. Lui and J. P. Wightman, *Journal of Applied Chemistry and Biotechnology*, 1971, **21**, 168

[69] Developments in Microwave Chemistry, RSC Special Report, *Chemistry World*, **2** (4), 2005

[70] A. G. Whittaker and D. M. P. Mingos, *Journal of the Chemical Society Dalton Transactions*, 1993, 2541

[71] J. D. Houmes and H. –C. zur Loye, *Journal of Solid State Chemistry*, 1997, **130**, 266

[72] N. Sorbie , R. I. Smith and D. H. Gregory, *unpublished results*

[73] D. H. Gregory, *The Chemical Record*, 2008, **8**, 229

[74] T. K. Mandal and D. H. Gregory, *Annual Reports on the Progress of Chemistry Section A*, 2009, **105**, 21

[75] Targets for Onboard Hydrogen Storage Systems for Light-Duty Vehicles, US Department of Energy, Office of Energy Efficiency and Renewable Energy and The Freedom CAR and Fuel Partnership, 2009

[76] B. Sakintuna, F. Lamari-Darkrim and M. Hirscher, *International Journal of Hydrogen Energy*, 2007, **32**, 1121

[77] S. Orimo, Y. Nakamori, J. R. Eliseo, A. Züttel and C. M. Jensen, *Chemical Reviews*, 2007, **107**, 4111

[78] P. Chen, Z. Xiong, J. Luo, J. Lin and K. L. Tan, *Journal of Physical Chemistry B*, 2003, **107**, 10967

[79] Y. H. Hu and E. Ruckenstein, *Industrial and Engineering Chemistry Research*, 2003, **42**, 5135

[80] Y. H. Hu and E. Ruckenstein, *Journal of Physical Chemistry A*, 2003, **107**, 10967

[81] P. Chen, Z. Xiong, J. Luo, J. Lin and K. L. Tan, *Nature*, 2002, **420**, 302

[82] F. W. Dafert and R. Miklauz, *Monatshefte für Chemie*, 1909, **30**, 649

[83] F. W. Dafert and R. Miklauz, *Monatshefte für Chemie*, 1910, **31**, 981

[84] F. W. Dafert and R. Miklauz, *Monatshefte für Chemie*, 1912, **33**, 63

[85] O. Ruff and H. Goeres, *Chemische Berichte*, 1911, **44**, 502

[86] R. Juza and K. Opp, *Zeitschrift für Anorganische und Allgemeine Chemie*, 1951, **266**, 325

[87] R. Juza and K. Opp, *Zeitschrift für Anorganische und Allgemeine Chemie*, 1951, **266**, 313

[88] T. Ichikawa, S. Isobe, N. Hanada and H. Fujii, *Journal of Alloys and Compounds*, 2004, **365**, 271

[89] Y. Kojima and Y. Kawai, *Journal of Alloys and Compounds*, 2005, **395**, 236

[90] G. Miceli, C. S. Cucinotta, M. Bernasconi and M. Parrinello, *Journal of Physical Chemistry C*, 2010, **114**, 15174

[91] L. L. Shaw, W. Osborn, T. Markmaitree and X. Wan, *Journal of Power Sources*, 2008, **177**, 500

[92] Y. Kojima and Y. Kawai, *Chemical Communications*, 2004, 2210

[93] H. Y. Leng, T. Ichikawa, S. Isobe, S. Hino, N. Hanada and H. Fujii, *Journal of Alloys and Compounds*, 2005, **404-406**, 443-447

[94] T. Markmaitree, R. Ren and L. L. Shaw, *Journal of Physical Chemistry B*, 2006, **110**, 20710

[95] C. B. Minella, C. Rongeat, R. Domènech-Ferrer, I. Lindemann, L. Dunsch, N. Sorbie, D. H. Gregory and O. Gutfleisch, *Faraday Discussions*, 2011, Advance article

[96] W. I. F. David, M. O. Jones, D. H. Gregory, C. M. Jewell, S. R. Johnson, A. Walton and P. P. Edwards, *Journal of the American Chemical Society*, 2007, **129**, 1594-1601

[97] A. Huq, J. W. Richardson, E. R. Maxey, D. Chandra and W.-M. Chien, *Journal of Physical Chemistry C*, 2007, **111**, 10712

[98] Y. B. Yang, X. D. Zhou, Q. Cai, W. J. James and W. B. Yelon, *Applied Physics Letters*, 2006, **88**, 041914

[99] H. Jacobs and R. Juza, *Zeitschrift für Anorganische und Allgemeine Chemie*, 1972, **391**, 271

[100] K. Ohoyama, Y. Nakamori, S. Orimo and K. Yamada, *Journal of the Physical Society of Japan*, 2005, **74**, 483

[101] T. Noritake, H. Nozaki, M. Aoki, S. Towata, G. Kitahara, Y. Nakamori and S. Orimo, *Journal of Alloys and Compounds*, 2005, **393,** 264

[102] M. P. Balogh, C. Y. Jones, J. F. Herbst, L. G. Hector Jr. and M. Kundrat, *Journal of Alloys and Compounds*, 2006, **420**, 326

[103] R. Marx, *Zeitchrift für Anorganische und Allgemeine Chemie*, 1997, **623**, 1912

[104] R. Niewa and D. A. Zherebtsov*, Zeitschrift für Kristallographie - New Crystal Structures*, 2002, **217**, 317

[105] E. Weidner, D. J. Bull, I. L. Shabalin, S. G. Keens, M. T. F. Telling and D. K. Ross, *Chemical Physical Letters*, 2007, **444**, 76

[106] D. J. Bull, E. Weidner, I. L. Shabalin, M. T. F. Telling, C. M. Jewell, D. H. Gregory and D. K. Ross, *Physical Chemistry Chemical Physics*, 2010, **12**, 2089

[107] J. –C. Crivello, M. Gupta, R. Černý, M. Latroche and D. Chandra, *Physical Review B,* 2010, **81**, 104113

2 Experimental

Using a range of synthetic methods, including conventional and microwave syntheses, various nitrides were prepared including lithium nitride, lithium nitride hydride and lithium calcium nitride.

A full range of techniques were required to characterise the materials prepared in this work fully. Although powder X-ray diffraction (PXD) was the main method for characterisation, complimentary techniques such as powder neutron diffraction enabled further investigation into the materials being studied. Structural refinements using the Rietveld method provide useful information on multi-phase samples resulting in a full data analysis.

Furthermore, experimental techniques such as scanning electron microscopy were employed to analyse the morphology of materials and thermogravimetric analysis and differential thermal analysis were used to study the stability and structural changes in materials in relation to temperature.

2.1 Air sensitive handling techniques

2.1.1 Dry Glove Boxes

Alkali and alkaline earth metal compounds and their respective nitrides are all moisture and air sensitive and therefore they must be handled in a glove box under an inert atmosphere; either a recirculating nitrogen-filled or argon-filled glove box (Saffron Scientific). The glove box is made of stainless steel with a glass window and Neoprene rubber gloves are attached to the glove box at two ports at the front. The recirculating glove boxes are kept free from air and moisture by continuous cycling of the nitrogen or argon atmosphere through molecular sieves and a catalyst. Typically oxygen levels are in the 0-5 ppm range and moisture levels in the 0-30 ppm region; these are monitored by analysers on the front of the glove box. Every 2 months the catalyst is regenerated by heating under a flow of H_2/N_2 (10:90%) for approximately 12 hours to remove any oxygen which is adsorbed to the water followed by subsequent heating under vacuum to remove the water by-product. With regards to the molecular sieve, this is regenerated by heating under vacuum for 12 hours. Access into the glove box is possible using an evacuable transfer port.

2.2 Synthetic Techniques

2.2.1 Ball Milling

In order to grind materials or achieve a phase transformation by applying an unknown pressure, a planetary ball mill was employed. The Retsch PM100 has a single grinding station into which the sample jar sits (Figure 2-1). The jar and the sun wheel move in a 2:1 ratio and requires the presence of a counterweight to prevent any oscillations disturbing the machine.

The grinding balls within the grinding jar are subjected to superimposed rotational movements known as Coriolis forces. This force is dependent on the velocity of the moving object together with the centrifugal force to fully describe the motion.

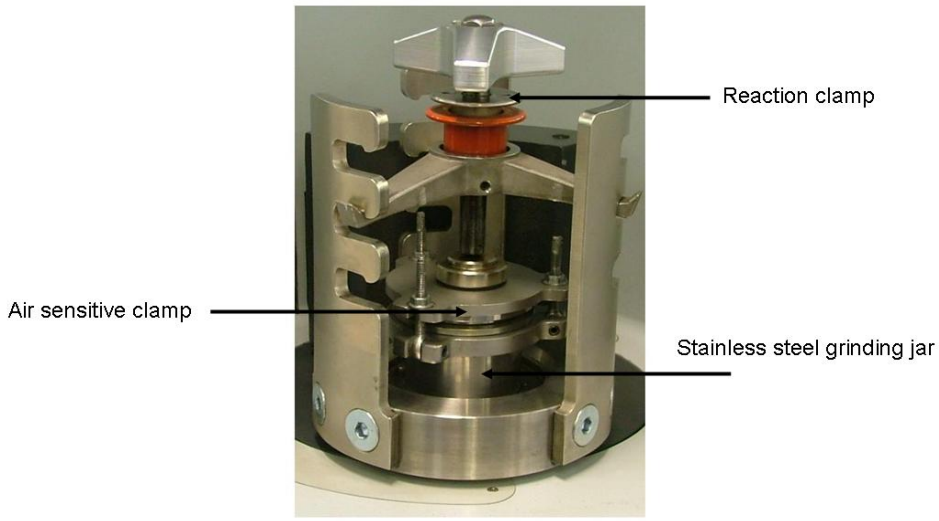

Figure 2-1: Retsch PM100 ball mill with air sensitive clamp for preparation of β–Li_3N

Various reaction parameters can be varied in order to achieve the desired product or result. The type of jar (e.g. agate or stainless steel), the type, number and size of grinding balls as well as the mass of material used all contribute to the formation of the final product.

2.2.2 Microwave Reactions

The synthesis of alkali metal binary nitrides and ternary nitrides (further details in respective sections) conventionally requires high temperatures and long reaction times but using microwaves can shorten reaction times markedly. In the electromagnetic spectrum (Figure 2-2), microwaves can be found between infrared radiation waves and radio waves (between 10^{-5} and 10^{3} m respectively) and they generally interact with materials in one of three ways: reflection, transmission or absorption.

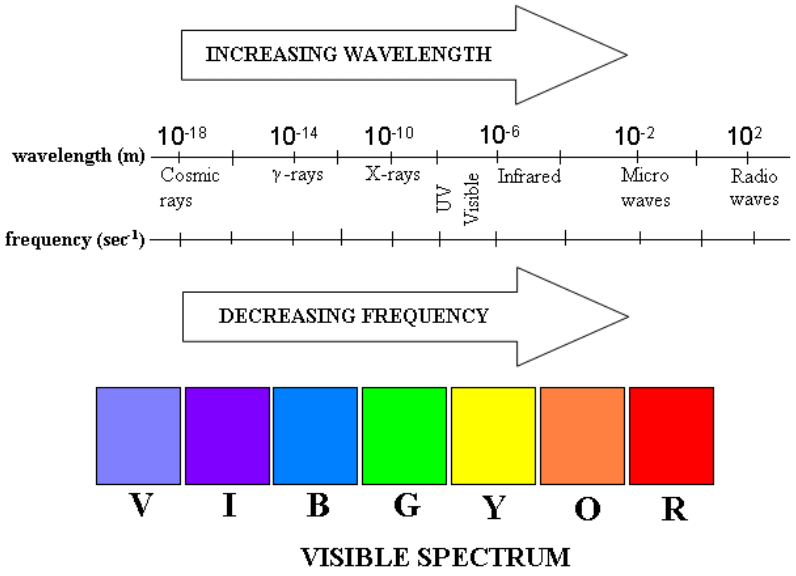

Figure 2-2: Schematic of the electromagnetic spectrum

Materials, like silica for example, transmit microwaves and therefore are used as reaction vessels. For synthetic purposes, microwave absorbing materials are employed as they use the energy generated from the microwave field, resulting in them heating quickly. Materials which couple to microwaves, such as ionic, dielectric, semi-conducting and semi-metallic materials, have dipolar absorption in the region of the reactor frequency, in these cases it is 2·45 GHz. Since not all materials couple to microwaves at this frequency, susceptors such as graphite or molybdenum can be used to aid heating.

For several decades, it has been known that electromagnetic waves can heat materials. [1] Two major effects are responsible for microwave heating; conduction and dipolar polarisation. In regards to the conduction mechanism, heat energy is generated through resistance to an electric current. The current is created by an oscillating electromagnetic field which causes oscillations of electrons or ions in the material. [2] The latter effect, dipolar polarisation, results from the difference in electronegativity values of individual atoms; ultimately creating a permanent electric dipole within the molecule. The resultant dipole is sensitive to electric fields and will constantly try to realign with them by rotating. This random rotating motion results in collisions between particles which is responsible for the generation of heat energy. The alignment of ions, in conduction and dipolar polarisation, in relation to the oscillating electromagnetic field is represented in Figure 2-3.

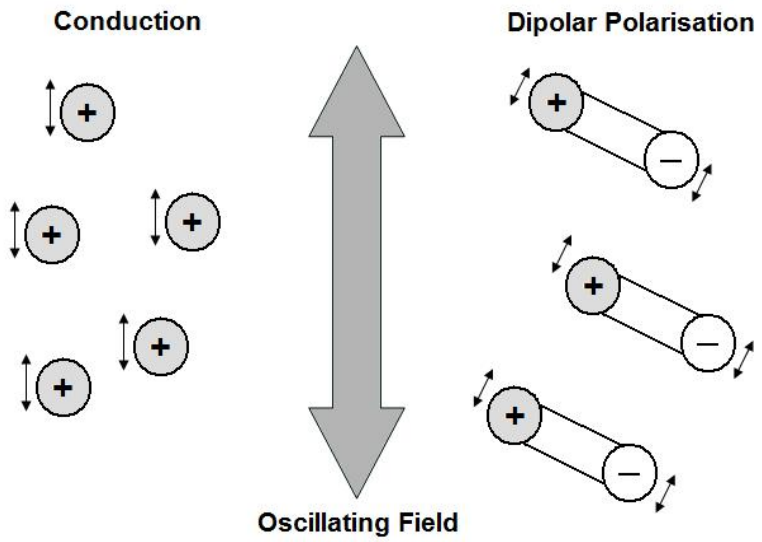

Figure 2-3: Schematic of Microwave Radiation Heating Methods

In order for dipolar polarisation to occur, the frequency of the oscillating field must be within a suitable range for allowance of particle-particle interaction. A very high frequency range results in the prevention of movement of particles within a polar molecule as the electric field does not allow sufficient time for molecules to realign. Therefore a very high frequency range inhibits inter-particle interaction resulting in no heating effect. In contrast, a low frequency range provides the polar molecule with ample time to align itself in phase with the electric field. Although some energy is gained by the molecule by in phase alignment, energy is also lost by random collisions and therefore, the heating effect is low. [2]

For electromagnetism to have a useful purpose with synthetic materials chemistry, a frequency between the two aforementioned extremes is required. Microwave irradiation fulfils this need as its frequency is low enough to allow dipoles time to rotate but high enough to ensure that alignment and rotation does not follow the electric field exactly. As the dipole of the molecule changes to align with the electric field, the electric field itself is already changing therefore creating a phase difference present between the orientation of the electric field and the dipole. It is the phase difference that causes energy to be lost from the system; the dipole loses energy in collisions which in turn gives rise to dielectric heating in an applied microwave field. Dielectric heating results in the formation of thermal energy which is responsible for driving the reaction. [3] The dielectric constant, ε^*, describes the dielectric properties of homogenous materials [4] and consists of two parts, ε' and ε'' .

It is expressed as:

$$\varepsilon^* = \varepsilon' + i\varepsilon'' \tag{1}$$

where ε′ is the relative permittivity (a measure of the ability of a molecule to be polarised by an electric field), ε″ is the dielectric loss (which is indicative of the ability of a material to convert stored energy to heat energy).

The dielectric loss must be taken into consideration. This factor relates directly to the electrical conductivity, σ, of the material and is expressed as:

$$\varepsilon'' = \frac{\sigma}{\varepsilon_o f} \tag{2}$$

where ε_0 is the permittivity of free space and f is the frequency.

Another factor must be considered at very high and very low frequencies or where a static field is present. If the frequency is unsuitable or a static field is present, ε′, will equal the total dielectric constant of the material but where there is energy conversion, for example when electromagnetic energy is converted to heat energy, ε″ (the dielectric loss) is non-zero indicating microwave absorption. Furthermore, the loss angle, δ, which defines the ability of the material to absorb microwaves and dissipate it as heat energy at a certain temperature and frequency must also be taken into consideration:

$$Tan\delta = \varepsilon'' / \varepsilon' \tag{3}$$

In certain cases, magnetic polarisation may also play a part in the heating effect. This is dependent on the magnetic properties of the material, however, a discussion of this is out with the scope of this work.

Although the frequency of a microwave reactor is usually fixed, the loss tangent is important since temperature affects the dielectric properties of the material. An increase in temperature results in a decrease in the relaxation time for the dipoles which allows the dipoles to follow the electric field more easily resulting in further heating. [5] On the assumption that the sample heats uniformly, in terms of a dielectric heating process, Eq. 4 applies.

$$\frac{dT}{dt} = \frac{K \cdot \varepsilon'' \cdot f \cdot E^2}{\rho \cdot C} \tag{4}$$

where *dT/dt* is the rate of change of temperature of the material, *K* is a constant, ρ is the density of the material (kg/m^2), *C* is the specific heat capacity of the material (J/kg ^{o}C) and *E* is the electric field strength.

Furthermore, it is necessary to account for any energy loss in the system which leads to a decrease in temperature due to surface radiation:

$$\frac{dT}{dt} = \frac{-e \cdot \alpha . A_s}{\rho \cdot C \cdot V_s} \cdot T^4 \tag{5}$$

where *e* is the sample emissivity ratio, α is the Stefan-Boltzmann constant, A_s is the surface area of the sample (m^2) and V_s is the volume of the sample (m^3).

Ultimately, the conversion of microwave energy into heat energy is dependent on both dielectric and thermal properties of a material. Dielectric and thermal properties affect each other however it is difficult to monitor a temperature rise due to the non-uniformity that occurs when using a microwave field and any changes that may occur in dielectric properties of a material at a given temperature. Microwave energy is not absorbed by solids at room temperature which is particularly important in regards to the dielectric properties of a material. With regards to alumina, for example, the conductivity of alumina increases as the temperature increases. It should be noted that an increase in temperature may have negative implications such as thermal runaway [6] where an increase in temperature can result in a change in reaction rate subsequently leading to a further increase in temperature. Close monitoring of the sample and of the reaction is required to prevent thermal runaway. [7]

2.2.3 Microwave Applicators

For the microwave reactions performed, two types of microwave apparatus were employed; a multi-mode domestic microwave oven and a single-mode microwave. The shape and forms of microwave cavities are varied however they are basically voids which are enclosed by high-conductivity metal walls. [8] The first domestic microwave oven was introduced commercially in 1947 and during 1980-82, microwave radiation was developed

for organic reactions by chemists. [2] Within multi-mode microwaves, the aim is to create a chaotic environment within the reactor to promote dispersion of the radiation therefore increasing the effective heating area. Creating disorder within the multi-mode microwave is promoted by avoiding the generation of a standing wave pattern inside. In contrast to this, generation of a standing wave pattern in single-mode microwave reactors is essential for heating. A standing wave is one which remains in a constant position. Figure 2-4 illustrates two identical standing (stationary) waves together with nodes and antinodes. Nodes represent points at which the amplitude is equal to zero and antinodes are the point at which the amplitude is at the maximum. In regards to microwave heating, the design of a single-mode reactor is crucial; the sample must be an appropriate distance from the magnetron to ensure heating therefore the sample must be placed at the antinodes of the standing electromagnetic wave pattern. The major advantage of employing a single-mode reactor over a multi-mode reactor is that the microwave field can be focussed at a certain location therefore heating the sample directly. [9]

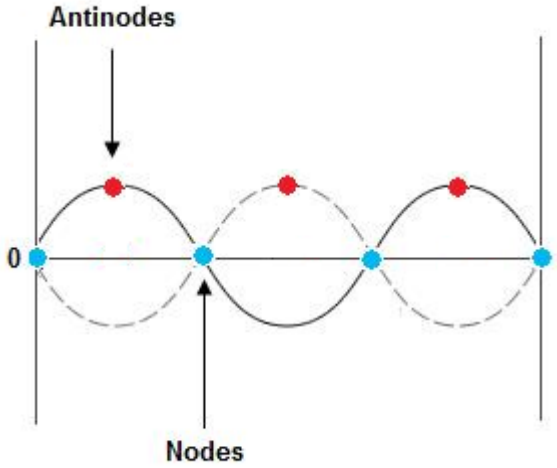

Figure 2-4: A standing wave pattern in a single-mode microwave reactor with antinodes highlighted in red and nodes highlighted in blue

2.2.4 Preparation of materials using microwave radiation

For microwave reactions, all preparations were carried out in a nitrogen-filled recirculating glove box. Material was loaded into thick-walled (~2 mm) silica tubes of 8 mm internal diameter. The silica tubes were then either sealed under a dynamic vacuum (10^{-4} Torr) using a glassblowing torch or using a rubber septum.

The silica tubes were then placed in either a domestic microwave oven in a fume hood or a single mode cavity microwave with a blast screen placed in front as a safety precaution. Tubes in the domestic microwave oven were supported by a firebrick stand. In both cases,

material was irradiated until no further reaction was visible (further details in respective sections). For microwave irradiation experiments, careful monitoring is required as temperatures can rise quickly.

2.3 Synthesis

2.3.1 Preparation of binary alkali metal nitrides (Li_3N, Ca_3N_2)

2.3.1.1 Preparation of α–Li_3N

Li_3N was synthesised by preparing a Li/Na alloy under an argon atmosphere in a recirculating glove box. [10] Approximately 7 g of lithium metal pieces were submerged in a pool of sodium metal (~ 50 g) in a stainless steel crucible. After cooling, the crucible was then transferred into a stainless steel reaction vessel containing a cold finger (Figure 2-5) which was evacuated before applying a positive nitrogen pressure and heating to 733 K for 72 h.

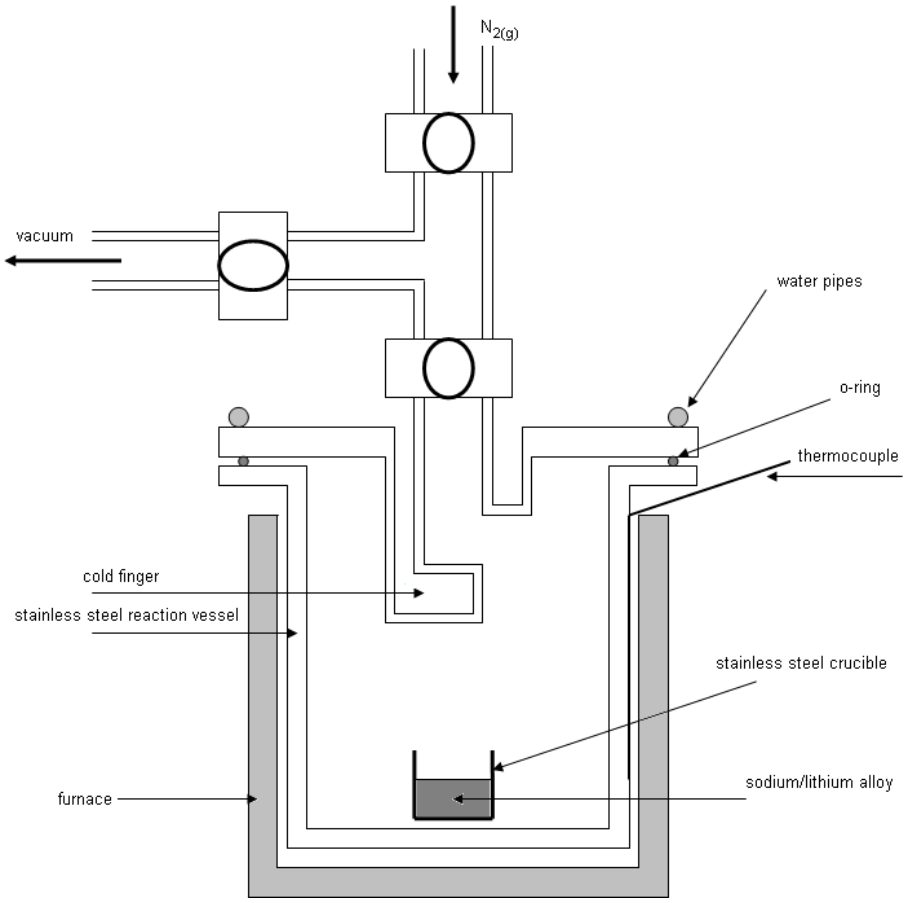

Figure 2-5: Schematic of the apparatus used for the preparation of α–Li_3N

The reaction was then allowed to cool before being heated again to 733 K for 12 h under vacuum to remove excess sodium metal. Afterwards, the reaction was allowed to cool and

was then opened under an argon-atmosphere and the purity of the product obtained was determined by PXD.

2.3.1.2 Preparation of β–Li_3N

Two synthetic methods were employed to prepare β-Li_3N; ball milling synthesis and a multi-anvil high pressure experimental method.

Firstly synthesis by ball milling was performed using both commercial or laboratory synthesised Li_3N (~ 0.7 g). The material was loaded into a 50 ml stainless steel jar together with ten 10 mm stainless steel grinding balls (Figure 2-6), under a nitrogen atmosphere. The jar was tightly sealed using an air-sensitive clamp before being removed from the glove box. The jar was then locked into the sun wheel of the planetary ball mill (PM100) and the material was milled for approximately 25 hours (with a 30 second interval every 5 minutes with reverse rotation).

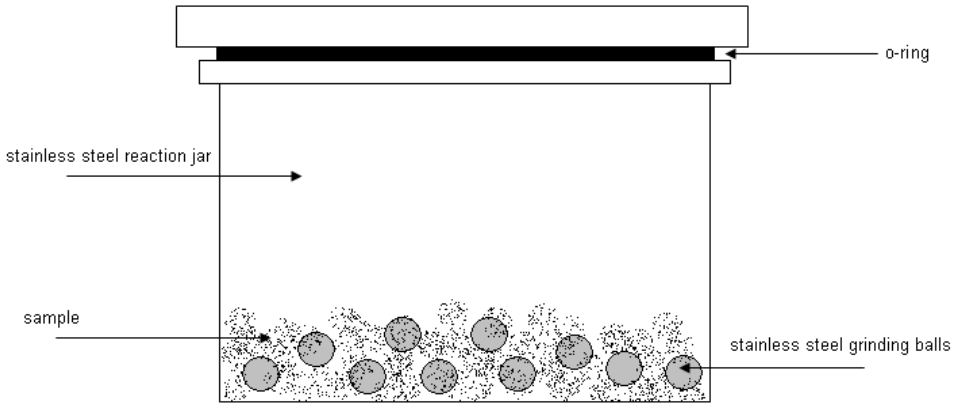

Figure 2-6: Schematic of apparatus used for the preparation of β–Li_3N

The material was then removed from the jar, under a nitrogen atmosphere of a recirculating glove box, appearing the same red/purple colour, identical to the un-milled sample. Product determination was done by PXD.

The second synthetic method employed for preparation of β-Li_3N was by a multi-anvil high pressure procedure. Experiments, using both commercial and laboratory-synthesised α-Li_3N, were performed by Dr. Gunter Heymann and Prof. Hubert Huppertz at the University of Innsbruck, Austria. Firstly, Li_3N was pre-compressed using a steel plunger before being loaded into a Mo capsule. The capsule was then placed inside a BN crucible (V = 35 mm^3). All preparations were performed within a recirculating glove box (MBraun Unilab (1200/780)) under a nitrogen atmosphere.

An octahedral pressure cell (Figure 2-7) was used and the sample was placed directly in the centre of the octahedron. In experiments where heating was required, an additional

zirconium sleeve was employed to provide thermal insulation and the temperature was measured using a thermocouple.

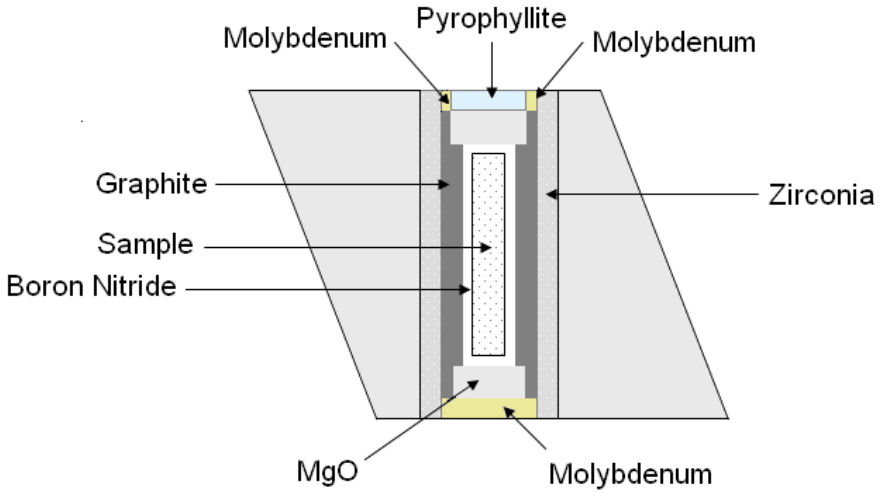

Figure 2-7: Schematic of a cross section of an octahedral pressure cell

After setting the inner part into a drilled octahedron, eight tungsten carbide cubes are placed around it where the triangular faces of the cubes have to fit onto the faces of the octahedron aided by pyrophyllite gaskets are employed as spacers to ensure a good fit. The assembly employed in this work was an 18/11 assembly where the octahedron has an edge length (OEL) of 18 mm and a truncation edge length (TEL) of 11 mm. [11] The completely assembled octahedron was placed inside a Walker module, [12] a simplified multi-anvil system for high pressure and high temperature experiments, of a Voggenreiter 1000 tonne press. [13]

2.3.1.3 Preparation of Ca_3N_2

Ca_3N_2 was synthesised by the direct reaction of calcium metal with nitrogen gas. [10] A piece of calcium metal (~ 6 g) was cleaned under an argon atmosphere in a recirculating glove box before being placed inside a stainless steel crucible. The crucible was then transferred into a stainless steel reaction vessel (see Figure 2-5), which was subsequently evacuated before being heated for 24 h at 923 K under a positive nitrogen pressure. After cooling, the reaction vessel was opened under a nitrogen atmosphere. The purity of the sample was then determined by PXD.

2.3.2 Preparation of Ternary Nitrides

2.3.2.1 Preparation of LiCaN

LiCaN can be synthesised conventionally [14] by reacting Li_3N and Ca_3N_2 under a static nitrogen atmosphere, using a 25 wt. % excess of Li_3N. The reactants were ground together in a nitrogen glove box before pelletising the material using a 13 mm pellet die; the pellet was pressed for 30 minutes under a pressure of approximately 3.3 kbar. The pellet was then transferred into a stainless steel crucible which was placed inside a stainless steel reaction vessel (Figure 2-8). The reaction vessel was heated to 973 K for 48 hours.

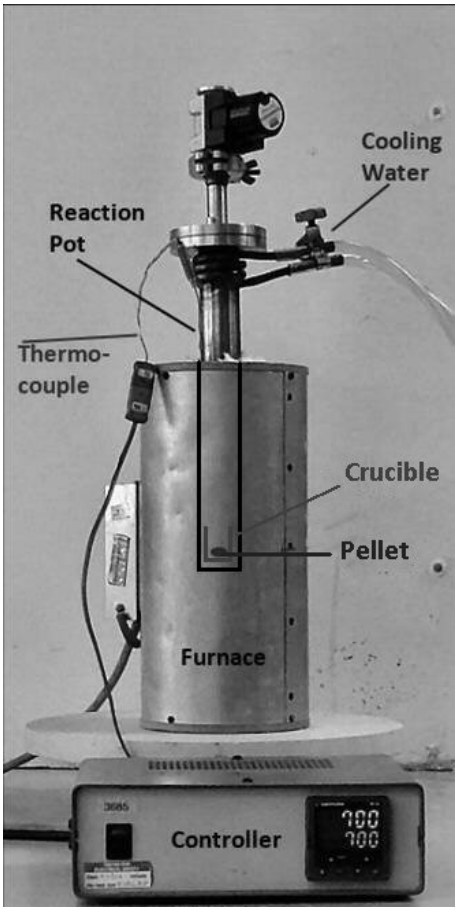

Figure 2-8: Apparatus for the conventional preparation of LiCaN

LiCaN can also be synthesised using microwave technology. Using the same stoichiometries, the material was loaded into a silica glass tube which was sealed either under vacuum or using a septum cap (Figure 2-9).

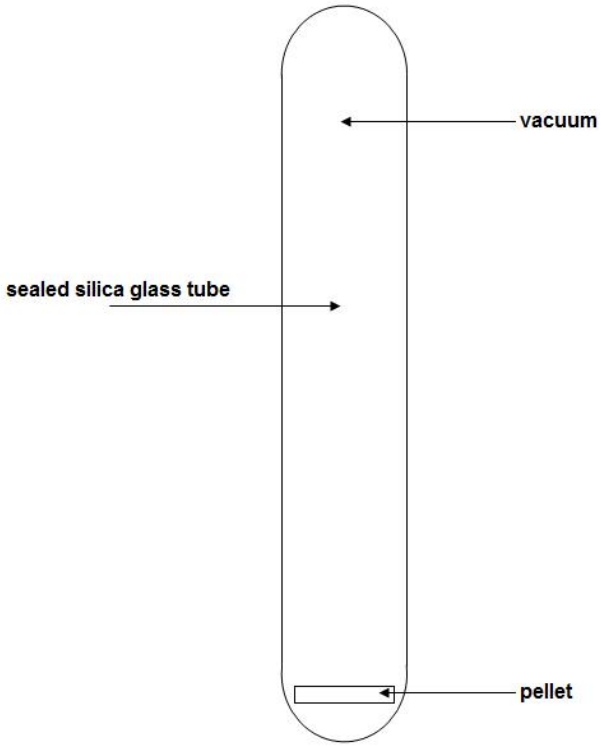

Figure 2-9: Schematic of a silica glass tube for the preparation of LiCaN

In a domestic microwave oven (Panasonic 4697 NN-TS53W) (Figure 2-10), the vacuum-sealed tube, supported by a firebrick, was reacted on medium power (approximately 400 watts) for 10 minutes. In addition to this, the product could be synthesised under a nitrogen atmosphere using a single mode microwave reactor (CEM Discover) (Figure 2-11). The silica glass tube was sealed with a septum cap under a nitrogen atmosphere of a recirculating glove box. The power was set to 300 watts and the reaction time was reduced to 2 minutes and 30 seconds. The purity of each sample was then determined by PXD.

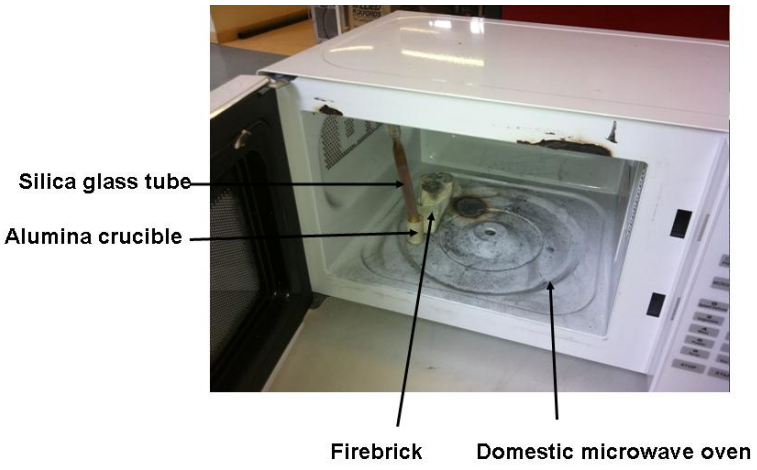

Figure 2-10: Reaction set-up using a multi-mode microwave reactor

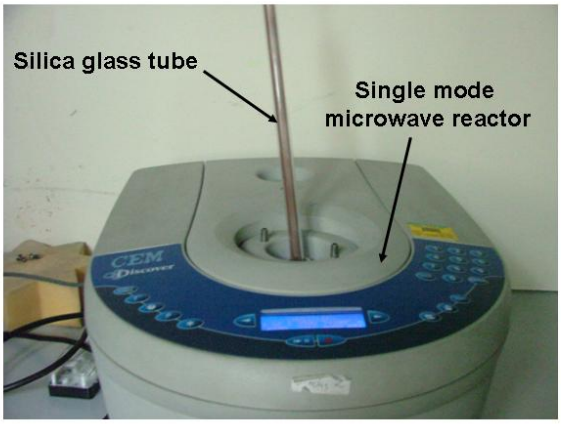

Figure 2-11: Reaction set-up using a single-mode microwave reactor

2.3.3 Preparation of Li-N-H compounds

2.3.3.1 Preparation of Li_4NH

Lithium nitride hydride [15] can be successfully synthesised both conventionally (under an argon atmosphere) and by microwave irradiation (under vacuum) by reacting Li_3N and LiH/D (LiD was used for PND experiments) in a 1:1·1 ratio. For both synthetic methods, the reactants were ground together under an inert atmosphere and pressed using a 13 mm pellet die for 30 minutes under an approximate pressure of 3.3 kbar.

Initially Li_4NH was synthesised conventionally; this involved placing the pelletised material into a stainless steel crucible which was transferred into a stainless steel reaction vessel. The reaction vessel (Figure 2-9) was sealed before removal from the glove box. After placing the reaction vessel inside a bench furnace, the temperature controller was programmed to heat for 6 h at 823 K.

In the second, novel method of synthesis (MW synthesis), a pellet was prepared and transferred into a silica glass tube, as illustrated in Figure 2-9, which was then sealed under vacuum using glass blowing equipment. The silica glass tube was then placed in either a multi-mode microwave reactor (Panasonic 4697 NN-TS53W) (Figure 2-10) or a single-mode microwave reactor (CEM Discover) (Figure 2-11).

2.3.3.2 Preparation of Li_2NH

The preparation of Li_2NH was performed by decomposing $LiNH_2$ (Sigma Aldrich, 95%). [16] Approximately 2 g of commercial $LiNH_2$ was loaded into a stainless steel crucible which was placed inside a stainless steel reaction vessel. The reaction vessel was sealed before removal from the glove box and then placed in a bench furnace. The set-up of the reaction is similar to the vacuum distillation stage of the synthesis of α-Li_3N (Figure 2-5). The reaction was heated to 823 K for 2 h under vacuum. The same procedure was followed for the preparation of Li_2ND for PND experiments ($LiND_2$ was provided by Dr D. J. Bull at the University of Salford).

2.4 Structure Determination and Product Characterisation

2.4.1 Powder X-ray Diffraction

For decades, powder X-ray diffraction (PXD) has become a vital tool for determining crystal structures in structural physics, chemistry and materials science [17] and is the main method for product characterisation in this thesis. PXD allows rapid identification of known phases within samples and enables the sample purity to be estimated. Further information can also be extracted from diffraction data by the indexing of unit cell parameters.

Characterising crystalline materials using X-ray diffraction allows the determination of the crystal type and the size of the unit cell. X-rays interact with the electron cloud surrounding the nucleus of an atom. Therefore there is a firm correlation between the atomic number of an atom and the intensity of the peaks in the powder pattern.

In 1913, W. H. Bragg and W. L. Bragg determined the first crystal structure of NaCl. [18, 19] After realising that X-ray diffraction behaves like reflections from planes of atoms within crystals, they continued to study diffraction and later explained the phenomenon as a series of equations.

Diffraction theory is conventionally based on Bragg's Law which describes why crystals appear to reflect X-rays at certain angles of incidence. Two parallel X-ray beams are diffracted by adjacent planes. Incident X-rays can reflect off a plane meaning that the angle of reflection will equal the angle of incidence. Constructive interference occurs if the waves are in phase and will arise at the angle where the path difference between waves is λ, an integer number of wavelengths.

The single Bragg equation, used as the basis for X-ray diffraction geometry, was derived by W. L. Bragg and expressed as:

$$n\lambda = 2dsin\theta \tag{6}$$

where *n* is an integer, λ describes the wavelength of incident X-rays, d is the perpendicular distance between the adjacent planes and θ is the angle of incidence.

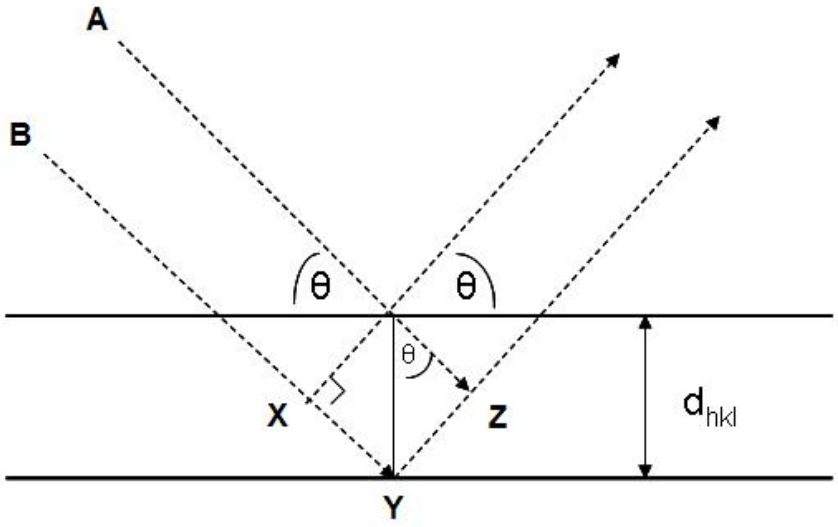

Figure 2-12: Schematic description for deriving Bragg's Law

In Figure 2-12, A and B denote two parallel incident X-ray beams and the 'reflected' beams must be in phase to produce constructive interference for reflection of reasonable intensity to be produced. Figure 2-12 shows that B must travel further, a distance of XYZ, than beam A to ensure that the beams remain in phase. The distance relationship between the intraplanar spacing d_{hkl} and the angle of incidence, θ, is given by:

$$XYZ = 2d\sin\theta \tag{7}$$

As previously stated, beam B must travel an extra distance of XYZ (the path difference) and this must be equal to a whole number of wavelengths:

$$XYZ = n\lambda \tag{8}$$

Therefore, combining the equations above achieves Bragg's law:

$$n\lambda = 2d\sin\theta \tag{9}$$

Patterns are obtained from X-ray diffraction due to the elastic scattering of the X-rays by the electrons present within the sample and are dependent on the appropriate orientation of a crystal in the X-ray beam. How well an atom scatters is dependent upon the number of electrons present in the atom. A greater number of electrons are present in heavier elements and therefore these elements will scatter more X-rays which will result in an increased intensity of the peaks observed. Comparatively, lighter elements do not have as many electrons and therefore do not scatter as well. Considering H, Li and N with the atomic numbers 1, 3 and 7 respectively, Figure 2-13 illustrates $(\sin\theta)/\lambda$ (which also means the scattering angle $2\theta = 0$) versus f (electrons). As $(\sin\theta)/\lambda$ (and therefore 2θ) increases, scattering from the electrons deceases as they become out of phase. Scattering points represent the difference associated with varying path lengths as 2θ increases.

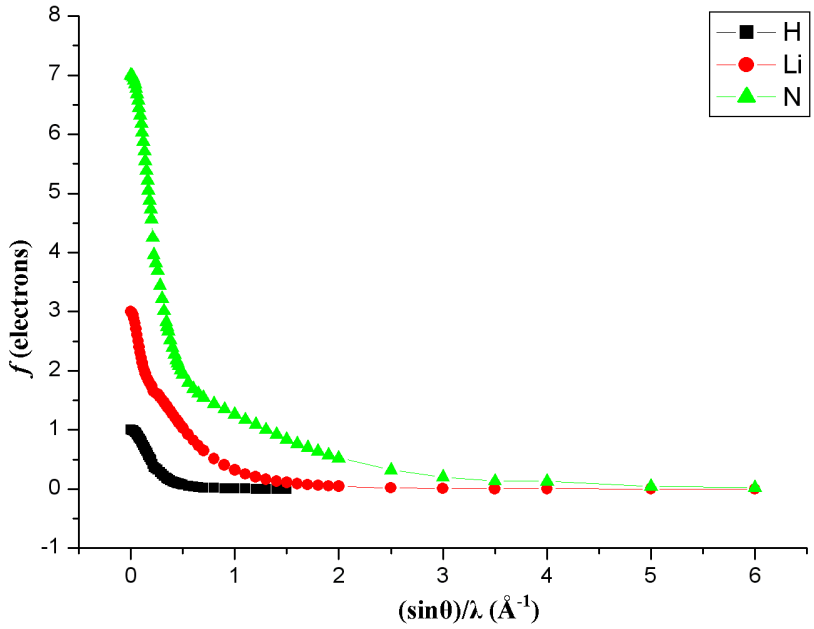

Figure 2-13: Dependence of atomic form factors, *f*, on scattering angle.

It should be noted that irregularities in diffraction patterns may occur and this can be due to preferred orientation. Powder X-ray diffraction is based on the principle that all crystalline orientations are present in the beam, however, if there appears to be non-random orientations of the crystal plane then this is referred to as preferred orientation.

Crystalline solids are composed of an array of identical points which are equivalent to each other by translational symmetry; this array is termed the lattice of the structure which, in turn, is composed of repeating units called the unit cell. The unit cell can be identified as the smallest repeating unit of the lattice which exhibits the full symmetry of the lattice, defined by having lengths a, b and c with angles α, β and γ (Figure 2-14).

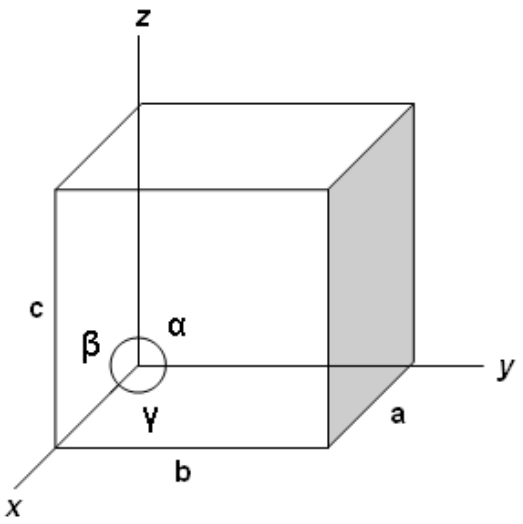

Figure 2-14: Definition of axis, unit cell dimensions and angles for a general unit cell [18]

All possible until cell shapes are shown in Table 2-1, these are known as the seven crystal systems.

Table 2-1: The seven crystal systems

System	Unit Cell
Triclinic	$\alpha \neq \beta \neq \gamma \neq 90^{o}$ $a \neq b \neq c$
Monoclinic	$\alpha = \gamma = 90^{o}, \beta \neq 90^{o}$ $a \neq b \neq c$
Orthorhombic	$\alpha = \beta = \gamma = 90^{o}$ $a \neq b \neq c$
Trigonal	$\alpha = \beta = \gamma \neq 90^{o}$ $a = b = c$
Hexagonal	$\alpha = \beta = 90^{o}, \gamma = 120^{o}$ $a = b = c$
Tetragonal	$\alpha = \beta = \gamma = 90^{o}$ $a = b \neq c$
Cubic	$\alpha = \beta = \gamma = 90^{o}$ $a = b = c$

The orientation of a crystal plane can be defined by considering where the plane cuts the *a, b* and *c* axes respectively and are called Miller Indices (*hkl*). These are a set of numbers which can be used to identify the plane or surface uniquely with the values being either positive, negative or zero. Each crystal system has an equation that denotes plane separation (d_{hkl}), these are expressed in Table 2-2.

Table 2-2: Equations for d-spacings in the different crystal systems

Crystal system	Expression for d_{hkl}
Cubic	$\frac{1}{d_{hkl}^2} = \frac{h^2+k^2+l^2}{a^2}$
Tetragonal	$\frac{1}{d_{hkl}^2} = \frac{h^2+k^2}{a^2} + \frac{l^2}{c^2}$
Orthorhombic	$\frac{1}{d_{hkl}^2} = \frac{h^2}{a^2} + \frac{k^2}{b^2} + \frac{l^2}{c^2}$
Hexagonal	$\frac{1}{d_{hkl}^2} = \frac{4}{3}\left(\frac{h^2+hk+k^2}{a^2}\right) + \frac{l^2}{c^2}$
Monoclinic	$\frac{1}{d_{hkl}^2} = \frac{1}{\sin^2\beta}\left(\frac{h^2}{a^2} + \frac{k^2\sin^2\beta}{b^2} + \frac{l^2}{c^2} - \frac{2hl\cos\beta}{ac}\right)$
Triclinic	$\frac{1}{d_{hkl}^2} = \frac{1}{V^2}[h^2b^2c^2\sin^2\alpha + k^2a^2c^2\sin^2\beta + l^2a^2b^2\sin^2\gamma + 2hkabc^2(\cos\alpha\cos\beta - \cos\gamma) + 2kla^2bc(\cos\beta\cos\gamma - \cos\alpha) + 2hlab^2c(\cos\alpha\cos\gamma - \cos\beta)]$ where $V = abc(1-\cos^2\alpha-\cos^2\beta-\cos^2\gamma+2\cos\alpha\cos\beta\cos\gamma)^{1/2}$

2.4.1.1 Powder X-ray diffraction instrumentation

The majority of data collection was carried out using a Bruker D8 or a PANalytical X'Pert PRO MPD powder diffractometer, both using Cu $K_{\alpha 1}$ radiation, and collected over a 2θ range of 5-85^{o} (phase analysis) or 10-120^{o} (structural refinement).

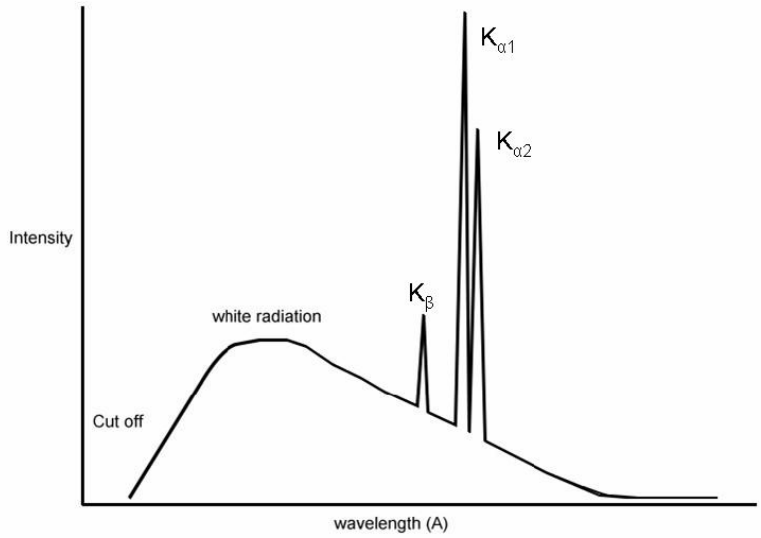

Figure 2-15: Schematic of Copper Emission

X-rays are emitted when an electron beam is fired at a metal target (e.g. copper) and when the incident beam hits the sample, diffraction will occur in every possible orientation of 2θ. A germanium crystal monochromator transmits a wavelength of 1·54056 Å of the Cu $K_{\alpha 1}$ wavelength, the most intense of the Cu K lines (Figure 2-15). This radiation is collimated by aperture slits before striking the sample which is in a capillary (Debye-Scherrer geometry) mounted using an aluminium head. The diffracted beam then passes through further slits before hitting an area detector. A schematic of a powder X-ray diffractometer is illustrated in Figure 2-16.

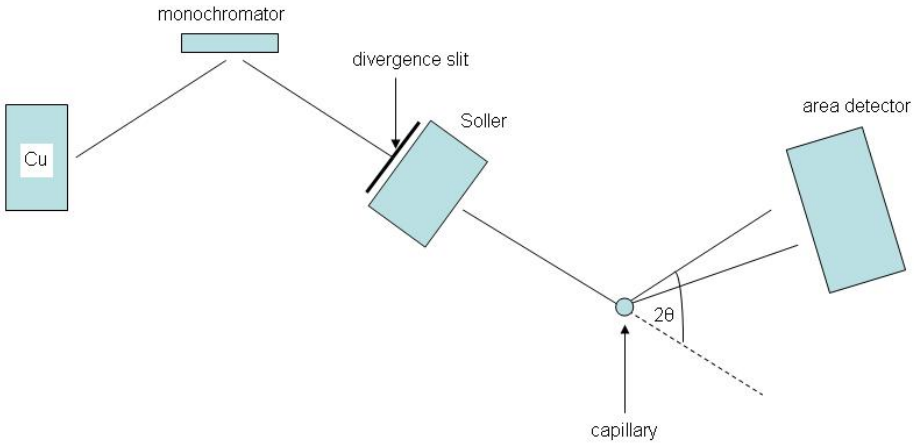

Figure 2-16: Schematic of a Powder X-ray Diffractometer

2.4.1.2 Powder X-ray diffraction sample preparation

The preparation of the samples were carried out in a $N_{2(g)}$ filled glove box due to the air-sensitive nature of the materials. Each sample was ground finely using an agate mortar and pestle, and then loaded into 0.5 mm glass capillaries, to an approximate height of 2.5 cm. The capillary was sealed with silica grease and removed from the glove box before being flame sealed.

2.4.2 Powder Neutron Diffraction (PND)

Although neutron diffraction can be a powerful tool, it is experimentally more expensive and therefore used less often than X-rays. However, since neutrons and X-rays interact differently with matter, neutron diffraction has many advantages over X-ray diffraction.

X-rays are scattered by the electrons of the atoms and so X-ray diffraction experiments show the distribution of electron density of the unit cell within the crystal. Neutrons, in comparison to X-rays, interact insignificantly with electrons - it is the nuclei of the atom that they interact with.

Elements such as hydrogen (and deuterium) and nitrogen are good neutron scatterers as the scattering factors for neutrons are not proportional to Z and they are not significantly affected by the scattering angle, θ. Furthermore, structural determination and thermal displacement parameters of the lighter elements in our materials can be performed by neutron diffraction, therefore making it an important and complementary tool to PXD in our research.

2.4.2.1 The POLARIS instrument at RAL

The neutron source at the ISIS facility of the Rutherford Appleton Laboratory in Oxfordshire was used for data collection. At a spallation source, such as ISIS, hydrogen gas is fed around a ring and ionized to H^- ions. The neutrons are produced by bombarding a heavy metal target with highly energetic particles. In this case, the target is made of tantalum. The energised particles are produced in a three-phase process. Firstly, an ion source produces H^- ions; this process begins with a linear accelerator injecting a pulse of 70 MeV H^- ions into a 800 MeV synchrotron ring. Here, the electrons are stripped away by thin alumina foil strips resulting in the production of H^+ ions. These ions are accelerated by a series of magnets before being extracted by a 'kicker' magnet and sent to the target station where high energy neutrons are produced. The neutrons which are produced have too short a wavelength to be used in diffraction experiments and therefore must be slowed down by several hydrogenous moderators placed around the target.

Since the neutrons are produced in the form of pulses, they exhibit a range of velocities and wavelengths and so a neutron spallation source diffractometer operates differently from a conventional diffractometer. In conventional diffraction experiments, the wavelength is fixed by the source, with d and the angle of detection θ being varied. In time of flight (TOF) experiments, only the detection angle θ is fixed and the variables are d and the wavelength of the neutron, λ.

In order to determine the wavelength, the linear relationship between TOF and d-spacing is utilized and derived from de Broglie's relationship and Bragg's law:

$$\begin{aligned} \lambda &= \frac{h}{p_n} \\ &= \frac{h}{m_n v_n} \\ &= 2d\sin\theta \end{aligned} \tag{10}$$

where h is Planck's constant, m_n is the mass, v_n is the velocity and p_n is the momentum, all of a single neutron with d and $\sin\theta$ consistent with that derived for Bragg's law.

The neutrons travel a known distance, L, where the primary flight path (moderator to sample) is L_1 and a secondary flight path (sample to detector) is L_2 with the corresponding times of flight being t_1 and t_2, the following equation is utilized:

$$\frac{h}{m_n}.\left[\frac{t_1+t_2}{L_1+L_2}\right]=2d\sin\theta=\lambda \tag{11}$$

This leads to a total neutron flight path, L, and time of flight, t, giving:

$$L_1 + L_2 = L \text{ and } t_1 + t_2 = t$$

And so:

$$t=2dL\left(\frac{m_n}{h}\right)\sin\theta \tag{12}$$

Therefore it can be concluded that the time of flight is directly proportional to wavelength and so the values for θ and λ can be employed to calculate *d*-spacing using Bragg's law.

The POLARIS diffractometer (Figure 2-17) is a high flux, medium resolution diffractometer which allows data collection to be performed relatively quickly. Variable temperature experiments can also be performed using either a cryostat or furnace depending on the requirements of individual investigations.

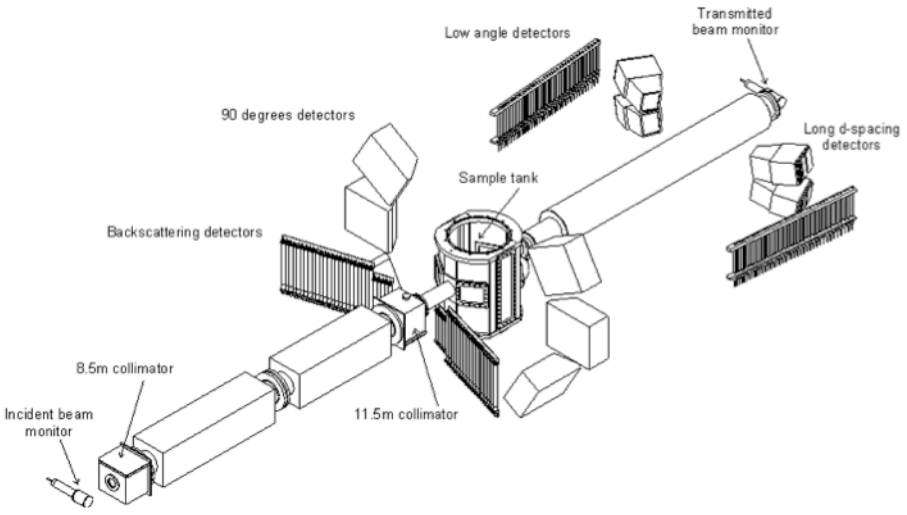

Figure 2-17: Schematic of POLARIS diffractometer [20]

The instrument consists of four detector banks; the A (35°) bank and C (backscattering, 145°) bank use ^{3}He detectors while the B (14°) bank and E (90°) bank use ZnS detectors.

2.4.2.2 Preparation of powder sample for PND

The preparation of each sample for PND was performed in an argon-filled glove box. Powdered samples were loaded into a cylindrical vanadium canister (Figure 2-18) with a copper or indium gasket (refer to respective sections for further information – 3.2.6, 4.2.7 and 5.2.6). Since neutrons do not scatter as well as X-rays, larger samples were required for each experiment (~ 1·5–2 g). The fundamental difference between X-rays and neutrons is that neutrons are scattered by atomic nuclei and not by the electron shells and therefore scattering factors for neutrons, unlike X-rays, are not proportional to Z. [21] The canister is then attached to a sample rod and inserted into the sample area.

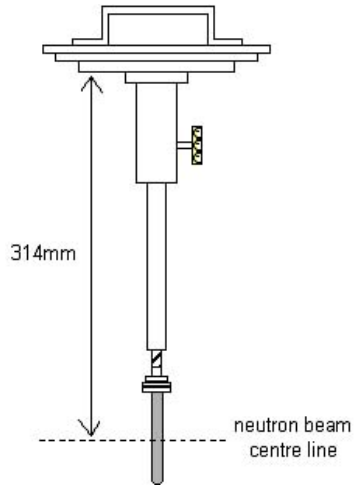

Figure 2-18: Sample rod and canister for POLARIS "candlestick" experiment. [20]
The sample occupies the full area of the canister which is below the neutron beam centre line.

2.4.3 Rietveld Refinement

The Rietveld refinement is a full profile refinement method that fits the observed diffraction data to a structural model of the sample. All powder diffraction data, both PXD and PND, were further analysed using Rietveld refinement, a method developed by Hugo Rietveld in the late 1960s. [22 23] Over the last few decades, there have been great advances in the ability to extract detailed crystal structural information from PXD and PND due to the work of Rietveld. [24] Furthermore, a set of guidelines were published by McCusker *et al* highlighting problems which may arise when refining data and offering possible solutions. [25]

In powder X-ray diffraction experiments, X-rays are diffracted from randomly orientated small crystallites which results in the formation of rings of diffracted X-rays. The PXD pattern is a one-dimensional slice through these rings. The presents a difficulty in terms of

the full extraction of the structure factor information from the powder data due to the overlapping of peaks. Due to this factor, the amount of structural information which could be obtained from PXD data was limited however when the revelation of the Rietveld method was proposed, it attained great importance in the extraction of detailed structural information from PXD and PND data. The Rietveld method is based on a least squares approach and refinements are performed until the best structural fit between the full experimental and calculated patterns is obtained. [24] On the realisation that many individual reflections may overlap and therefore could not be modelled singly, Rietveld proposed that the individual reflections could be fitted using peak shape parameters with the expectation that this would allow determination of the total intensity and peak shape of a cluster of reflections. Unfortunately, this could only be applied to single crystal systems however on the introduction of computers, Rietveld worked on sophisticated computer-based analytical procedures leading to the full pattern analysis of materials. As a consequence, this understanding enabled far more complex structural problems to be solved.

Firstly the structural refinement starts with the use of a good model from a similar crystal system. Although not impossible, performing a Rietveld refinement without a good starting model presents a difficulty as other methods of obtaining a usable starting model would be required. The next step involves introducing scale factors and background parameters which can either be manually set or calculated from a polynomial expression. Variation of lattice parameters and zero-point error correction (sample displacement from diffractometer centre) leads to accurate determination of the Bragg reflection positions of the sample. Next, refinement of the peak shape parameters can be introduced followed by varying atom positions to fit peak intensities. This was then followed by varying the temperature factors. As mentioned, the Rietveld method can take account of preferred orientations and intensity irregularities which may be caused by the thermal motion of the atoms within the sample. This can cause a slight decrease in the intensities of observed reflections and can be refined with isotropic or anisotropic temperature factors however this is usually only done for neutron data.

The Rietveld method has been applied to both X-ray and neutron data which has been collected at a constant wavelength and TOF. The software has the ability to cope with multi-phase samples, preferred orientation, peak asymmetry and temperature factors to give full structural data. Instrument parameters can also be varied and these are dependent on the particular experiment being carried out. Using a least squares approach is responsible for the refinement of accurate cell parameters and atomic positions. The quantity minimised during the least squares refinement is the function M.

$$M = \sum_i w_i (y_i^{obs} - y_i^{calc})^2 \tag{13}$$

where w_i is a weighting factor given by $1/y_i^{obs}$, y_i^{obs} is the observed intensity at each step/point I ($2\theta_I$ for PXD) and y_i^{calc} is the calculated intensity at each step.

For PXD data, y_i^{calc} values are determined from the $|F_k|^2$ values calculated from the structural model by summing of the calculated contributions from neighbouring Bragg reflections (k) plus a background b_i:

$$y_i^{calc} = s \sum_k L_k |F_k|^2 \phi(2\theta_i - 2\theta_k) P_k A + y_{bi} \tag{14}$$

where s is the scale factor, L_k contains Lorentz polarisation and multiplicity factors, ϕ is a reflection profile function, F_k is the structure factor for the kth Bragg reflections, P_k is the preferred orientation function, A is an absorption factor and y_{bi} is the background intensity at the ith step.

The structure factor, F, is related to the intensity of each diffraction maximum and is the sum contributions of the scattering amplitudes, f, and of the phases, δ, of each atom which is expressed as:

$$F = \sum_{j=1}^{N} f_j \exp[i\delta] \tag{15}$$

Total scattering $f(S)$ can be found by the summation of a particular atom as a whole where scattering contributions are defined as ($\rho(r)\ \delta V$) and $e^{2\pi iSr}$ is the phase difference.

$$f(S) = \int \rho(r) e^{2\pi iS.r}\, \delta V \tag{16}$$

where r is the radius, ρ(r) is the local charge density probability and δV is the volume. Therefore as r decreases, a decreasing value of the form factor, f, will result.

The structure factor for the kth Bragg reflection, F_k, is given by:

$$F_k = \sum_j N_j f_j \exp[2\pi(hx_j + ky_j + lz_j)] \exp[-M_j] \tag{17}$$

where h, k and l are the Miller indices, x_j, y_j and z_j are the position parameters of the jth atom in the unit cell and N_j is actual site occupancy divided by the site multiplicity.

M_j (from Equation 17) can be expressed as:

$$M_j = 8\pi^2 \overline{u_s^2} \sin^2\theta / \lambda^2 \tag{18}$$

where $\overline{u_s^2}$ is the root-mean-square thermal displacement of the *j*th atom parallel to the diffraction vector.

Young states that the background intensity can be obtained by either an operator-supplied table of background intensities, a linear interpolation between operator-selected points in the pattern or a specific background function. [24] For the fitting of powder diffraction data, there are currently seven background functions available for use within GSAS. For the purposes of the majority of this thesis, the first background function, shifted Chebyschev was employed. However, it should be noted that a manual background had to be employed for certain data sets and this will be discussed in the relevant chapter. With regards to background function one, in order to make the Chebyschev polynomial orthogonal, a conversion was applied:

$$X = \frac{2(T - T_{\min})}{T_{\max} - T_{\min}} - 1 \tag{19}$$

where T_{min} and T_{max} are the actual range of data used in the calculation. T is reported in milliseconds TOF or degrees 2θ.

The background intensity, I_b, is calculated from Equation 20.

$$I_b = \sum_{j=1}^{N} B_j T'_{j-1} \tag{20}$$

where I_b is the background value, B_j is an isotropic thermal parameter which is determined by a least squares method during Rietveld refinement and T'_{j-1} are the coefficients of the Chebyschev polynomial.

It is vital that the construction of the calculated profile accurately describes the peak shape of the Bragg reflections since a comparison of intensities is performed at every point. Generally, peak shape is dictated by the instrument and modelled using a pseudo-Voigt function (pV) - a combination of Gaussian and Lorentzian functions:

$$\eta L + (1 - \eta) G \tag{21}$$

where L and G are the Lorentzian and Gaussian contributions to the peak shape and η is the mixing parameter which can be refined as a linear function of 2θ:

$$\eta = N_A + N_B(2\theta) \tag{22}$$

where N_A and N_B are refinable parameters.

The Gaussian (G) and Lorentzian (L) contributions to the peak shape are represented by the equations:

$$G = \frac{(4\ln 2)^{1/2}}{H_k\sqrt{\pi}} \exp\left(-4\ln 2\left(2\theta_i - 2\theta_k\right)^2 / H_k^2\right) \tag{23}$$

and

$$L = \frac{2}{\pi H_k} 1 \Big/ \left[1 + 4\frac{(2\theta_i - 2\theta_k)^2}{H_k^2}\right] \tag{24}$$

where $2\theta_k$ is the calculated position for the kth Bragg peak corrected for the counter zero-point and H_k is the full-width-at-half-maximum (FWHM) of the kth Bragg reflection.

The full width at half maximum (FWHM), H_k, of a peak has been shown to vary with the scattering angle $2\theta_k$ and is modelled as:

$$H_k^2 = U\tan^2\theta + V\tan\theta + W \tag{25}$$

where U, V and W are the refinable parameters and are both instrument and sample dependent. Therefore, Equation 25 can account for peak broadening effects resulting from particle size.

In any refinement, the parameters that can be varied fall into two distinct groups. The first group are the structural parameters that describe the contents of the unit cell and include the overall temperature factors, co-ordinates and occupancies of each individual atom. The second group contains the profile parameters that define the position, shape and FWHM of each peak. This group consists of the profile scale factor, unit cell parameters, U, V, W (Equation 25), zero-point, asymmetry and preferred orientation correction. To make a quantitative assessment of the agreement between the observed and calculated profiles, a number of reliability factors are defined, $R_{profile}$, $R_{expected}$, $R_{weighted\ profile}$.

The *R* factors are described by the following equations:

$$R_{profile} = R_p = \left[\frac{\sum_i \left| y_i^{obs} - y_i^{calc} \right|}{\sum_i y_i^{obs}} \right] \tag{26}$$

and

$$R_{\exp ected} = R_{\exp} = \left[\frac{(N - P + C)}{\sum_i \omega_i (y_i^{obs})^2} \right]^{1/2} \tag{27}$$

where R_{exp} is defined from the statistics of the refinement and N is the number of observations, P is the number of refinable parameters and C is the number of constraints.

From a mathematical perspective, $R_{weighted\ profile}$ (R_{wp}) is the most important and meaningful of the *R*-factors because the numerator is the residual being minimised (Equation 28). For the same reason, R_{wp} also best reflects the progress of the refinement and is given by:

$$R_{wp} = 100 \left[\frac{\sum_i \omega_i \left[y_i^{obs} - y_i^{calc} \right]^2}{\sum_i \omega_i \left[y_i^{obs} \right]^2} \right]^{1/2} \tag{28}$$

The final measure of the whole fit, minimised during the refinement, is the chi-squared parameter which is defined by:

$$\chi^2 = \left[\frac{R_{weightedprofile}}{R_{\exp}} \right]^2 \tag{29}$$

In conclusion, for a good fit, the $R_{weighted\ profile}$ should approach the statistically expected *R* factor (R_{exp}). The quality of fit can also be measured by examination of the plot of the profile fit. If the fit is good, the difference line between the calculated and the observed patterns should be as flat as possible.

All Rietveld refinements presented in this thesis were performed using the Generalised Structure Analysis Suite (GSAS) of von Dreele and Larson [26] using the EXPGUI interface. [27]

2.4.4 Scanning Electron Microscopy (SEM)

Determining the topography and morphology of bulk material can be done by scanning electron microscopy. This type of imaging allows a large amount of the sample to be in focus at any one time and due to high magnification, the result is a high quality representation of the three dimensional sample.

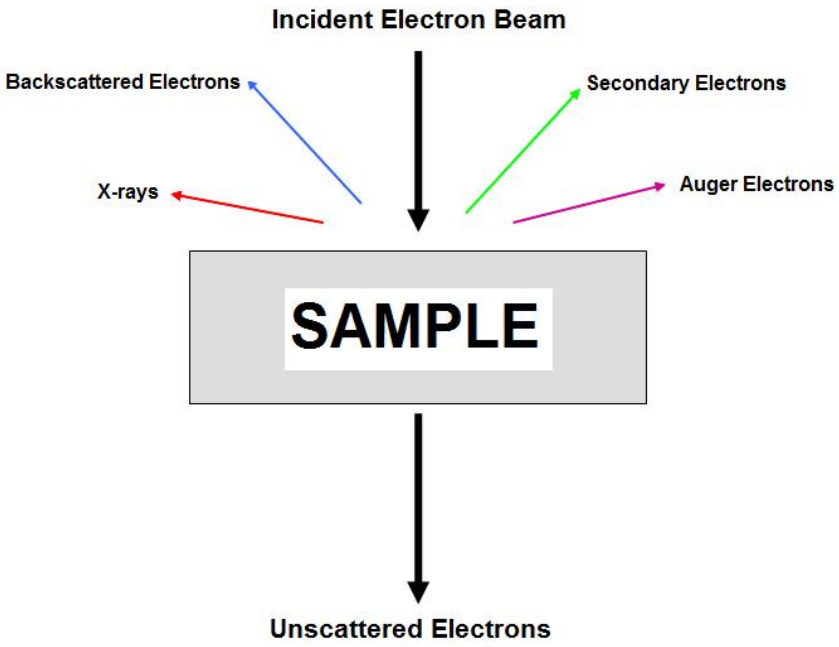

Figure 2-19: Schematic of possible scattering of electrons from SEM experiment

Electrons can either interact with the sample elastically or inelastically. Elastic interaction occurs when scattered electrons have the same energy as the incident electrons whereas inelastic interaction occurs when the energy of the scattered electron changes. When electrons from the incident beam reach the sample, several different outcomes result as shown in Figure 2-19. An elastic collision results in the ejection of high energy electrons referred to as backscattered electrons and are used for imaging and diffraction. [28] The images obtained from backscattered electrons provide information about the elemental distribution in a sample; this is due to the fact that the resulting signal is strongly related to the atomic number (Z) of an element.

Secondary electrons result from inelastic scattering and are a consequence of an incident electron passing near an atom in the sample. [28] The incident electron must be close enough to an atom so it can pass on some of its energy to a lower energy electron which is typically in the K shell. The electron in the atom of the sample becomes ionised (and

termed a secondary electron); this then leaves the atom with a low kinetic energy (typically 50 eV or less). Secondary electrons are responsible for imaging in a SEM.

The incident beam also causes characteristic X-ray electrons to be emitted on removal of an inner shell electron from an atom in a sample. A higher energy electron occupies this vacancy resulting in a release of energy. Characteristic X-ray electrons are employed to identify the composition of a sample and aid the measurement of element abundance within a sample. Lastly, Auger electrons can be emitted from a sample and arise from an 'autoionisation' process within an excited atom. [29] The process involves the photoemission of a core electron by an incident electron creating a vacancy. Consequently, an electron from a level of lower binding energy may occupy this vacancy resulting in the release of energy which may be removed from the atom as a photon (X-ray fluorescence). Alternatively, the energy may be transferred to a third electron and it is this electron that is named the Auger electron, after discovery by Pierre Auger.

A beam of high energy incident electrons is emitted by an electron gun and these electrons travel down towards the sample through a series of magnetic lenses. The system is operated under vacuum. It is important that the whole sample can be scanned and so scanning coils can move the focused beam across the sample, and a detector counts the low energy secondary electrons which are responsible for imaging. Images are observed on a PC monitor on which they can be manipulated.

Scanning electron microscopy (SEM) was performed using either a Philips XL30 ESEM which was run in high vacuum mode with an applied accelerating voltage of 20 kV and a working distance of 10 mm for imaging or carried out by J. Gallagher on a Hitachi S-4700 SEM with an applied accelerating voltage of 5 kV and a working distance of 12.5 mm. A schematic representation of a SEM is illustrated in Figure 2-20.

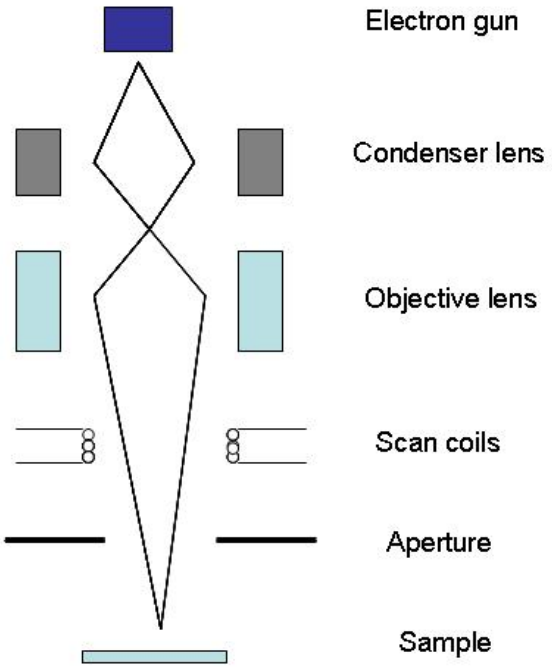

Figure 2-20: Schematic of a Scanning Electron Microscope

Energy-dispersive X-ray (EDX) spectroscopy is a complementary tool to SEM and can be used for elemental analysis or chemical characterisation of the sample however no EDX was performed throughout this work. Considering the samples that were being investigated, the usefulness of EDX would have been minimal since the samples consisted of lighter elements.

2.4.4.1 Preparation of sample for SEM

A small amount of sample was deposited onto aluminium stubs using adhesive carbon tabs under the recirculating atmosphere of a glove box. It is important that the material adheres well to the carbon tabs; this ensures that the material does not detach itself from the tab when encountering the pressure of the vacuum inside the SEM. The stub was then removed from the glove box in a sealed glass vial to prevent exposure to air.
The sample is placed inside the vacuum column of the microscope which is then shut using an air-tight door and then the chamber is evacuated.

2.4.5 Thermal Analysis

In this work, samples were studied using a Netzsch STA 409 PC simultaneously combining thermogravimetric analysis (TGA) and differential thermal analysis (DTA).
Thermogravimetric analysis principally allows the determination of mass changes in relation to temperature changes and is used in conjunction with differential thermal

analysis (DTA). TGA/DTA analysis in solid state chemistry can prove to be a powerful method in the study of thermal decompositions and phase transformations.

Decomposition can take place over a range of temperatures for a particular sample. The outcome from TGA/DTA experiments can be a result of several factors including the programmed heating rate as well as the particle size of the solid and the atmosphere under which the reaction is being conducted.

In DTA, the sample and an inert reference (either Al_2O_3 or Ni depending on the material being studied and the reaction parameters being followed) undergo identical thermal cycles. Temperatures of both should be identical until a change occurs; either an exothermic or endothermic event, for example, melting, sublimation or crystallization. In such cases, an exothermic change will result in the temperature of the sample increasing quicker than the reference or slower if the change is endothermic.

Although DTA gives a more complete idea of the results of the experiment since TGA only records mass change, it is normally more useful to record both sets of data simultaneously. This enables categorization of thermal events (for example exothermic and/or endothermic events); whether these thermal events occur with or without a change in the sample mass. Recording data as the sample cools again can also provide useful information as this will show whether a thermal event is reversible or not.

The crucibles, both sample and reference, are placed side by side in the STA contained within a recirculating glove box (Braun). Material (~0·5-0·6 g) is added to the sample crucible and the sample chamber is then closed before heating begins. Heating programmes are created on the PC which is connected to the STA. Firstly, the appropriate crucible type is selected before generating a suitable heating programme where heating rates can vary from 1 K min^{-1} to 10 K min^{-1} depending on the sample and the data required.

2.4.5.1 Coupled Mass Spectrometry; evolved gas analysis

Coupled Mass spectrometry (MS) is an important complementary tool to TG/DTA and is an analytical technique that facilitates the measurement of the mass-to-charge ratio of charged particles. The Hiden Analytical HPR20 mass spectrometer allows determination of masses of particles, elemental compositions and aids investigation of chemical structures.

A typical MS procedure consists of four stages. The first stage is ionisation of the sample where the atoms are ionised by stripping off one or more electrons resulting in the formation of a positive ions. Stage two involves acceleration of these ions so that they all have the same kinetic energy. The third stage involves deflection of the ions by a magnetic field. Ions are deflected according to their masses; the lighter an ion is, the more it is

deflected; this is according to Newton's second law of motion acceleration of a particle being inversely proportional to its mass:

$$f = ma \tag{30}$$

where f is the force, m is the mass and a is the acceleration.

Furthermore, how positively charged an ion is also contributes to how deflected it will be; the more positively charged an ion is, the more it will be deflected. Finally, the beam of ions which has been formed is detected electrically resulting in a signal being processed into the mass spectra. A schematic of a quadruple mass spectrometer is illustrated in Figure 2-21 and the operating principle of a mass spectrometer is represented in Figure 2-22.

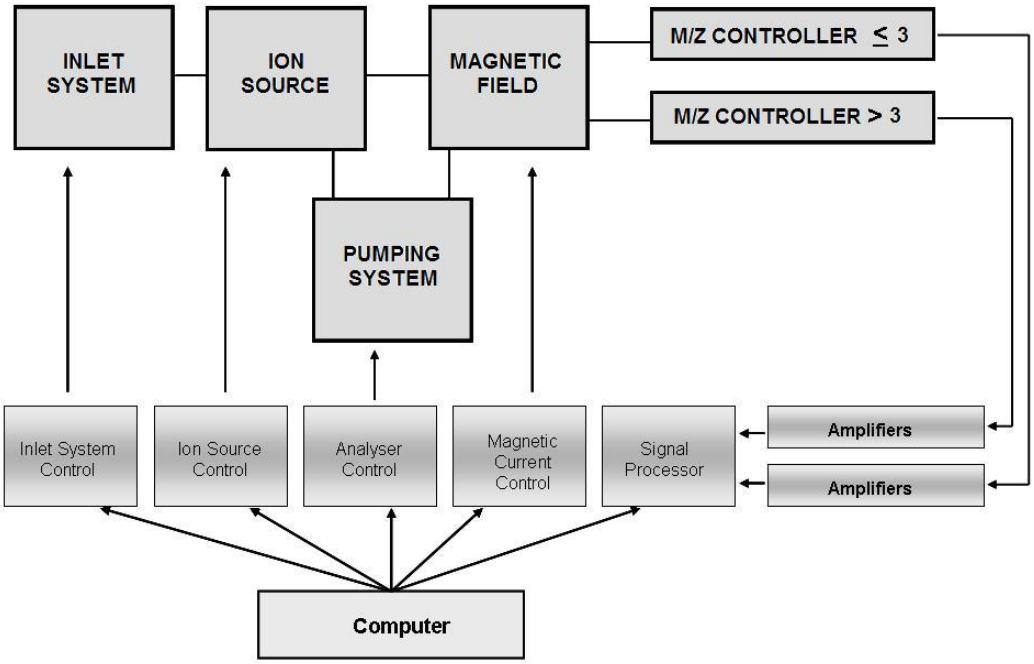

Figure 2-21: Schematic of a mass spectrometer

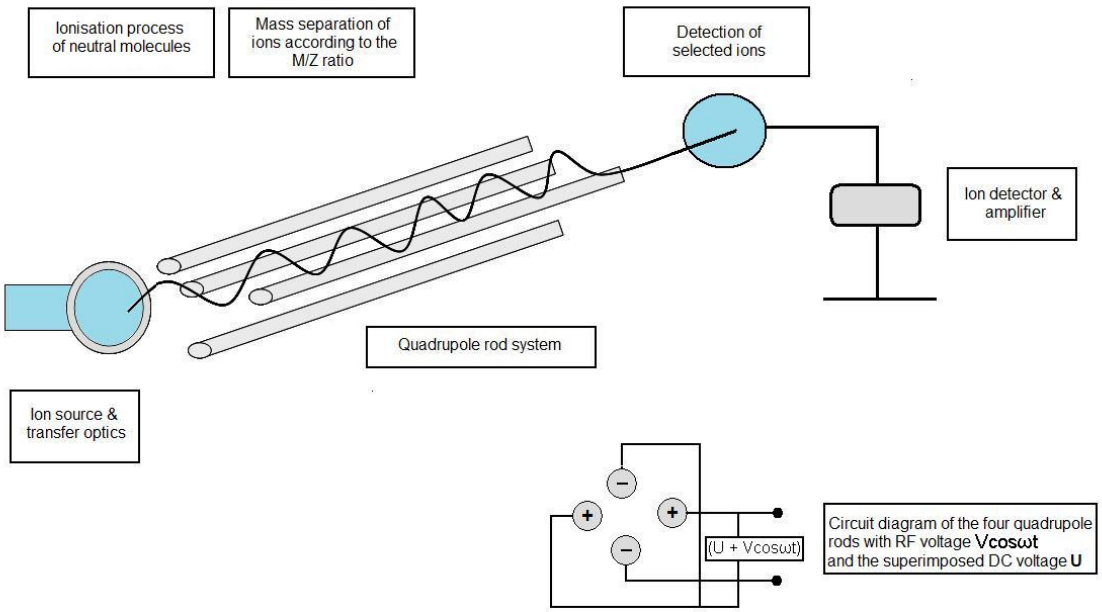

Figure 2-22: Operating principle of a quadruple mass spectrometer based on a Hiden Analytical HPR20 mass spectrometer

Due to the fact that this technique has both qualitative and quantitative uses, including the identification of the composition of samples and the amount of a certain element within samples respectively, MS is a very common technique used throughout various branches of chemistry.

Programmes were set-up using the Hiden Analytical HPR20 mass spectrometer to enable detection of specific evolved gases such as nitrogen, hydrogen and ammonia gases. Before each MS experiment, pre-work was performed – this involved checking for the presence of moisture. This pre-work was vital to ensure that there was no contact between the sample and any moisture that may be present in the system. Typically this assessment of the system took approximately 30 minutes and the presence of moisture could be traced on a computer which was connected to the mass spectrometer.

2.5 References:

[1] H. Sobol and K. Tomiyasu, *IEEE Transactions Microwave Theory and Techniques*, 2002, **50**, 594

[2] Developments in Microwave Chemistry, RSC Special Report, *Chemistry World*, 2(4), 2005

[3] C. Gabriel, S. Gabriel, E. H. Grant, B. S. J. Halstead and D. M. P Mingos, *Chemical Society Reviews*, 1998, **27**, 213

[4] Engineers' Handbook of Industrial Microwave Heating, R. Meredith, *Short Run Press Ltd*, 1998, 20

[5] J. E. Atwater and R. R. J. Wheeler, *Applied Physics A – Materials Science and Processing*, 2004, **79**, 125

[6] G. J. Kriegsmann, *Journal of Applied Physics*, 1992, **71**, 1960

[7] Industrial Microwave Heating, A. C. Metaxas and R. J. Meredith, *IEEE Power Engineering Series 4*, Peter Peregrinus Ltd, 1983, 54-55

[8] Microwave/RF applicators and probes for Material Heating, Sensing and Plasma Generation, M. Mehdizadeh, *Elsevier*, 2009, 110

[9] E. T. Thostenson and T. –W. Chou, *Composites: Part A*, 1999, **30**, 1055

[10] M. A. Brogan, *PhD Thesis*, University of Nottingham, 2006

[11] H. Huppertz, *Zeitschrift für Kristallographie*, 2004, **219**, 330

[12] D. Walker, M. A. Carpenter and C. M. Hitch, *American Mineralogist*, 1990, **75**, 1020

[13] H. Huppertz, *Chemical Communications*, 2011, **47**, 131

[14] D. Siddons, *PhD Thesis*, University of Nottingham, 1997

[15] R. Marx, *Zeitschrift für Anorganische und Allgemeine Chemie*, 1997, **623**, 1912

[16] Y. Kojima and Y. Kawai, *Journal of Alloys and Compounds*, 2005, **395**, 236

[17] Structure Determination from Powder Diffraction Data, Edited by W. I. F. David, K. Shankland, L. B. McCusker and Ch. Baerlocher, *Oxford University Press*, 2006

[18] W. L. Bragg, *Proceedings of the Cambridge Philosophical Society*, 1913, **17**, 43

[19] Solid State Chemistry, An introduction, 1st Edition, L. Smart and E. Moore, *Chapman and Hall*, 1992

[20] R. I. Smith and S. Hull, User Guide for the Polaris Powder Diffractometer at ISIS Rutherford Appleton Laboratory Report, 1997, RAL-TR-97-038

[21] Crystal Structure Determination, 2nd Edition, W. Massa, *Springer-Verlag Berlin Heidelberg*, 2004

[22] H. M. Rietveld, *Acta Crystallographica B*, 1967, **22**, 151

[23] H. M. Rietveld, *Journal of Applied Crystallography*, 1969, **2**, 65

[24] The Rietveld Method, R. A. Young, *Oxford University Press*, 1993

[25] L. B. McCusker, R. B. von Dreele, D. E. Cox, D. Louër and P. Scardi, *Journal of Applied Crystallography*, 1999, **32**, 36

[26] A.C. Larson and R.B. Von Dreele, Generalized Structure Analysis System, 1990, MS-H805, Los Alamos, NM 87545

[27] B. H. Toby, *Journal of Applied Crystallography*, 2001, **34**, 210

[28] Scanning Electron Microscopy and X-ray Microanalysis 3rd Edition, J. Goldstein, D. Newbury, D. Joy, C. Lyman, P. Echlin, E. Lifshin, L. Sawyer, J. Michael, *Springer Science and Business Media Inc.*, 2003, Chapter 3

[29] Surfaces, G. Attard and C. Barnes, Oxford Chemistry Primers, *Oxford University Press*, 1998, 43

3 Structural Investigation of β-Lithium Nitride

3.1 Introduction

There has been a marked increase in research within nitride chemistry in recent years [1, 2] involving several structural studies of Li_3N, [3, 4] a compound which dominates nitride chemistry. Lithium nitride is the only known, stable binary nitride of the alkali metals and exists in three known polymorphs of Li_3N; alpha, [5] beta, [6] which are both hexagonal, and gamma [7] which is cubic and only accessible at high pressures.

Alpha-Li_3N (Figure 3-1) is a unique structure which crystallises in the *P6/mmm* space group with lattice parameters of a = 3.658 (4) Å and c = 3.882 (4) Å. [5] The structure of the alpha polymorph was re-determined by Rabenau and Schulz in 1976. [8] On application of pressure (p > 0.6 GPa), [6] this material can undergo a phase transformation from α-Li_3N to β-Li_3N where co-ordination of the nitrogen atoms changes from hexagonal bipyramidal in the alpha structure to trigonal bipyramidal in the beta structure. This pressure induced phase was first reported by Mali *et al* using ^{7}Li quadrupolar NMR at 0.42 GPa at 300 K in a Li_3N single crystal. [9] The hexagonal β-Li_3N structure (Figure 3-2) is reported in the literature to crystallise in the *P6$_3$/mmc* with lattice parameters of a = 3.552 (1) Å and c = 6.311 (3) Å. [6]

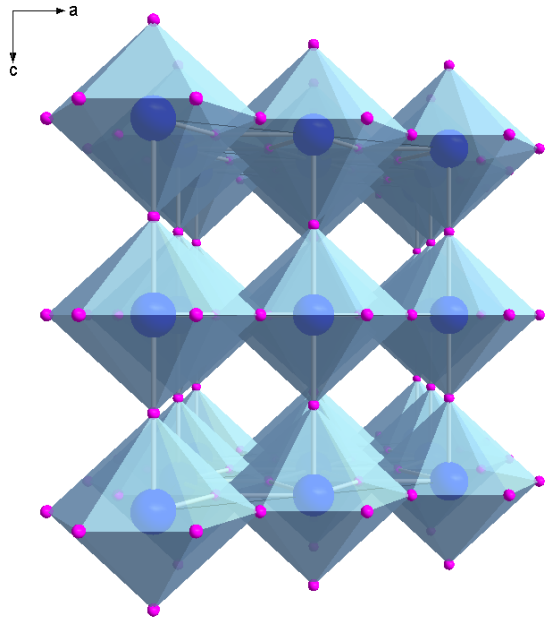

Figure 3-1: Hexagonal structure adopted by α-Li_3N (Li^+ - pink, N^{3-} - blue) showing N centred coordination polyhedra.

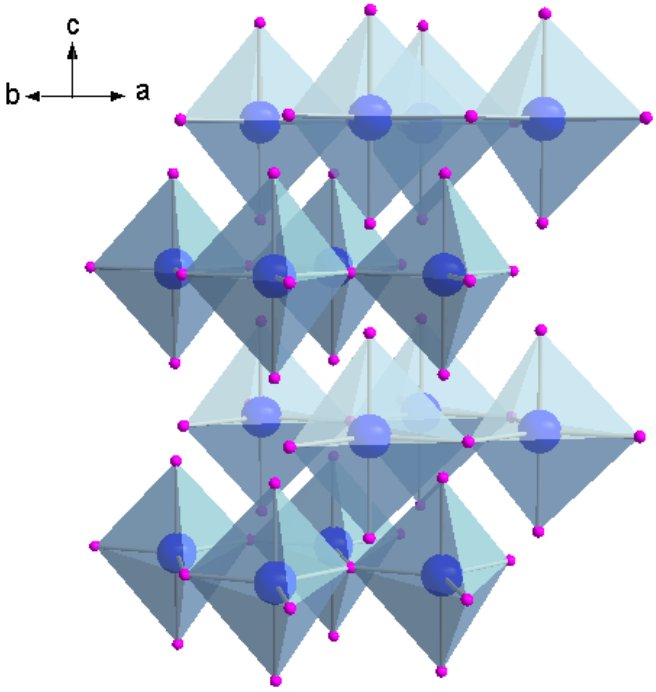

Figure 3-2: Hexagonal structure adopted by β-Li_3N (Li^+ - pink, N^{3-} - blue) showing N centred coordination polyhedra.

A variable temperature single crystal X-ray diffraction experiment involving Li_3N highlighted the fact that it was composed of Li^+ and N^{3-} ions where the N^{3-} is stabilised by the presence of surrounding Li^+ cations. [10] Subsequent spectroscopic studies including infrared and Raman strengthened the argument for the presence of a highly polar N^{3-} anion within Li_3N. [11] From initial PXD studies, a 1-2% vacancy of the Li position within the $[Li_2N]$ planes was reported. [12, 13] A subsequent powder neutron diffraction investigation was conducted on the alpha polymorph of Li_3N confirming the presence of Li^+ vacancies (approximately 3%) at room temperature. [3] Furthermore, extensive structural studies of commercial Li_3N using PND, over a temperature range of 20 – 673 K were carried out by Huq *et al*. [4] From the results obtained, it was reported that at temperatures above 473 K, the percentage of β-phase present decreased. Further exploration was carried out by Gregory *et al* to investigate the effects of temperature on α-Li_3N and commercial Li_3N. [14]
The chemistry of Li_3N and H_2 was first introduced 1909 by Dafert and Miklauz [15, 16] however it was not until a breakthrough decades later in 2002 that Li_3N was exposed as a potential hydrogen store. [17] Reports have stated that there is a link between the presence of hydrogen and the ionic conductivity of a material; by doping Li_3N with hydrogen, there is an increase in ionic conductivity which was detected by infrared spectroscopy measurements. [18, 19, 20] Single crystal neutron diffraction was also employed to study the interaction between Li_3N and H_2/D_2 and data were collected for a D-doped Li_3N material.

The Li-N-D material was reported to have a composition of $Li_{2.98}ND_{0.02}$ and contained disordered ND^{2-} anions. [21]

Another structural study involving the deuteration and de-deuteration of Li_3N was conducted by Huq *et al* using *in-situ* neutron diffraction. [22] It was proposed that the mechanism for absorption and desorption of D_2 in this system was dictated by a defect formation present in the lattice of cubic Li_2ND. In addition to this, further studies involving the interaction of commercial and single phase α-Li_3N with gaseous D_2 at variable temperatures was also investigated by Gregory *et al*. [14] These studies conducted by Gregory *et al* [14] have led to a PND experiment using β-Li_3N to investigate the structural differences of this polymorph type over a temperature range of 4.2 – 600 K, with further experimental analysis to study the interaction of this polymorph with gaseous D_2.

This chapter describes the synthesis and characterisation of the alpha and beta polymorphs of lithium nitride. An in-depth study of the structure of β-Li_3N was investigated by PXD and PND and the results of the interaction between this polymorph and gaseous D_2 are also presented.

3.2 Experimental

3.2.1 Synthesis of α-Li_3N

The alpha form of lithium nitride was prepared by reacting lithium metal with nitrogen gas using a sodium flux as a solvent medium. The preparation for the reaction was carried out in a glove box under an inert atmosphere. A piece of lithium metal (~ 7 g) was cut from a larger ingot which was then cleaned of the covering oxide layer using a metal file. This piece of lithium metal was then cut into smaller pieces before being submerged in molten sodium (~ 50 g) in a stainless steel crucible. After cooling, the crucible was transferred into a stainless steel reaction vessel containing a cold finger which was made air-tight by using a rubber o-ring between the vessel and the lid (a schematic is presented in Figure 2-5). Upon removal of the reaction vessel from the glove box, the vessel was evacuated before applying a positive nitrogen pressure and heating to 733 K for 72 hours.

After cooling to room temperature, the nitrogen gas supply was disconnected and the reaction was then heated to 733 K for a further 12 hours under vacuum to remove excess sodium metal. Upon reaction completion and cooling, the reaction vessel was returned to the glove box and opened under an argon-filled atmosphere. The product was a purple/red crystalline solid which had deposited within and around the stainless steel crucible. Using

an agate mortar and pestle, the material was then ground before preparing a capillary for a PXD measurement.

3.2.2 Synthesis of β-Li_3N

3.2.2.1 Balling Milling Procedure

Synthesis of β-Li_3N was performed using either commercial Li_3N (Alfa Aesar, 99.4%) or α-Li_3N. Approximately 0.7 g of material was loaded into a 50 ml stainless steel jar with ten 10 mm stainless steel grinding balls, under a nitrogen atmosphere (Figure 2-6). Using an air-sensitive clamp and a rubber o-ring, the jar was made air-tight before being removed from the glove box. The jar was then placed into the planetary ball mill (PM100) and locked into the sun wheel. The material was then milled, at 450 rpm, for times up to 25 hours (with a 30 second interval every 5 minutes with reverse rotation).

Upon removal from the ball mill, the jar was returned to the glove box and opened under a nitrogen atmosphere. During the milling process, the material adhered to the wall of the jar and so it had to be physically removed. The subsequently milled material appeared identical to the starting material.

3.2.2.2 High Pressure Procedure

An alternative method for preparing β-Li_3N is by employing a multi-anvil high pressure procedure using both commercial and laboratory-synthesised α-Li_3N. This work was performed at the Leopold-Franzens-Universität, Innsbruck, Austria by Dr. Gunter Heymann and Prof. Hubert Huppertz. Li_3N was pre-compressed using a steel plunger and loaded into a Molybdenum capsule which was then placed inside a BN crucible. All preparations were performed within a recirculating glove box under a nitrogen atmosphere. Further details are described in Section 2.3.1.2.

3.2.3 Scanning Electron Microscopy (SEM)

A small amount of the required sample was deposited onto aluminium stubs using adhesive carbon tabs. All preparations were carried out under a nitrogen atmosphere in the glove box. Each tab was placed inside a glass vial which was sealed before removal from the glove box to minimise exposure to the air.

The sample was then transferred quickly from the glass vial into the vacuum column of the microscope, once again to minimise exposure to the air. This was then shut using an air-tight door which was then followed by evacuation of the chamber.

Each sample was then examined closely under the microscope at a working distance of 10 mm for imaging. For more crystalline samples, a higher magnification was used to obtain a better image. Charging was often encountered with the commercial sample and this presented a difficulty in obtaining suitable images (see Section 3.3.2).

3.2.4 Powder X-ray Diffraction (PXD) Experiments

All compounds which were synthesised were initially characterised by PXD, as described in Section 2.4.1.2. Capillaries of the materials were prepared for each PXD measurement. Data was collected from 5-85^{o} 2θ or 10-110^{o} 2θ for 1 hour or 12 hours respectively. Initial 1 hour scans were used for phase analysis whilst longer scans were performed on high quality samples for subsequent Rietveld refinements. Capillaries were prepared for PXD for samples, after milling times of 5, 10, 15, 20 and 25 hours respectively.

3.2.5 Rietveld refinement against PXD data

The structures of the commercial material as well as the lab-synthesised materials of alpha and beta Li_3N were refined using the General Structure Analysis System (GSAS) [23] with an EXPGUI interface. [24]

For the commercial Li_3N starting material, the background was successfully modelled in GSAS using function 8, a reciprocal interpolation function. This was followed by refinement of the cell parameters, atomic positions, profile coefficients, peak widths and anisotropic temperature factors. Peak profiles were modelled using function 2 within GSAS, a multi-term Simpson's rule integration of the pseudo-Voigt function.

Manually fitting the background using 14 coefficients gave the best fit for lab synthesised α-Li_3N. This was followed by refinement of the cell, atomic positions, profile coefficients, peak widths and anisotropic temperature factors. Once again, peak profiles were modelled using function 2 within GSAS.

The refinements for lab-synthesised β-Li_3N were carried out as described above with a background that was modelled manually.

3.2.6 Powder Neutron Diffraction (PND) Experiments

Powder neutron diffraction studies were carried out on the POLARIS instrument at ISIS, Rutherford Appleton Laboratory which is a high intensity, medium resolution diffractometer [25] and described more fully in Section 2.4.2.1. Initially, PND data were collected for a sample of commercial Li_3N at room temperature. The material was loaded into a canister and sealed under an argon-filled atmosphere in a glove box. The canister

was then connected to a candlestick and data collection was carried out using the 90^{o} (E) detector bank.

The first main experiment involved an investigation into the variation of lattice parameters throughout a temperature range of 4.2 – 600 K. Approximately 1 g of β-Li_3N was loaded into an 8 mm vanadium canister which were made air-tight using an indium wire gasket. Due to the air-sensitive nature of the material, the preparation was carried out in a glove box under an argon atmosphere. Data were collected using a cryofurnace for approximately 2.5 hours using three detector banks; 145^{o} (C), 90^{o} (E) and 35^{o} (A).

The concluding experiment involved the interaction of D_2 gas with β-Li_3N. Approximately 1 g of β-Li_3N was loaded into stainless steel canister with a copper ring gasket, in a glove box under an argon atmosphere. A boron nitride collimator was also used to avoid steel scattering. The sample canister was attached to the centre stick and connected to the D_2 gas supply at a pressure of 10 bar. Data were collected over a temperature range of 4.2 – 600 K for between 4.5 - 9.5 hours. After data collection was complete, a linear type absorption correction was applied to the PND data by Dr. R. I. Smith at ISIS.

3.2.7 Rietveld refinement against PND data

The General Structure Analysis System (GSAS) [23] using an EXPGUI interface [24] was employed to carry out Rietveld refinements of the collected PND time of flight data. Using an appropriate starting model, data from the three detector banks; A bank (35 ^{o}), E bank (90 ^{o}) and C bank (145 ^{o}) were refined consecutively. In total, nine data sets collected at various temperatures; 4.2, 15, 50, 100, 200, 300, 400, 500 and 600 K. For the first eight data sets which were collected, (4.2 – 500 K), only the beta phase could be refined. Since only a very small amount of alpha phase was present in the starting material and the data collected were rather noisy, it was impossible to obtain a good fit for this second phase. Beta-Li_3N was modelled against the starting model [6] where the *$P6_3/mmc$* space group is adopted.

Firstly, data for the backscattering (C) bank was employed followed by the addition of the E and A banks respectively. Due to the nature of the material and the method in which it was synthesised, peak shape broadening made it difficult to refine the background using the functions suggested (in GSAS) and therefore the background had to be fitted manually for each histogram, using 12 to 20 coefficients. Firstly, the unit cell parameters were refined followed by peak profile parameters and isotropic temperature factors. Modelling of the peak shape was carried out using function 4, which allows for strain broadening and was developed by P. Stephens. [26] Lastly, the anisotropic temperature factors were refined.

The *in-situ* experiment involving β-Li_3N and gaseous D_2 at variable temperature employed data collected from only the 90° (E) bank. Once again, the background was difficult to model and so it was fitted manually using between 12 and 16 coefficients. The unit cell parameters were refined followed by peak profile parameters and isotropic temperature factors. Modelling of the peak shapes was carried out using GSAS function 3, a convolution of back-to-back exponentials and pseudo-Voigt combination with Lorentzian broadening. Temperature factors were refined anisotropically except at the lowest and highest temperatures; 4.2-15 K and 500-600 K, where isotropic models were used.

3.2.8 Summary of Reactions

Table 3-1: Summary of samples prepared by ball milling at various times.

Sample	Material	Duration of milling (h)
1	Commercial Li_3N	0
2	Commercial Li_3N	5
3	Commercial Li_3N	10
4	Commercial Li_3N	15
5	Commercial Li_3N	20
6	Commercial Li_3N	25
7	Lab-synthesised α-Li_3N	0
8	Lab-synthesised α-Li_3N	5
9	Lab-synthesised α-Li_3N	15
10	Lab-synthesised α-Li_3N	20
11	Lab-synthesised α-Li_3N	25

Table 3-2: Summary of samples prepared by pressure experiments.

Sample	Pressure (GPa)	Material	Heating Programme	Reaction Time (h)
12	1.5	Lab-synthesised α-Li_3N	-	4 h
13	5.0	Lab-synthesised α-Li_3N	-	10 h 20 m
14	4.0	Lab-synthesised α-Li_3N	523 K / 180 mins	10 h
15	7.0	Lab-synthesised α-Li_3N	523 K / 180 mins	23 h 20 m
16	1.5	Commercial Li_3N	-	4 h
17	5.0	Commercial Li_3N	-	10 h 20 m

Table 3-3: Summary of data collected on commercial Li_3N by PND.

Sample	Temperature (K)	Duration
18	293	1 h 10 m

Table 3-4: Summary of data collected during a variable temperature PND experiment using pristine β-Li_3N.

Sample	Temperature (K)	Duration
19	4.2	2 h 40 m
20	15	2 h 40 m
21	50	2 h 40 m
22	100	2 h 40 m
23	200	2 h 40 m
24	300	2 h 40 m
25	400	2 h 40 m
26	500	2 h 40 m
27	600	2 h 15 m

Table 3-5: Summary of data collected during a variable temperature *in-situ* PND experiment of β-Li_3N under D_2 gas.

Sample	Temperature (K)	Duration
28	4.2	4 h 50 m
29	15	5 h 15 m
30	50	4 h 45 m
31	100	9 h 40 m
32	200	7 h 10 m
33	300	6 h 20 m
34	400	6 h 45 m
35	500	7 h 45 m
36	600	6 h 05 m

3.3 Results and Discussion

3.3.1 Synthesis of α-Li_3N and β-Li_3N

Laboratory synthesised Li_3N (sample **7**) was a vibrant red/purple powder which had a lustrous effect. The pattern obtained from PXD analysis (Figure 3-3) confirmed the sample had no oxide or hydroxide impurities. The experimental pattern fits well with the theoretical pattern. Indexing yielded cell parameters where a = 3.659 (2) Å and c = 3.879 (1) Å and a cell volume of 45.0 (2) $Å^3$, which are in good agreement with literature values.[5] The models for each of the calculations, performed by CELREF V3, were obtained from the online Inorganic Crystal Structure Database (ICSD) and Powdercell 2.4 was used to obtain a visual comparison between the experimental and theoretical models.

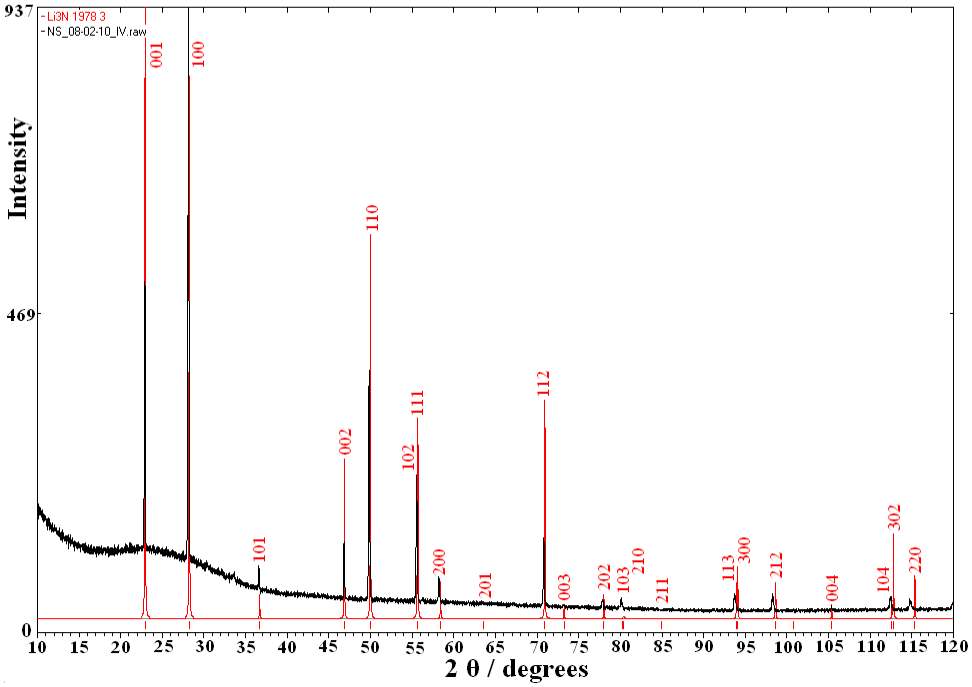

Figure 3-3: PXD analysis showing the experimental (black) and calculated (red) [5] patterns for laboratory synthesised α-Li_3N (sample 7).

Commercial lithium nitride was a dark purple/red colour (sample **1**) and after ball milling the material, the colour did not change (sample **6**). Powder X-ray diffraction revealed that after ball milling, the presence of α–Li_3N had decreased markedly however there was still a small amount present as manifested by reflections at ~23 and 55.5° 2theta. The experimental pattern fits well with the theoretical pattern (Figure 3.4).

Refined lattice parameters for β–Li_3N, a = 3.560 (5) Å and c = 6.355 (2) Å and a cell volume of 70.0 (1) $Å^3$, were obtained from CELREF V3. The number and intensity of reflections for α-Li_3N were too low to allow accurate indexing.

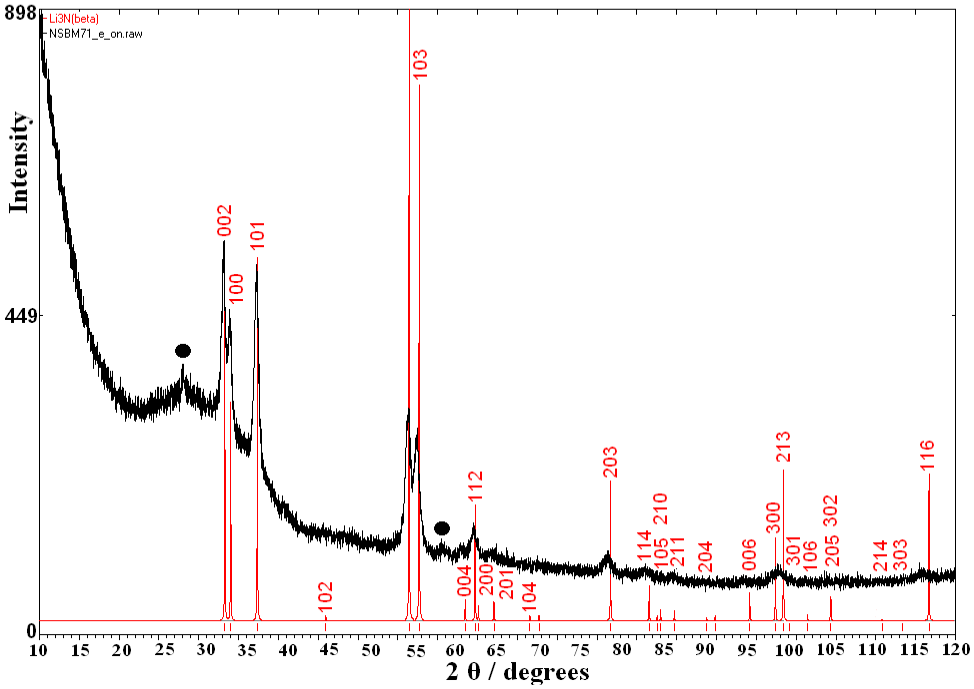

Figure 3-4: PXD analysis for sample 6 showing the experimental pattern (black) and the calculated pattern (red) [6] for laboratory synthesised β-Li_3N.
Black circle indicates reflection from α-Li_3N.

3.3.2 *Scanning Electron Microscopy*

SEM micrographs for commercial Li_3N (sample **1**) showed the morphology of the material was poorly defined. The as-received material was composed of irregular particles (Figure 3-5). Typically, the particles ranged from 1-6 μm throughout the sample.

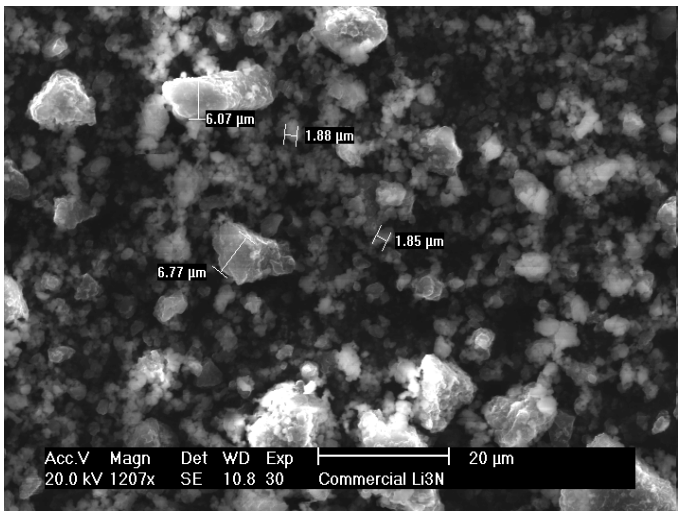

Figure 3-5: SEM micrograph of as-received commercial Li_3N showing the presence of a range of particle sizes ranging from 1-6 μm.

A similar particle non-uniformity was not observed for lab-synthesised α-Li_3N (sample **7**). The micrographs of this material showed that the sample was composed of well-defined hexagonal rods with the tendency to align in stacked arrays, evident in Figure 3-6 (a). These hexagonal rods were 5-10 μm in cross section and much longer in length as shown in Figure 3-6 (b).

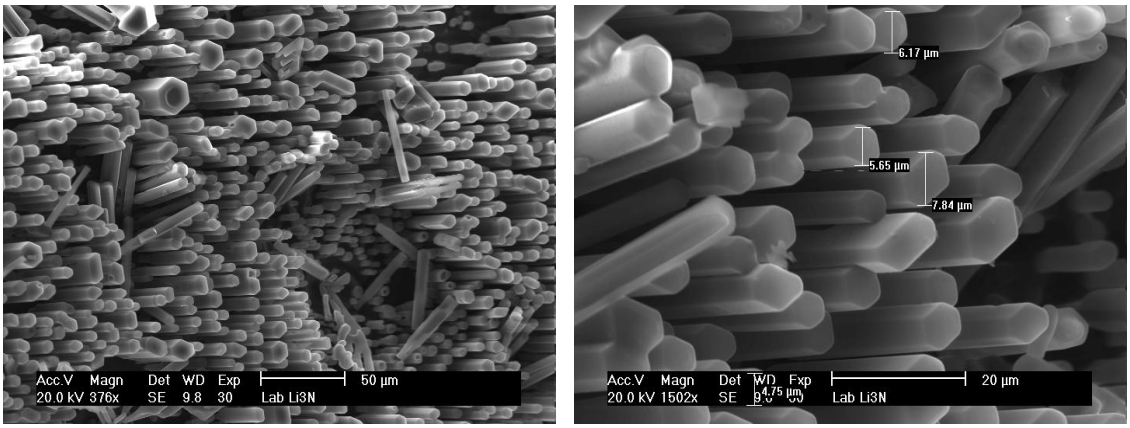

Figure 3-6: SEM micrographs of lab-synthesised α-Li_3N at (a) 50 μm and (b) 20 μm.

3.3.3 Ball milling of Li_3N

In order to achieve quality data suitable for Rietveld refinement purposes, the samples of ball milled Li_3N required overnight data collection to reduce the noise present in the background. From Figure 3-7, it is evident that overnight data collection gives a superior signal : noise ratio and therefore was more suitable for Rietveld refinement.

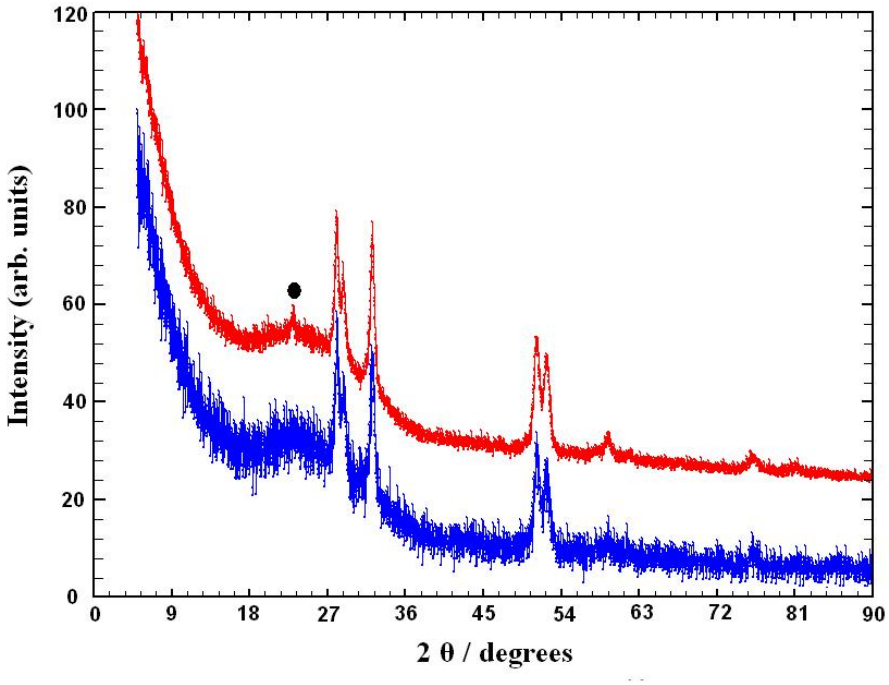

Figure 3-7: Comparison of 1 h PXD data collection vs. 12 h PXD data collection for commercial Li_3N which had been ball milled for 25 hours.
(red – overnight data set, blue – 1 hour data set) where the black circle represents a reflection from α-Li_3N.

Ball milling commercial Li_3N for 5 h and more led to the synthesis of β-Li_3N. After 5 hours, it was evident that the main phase of the material was β-Li_3N however one small peak matching to the alpha phase of Li_3N was still present. To eliminate any presence of α-Li_3N, milling of the material was continued for further 5 hour intervals in attempt to synthesise single phase β-Li_3N however a small amount of α-Li_3N could still be observed by PXD after 25 h (Figure 3-8).

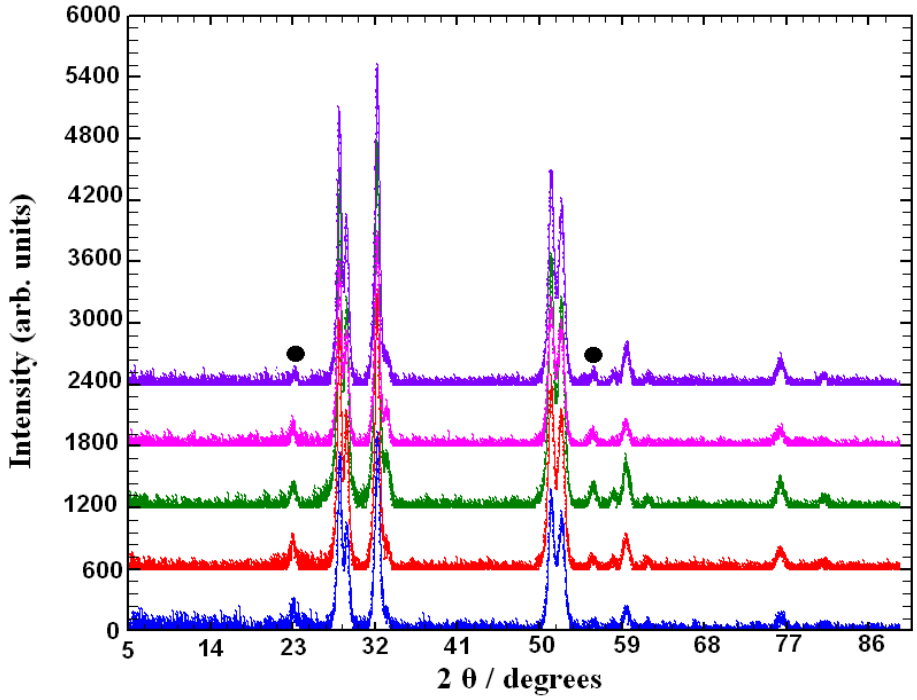

Figure 3-8: Comparison of subtracted background PXD data collected after ball milling commercial Li_3N.
5 h (blue), 10 h (red), 15 h (green), 20 h (magenta) and 25 h (purple), samples 2-6. The black circles indicate reflections for α-Li_3N.

The same method of transformation by ball milling was followed using laboratory synthesised α-Li_3N. After the initial 5 h milling period, the main phase of the material appeared to be β-Li_3N with no α-Li_3N present (Figure 3-9). A slight impurity was present in some samples however, in the form of Li_2O which could have been due to the stainless steel milling jar not being clamped properly as the starting material was single phase α-Li_3N with no impurities.

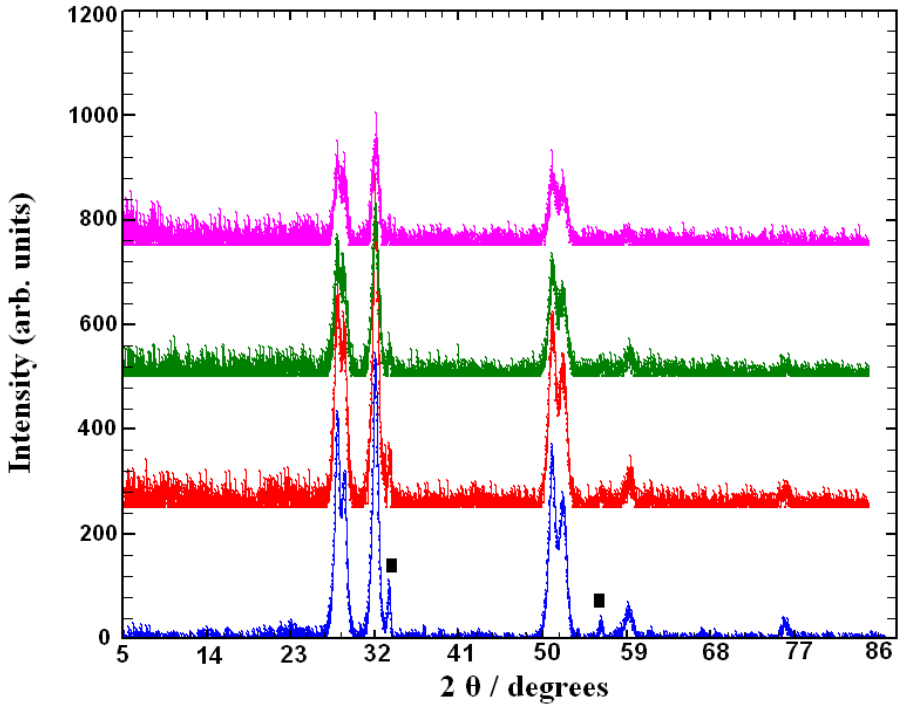

Figure 3-9: Comparison of subtracted background PXD data collected after ball milling lab-synthesised Li_3N.
5 h (blue), 15 h (red), 20 h (green) and 25 h (magenta), samples 8-11. The black squares indicate reflections for Li_2O.

Initially Rietveld refinements against PXD data were performed (Figure 3-10, Figure 3-11, Figure 3-12) in order to obtain weight percentage values for alpha and beta phases of commercial Li_3N pre- and post-milling. Table 3-1 highlights the fact that as-received commercial Li_3N (sample **1**) is an approximate 50:50 mixture of both phases. Selected Rietveld refinement data are presented in Table 3-6 and the observed, calculated and difference plot is displayed in Figure 3.10.

Atomic positions and isotropic temperature factors for both alpha and beta phases of Li_3N are shown in Table 3-7 and Table 3-8. For each phase, it was only possible to refine each atom isotropically due to the fact that the atoms are light and there are a large number of peaks present. Only the z atomic coordinate of β-Li_3N could be refined as the other atoms are all located on special positions. Tables displaying interatomic distances and bond angles obtained from Rietveld refinements of PXD data for ball milled samples are presented in the appendix.

Table 3-6: Selected Rietveld refinement data from the X-ray refinement of sample 1, un-milled commercial Li_3N at 293 K.

Empirical Formula	α-Li_3N	β-Li_3N
Collection temperature (K)	293	
Crystal system	Hexagonal	Hexagonal
Space Group	*P6/mmm*	*P6$_3$/mmc*
Lattice parameters	*a* = 3.6446 (3)	*a* = 3.5671 (4)
	c = 3.8710 (5)	*c* = 6.3417 (10)
V / Å ^{3}	44.529 (8)	69.884 (15)
Z	1	2
Unit cell formula weight, M_w	34.830	69.660
Density (g/cm^3)	1.299	1.655
wt. %	48.17 (1)	51.83 (1)
No. of varied parameters	39	
No. of observations	4663	
R_{wp}	0.0757	
R_p	0.0576	
χ^2	1.213	

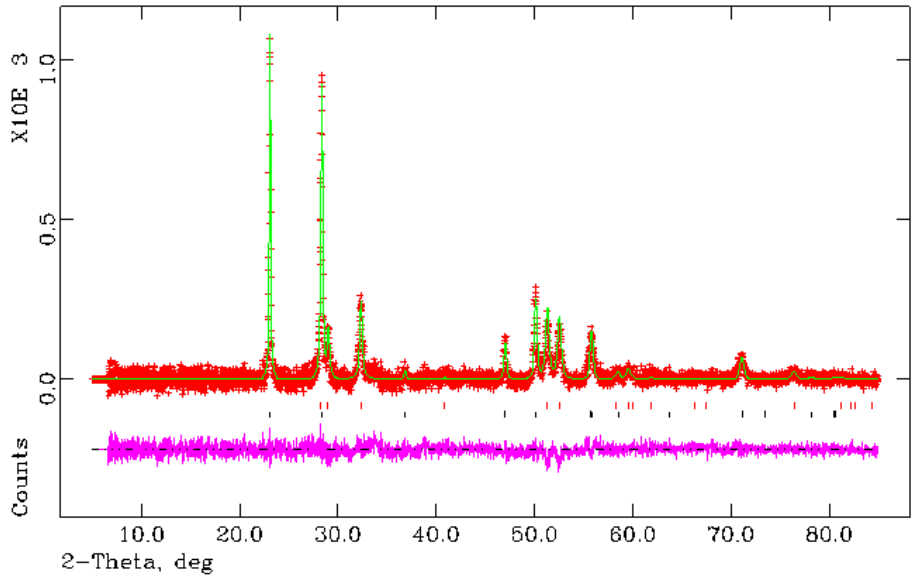

Figure 3-10: Observed, calculated and difference (OCD) plot obtained from X-ray Rietveld refinement of sample 1, un-milled commercial Li_3N at 293 K.
The black tickmarks indicate reflections from α-Li_3N and the red tickmarks indicate reflections from β-Li_3N.

Table 3-7: Atom positions and isotropic temperature factors generated by X-ray Rietveld refinement of the alpha polymorph of Li_3N in the un-milled commercial material at 293 K.

Atom	Li (1)	Li (2)	N
site	1b	2c	1a
x	0	0.3333	0
y	0	0.6667	0
z	0.5	0	0
100 x U_{iso} / Å^2	5.5 (5)	5.7 (4)	5.4 (3)
Occupancy	1.00	1.00	1.00

Table 3-8: Atom positions and isotropic temperature factors generated by X-ray Rietveld refinement of the beta polymorph of Li_3N in the un-milled commercial material at 293 K.

Atom	Li (1)	Li (2)	N
site	2b	4f	2c
x	0	0.3333	0.3333
y	0	0.6667	0.6667
z	0.25	0.5782 (18)	0.25
100 x U_{iso} / Å^2	5.4 (7)	5.7 (4)	5.5 (5)
Occupancy	1.00	1.00	1.00

After only 5 hours of ball milling, there was a marked change in this ratio with β-Li_3N as the main phase with a phase fraction of 98.135 % (3). Selected data obtained from the Rietveld refinement of the commercial Li_3N after ball milling for 5 h (sample 2) are presented in Table 3-9 and the observed, calculated and difference plot is illustrated in Figure 3-11. Isotropic temperature factors for β-Li_3N are shown in Table 3-10. Due to the fact that the sample was composed of predominantly β-Li_3N (~98%), the isotropic temperature factors of the remaining 2% of α-Li_3N could not be refined since it is a very small fraction of a poorly crystalline sample (Table 3-11).

Table 3-9: Selected Rietveld refinement data from the X-ray refinement of sample 2, commercial Li_3N after ball milling for 5 h at 293 K.

Empirical Formula	β-Li_3N	α-Li_3N
Collection temperature (K)	293	
Crystal System	Hexagonal	Hexagonal
Space Group	*$P6_3/mmc$*	*P6/mmm*
Lattice parameters	*a* = 3.5537 (5)	*a* = 3.6261 (24)
	c = 6.3340 (11)	*c* = 3.8224 (32)
V / Å ^{3}	69.273 (2)	43.52 (5)
Z	2	1
Unit cell formula weight, M_w	69.660	34.830
Density (g/cm^3)	1.670	1.328
wt. %	98.135 (3)	1.865 (3)
No. of varied parameters	15	
No. of observations	4999	
R_{wp}	0.0323	
R_p	0.0241	
χ^2	1.822	

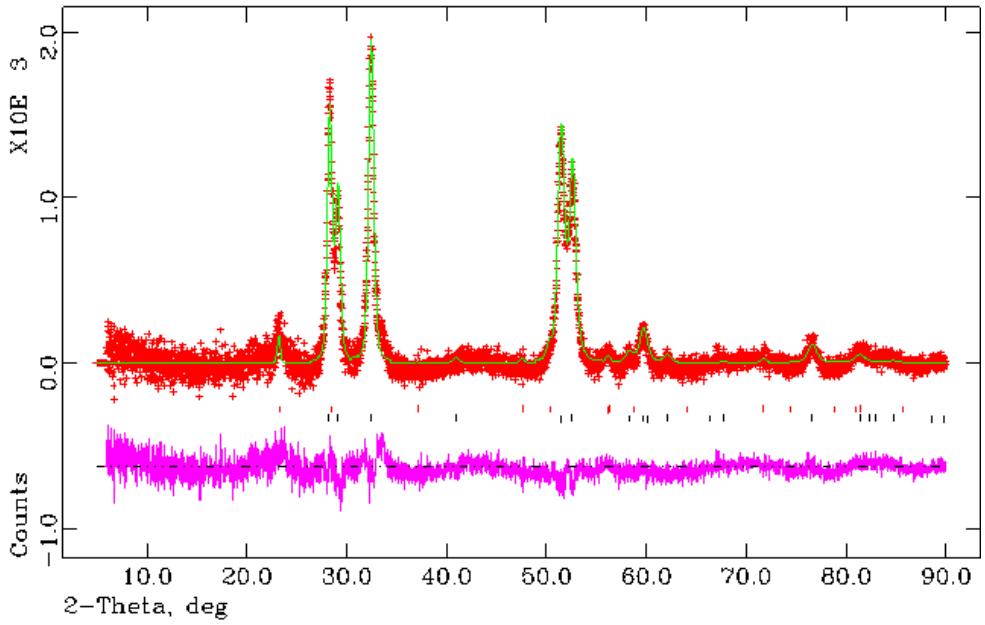

Figure 3-11: Observed, calculated and difference (OCD) plot obtained from X-ray Rietveld refinement of sample 2, commercial Li_3N after milling for 5 h.
The black tickmarks indicate reflections from β-Li_3N and the red tickmarks indicate reflections from α-Li_3N.

Table 3-10: Atom positions and isotropic temperature factors generated by X-ray Rietveld refinement of the beta polymorph of Li_3N in the milled (5 h) commercial material at 293 K.

Atom	Li (1)	Li (2)	N
Site	2b	4f	2c
x	0	0.3333	0.3333
y	0	0.6667	0.6667
z	0.25	0.5729 (5)	0.25
100 x U_{iso} / Å^2	6.3 (3)	7.8 (1)	6.3 (2)
Occupancy	1.00	1.00	1.00

Table 3-11: Atom positions and isotropic temperature factors generated by X-ray Rietveld refinement of the alpha polymorph of Li_3N in the milled (5 h) commercial material at 293 K.

Atom	Li (1)	Li (2)	N
Site	1b	2c	1a
x	0	0.3333	0
y	0	0.6667	0
z	0.5	0	0
100 x U_{iso} / Å^2	2.50	2.50	2.50
Occupancy	1.00	1.00	1.00

In order to obtain single phase β-Li_3N, the duration of ball milling was increased. After 25 h, there are no observed reflections of α-Li_3N (sample **6**). At this point, the particle size has been decreased further due to the increased duration of milling. As a consequence of increased milling, peak broadening occurs and ultimately the crystallinity of the sample is reduced markedly. Selected Rietveld refinement data is presented in Table 3-12 for sample 6 and a representation of the observed, calculated and difference plot is shown in Figure 3-12. Atomic positions and isotropic temperature factors are presented in Table 3-13. It is possible that a small fraction of α-Li_3N is present in sample **6** which is concealed by background noise however there is other evidence to suggest this.

Table 3-12: Selected Rietveld refinement data from the X-ray refinement of sample 6, commercial Li_3N after ball milling for 25 h at 293 K.

Empirical Formula	β-Li_3N
Collection temperature (K)	293
Crystal System	Hexagonal
Space Group	*P6₃/mmc*
Lattice parameters	*a* = 3.5660 (6)
	c = 6.3562 (17)
V / Å ^{3}	70.00 (2)
Z	2
Unit cell formula weight, M_w	69.660
Density (g/cm^3)	1.652
No. of varied parameters	9
No. of observations	4786
R_{wp}	0.1421
R_p	0.1011
χ^2	1.358

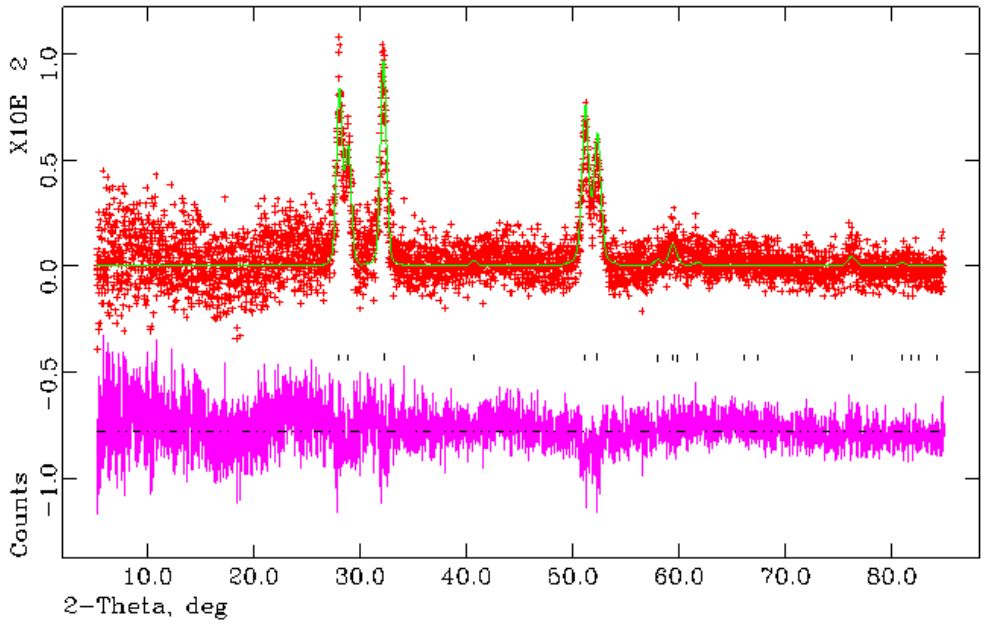

Figure 3-12: Observed, calculated and difference (OCD) plot obtained from X-ray Rietveld refinement of sample 6, commercial Li_3N after milling for 25 h.
The black tickmarks indicate reflections from β-Li_3N.

Table 3-13: Atom positions and isotropic temperature factors generated by X-ray Rietveld refinement of the beta polymorph of Li_3N in the milled (25 h) commercial material at 293 K.

Atom	Li (1)	Li (2)	N
Site	2b	4f	2c
x	0	0.3333	0.3333
y	0	0.6667	0.6667
z	0.25	0.5769 (15)	0.25
100 x U_{iso} / Å^2	7.6 (7)	9.9 (4)	9.8 (7)
Occupancy	1.00	1.00	1.00

The same experiment was repeated using laboratory synthesised α-Li_3N (samples 7-11) as the starting material and subsequent Rietveld refinements were performed (Figure 3-13, Figure 3-14, Figure 3-15). The initial starting material was single phase α-Li_3N however after milling a slight Li_2O impurity phase was present which was most likely to be due to experimental error. Selected Rietveld refinement data are presented in Table 3-14 and atomic positions and anisotropic temperature factors are displayed in Table 3-15. Each atom present in α-Li_3N was refined anisotropically.

Table 3-14: Selected Rietveld refinement data from the X-ray refinement of sample 7, un-milled laboratory synthesised α-Li_3N at 293 K).

Empirical Formula	α-Li_3N
Collection temperature (K)	293
Crystal System	Hexagonal
Space Group	*P6/mmm*
Lattice parameters	*a* = 3.64822 (4)
	c = 3.87378 (6)
V / Å ^{3}	44.6507 (9)
Z	1
Unit cell formula weight, M_w	34.830
Density (g/cm^3)	1.295
No. of varied parameters	14
No. of observations	4786
R_{wp}	0.0503
R_p	0.0356
χ^2	2.758

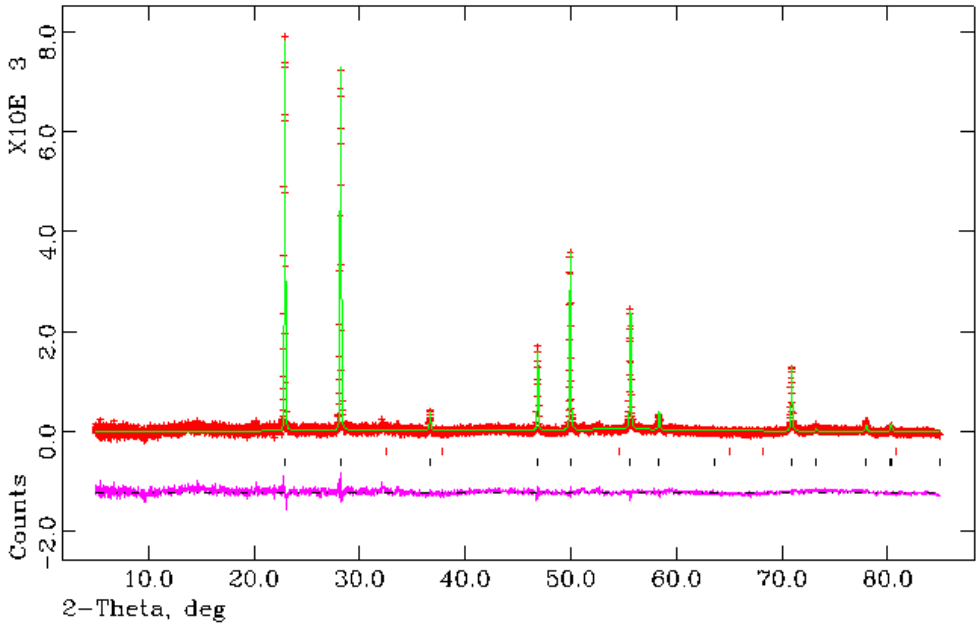

Figure 3-13: Observed, calculated and difference (OCD) plot obtained from X-ray Rietveld refinement of sample 7 (lab-synthesised α-Li_3N).
The black tickmarks indicate reflections from α-Li_3N and the red tickmarks indicate reflections from Li_2O.

Table 3-15: Atom positions and anisotropic temperature factors generated by X-ray Rietveld refinement of the alpha polymorph of Li_3N in the un-milled laboratory synthesised α-Li_3N material at 293 K.

Atom	Li (1)	Li (2)	N
Site	1b	2c	1a
x	0	0.3333	0
y	0	0.6667	0
z	0.5	0	0
100 x U_{11} / Å^2	2.8 (5)	4.9 (2)	3.5 (2)
100 x U_{22} / Å^2	2.8 (5)	4.9 (2)	3.5 (2)
100 x U_{33} / Å^2	3.9 (6)	6.2 (5)	2.5 (4)
100 x U_{12} / Å^2	1.4 (2)	2.44 (9)	1.7 (1)
100 x U_{13} / Å^2	0	0	0
100 x U_{23} / Å^2	0	0	0
Occupancy	1.00	1.00	1.00

After milling laboratory synthesised α-Li_3N for 5 hours, the alpha phase had fully converted to beta phase (Figure 3-14). Selected Rietveld refinement data is presented in Table 3-16 and atomic positions and isotropic temperature factors are shown in Table 3-17. Atomic positions and isotropic temperature factors for the impurity phase, Li_2O, are shown in Table 3-18.

Table 3-16: Selected Rietveld refinement data from the X-ray refinement of sample 8, laboratory synthesised α-Li_3N after ball milling for 5 h at 293 K.

Empirical Formula	**β-Li_3N**	**Li_2O**
Collection temperature (K)	293	
Crystal System	Hexagonal	Cubic
Space Group	*$P6_3/mmc$*	*Fm-3m*
Lattice parameters	*a* = 3.564 (2)	*a* = 4.6041 (8)
	c = 6.3384 (5)	-
V / Å ^{3}	69.736 (7)	97.599 (28)
Z	2	4
Unit cell formula weight, M_w	69.660	119.524
Density (g/cm^3)	1.659	2.034
wt. %	98.285 (1)	1.715 (1)
No. of varied parameters	14	
No. of observations	3903	
R_{wp}	0.0382	
R_p	0.0298	
χ^2	1.803	

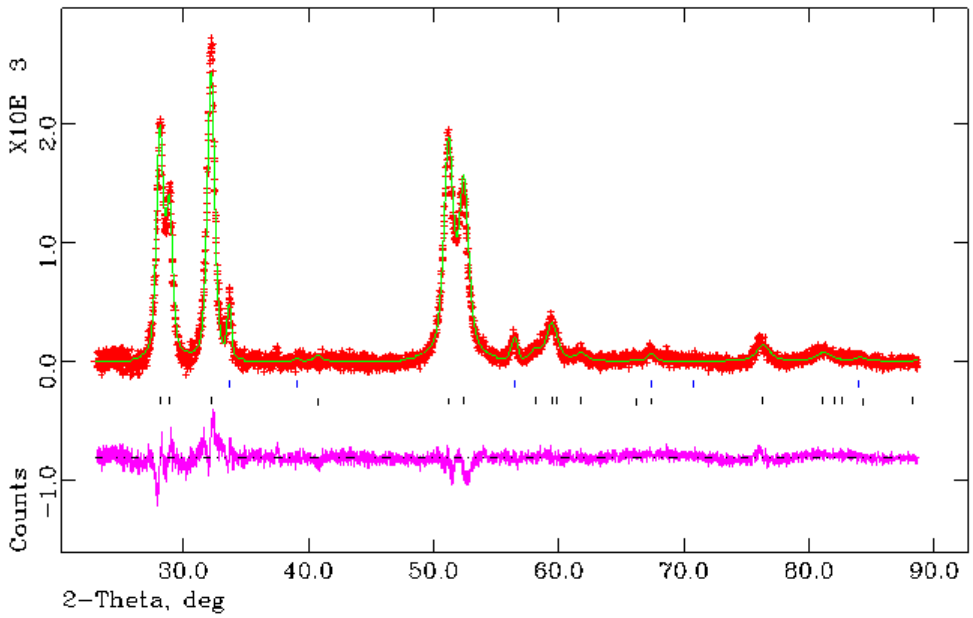

Figure 3-14: Observed, calculated and difference (OCD) plot obtained from X-ray Rietveld refinement of sample 8, lab-synthesised α-Li_3N after milling for 5 hours.
The black tickmarks indicate reflections from β-Li_3N and the blue tickmarks indicate reflections from Li_2O.

Table 3-17: Atom positions and isotropic temperature factors generated by X-ray Rietveld refinement of the beta polymorph of Li_3N in the milled (5 h) laboratory synthesised α-Li_3N material at 293 K.

Atom	Li (1)	Li (2)	N
Site	2b	4f	2c
x	0	0.3333	0.3333
y	0	0.6667	0.6667
z	0.25	0.5745 (4)	0.25
100 x U_{iso} / Å^2	4.5 (2)	7.76 (9)	5.9 (1)
Occupancy	1.00	1.00	1.00

Table 3-18: Atom positions and isotropic temperature factors generated by X-ray Rietveld refinement of Li_2O in milled (5 h) laboratory synthesised α-Li_3N material at 293 K.

Atom	Li	O
Site	8c	4b
x	0.25	0
y	0.25	0
z	0.25	0
100 x U_{iso} / Å^2	2.50	2.50
Occupancy	1.00	1.00

Although full conversion of α-Li_3N to β-Li_3N using laboratory synthesised α-Li_3N had been achieved after 5 hours, further milling (25 h) was performed on the sample so that a direct comparison of lattice parameters between both starting materials could be obtained. Selected Rietveld refinement data for sample **11** is presented in Table 3-19 and the observed, calculated and difference plot is illustrated in Figure 3-15. Atomic positions and isotropic temperature factors are shown in Table 3-20.

Table 3-19: Selected Rietveld refinement data from the X-ray refinement of sample 11, laboratory synthesised α-Li_3N after ball milling for 25 h at 293 K.

Empirical Formula	β-Li_3N
Collection temperature (K)	293
Crystal System	Hexagonal
Space Group	*$P6_3/mmc$*
Lattice parameters	*a* = 3.5624 (6)
	c = 6.3364 (17)
V / Å ^{3}	69.641 (25)
Z	2
Unit cell formula weight, M_w	69.660
Density (g/cm^3)	1.661
No. of varied parameters	9
No. of observations	4165
R_{wp}	0.0799
R_p	0.0616
χ^2	1.224

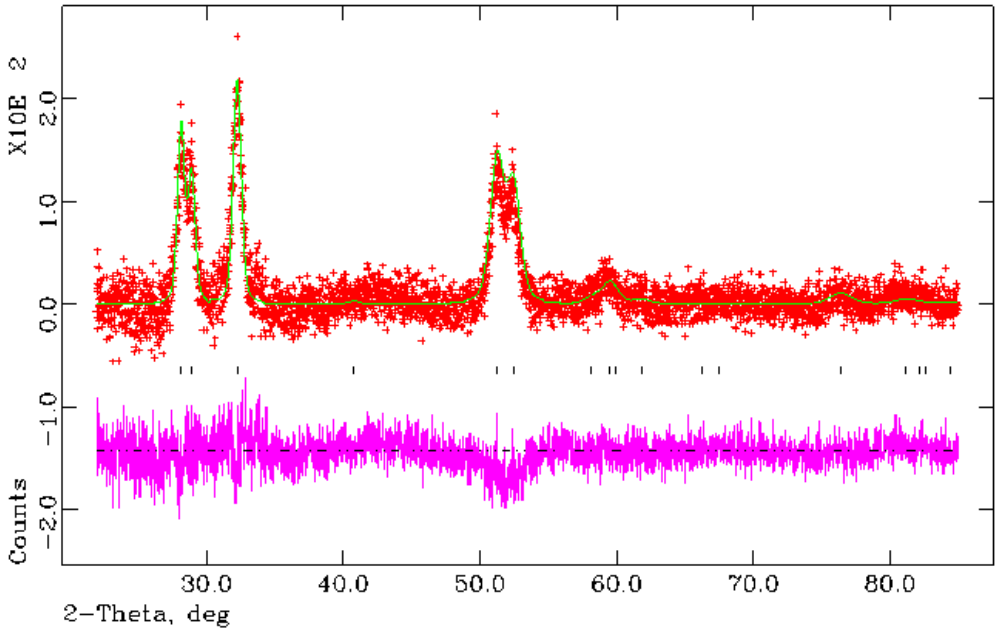

Figure 3-15: Observed, calculated and difference (OCD) plot obtained from X-ray Rietveld refinement of sample 11, laboratory synthesised α-Li_3N after milling for 25 h.
The black tickmarks indicate reflections from β-Li_3N.

Table 3-20: Atom positions and isotropic temperature factors generated by X-ray Rietveld refinement of the beta polymorph of Li_3N in the milled (25 h) laboratory synthesised α-Li_3N material at 293 K.

Atom	Li (1)	Li (2)	N
Site	2b	4f	2c
x	0	0.3333	0.3333
y	0	0.6667	0.6667
z	0.25	0.5733 (13)	0.25
100 x U_{iso} / Å^2	4.9 (6)	6.7 (3)	5.3 (4)
Occupancy	1.00	1.00	1.00

A comparison of the statistical values obtained for commercial Li_3N after milling for 25 h (sample **6**) with regards to milled (25 h) laboratory synthesised α-Li_3N (sample **11**) reveals that values obtained for the latter sample are statistically better. It is likely that statistical data for the laboratory synthesised α-Li_3N starting material is better due to the fact that it is highly crystalline unlike the commercial Li_3N starting material.

3.3.4 Synthesis of β-Li_3N by pressure

In addition to ball milling methods, β-Li_3N was synthesised using high pressures. [6] Commercial and laboratory synthesised α-Li_3N were loaded into a molybdenum capsule before being pressurised. The experiments were carried out at Leopold-Franzens-Universität, Innsbruck, Austria by Dr. Gunter Heymann and Prof. Hubert Huppertz.

Powder X-ray diffraction patterns from pressurised samples are shown in Figure 3-16. On pressurising a sample of laboratory synthesised α-Li_3N (sample **12**) at 1.5 GPa with a total reaction time (including pressurising, and depressurising of the sample) of 4 h, resulted in the detection of only a very small amount of β-Li_3N. The remainder of the sample consisted of α-Li_3N as well as LiOH and Li_2O impurities. On increasing the pressure to 5 GPa and increasing the overall reaction time to approximately 10 h (sample **13**), the main phase present in the sample became β-Li_3N. A small amount of α-Li_3N as well as LiOH and Li_2O impurities were also present in the sample.

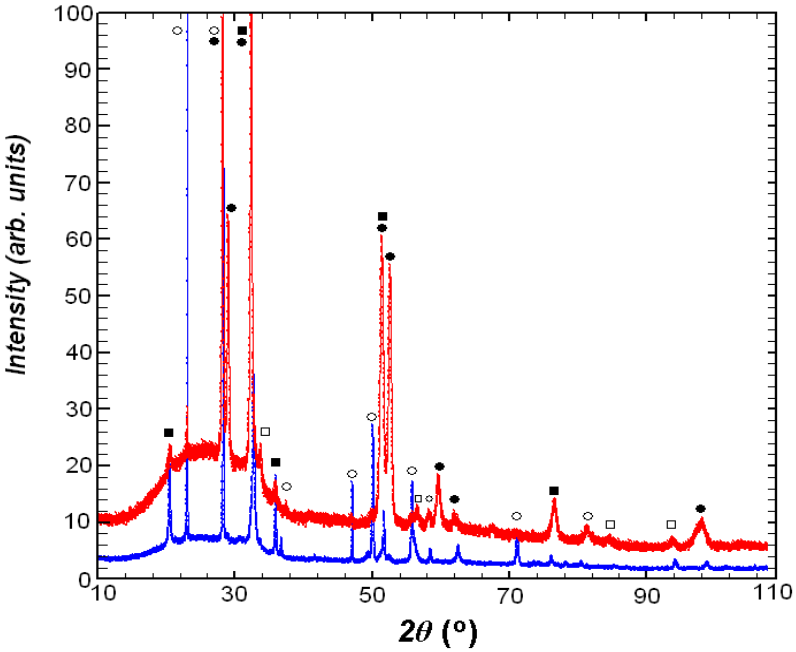

Figure 3-16: Comparison of PXD data of lab-synthesised Li_3N after application of pressure. The pattern shown in blue shows reflections exhibited by the sample treated at 1.5 GPa (sample 12).

The pattern shown in red are obtained when the sample has been pressurised at 5 GPa (sample 13). The white circle represents reflections from α-Li_3N, the black circle represents reflections from β-Li_3N, the white square represents reflections from Li_2O the black square represents reflections from LiOH.

Combining high pressures with a heating programme made it possible to achieve conversion to β-Li_3N (Figure 3-17). The employment of a heating programme facilitated the conversion of α-Li_3N to β-Li_3N, providing a more complete conversion that using pressure alone. Using a lower pressure of 4 GPa and a total reaction time of 10 h with the addition of a heating programme set to 250 °C for 3 h before being quenched facilitates the synthesis of β-Li_3N (sample **14**). In attempt to improve the crystallinity of the product, the pressure applied to the sample was increased further, to 7 GPa. Furthermore, by increasing the overall reaction time to approximately 23 h whilst continuing to apply the same heating programme successfully enabled the synthesis of a more crystalline sample of β-Li_3N (sample **15**). Refinement of the observed reflections gave values of a = 3.5700 (6) Å and c = 6.3436 (2) Å and a cell volume of 70.01 (1) Å^3. The refined lattice parameters obtained after performing the high pressure experiments are in agreement with those obtained from the refinements from the ball milled samples.

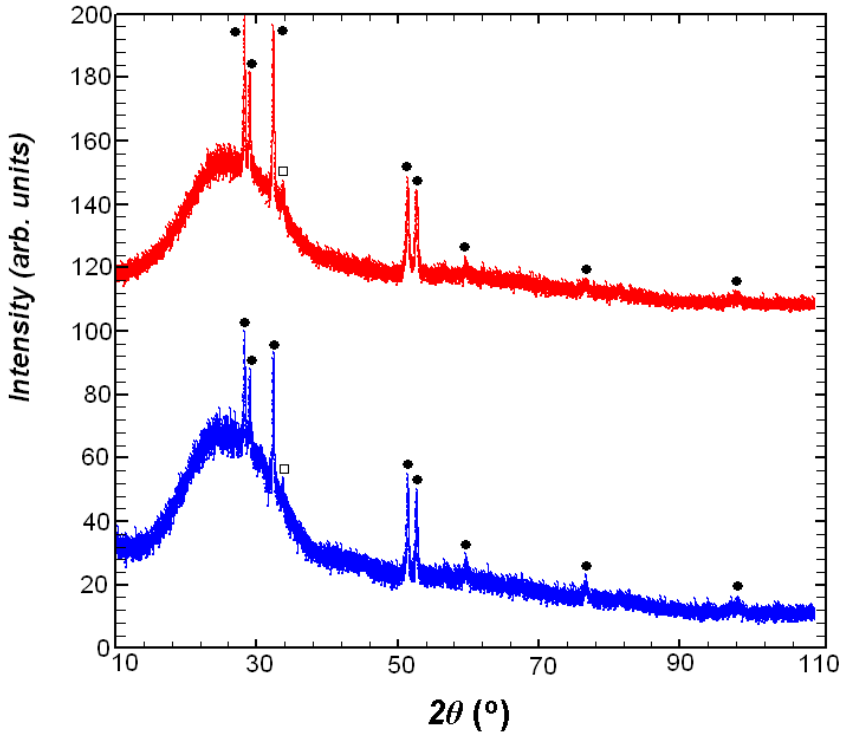

Figure 3-17: Comparison of PXD data of lab-synthesised Li_3N after application of pressure with simultaneous heating to 523 K.

The pattern shown in blue shows reflections exhibited by the sample treated at 4.0 GPa (sample 14). The pattern shown in red are obtained when the sample has been pressurised at 7.0 GPa (sample 15). The black circle represents reflections from β-Li_3N and the white square represents reflections from Li_2O.

Subsequent experiments were performed on commercial Li_3N to investigate if this material could also undergo a phase transition from α-Li_3N to β-Li_3N by applying pressure in agreement with the behaviour of laboratory synthesised α-Li_3N.

Although the X-ray patterns shown in Figure 3-18 exhibit reflections from Li_2O and LiOH impurity phases, there are reflections consistent with β-Li_3N. The phase fraction of β-Li_3N and the crystallinity of this phase increased as the pressure did so. On applying a pressure of 1.5 GPa for 4 h (sample **16**), the lattice parameters varied slightly from those reported in the literature, where a = 3.572 (8) Å and c = 6.342 (3) Å with a cell volume of 70.1 (2) $Å^3$. On comparing refined lattice parameters at varying pressures (1.5 GPa and 5 GPa), the a parameter remained consistent. After applying a pressure of 5 GPa for 10 h (sample **17**), a = 3.572 (2) Å and c = 6.3496 (6) Å and the cell volume was 70.15 (5) $Å^3$.

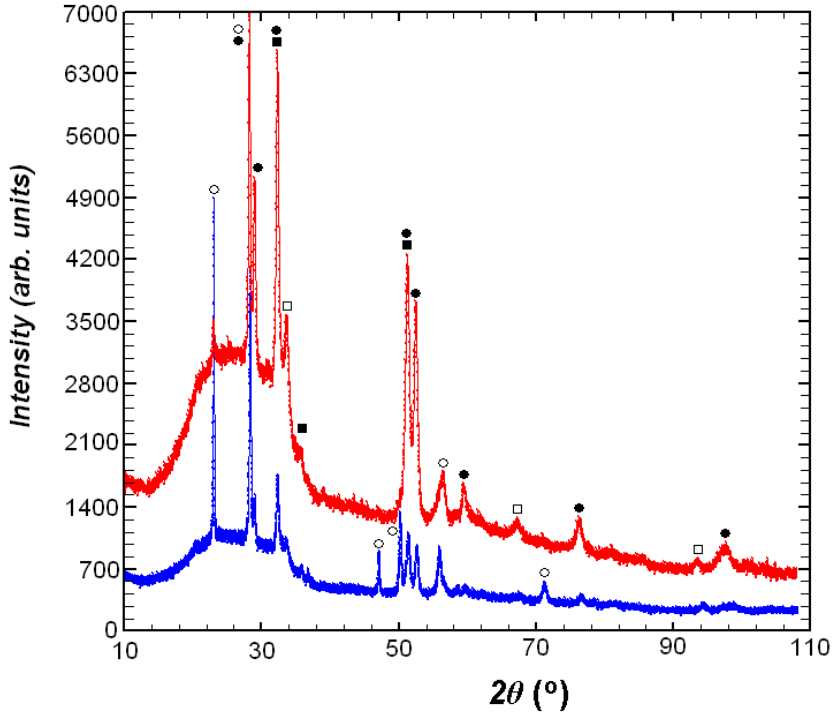

Figure 3-18: Comparison of PXD data of commercial Li_3N after application of pressure. The pattern shown in blue shows reflections exhibited by the sample after applying a pressure of 1.5 GPa (sample 16). The pattern shown in red are obtained when the sample has been pressurised at 5 GPa (sample 17). The white circle represents reflections from α-Li_3N, the black circle represents reflections from β-Li_3N, the white square represents reflections from Li_2O the black square represents reflections from LiOH.

It is evident from the samples investigated and the reactions performed that application of pressure alone is not sufficient to induce complete conversion from α-Li_3N to β-Li_3N. From the results shown in Figure 3-17 (samples **14** and **15**), the employment of a heating programme aids conversion however it should be noted that although pressure alone was

insufficient to induce a phase transformation under these conditions, using higher pressures may eliminate the need for a heating programme.

Although no heating programme was applied to commercial Li_3N, it is believed that if a heating programme were to be applied to this material, complete conversion would occur in agreement with laboratory-synthesised α-Li_3N due to their similar behaviour under pressure alone and the fact that the degree of crystallinity in each sample is comparable. A phase transformation from β-Li_3N to α-Li_3N at temperatures above 473 K has been reported, [6] however the application of pressure prevents this transformation from occurring.

A pressure-induced phase in a Li_3N single crystal was initially described my Mali *et al* [9] where phase conversion begins around 0.42 GPa at 300 K and as the pressure increases, the phase fraction of β-Li_3N continues to rise until 0.7 GPa. At this higher pressure, it was reported that there is only 2% of the alpha polymorph remaining. These investigations were performed *in-situ* using a beryllium-copper NMR probe and employing He as the pressure transmitting medium. [27] In comparison, experiments in this work were performed using powdered samples (samples **12**-**17**) and exploiting a multi-anvil method at much higher pressures. Further investigations would be required to ascertain the importance of the method employed and the pressures used in regards to aiding phase conversion.

3.3.5 Powder Neutron Diffraction Experiments

3.3.5.1 PND study of commercial Li_3N at room temperature

Figure 3-19 displays the observed, calculated and difference (OCD) plot for the data collected for a sample of commercial Li_3N at room temperature (sample **18**). Selected refinement data are presented in Table 3-21. The experimental model for both the alpha and beta phases are in good agreement with the literature structures proposed by Zintl and Brauer, and Biester *et al* respectively. [5, 6]

Table 3-21: Selected Rietveld refinement data from the PND Rietveld refinement of sample 18, commercial Li_3N at 293 K.

Empirical Formula	α-Li_3N	β-Li_3N
Collection temperature (K)	293	
Crystal system	Hexagonal	Hexagonal
Space Group	*P6/mmm*	*P6$_3$/mmc*
Lattice parameters	*a* = 3.6468 (1)	*a* = 3.5692 (1)
	c = 3.8734 (2)	*c* = 6.3424 (5)
V / Å ^{3}	44.608 (3)	69.971 (6)
Z	1	2
Unit cell formula weight, M_w	34.830	69.660
Density (g/cm^3)	1.297	1.653
wt. %	52.803 (2)	47.197 (2)
No. of varied parameters	32	
No. of observations	4056	
R_{wp}	0.0262	
R_p	0.0424	
χ^2	1.520	

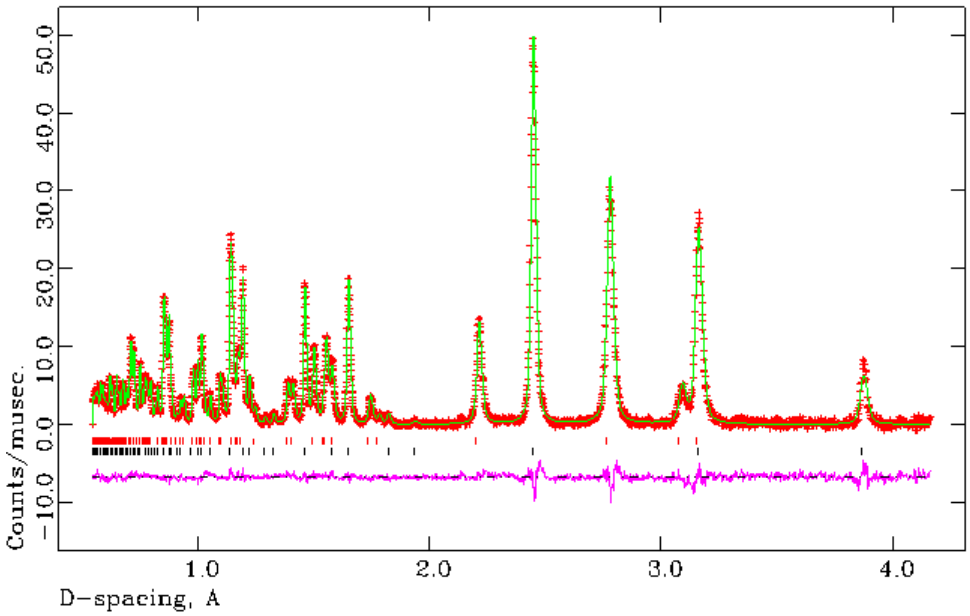

Figure 3-19: Observed, calculated and difference (OCD) plot from the PND Rietveld refinement of sample 18, commercial Li_3N at room temperature from PND data, 90° (E) bank. The black tickmarks indicate reflections from α-Li_3N and the red tickmarks indicate reflections from β-Li_3N.

With regard to the alpha and beta phases of commercial Li_3N, although the lattice parameters obtained for PXD and PND are comparable, the percentage weight fractions differ. Table 3.6 (sample **1**) shows that the percentages for α-Li_3N and β-Li_3N are approximately 48 % and 52 % respectively however data obtained from Rietveld refinements of PND data contradicts this where the approximate phase fraction of α-Li_3N in commercial Li_3N is 53 % and that β-Li_3N was 47 % (Table 3-21, sample **18**). It is likely that the phase fractions obtained from the Rietveld refinement of the PND data are more accurate since scattering for Li and N atom in PND is much stronger for these atoms than in comparison to PXD. It should also be noted that the R factors obtained for the PND data are better. Even though these phase fractions were not consistent, this did not have any bearing on subsequent synthesis of β-Li_3N (as shown in Section 3.3.3).

Li (1) and N (1) were varied anisotropically however Li (2) could only be varied isotropically. Unlike α-Li_3N, which contains close to 3% vacancies at room temperature, [3] data showed that both alpha and beta phases of the commercial material do not contain vacancies; the fractional occupancy of the Li atoms does not vary from 1. Atomic positions and anisotropic temperature factors are displayed in Table 3-22 and Table 3-23 for α-Li_3N and β-Li_3N respectively. The interatomic distances and bond angles generated from Rietveld refinement of sample 18 are displayed in Table 3-24 and Table 3-25 respectively.

Table 3-22: Atom positions and anisotropic temperature factors for the PND Rietveld refinement of the alpha polymorph of Li_3N in the commercial material at 293 K.

Atom	Li (1)	Li (2)	N
site	1b	2c	1a
x	0	0.3333	0
y	0	0.6667	0
z	0.5	0	0
100 x U_{iso} / Å^2	-	1.90 (5)	-
100 x U_{11} / Å^2	1.93 (8)	-	0.92 (2)
100 x U_{22} / Å^2	1.93 (8)	-	0.92 (2)
100 x U_{33} / Å^2	0.05 (9)	-	1.49 (3)
100 x U_{12} / Å^2	0.97 (4)	-	0.46 (1)
100 x U_{13} / Å^2	0	-	0
100 x U_{23} / Å^2	0	-	0
Occupancy	1.00	1.00	1.00

Table 3-23: Atom positions and anisotropic temperature factors for the PND Rietveld refinement of the beta polymorph of Li_3N in the commercial material at 293 K.

Atom	Li (1)	Li (2)	N
Site	2b	4f	2c
x	0	0.3333	0.3333
y	0	0.6667	0.6667
z	0.25	0.5782 (4)	0.25
100 x U_{iso} / Å^2	-	2.09 (5)	-
100 x U_{11} / Å^2	0.93 (7)	-	1.06 (2)
100 x U_{22} / Å^2	0.93 (7)	-	1.06 (2)
100 x U_{33} / Å^2	1.97 (16)	-	0.97 (3)
100 x U_{12} / Å^2	0.46 (4)	-	0.529 (9)
100 x U_{13} / Å^2	0	-	0
100 x U_{23} / Å^2	0	-	0
Occupancy	1.00	1.00	1.00

Table 3-24: Interatomic distances generated by PND Rietveld refinement of sample 18 (293 K).

Interatomic Distance / Å	α-Li_3N	β-Li_3N
2x Li1-N1	1.93667 (10)	2.06076 (8)
6x Li2-N1	2.10521 (7)	(3x) 2.0814 (25)
Li1-Li2	2.86052 (8)	2.9287 (18)

Table 3-25: Bond angles generated by PND Rietveld refinement of sample 18.

Angle / ^{o}	α-Li_3N	β-Li_3N
N1-Li1-N1	4x 180.0 (0)	2x120.00 (0) 2x119.99 (0)
Li1-N1-Li2	4x 90.0 (0)	2x 90.00 (0) 4x 63.77 (1) 4x 63.76 (1)
Li2-N1-Li2	4x 60.0 (0)	2x 117.87 (5) 2x 62.13 (5)

3.3.5.2 PND variable temperature measurements on β-Li_3N

In order to understand the structural behaviour of the beta polymorph of Li_3N at variable temperatures, a PND study was conducted on POLARIS at ISIS. The data collected from the PND investigation (samples **19**-**27**) were analysed using the Rietveld method. Selected Rietveld refinement data is presented in Table 3-26 and Figure 3-20, Figure 3-21 and Figure 3-22 show the observed, calculated and difference (OCD) plots for sample **19**. Data for this sample was collected at 4.2 K for the 145^{o}, 90^{o} and 35^{o} detector banks.

Table 3-26: Selected Rietveld refinement data from the PND Rietveld refinement of sample 19 (β-Li_3N at 4.2 K).

Empirical Formula	β-Li_3N
Collection Temperature / K	4.2
Space Group	Hexagonal
Crystal system	*$P6_3/mmc$*
Lattice parameters / Å	*a* = 3.5550 (3)
	c = 6.3356 (6)
V / $Å^3$	69.34 (1)
Z	2
Unit cell formula weight, M_w	69.660
Density / g/cm^3	1.668
No. of varied parameters	28
No. of observations	11202
R_{wp}	0.0155
R_p	0.0276
χ^2	4.296

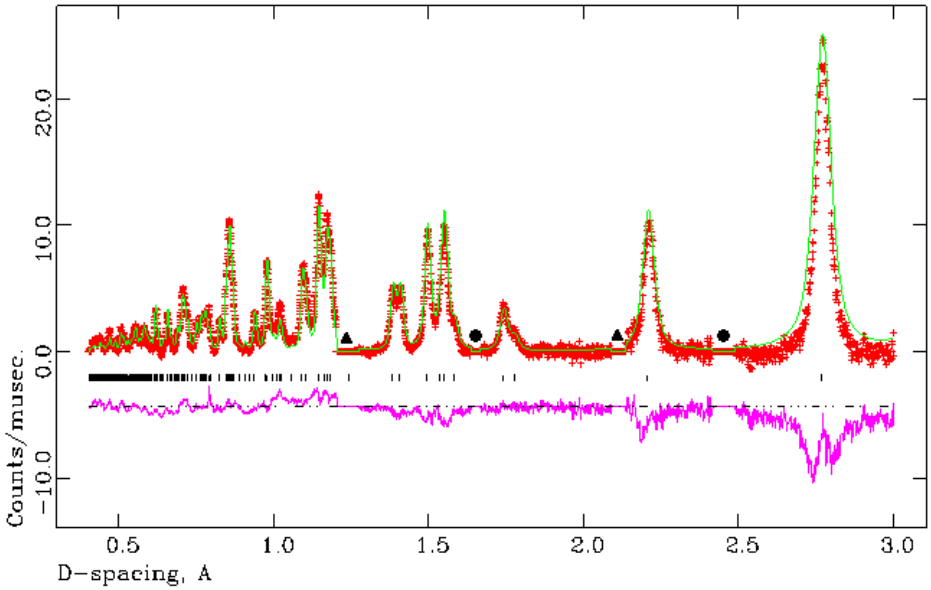

Figure 3-20: Observed, calculated and difference (OCD) plot from the PND Rietveld refinement of sample 19 (β-Li_3N at 4.2 K) from PND data, 145° (C) bank.
The black tickmarks indicate reflections from β-Li_3N. The black circles represent reflections from α-Li_3N and the black triangles represent reflections from the cryofurnace, both of which have been excluded.

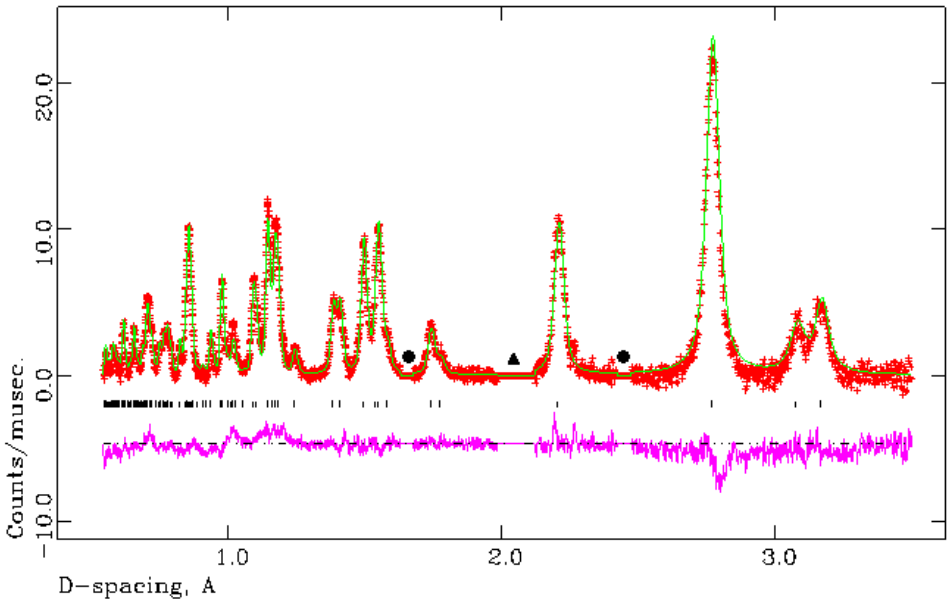

Figure 3-21: Observed, calculated and difference (OCD) plot from the PND Rietveld refinement of sample 19 (β-Li_3N at 4.2 K) from PND data, 90° (E) bank.
The black tickmarks indicate reflections from β-Li_3N. The black circles represent reflections from α-Li_3N and the black triangles represent reflections from the cryofurnace, both of which have been excluded.

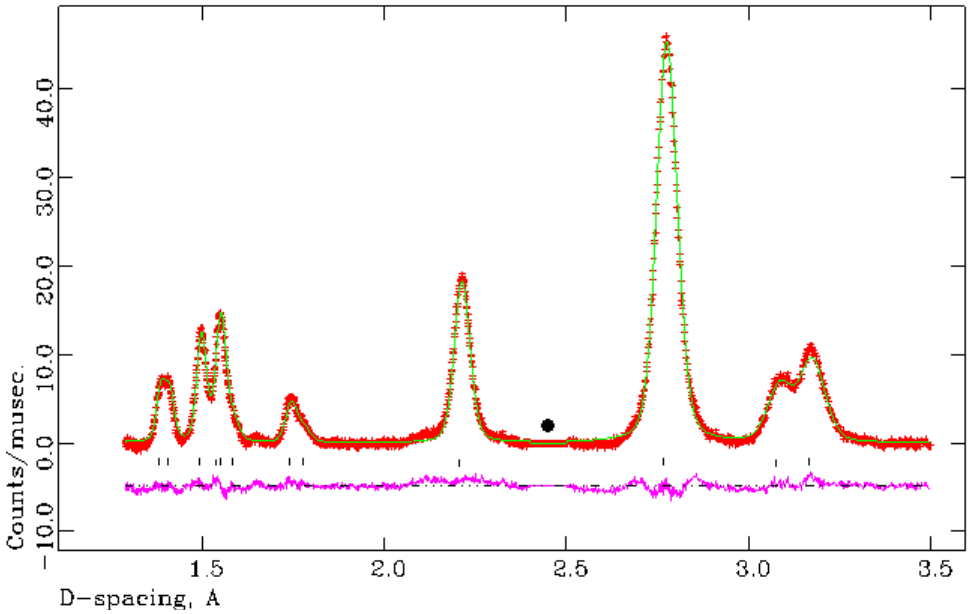

Figure 3-22: Observed, calculated and difference (OCD) plot from the PND Rietveld refinement of sample 19 (β-Li_3N at 4.2 K) from PND data, 35° (A) bank.
The black tickmarks indicate reflections from β-Li_3N. The black circle represents a reflection from α-Li_3N which has been excluded.

A small amount of α-Li_3N present in the starting material however this phase could not be fitted in the refinement as the intensity of the peak was too small and therefore the reflections were excluded as illustrated in Figure 3-20, Figure 3-21 and Figure 3-23. Complications arose when Rietveld refinements were carried out on these data due to particle size broadening of the material after ball milling.

The lattice parameters obtained, a = 3.5550 (3) Å and c = 6.3356 (6) Å vary slightly from those reported in the literature by Biester *et al* (a = 3.552 (1) Å and c = 6.311 (3) Å) [6] and by Huq *et al* (a = 3.5556 (1) Å and c = 6.3207 (4) Å). [4] Due to the fact that the experimental values (of sample **19**) were obtained at 4.2 K and those reported in the literature were obtained at 293 K, it is surprising that the refined lattice parameters are comparable. At lower temperatures, it would have been expected that the lattice parameters would be much smaller than reported however the accuracy of the experimental values is questionable due to the relatively poor fit of data obtained.

From the refinement, atomic positions, Wyckoff sites and anisotropic temperature factors were obtained and are displayed in Table 3-27. Of the atomic positions, only that of Li (2) could be varied within the symmetry of the space group and the fractional occupancies did not vary. The interatomic distances and bond angles generated from Rietveld refinement of sample 19 are displayed in Table 3-28 and Table 3-29.

Table 3-27: Atom positions and anisotropic temperature factors generated by PND Rietveld refinement of sample 19 (4.2 K).

Atom	Li (1)	Li (2)	N
Site	2b	4f	2c
x	0	0.3333	0.3333
y	0	0.6667	0.6667
z	0.25	0.5784 (3)	0.25
100 x U_{iso} / Å^2	-	1.77 (4)	-
100 x U_{11} / Å^2	1.79 (7)	-	1.37 (1)
100 x U_{22} / Å^2	1.79 (7)	-	1.37 (1)
100 x U_{33} / Å^2	2.94 (16)	-	1.51 (2)
100 x U_{12} / Å^2	0.90 (3)	-	0.684 (7)
100 x U_{13} / Å^2	0	-	0
100 x U_{23} / Å^2	0	-	0
Occupancy	1.00	1.00	1.00

Table 3-28: Interatomic distances generated by PND Rietveld refinement of sample 19 (4.2 K).

Interatomic Distance / Å	β-Li_3N
2x Li1-N1	2.0526 (2)
3x Li2-N1	2.0804 (18)
Li1-Li2	2.9225 (13)

Table 3-29: Bond angles generated by PND Rietveld refinement of sample 19 (4.2 K).

Angle / ^{o}	β-Li_3N
N1-Li1-N1	4x 120.00 (0) 2x 119.99 (0)
Li1-N1-Li2	2x 89.99 (0) 4x 63.78 (1) 4x 63.77 (1)
Li2-N1-Li2	2x 117.92 (4) 2x 62.09 (4)

Selected Rietveld refinement data for sample **22** is presented in Table 3.30 and Figure 3-23, Figure 3-24 and Figure 3-25 show the observed, calculated and difference (OCD) plots. Data was collected at 100 K for the 145o, 90o and 35o detector banks. As is true for data collected at 4.2 K, only the β-polymorph of Li_3N could be fitted at this temperature whilst maintaining refinement stability. The lattice parameters reported in Table 3-30 are consistent with the data collected in this work, i.e. as the temperature increases, the lattice parameters increase but the values differ from those reported in the literature, a = 3.552 (1) Å and c = 6.311 (3) Å. 6 Table 3-31 displays the temperature factors which were refined anisotropically for Li (1) and N (1) however Li (2) could only be refined isotropically. The interatomic distances and bond angles generated from Rietveld refinement of sample **22** are displayed in Table 3-32 and Table 3-33.

Table 3-30: Selected Rietveld refinement data from the PND Rietveld refinement of sample 22 (β-Li_3N at 100 K).

Empirical Formula	β-Li_3N
Collection Temperature / K	100
Space Group	*P6₃/mmc*
Crystal system	Hexagonal
Lattice parameters / Å	*a* = 3.5552 (2)
	c = 6.3395 (5)
V / Å ^{3}	69.394 (8)
Z	2
Unit cell formula weight, M_w	69.660
Density / g/cm^3	1.667
No. of varied parameters	28
No. of observations	12471
R_{wp}	0.0124
R_p	0.0225
χ^2	2.659

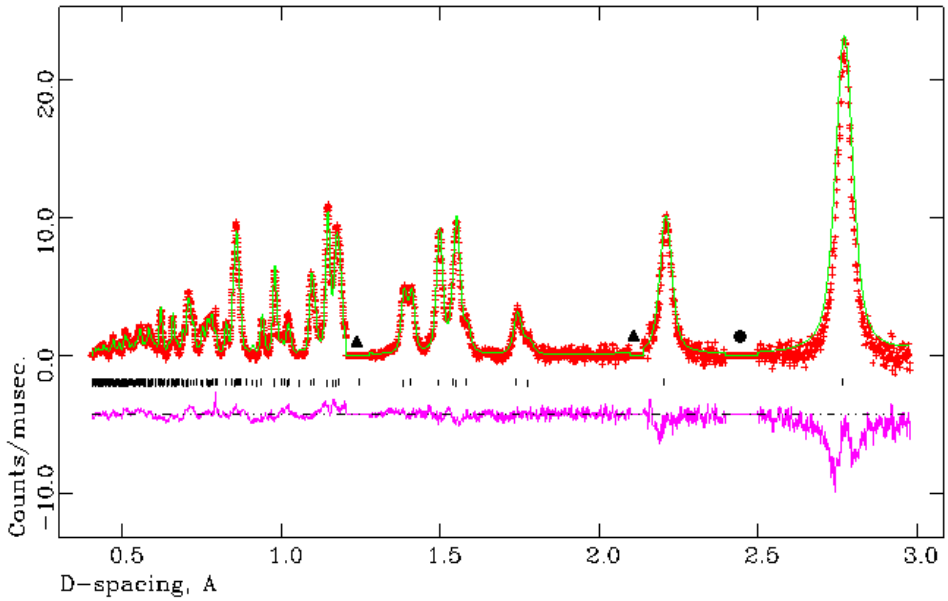

Figure 3-23: Observed, calculated and difference (OCD) plot from the PND Rietveld refinement of sample 22 (β-Li_3N at 100 K) from PND data, 145° (C) bank.

The black tickmarks indicate reflections from β-Li_3N. The black triangles represent reflections from the sample environment and the black circle represents a reflection from α-Li_3N, both of which have been excluded.

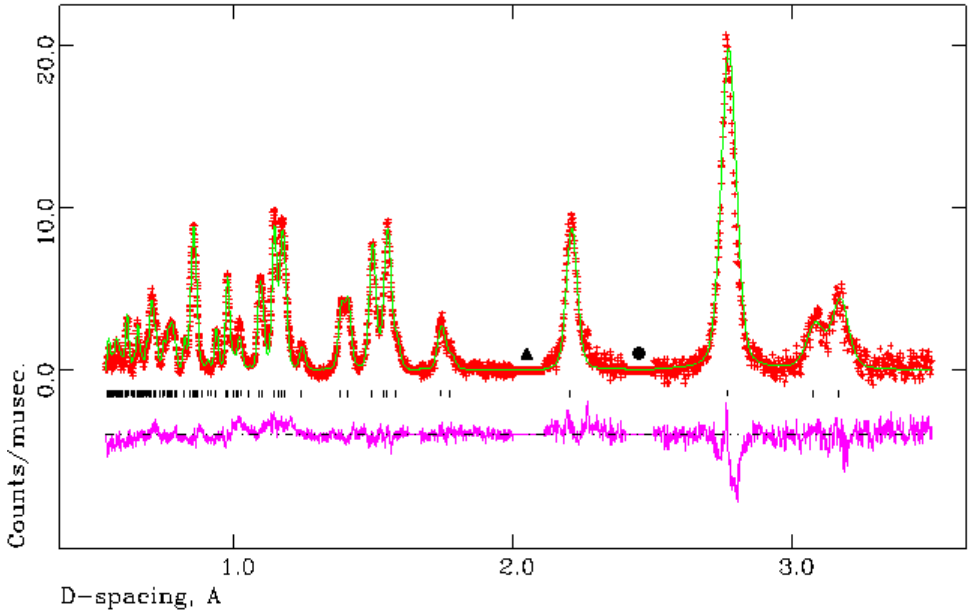

Figure 3-24: Observed, calculated and difference (OCD) plot from the PND Rietveld refinement of sample 22 (β-Li_3N at 100 K) from PND data, 90° (E) bank.

The black tickmarks indicate reflections from β-Li_3N. The black triangle represents reflections from the sample environment and the black circle represents a reflection from α-Li_3N, both of which have been excluded.

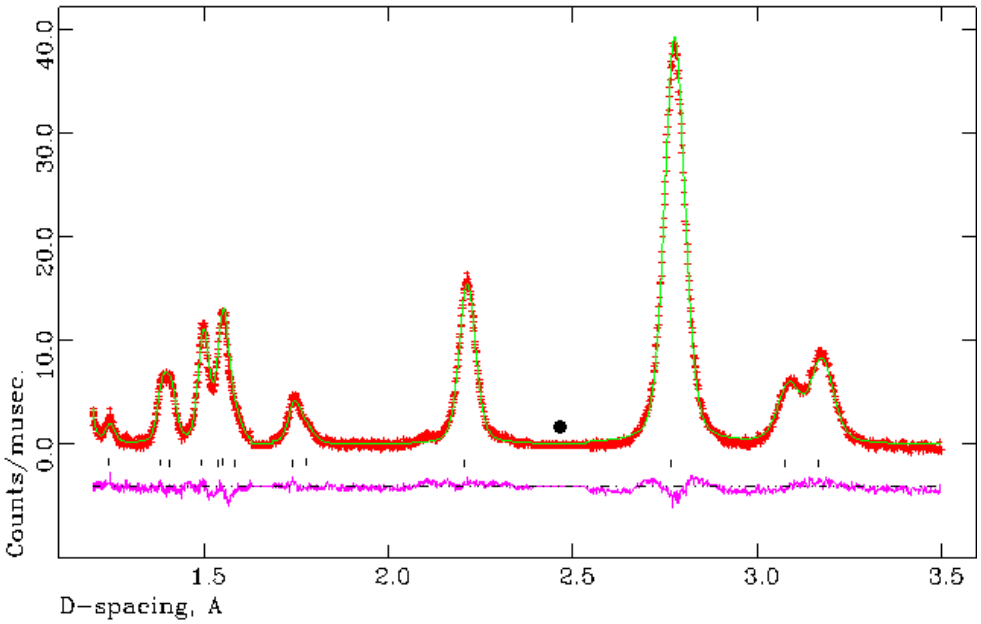

Figure 3-25: Observed, calculated and difference (OCD) plot from the PND Rietveld refinement of sample 22 (β-Li_3N at 100 K) from PND data, 35° (A) bank.
The black tickmarks indicate reflections from β-Li_3N. The black circle represents a reflection from α-Li_3N which has been excluded.

Table 3-31: Atom positions and anisotropic temperature factors generated by PND Rietveld refinement of sample 22 (100 K).

Atom	Li (1)	Li (2)	N
Site	2b	4f	2c
x	0	0.3333	0.3333
y	0	0.6667	0.6667
z	0.25	0.5796 (2)	0.25
100 x U_{iso} / Å^2	-	1.81 (3)	-
100 x U_{11} / Å^2	1.08 (5)	-	1.013 (9)
100 x U_{22} / Å^2	3.16 (5)	-	2.065 (9)
100 x U_{33} / Å^2	3.55 (14)	-	1.45 (2)
100 x U_{12} / Å^2	1.58 (3)	-	1.033 (5)
100 x U_{13} / Å^2	0	-	0
100 x U_{23} / Å^2	0	-	0
Occupancy	1.00	1.00	1.00

Table 3-32: Interatomic distances generated by PND Rietveld refinement of sample 22 (100 K).

Interatomic Distance / Å	β-Li_3N
2x Li1-N1	2.0527 (1)
3x Li2-N1	2.0893 (15)
Li1-Li2	2.9287 (10)

Table 3-33: Bond angles generated by PND Rietveld refinement of sample 22 (100 K).

Angle / ^{o}	β-Li_3N
N1-Li1-N1	4x 120.00 (0) 2x 119.99 (0)
Li1-N1-Li2	2x 89.99 (0) 4x 63.74 (8) 4x 63.73 (8)
Li2-N1-Li2	2x 117.76 (3) 2x 62.24 (3)

Further data were collected at 200, 300, 400, 500 (see appendix) and 600 K. At 600 K, the sample is composed of both the alpha and beta polymorphs of Li_3N. Biester *et al* reported that β-Li_3N can be converted into α-Li_3N at temperatures above 473 K. [6] In previous PND studies carried out by Gregory *et al*, phase conversion was not evident until a temperature of 600 K was reached. [14] At 600 K, sample **27** consisted of 40.448 (4) % of the alpha polymorph. The lattice parameters for this phase are larger than those reported in the literature by Gregory *et al* (a = 3.6576 (1) Å and c = 3.8735 (1) Å at 293 K) [3] since the data collected in this work are at a higher temperature. Furthermore, the lattice parameters obtained for the beta polymorph of sample **27** were also larger than those reported by both Beister *et al* (a = 3.552 (1) Å and c = 6.311 (3) Å) and Huq *et al* (a = 3.5556 (1) Å and c = 6.3207 (4) Å). [4, 6] The values stated for the aforementioned authors were obtained at room temperature therefore the increase in lattice parameters observed at 600 K is not unexpected due to the fact that thermal expansion occurs as temperature increases. At 600 K, the crystallinity of the sample was enhanced and therefore the fitting of the peak shape was slightly less problematic hence the overall fit of the experimental data was better than in comparison to that at lower temperatures.

Figure 3-26, Figure 3-27 and Figure 3-28 show the observed, calculated and difference (OCD) plots for sample 27. Data was collected at 600 K for the 145°, 90° and 35° detector banks. Selected refinement data are shown in Table 3.34 and atomic positions and anisotropic temperature factors are presented for α-Li_3N and β-Li_3N in Table 3-35 and

Table 3-36 respectively. The interatomic distances and bond angles generated from Rietveld refinement of sample 27 are displayed in Table 3-37 and Table 3-38.

Table 3-34: Selected Rietveld refinement data from the PND Rietveld refinement of sample 27 (α-Li_3N at 600 K).

Empirical Formula	α-Li_3N	β-Li_3N
Collection temperature (K)	600	
Crystal system	Hexagonal	Hexagonal
Space Group	*P6/mmm*	*$P6_3/mmc$*
Lattice parameters	*a* = 3.6800 (2)	*a* = 3.5986 (2)
	c = 3.8837 (2)	*c* = 6.4000 (4)
V / Å ^{3}	45.549 (4)	71.776 (6)
Z	1	2
Unit cell formula weight, M_w	34.830	69.660
Density (g/cm^3)	1.270	1.612
wt. %	40.448 (4)	59.552 (4)
No. of varied parameters	42	
No. of observations	11499	
R_{wp}	0.0117	
R_p	0.0223	
χ^2	2.063	

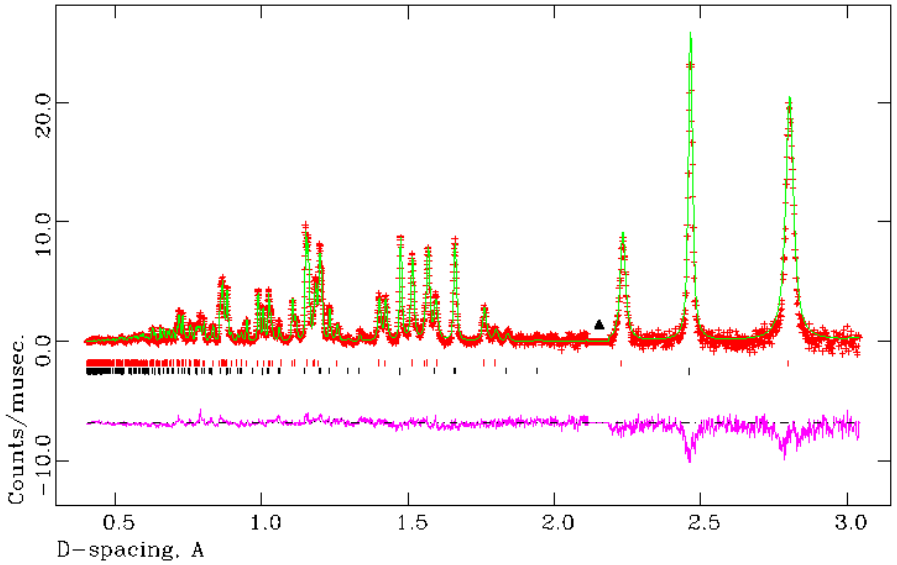

Figure 3-26: Observed, calculated and difference (OCD) plot from the PND Rietveld refinement of sample 27 (600 K) from PND data, 145° (C) bank.
The red tickmarks indicate reflections from β-Li_3N and the black tickmarks indicate reflections from α-Li_3N.

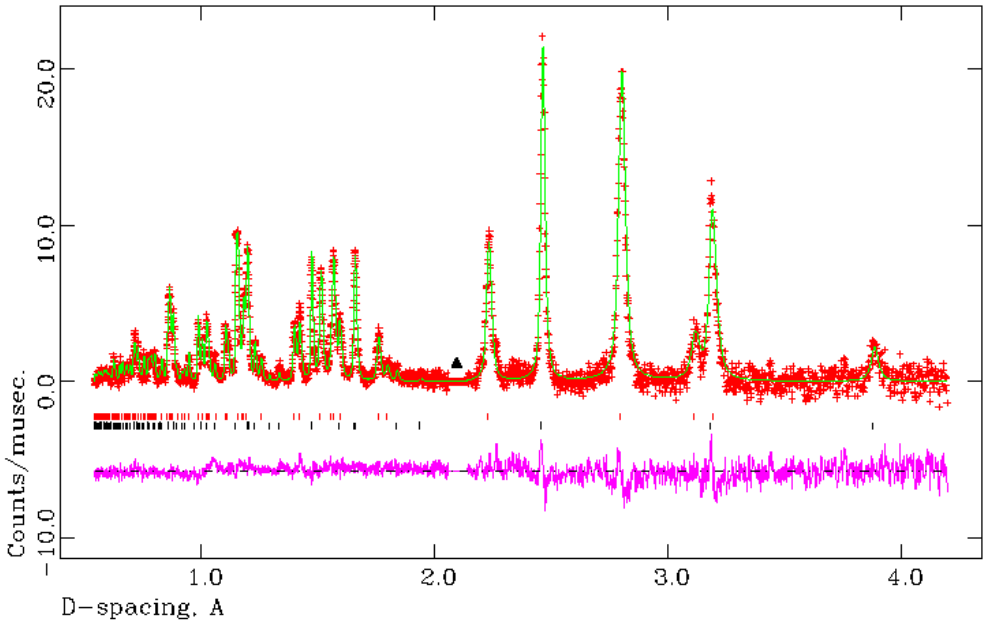

Figure 3-27: Observed, calculated and difference (OCD) plot from the PND Rietveld refinement of sample 27 (600 K) from PND data, 90° (E) bank.
The red tickmarks indicate reflections from β-Li_3N and the black tickmarks indicate reflections from α-Li_3N.

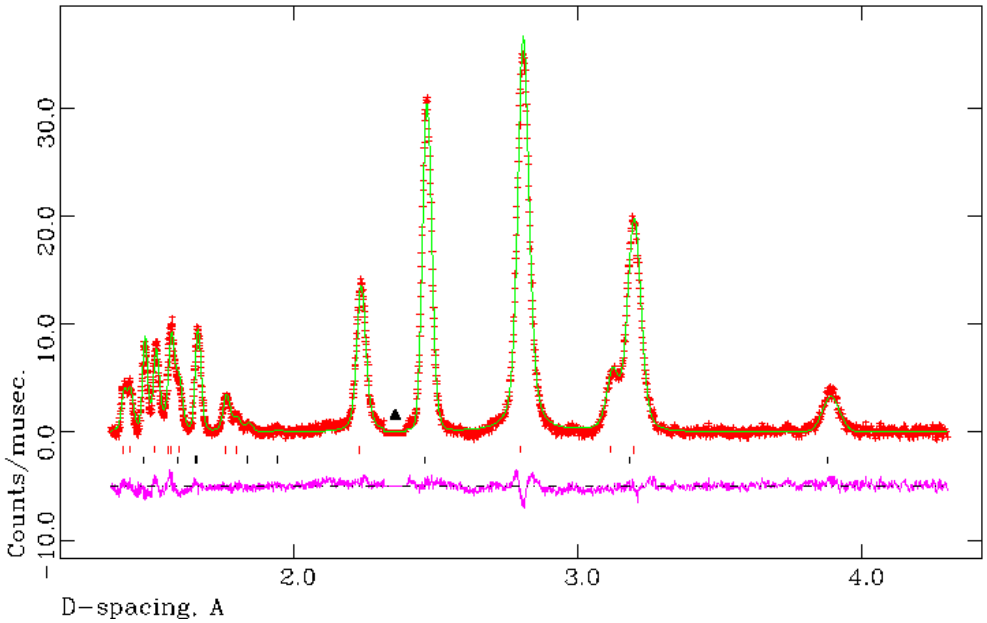

Figure 3-28: Observed, calculated and difference (OCD) plot from the PND Rietveld refinement of sample 27 (600 K) from PND data, 35° (A) bank.
The red tickmarks indicate reflections from β-Li_3N and the black tickmarks indicate reflections from α-Li_3N.

Table 3-35: Atom positions and anisotropic temperature factors for the α-phase of Li_3N in sample 27 generated by PND Rietveld refinement (600 K).

Atom	Li (1)	Li (2)	N
Site	1b	2c	1a
x	0	0.3333	0
y	0	0.6667	0
z	0.5	0	0
100 x U_{iso} / Å^2	-	3.0 (1)	-
100 x U_{11} / Å^2	4.6 (2)	-	2.15 (3)
100 x U_{22} / Å^2	4.6 (2)	-	2.15 (3)
100 x U_{33} / Å^2	0.5 (2)	-	3.02 (6)
100 x U_{12} / Å^2	2.28 (9)	-	1.07 (2)
100 x U_{13} / Å^2	0	-	0
100 x U_{23} / Å^2	0	-	0
Occupancy	1.00	1.00	1.00

Table 3-36: Atom positions and anisotropic temperature factors for the β-phase of Li_3N in sample 27 generated by PND Rietveld refinement (600 K).

Atom	Li (1)	Li (2)	N
Site	2b	4f	2c
x	0	0.3333	0.3333
y	0	0.667	0.6667
z	0.25	0.5800 (4)	0.25
100 x U_{iso} / Å^2	-	3.87 (7)	-
100 x U_{11} / Å^2	3.3 (1)	-	2.30 (2)
100 x U_{22} / Å^2	3.3 (1)	-	2.30 (2)
100 x U_{33} / Å^2	2.2 (2)	-	2.25 (4)
100 x U_{12} / Å^2	1.64 (6)	-	1.15 (1)
100 x U_{13} / Å^2	0	-	0
100 x U_{23} / Å^2	0	-	0
Occupancy	1.00	1.00	1.00

Table 3-37: Interatomic distances generated by PND Rietveld refinement of the alpha and beta phases of Li_3N in sample 27 (600 K).

Interatomic Distance / Å	α-Li_3N	β-Li_3N
2x Li1-N1	1.9419 (1)	2.07776 (8)
3x Li2-N1	2.124476 (9)	2.112 (3)
Li1-Li2	2.8785 (1)	2.962 (2)

Table 3-38: Bond angles generated by PND Rietveld refinement of the alpha and beta phases of Li_3N in sample 27 (600K).

Angle / ^{o}	α-Li_3N	β-Li_3N
N1-Li1-N1	4x 180.0 (0)	4x 120.00 (0) 2x119.99 (0)
Li1-N1-Li2	4x 95.146 (4)	2x 89.99 (0) 4x 63.71 (2) 4x 63.70 (2)
Li2-N1-Li2	4x 79.474 (3)	2x 117.64 (6) 2x 62.35 (6)

A comparison of the interatomic distances of Li(1)-N, Li(2)-N and Li(1)-Li(2) are shown in Figure 3-29. Rietveld refinements were performed on all data collected and these data are presented in the appendix. The bond lengths are generally consistent with thermal expansion however at temperatures below 50 K, a subtle negative thermal expansion effect occurs (also refer to Appendix). This NTE effect is likely to be due to the Li(1)-N bond which contracts at 15 K before expanding again as the temperature increases. This finding was confirmed by analysis of the lattice parameters at variable temperatures (refer to Figure 3.34). Contraction of solids as temperature increases seems uncharacteristic and it would be sensible that as the temperature increases, atoms would need more space to vibrate therefore positive thermal expansion would result based on anharmonicity. [28] The vibration of atoms along a line connecting anharmonic pair potentials can be used to explain positive thermal expansion since, on an increase of temperature, there is an increase in the mean distance between the atoms. In contrast, if negative thermal expansion occurs then the mean distance of the two atoms tends to decrease therefore contraction of the solid occurs.

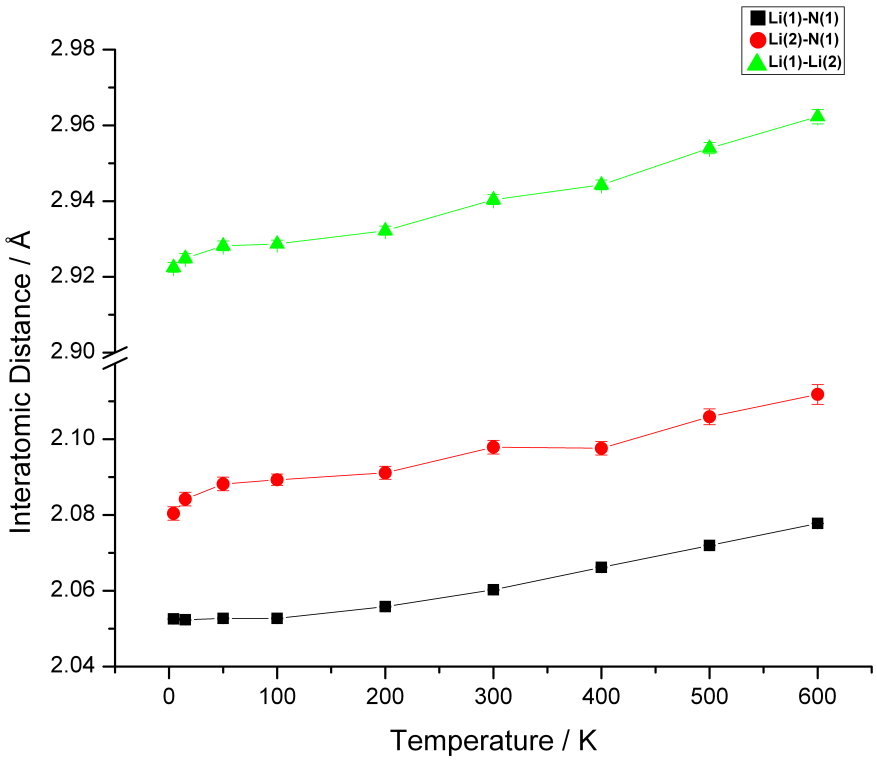

Figure 3-29: Comparison of the interatomic distances generated by Rietveld refinement of β-Li_3N with varying temperature (samples 19-27).

3.3.5.3 In-situ PND variable temperature measurements under D_2

The second PND experiment carried out involved an investigation of the interaction between β-Li_3N and gaseous D_2 to compare observed structural changes against temperature and as a given amount of D_2 is reacted with the sample. The proposed mechanism is shown in Equation 1.

$$Li_3N + 2D_2 \rightarrow Li_2ND + LiD + D_2 \rightarrow LiND_2 + 2LiD \quad (1)$$

Li^+ vacancies within α-Li_3N were reported by Gregory *et al* [3] and are responsible for high Li^+ conductivity [29] and Li^+ conductivity is also exceptional in β-Li_3N (2.085×10^{-4} S cm^{-1}). [30] It is also likely that these Li^+ vacancies are a significant contributor to H^+ transport. In order to investigate if a (potential) defect structure, and therefore its likely significance as a H^+ transporter, exists within the beta polymorph of Li_3N, it is essential to understand the reaction that occurs between this polymorph and hydrogen (deuterium). An initial INS study was conducted on the uptake of hydrogen in Li_3N which revealed a result of negative thermal expansion. [14] A follow-up PND experiment was performed on α-Li_3N and commercial Li_3N, both of which exhibited negative thermal expansion below 50 K in agreement with the results of the preceding INS experiment. As a consequence of the previous discovery using PND, it was sensible to perform the study over a variable

temperature range (4.2, 15, 50, 100, 200, 300, 400, 500 and 600 K) to observe if the same trend emerged.

Structural refinement using the Rietveld method was employed for each data set collected. The observed, calculated and difference (OCD) plot for data collected at 4.2 K for the 90^{o} bank is displayed in Figure 3-30. In comparison to the data collected in the absence of gaseous D_2, it was not necessary to fit the peak profiles using GSAS function 4, Stephen's broadening.

At temperatures below 50 K, solid deuterium was present in the samples corresponding to the space group *P63/mmc*. The presence of D_2 reflections was due to the solidification of D_2 at 4.2 and 15 K under a pressure of 10 bar. Solidification of D_2 at approximately 18 K under a pressure of 3-4 bar was reported by Demin *et al* therefore the observation of clear Bragg reflections of D_2 is perfectly feasible at the temperatures and pressure stated. 31 The lattice parameters obtained from the Rietveld refined data (a = 3.6082 (8) Å and c = 5.888 (2) Å) were in agreement with those reported by Schuch and Mills (a = 3.600 (4) Å and c = 5.858 (7) Å). [32] The refinement model and lattice parameters (Table 3-39) obtained for the beta phase is in agreement with the published structure. [6] The temperature factors for each atom could not be varied anisotropically which may be due to the instability of the structure at these low temperatures (Table 3-40 and Table 3-41). The interatomic distances and bond angles generated from Rietveld refinement of sample **28** are displayed in Table 3-42 and Table 3-43.

Table 3-39: Selected Rietveld refinement data from the PND Rietveld refinement of sample 28, β-Li_3N under D_2 gas at 4.2 K.

Empirical Formula	β-Li_3N	D_2
Collection Temperature / K	4.2	
Crystal system	Hexagonal	Hexagonal
Space Group	*P6₃/mmc*	*P6₃/mmc*
Lattice parameters / Å	*a* = 3.5477 (7)	*a* = 3.6082 (8)
	c = 6.345 (2)	*c* = 5.888 (2)
V / Å ^{3}	69.16 (3)	66.38 (3)
Z	2	1
Unit cell formula weight, M_w	69.66	4.028
Density / g/cm^3	1.672	0.101
wt. %	91.835 (3)	8.165 (3)
No. of varied parameters	15	
No. of observations	3964	
R_{wp}	0.0258	
R_p	0.0476	
χ^2	1.289	

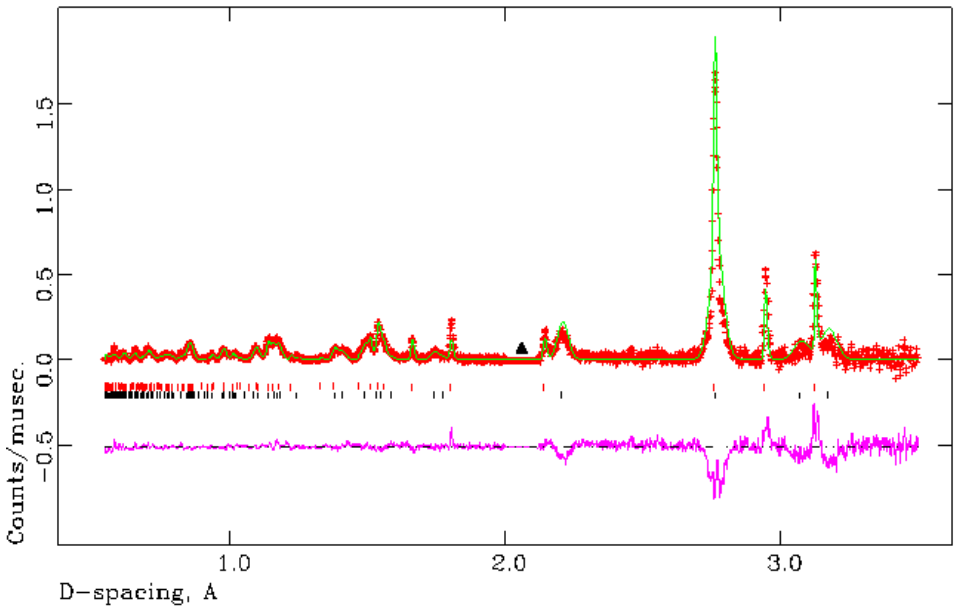

Figure 3-30: Observed, calculated and difference (OCD) plot from the PND Rietveld refinement of sample 28 (β-Li_3N under D_2 gas at 4.2 K) from PND data, 90° (E) bank. The black tickmarks indicate reflections from β-Li_3N and the red tickmarks indicate D_2.

Table 3-40: Atom positions and isotropic temperature factors for sample 28 generated by PND Rietveld refinement (4.2 K).

Atom	Li (1)	Li (2)	N
site	2b	4f	2c
x	0	0.3333	0.3333
y	0	0.6667	0.6667
z	0.25	0.5678 (12)	0.25
100 x U_{iso} / Å^2	0.2 (2)	0.5 (1)	0.07 (2)
Occupancy	1.00	1.00	1.00

Table 3-41: Atom positions and isotropic temperature factors for the D_2 phase of sample 28 generated by PND Rietveld refinement (4.2K).

Atom	D
Site	2c
x	0.3333
y	0.6667
z	0.25
100 x U_{iso} / Å^2	3.9 (2)
Occupancy	1.00

Table 3-42: Interatomic distances generated by PND Rietveld refinement of sample 28 (4.2 K).

Interatomic Distance / Å	β-Li_3N
2x Li1-N1	2.0481 (4)
3x Li2-N1	2.016 (8)
Li1-Li2	2.874 (6)

Table 3-43: Bond angles generated by PND Rietveld refinement of sample 28 (4.2 K).

Angle / ^{o}	β-Li_3N
N1-Li1-N1	4x 120.00 (1) 2x 119.99 (1)
Li1-N1-Li2	2x 90.00 (0) 4x 64.19 (5) 4x 64.18 (5)
Li2-N1-Li2	2x 119.4 (2) 2x 64.19 (5)

By a collection temperature of 50 K, D_2 was no longer present in diffraction patterns (see appendix). Selected refinement data are presented in Table 3-44 and Figure 3-31 displays the observed, calculated and difference (OCD) plots for sample **31**. Data were collected from the 90° detector bank. At this temperature, the only phase present was β-Li_3N. Anisotropic temperature factors for this TOF PND refinement are shown in Table 3-45. The interatomic distances and bond angles generated from Rietveld refinement of sample **31** are displayed in Table 3-46 and Table 3-47.

Table 3-44: Selected Rietveld refinement data from the PND Rietveld refinement of sample 31 (β-Li_3N under D_2 gas at 100 K).

Empirical Formula	**β-Li_3N**
Collection Temperature / K	100
Crystal system	Hexagonal
Space Group	*$P6_3/mmc$*
Lattice parameters / Å	*A* = 3.5499 (8)
	c = 6.332 (2)
V / Å ^{3}	69.11 (3)
Z	2
Unit cell formula weight, M_w	69.660
Density (gm/cm^3)	1.674
No. of varied parameters	13
No. of observations	3567
R_{wp}	0.0205
R_p	0.0211
χ^2	1.094

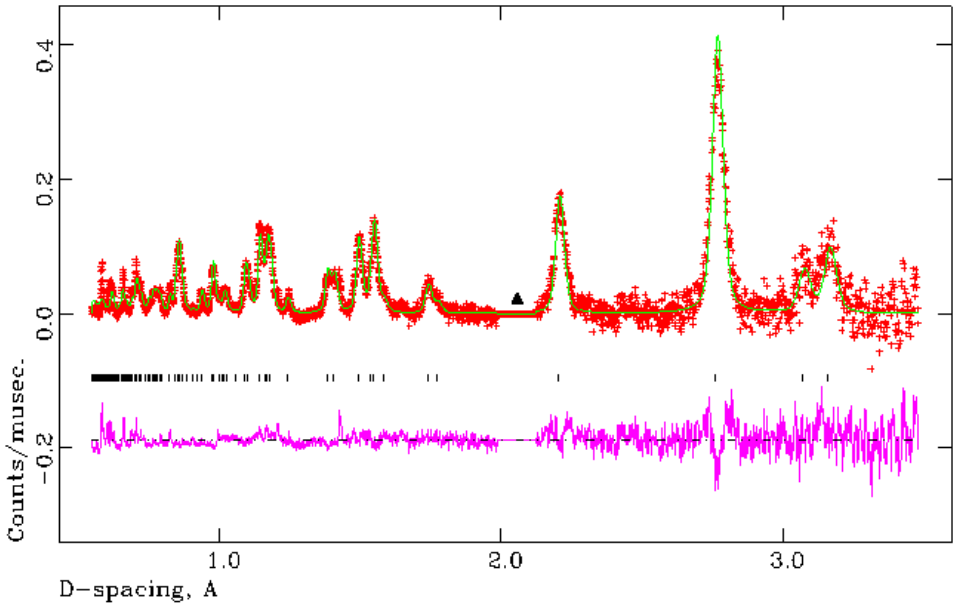

Figure 3-31: Observed, calculated and difference (OCD) plot from the PND Rietveld refinement of sample 31 (β-Li_3N under D_2 gas at 100 K) from PND data, 90° (E) bank. The black tickmarks indicate reflections from β-Li_3N. The black triangle represents reflections from the sample environment which has been excluded.

Table 3-45: Atom positions and anisotropic temperature factors for sample 31 generated by PND Rietveld refinement (100 K).

Atom	Li (1)	Li (2)	N
Site	2c	4f	2c
x	0	0.3333	0.3333
y	0	0.6667	0.6667
z	0.25	0.5712 (10)	0.25
100 x U_{11} / Å^2	1.79 (16)	3.57 (16)	1.71 (4)
100 x U_{22} / Å^2	1.79 (16)	3.57 (16)	1.71 (4)
100 x U_{33} / Å^2	1.23 (27)	0.87 (23)	1.90 (7)
100 x U_{12} / Å^2	0.90 (8)	1.79 (8)	0.85 (2)
100 x U_{13} / Å^2	0	0	0
100 x U_{23} / Å^2	0	0	0
Occupancy	1.00	1.00	1.00

Table 3-46: Interatomic distances generated by PND Rietveld refinement of sample 31 (100 K).

Interatomic Distance / Å	β-Li_3N
2x Li1-N1	2.0497 (4)
3x Li2-N1	2.0265 (6)
Li1-Li2	2.8821 (5)

Table 3-47: Bond angles generated by PND Rietveld refinement of sample 31 (100 K).

Angle / ^{o}	β-Li_3N
N1-Li1-N1	4x 120.00 (0) 2x 119.99 (0)
Li1-N1-Li2	2x 90.00 (0) 4x 63.74 (8) 4x 63.73 (8)
Li2-N1-Li2	2x 117.76 (3) 2x 62.24 (3)

At 500 K (data displayed in appendix), approximately 60 % of sample **35** was composed of β-Li_3N however the remainder of the sample had begun to react with $D_{2\,(g)}$ leading to the formation of $LiND_2$ which crystallises in the *I-4* space group and LiD which crystallises in the cubic *Fm-3m* space group. From the data collected, there is no evidence of Li_2ND present at any stage during the reaction. Perhaps if data had been collected at additional temperatures between 400 and 500 K then a presence of Li_2ND may have been observed throughout this range.

On increasing the temperature to 600 K, sample **36** had fully converted to $LiND_2$ (~ 56 %) and LiD (~ 43 %). Selected Rietveld refinement data are presented in Table 3-48 and the observed, calculated and difference (OCD) plot for data collected at 600 K in the 90^o bank is shown in Figure 3-32.

Table 3-48: Selected Rietveld refinement data from the PND Rietveld refinement of sample 36 (β-Li_3N under D_2 gas at 600 K).

Empirical Formula	$LiND_2$	LiD
Collection Temperature / K	600	
Crystal system	Tetragonal	Cubic
Space Group	*I -4*	*Fm-3m*
Lattice parameters / Å	*a* = 5.0949 (5)	*a* = 4.1213 (2)
	c = 10.3159 (1)	-
V / $Å^3$	267.78 (5)	70.003 (7)
Z	8	4
Unit cell formula weight, M_w	199.808	35.820
Density (g/cm^3)	1.239	0.850
wt. %	56.85 (1)	43.15 (1)
No. of varied parameters	19	
No. of observations	4078	
R_{wp}	0.0173	
R_p	0.0326	
χ^2	0.6193	

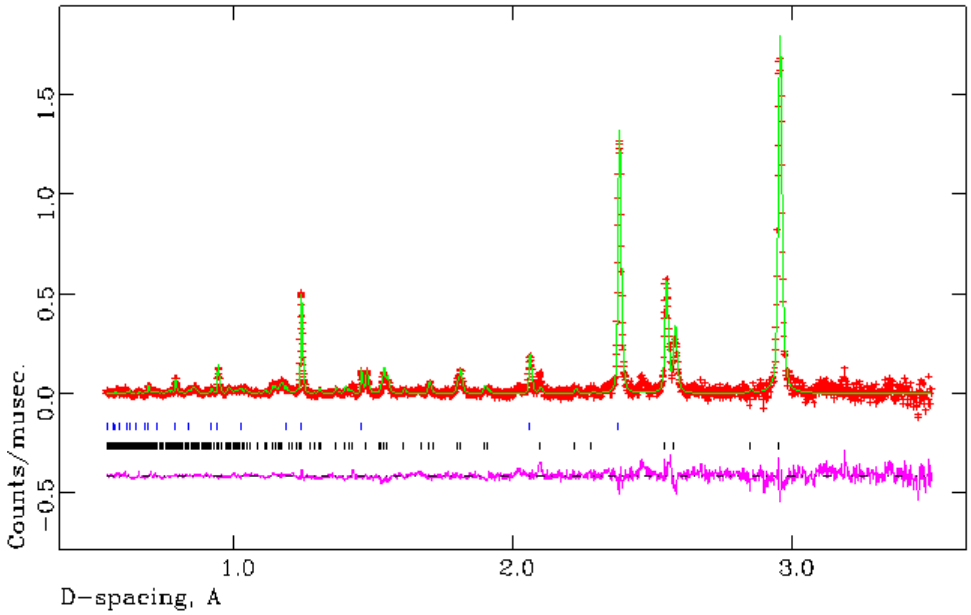

Figure 3-32: Observed, calculated and difference (OCD) plot from the PND Rietveld refinement of sample 36 (β-Li_3N under D_2 gas at 600 K) from PND data, 90° (E) bank. The blue tickmarks indicate reflections from LiD and black tickmarks indicate $LiND_2$.

The lattice parameters obtained from Rietveld refinement for $LiND_2$ and LiD of sample **36** are shown in Table 3-48. In comparison to the lattice parameters reported by Sorby *et al* (*a* = 5.03164 (8) Å and *c* = 10.2560 (2) Å), [33] those reported in this work are larger however this is not unexpected due to the fact that the lattice parameters in this work are reported at 600 K, which is higher than the temperature stated in the literature. In regards to LiD, the *a* lattice parameter obtained from Rietveld refinement of the experimental data is also larger than that reported by Zintl and Harder (*a* = 4.065 (1) Å). [34] At these higher temperatures, only the isotropic temperature factors could be varied (Table 3-49 and Table 3-50). Interatomic distances generated from Rietveld refinement of data collected for sample **36** are presented in Table 3-51 (further details on interatomic distances and bond angles are also reported in the appendix).

Table 3-49: Atom positions and isotropic temperature factors for $LiND_2$ in sample 36 generated by PND Rietveld refinement (600 K).
(NB. The values without errors are fixed values).

Atom	Li (1)	Li (2)	Li (3)	N (1)	D (1)	D (2)
Site	2a	2d	4f	8g	8g	8g
x	0	0	0	0.2298	0.2260	0.370 (3)
y	0	0.50	0.50	0.2470	0.1328	0.357 (4)
z	0	0.25	0.001	0.1147	0.1905	0.141 (1)
100 x U_{iso} / $Å^2$	3.2 (3)	1.8 (3)	1.8 (3)	2.44 (7)	5.5 (2)	5.5 (2)
Occupancy	1.00	1.00	1.00	1.00	1.00	1.00

Table 3-50: Atom positions and isotropic temperature factors for LiD in sample 36 generated by PND Rietveld refinement (600 K).

Atom	Li	D
Site	4a	4b
x	0	0.5
y	0	0.5
z	0	0.5
100 x U_{iso} / $Å^2$	2.0 (1)	3.25 (7)
Occupancy	1.00	1.00

Table 3-51: Interatomic distances generated by PND Rietveld refinement of sample 36 (600 K).

Interatomic Distance / Å	$LiND_2$
4x Li1-Li3	2.5475 (3)
4x Li1-N1	2.0868 (2)
4x Li1-D1	2.3760 (2)

With regard to Figure 3-33, an effect of negative thermal expansion (NTE) is evident at 50 K in the β-Li_3N/D_2 experiment. It is evident from Figure 3.33 that the NTE effect is greater where D_2 is present than in comparison to the subtle effect in the β-Li_3N variable temperature experiment. Furthermore, the temperature at which the negative thermal

expansion occurs varies between the PND experiments; in the first experiment, performed in the absence of D_2, NTE occurs at 15 K and where D_2 is present, NTE occurs at 50 K. It is possible that the presence of solid D_2 at 4.2 and 15 K inhibits NTE and since D_2 is no longer present as a solid at 50 K, the NTE effect therefore occurs at this temperature.

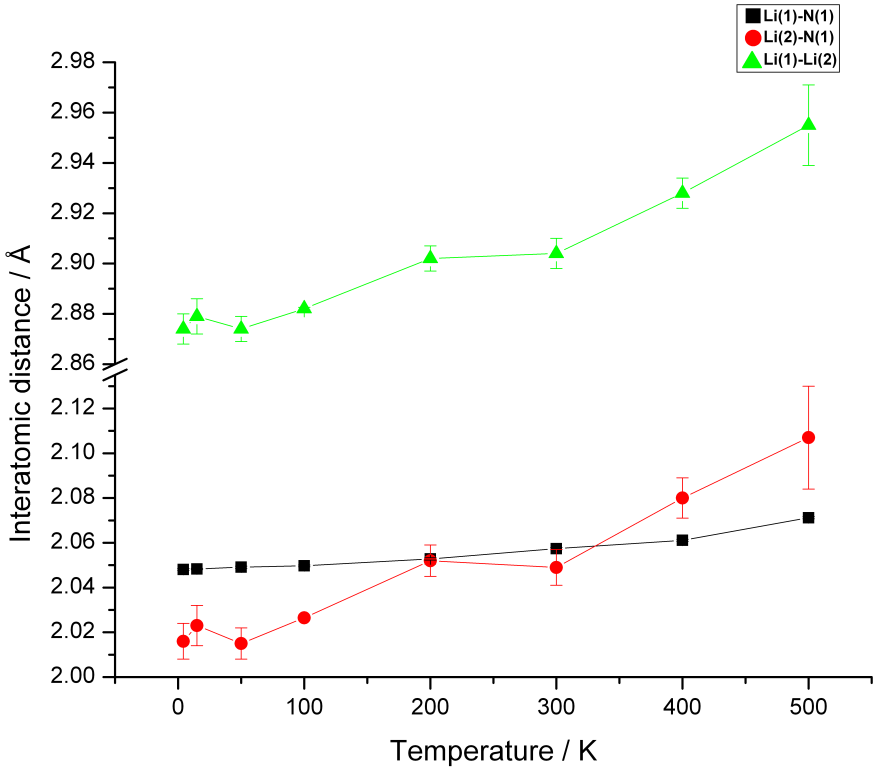

Figure 3-33: Comparison of interatomic distances with increasing temperature (samples 28-36).

Although negative thermal expansion is evident on comparison of the bond distances, the argument is confirmed by comparison of the lattice parameters in the presence and absence of D_2 (Figure 3-34) and is therefore in agreement with the findings stated above. The results obtained from both PND experiments highlight the fact that as the temperature increases from 4.2 to 15 K (with regards to the experiment conducted under the absence of $D_{2(g)}$) and 15 K to 50 K (with regards to the experiment conducted in the presence of $D_{2(g)}$), the lattice contracts slightly.

On the heating of samples **19** and **20**, in the absence of $D_{2(g)}$, thermal expansion occurs along on the *a* axis however the effect is very subtle in this case. In comparison, when β-Li_3N is heated under the presence of $D_{2(g)}$, a more prominent negative thermal expansion effect is evident which occurs along the *c* axis. When reaching a temperature of 50 K, the lattice increases in size as a result of thermal expansion. On analysis of the interatomic distances obtained from the Rietveld refinements of the data collected during the

experiment involving only β-Li_3N, it is the Li(1)-N bond that contracts between 4.2 and 15 K, indicative of an effect of negative thermal expansion. With regards to the *in-situ* experiment involving β-Li_3N and $D_{2(g)}$, at 50 K, it is the Li(1)-Li(2) bond distance that contracts therefore exhibiting negative thermal expansion before the bond begins to expand at higher temperatures.

Due to the hexagonal symmetry adopted by the lithium nitride structure, varying temperatures caused anisotropic thermal stress. This is closely related to the elastic properties of the material. The negative thermal expansion results obtained from the powder neutron diffraction data of β-Li_3N are in agreement with the data collected for both α-Li_3N and the commercial material. [14] Figure 3-34 illustrates the effect described above.

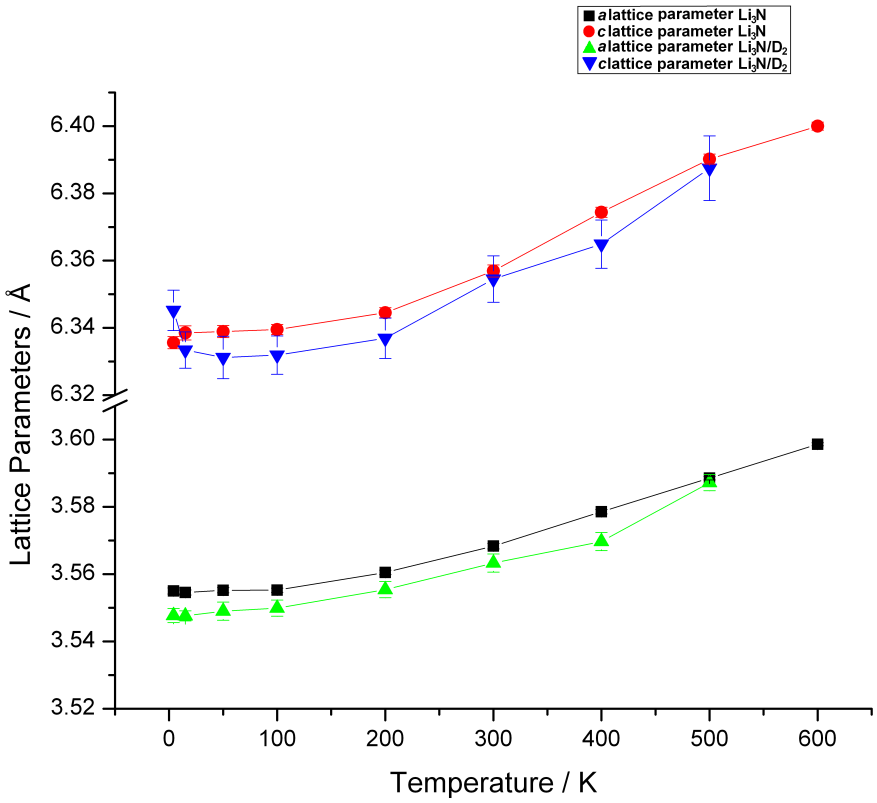

Figure 3-34: Variation of lattice parameters with temperature, generated by Rietveld refinement, in the absence and presence of D_2 with 3-sigma error bars.

With regard to the difference in lattice parameters between the β-Li_3N and β-Li_3N/D_2, the values generated by Rietveld refinement differ. For the experiment focussing solely on the structure of β-Li_3N at variable temperature, the lattice parameters were consistently larger than those obtained for the β-Li_3N/D_2 experiment. The presence of $D_{2(g)}$ would appear to inhibit expansion of the bonds within β-Li_3N which is evident from the interatomic distances generated by Rietveld refinement (see appendix) and this factor therefore has a subsequent effect on the lattice parameters. In order to reach a definitive conclusion

regarding the effect of $D_{2(g)}$ on the structure of β-Li_3N, repeating the experiment using an inert gas, such as $Ar_{(g)}$, instead of $D_{2(g)}$ would possibly indicate whether the likely inhibition of lattice expansion is only a function of pressure or if the $D_{2(g)}$ is in some other way affecting the structure.

It should be noted that, to-date, there have been no reports of NTE occurring in Li_3N with the exception of previous works on α-Li_3N and commercial Li_3N. [14] However, with regard to other compounds, literature reporting the effects of NTE is vast, for example, strong NTE has been reported in structures such as ZrW_2O_8 and HfW_2O_8 from low temperatures (0.3 K) up to their decomposition temperatures of approximately 1050 K. [35] Furthermore, antiperovskite manganese nitrides, e.g. $Mn_3(Cu_{0.6}Si_xGe_{0.4-x})N$, ($x$ = 0 - 0.2) exhibit NTE from 80 to 300 K. [36]

3.4 Conclusions

Successful synthesis of β-Li_3N from laboratory synthesised α-Li_3N and the commercial material by ball milling was performed. Subsequent PXD experiments were carried out to confirm the composition of the material before performing PND experiments where commercial Li_3N was used as the starting material. Furthermore, by employment of high pressures aided by a temperature of 523 K on laboratory synthesised α-Li_3N results in the formation of a more crystalline sample of β-Li_3N in comparison to that obtained by ball milling.

Structural investigations on β-Li_3N have been carried out using powder X-ray diffraction and powder neutron diffraction. The structure of the beta polymorph, [6] which crystallises in the *P6₃/mmc* was refined against a starting model proposed by Biester *et al*. [6] The initial variable temperature PND experiment confirmed that the beta polymorph can be transformed back to the alpha polymorph at a temperature of 600 K, and the lattice parameters obtained were consistent with those reported in the literature initially by Zintl and Brauer [5] and then by Rabenau and Schulz. [8] On refining the data collected in the initial PND experiment, fitting the experimental model proved problematic due to particle size broadening which occurred when synthesising the material by ball milling. To accommodate this, Stephen's broadening (peak profile function 4 of GSAS) was employed.

The subsequent PND experiment involving the study of β-Li_3N with gaseous D_2 highlighted the point that at temperatures below 50 K, solid D_2 (space group - *P6₃/mmc*) was present. Between 50 and 400 K, the only phase present was β-Li_3N. On reaching 500 and 600 K, $LiND_2$ and LiD were present (space groups *I-4* and *Fm-3m* respectively). It

should be noted that Li_2ND was not observed at any point throughout analysis of the experimental data. The presence of $LiND_2$ and LiD at such a temperature is in agreement with the literature. [37] With regards to the negative thermal expansion observed, especially in the presence of D_2, this result is consistent with previous works of the group on the alpha polymorph and commercial material. [14]

3.5 References

[1] D. H. Gregory, *Journal of the Chemical Society Dalton Transactions*, 1999, 259

[2] D. H. Gregory, *Coordination Chemistry Reviews*, 2001, **215**, 301

[3] D. H. Gregory, P. M. O'Meara, A. G. Gordon, J. P. Hodges, S. Short, J. D. Jorgensen, *Chemistry of Materials*, 2002, **14**, 2063

[4] A. Huq, J. W. Richardson, E. R. Maxey, D. Chandra and W.-M. Chien, *Journal of Alloys and Compounds,* 2007, **436**, 256

[5] E. Zintl, G. Brauer, *Zeitschrift fuer Elektrochemie und Angewandte Physikalische Chemie*, 1935, **41**, 102

[6] H. J. Beister, S. Haag, R. Kniep, K. Stroessner, K. Syassen, *Angewandte Chemie*, 1988, **100**, 1116

[7] A. B. Gordienko, *Russian Physics Journal*, 2009, **52**, 978

[8] A. Rabenau and H. Schulz, *Journal of the Less Common Metals*, 1976, **50**, 155

[9] M. Mali, J. Roos and D. Brinkmann, *Physical Review B*, 1987, **36**, 3888

[10] H. Schulz and K. Schwarz, *Acta Crystallographica A*, 1978, **34**, 999

[11] H. R. Chandrasekhar, G. Bhattacharya, R. Migoni and H. Bilz, *Physical Review B*, 1980, **22**, 4620

[12] H. Schulz and K. Thiemann, *Acta Crystallographica A*, 1979, **35**, 309

[13] U. H. Zucker and H. Schulz, *Acta Crystallographica A*, 1982, **38**, 568

[14] C. M. Jewell, J. Yao and D. H. Gregory, *unpublished results*

[15] F. W. Dafert and R. Miklauz, *Monatschefte für Chemie*, 1909, **30**, 649

[16] F. W. Dafert and R. Miklauz, *Monatschefte für Chemie*, 1910, **31**, 98

[17] P. Chen, Z. Xiong, J. Luo, J. Lin and K. Tan, *Nature*, 2002, **420**, 302

[18] J. Wahl, *Solid State Communications*, 1979, **29**, 485

[19] A. Hooper, T. Laap and S. Skaarup, *Materials Research Bulletin*, 1979, **14**, 1617

[20] M. F. Bell, A. Breitschwerdt and U. von Alpen, *Materials Research Bulletin*, 1981, 16, 267

[21] J. O. Thomas and R. Tellgren, *Solid State Ionics*, 1981, **5**, 407

[22] A. Huq, J. W. Richardson, E. R. Maxey, D. Chandra and W. –M. Chien, *Journal of Physical Chemistry C*, 2007, **111**, 10712

[23] A.C. Larson and R.B. Von Dreele, Generalized Structure Analysis System, 1990, MS-H805, Los Alamos, NM 87545

[24] B. H. Toby, *Journal of Applied Crystallography*, 2001, **34**, 210

[25] R. I. Smith and S. Hull, User Guide for the Polaris Powder Diffractometer at ISIS Rutherford Appleton Laboratory Report, 1997, RAL-TR-97-038

[26] P. Stephens, *Journal of Applied Crystallography*, 1999, **32**, 281

[27] H. Huber, M. Mali, J. Roos and D. Brinkmann, *Review of Scientific Instruments*, 1984, **55**, 1325

[28] G. D. Barrera, J. A. O. Bruno, T. H. K. Barron and N. L. Allan, *Journal of Physics: Condensed Matter*, 2005, **17**, R217

[29] B. Bader, P. Heitjans, H. –J. Stöckmann, H. Ackermann, W. Buttler, P. Freiländer, G. Kiese, C. van der Marel and A. Schirmer, *Journal of Physics: Condensed Matter*, 1992, **4**, 4779

[30] W. Li, G. Wu, C. Moysés Araújo, R. H. Scheicher, A. Blomqvist, R. Ahuja, Z. Xiong, Y. Feng and P. Chen, *Energy and Environmental Science*, 2010, **3**, 1524

[31] D. L. Demin, V. P. Dzhelepov, N. N. Grafov, V. G. Grebinnik, A. D. Konin, A. I. Rudenko, Yu. A. Sorokina, Yu. G. Zhestkov and V. G. Zinov, *Hyperfine Interactions*, 1996, **101**, 583

[32] A. F. Schuch and R. L. Mills, *Physical Review Letters*, 1966, **16**, 616

[33] M. H. Sørby, Y. Nakamura, H. W. Brinks, T. Ichikawa, S. Hino, H. Fujii, B.C. Hauback, *Journal of Alloys and Compounds*, 2007, **428**, 297

[34] E. Zintl, A. Harder, *Zeitschrift für Physikalische Chemie, Abteilung B: Chemie der Elementarprozesse, Aufbau der Materie*, 1935, **28**, 478

[35] J. S. O. Evans, T. A. Mary, T. Vogt, M. A. Subramanian, and A. W. Sleight, *Chemistry of Materials*, 1996, **8**, 2809

[36] Rongjin Huang, Laifeng Li, Fangshuo Cai, Xiangdong Xu, and Lihe Qian, *Applied Physics Letters*, 2008, **93**, 081902

[37] P. Chen, Z. Xiong, J. Luo, J. Lin, K. L. Tan, *Journal of Physical Chemistry B*, 2003, **107**, 10967

4 The Li-N-H system

4.1 Introduction

Chen *et al* reported that Li_3N shows promise as a hydrogen storage candidate which has the ability to reversibly store 11.5 wt. % of H_2. [1] This process occurs via two exothermic steps (Equations 1 and 2):

$$Li_3N + H_2 \rightarrow Li_2NH + LiH \qquad \Delta H = -165 \text{ kJ/mol } H_2 \qquad (1)$$

$$Li_2NH + H_2 \rightarrow LiNH_2 + LiH \qquad \Delta H = -44.5 \text{ kJ/mol } H_2 \qquad (2)$$

It has been suggested that the reaction pathway (Equations 1 and 2) demonstrated by Chen *et al* may be more complex than originally indicated. Weidner *et al* [2] and Bull *et al* [3] have suggested, by *in-situ* powder neutron diffraction experiments, the possibility of a pathway involving the formation of a minority phase, Li_4NH. [4, 5] At sub-amibent pressures, the formation of LiH is suppressed elucidating to the pathway shown in Equation 3:

$$2Li_3N + H_2 \rightarrow Li_4NH + Li_2NH \qquad (3)$$

Marx had reported that during a solid state reaction between the products formed in Eq. 3 at 450^{o}C, a non-stoichiometric phase results which has a combination of N^{3-}, H^{-} and $(NH)^{2-}$ anions (Equation 4): [4]

$$(1-x)Li_4NH + xLi_2NH \rightarrow Li_{4-2x}N_{1-x}H_{1-x}(NH)_x \qquad (4)$$

There are certain clear structural relationships between tetragonal Li_4NH and cubic Li_2NH. Li_2NH adopts an *anti*-fluorite structure where the Li^{+} cations occupy the tetrahedral sites of the fcc lattice and the $(NH)^{2-}$ anions are positioned at the fcc sites. Lithium nitride hydride essentially comprises two *anti*-fluorite cells where the Li^{+} cations occupy the tetrahedral sites and N^{3-} and H^{-} anions are located on the face centred cubic (fcc) sites. The structural connections between Li_2NH and Li_4NH with regards to the position of the Li^{+} cations and the anions are illustrated in Figure 4-1.

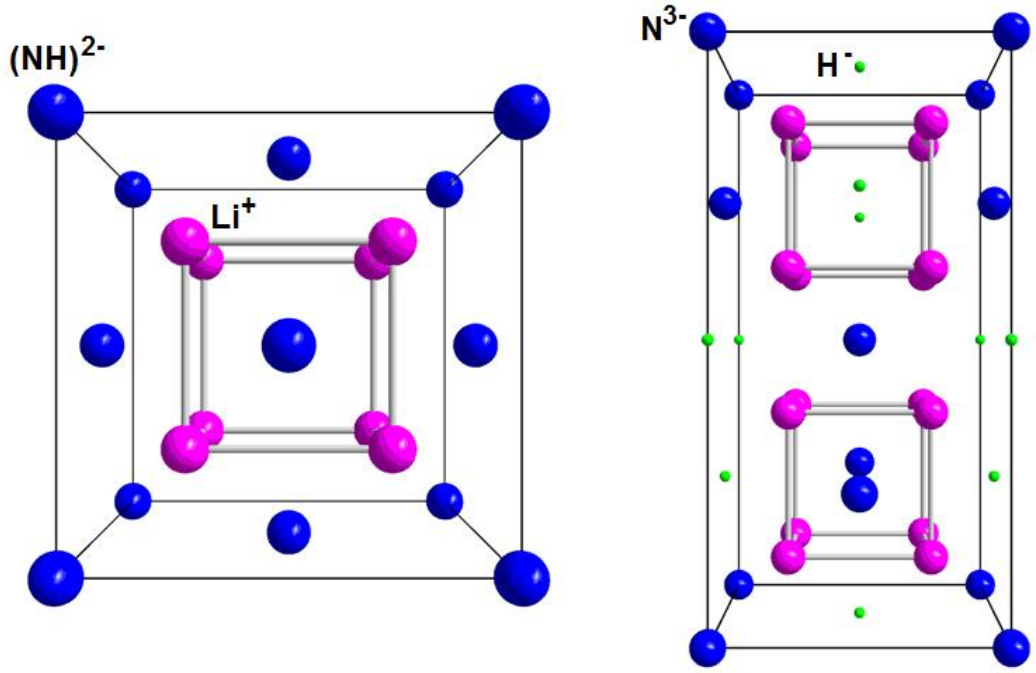

Figure 4-1: Schematic of the structures of Li_2NH and Li_4NH.
The idealised structure of Li_4NH has the Li atoms remaining on their cubic sites in order to illustrate the structural similarities (Li^+ - pink, N^{3-} - blue and H^+ - green).

This chapter describes the synthesis of Li_4NH both conventionally and by a novel route using microwaves. Thermogravimetric and differential thermal analyses were carried out on Li_4NH and Li_2NH samples. Variable temperature PND experiments were performed on Li_4ND and Li_2ND and a study of the interaction of Li_4ND and Li_2ND was carried out by *in-situ* PND.

4.2 Experimental

4.2.1 Synthesis of Lithium Nitride Hydride

The conventional synthesis of Li_4NH was investigated by a visiting summer student, Martina Huckova. Numerous reactions were performed to determine suitable reaction parameters for the synthesis of Li_4NH. Temperature, duration, ratio of reactants and mixing method (e.g. manually or by mechanical ball milling) were varied in order to achieve the most appropriate reaction conditions.

Lithium nitride hydride can be successfully synthesised both conventionally (under an argon atmosphere) and by microwave irradiation (under vacuum) by reacting Li_3N and LiH/D (LiD was used for PND experiments) in a 1:1·1 ratio. For both methods of synthesis, the reactants were ground together under an argon atmosphere in a recirculating glove box and then pressed using a 13 mm pellet die for 30 minutes. When synthesising

the material conventionally, the pellet was transferred into a stainless steel crucible which was then placed in a stainless steel reaction vessel. The reaction vessel was sealed before removal from the glove box. Details of the reaction are presented in Table 4-1.

Table 4-1: Summary of the reaction parameters employed during the synthesis of Li_4NH using a conventional method

Sample number	Temperature (K)	Time (hr)	Conditions	Results
1	823	6	$Ar_{(g)}$ atmosphere, quenched	Li_4NH, Li_2O

The second synthetic method involved using microwave irradiation to obtain the desired product. A pellet, similar to that described above, was transferred into a silica glass tube under an argon atmosphere. The silica glass tube was sealed under vacuum using a glass blowing torch before being reacted in a CEM discover single mode microwave reactor. The power was set to 300 watts and the reaction took approximately 3.5 minutes to reach completion.

The synthesis of Li_4NH required strict reaction conditions and due to the novelty of this method, numerous reactions were carried out sequentially with varying parameters to achieve the most appropriate and suitable reaction conditions. In order to obtain the desired product, the importance of the atmosphere under which the reaction was conducted was investigated. Under an atmosphere of argon, Li_4NH formed however un-reacted Li_3N and LiH were still present. Further reaction parameters were altered including increasing the duration of irradiation of the sample (3 – 16 minutes) and the type of microwave reactor used, from a domestic microwave oven (DMO) to a single mode microwave reactor. When using the DMO reactor (Panasonic 4697 NN-TS53W), a molybdenum or graphite susceptor was employed to aid heating (a schematic of the set-up is displayed in Chapter 2, Figure 2-10). These factors did not encourage the formation of single phase Li_4NH. Performing the experiment under a nitrogen atmosphere was avoided since the temperature of the microwave reactors cannot be measured accurately and reports in the literature suggest that Li_4NH decomposes under this particular atmosphere to Li_2NH at temperatures around 673 K. [4]

Numerous reactions were performed in order to ascertain the appropriate reaction conditions for synthesis of Li_4NH. An overview of the varying experimental parameters are presented in Table 4-2. It should be noted that the reaction times stated in Table 4-2 were not continuous; each reaction was stopped at various intervals to allow for cooling in attempts to avoid cracking of the silica glass tube.

Table 4-2: Summary of Li_3N + LiH reactions using a domestic microwave oven (800 watts)

Sample number	Power	Time (seconds)	Conditions	Results
2	'Med/High'	960	$Ar_{(g)}$ atmosphere	LiH, α-Li_3N
3	'Medium'	180	$Ar_{(g)}$ atmosphere, Iron susceptor	Li_4NH, α-Li_3N, LiH
4	'Medium'	70	$Ar_{(g)}$ atmosphere, Carbon (graphite) susceptor	Li_4NH, α-Li_3N, LiH
5	'Med/High'	480	Vacuum, Carbon (graphite) susceptor	Li_4NH, α-Li_3N, LiH
6	'Medium'	390	Vacuum, Carbon (graphite) susceptor	Li_4NH
7	'Medium'	360	Vacuum, Carbon (graphite) susceptor	Li_4NH
8	'Medium'	300	Vacuum, Carbon (graphite) susceptor	Li_4NH, α-Li_3N, LiH
9	'High'	240	Vacuum	Li_4NH, α-Li_3N, LiH

Following the reaction conditions highlighted for samples **6** and **7**, it was shown to be possible to synthesise single phase Li_4NH. From the investigation, it was evident that when using a domestic microwave oven to synthesise single phase Li_4NH, a susceptor was needed to aid heating and to permit the starting materials to fully react. Furthermore, conducting the reaction under vacuum was vital to the success of the reaction.

One disadvantage of synthesising Li_4NH using a domestic microwave oven was that the result was difficult to reproduce. Therefore an alternative method of synthesis using a single mode microwave reactor was developed. Using a single mode microwave reactor ensured that the microwaves are focussed directly at the material and therefore promoted the formation of single phase Li_4NH. During successful reactions, purple plasma formed suggesting that Li_3N was reacting evolving $N_{2(g)}$ and when the plasma could no longer be observed, this indicated that the reaction had reached completion (this is also true for reactions performed using a DMO). Details of the experimental parameters followed in attempt to synthesise Li_4NH using a single mode microwave reactor are displayed in Table 4-3. As stated previously, reaction times were not continuous; cooling intervals were introduced to avoid cracking of the silica glass tube.

Table 4-3: Summary of Li_3N + LiH reactions using a single mode microwave reactor

Reaction number	Power (watts)	Time (seconds)	Conditions	Results
10	300	150	Ar(g) atmosphere	Li_4NH, α-Li_3N, LiH
11	300	270	Ar(g) atmosphere	Li_4NH, α-Li_3N, LiH
12	300	360	Under vacuum, pelletised material	Failed reaction – cracked tube
13	150	270	Under vacuum, pelletised material	Li_4NH, α-Li_3N, LiH
14	250	270	Under vacuum, pelletised material	Li_4NH, α-Li_3N, LiH
15	300	240	Under vacuum, pelletised material	Li_4NH
16	300	180	Under vacuum, pelletised material	Li_4NH

It was evident from PXD data collected for samples **15** and **16** that single phase Li_4NH could be successfully synthesised; no reflections from α-Li_3N or LiH were observed. Using this type of microwave reactor, the synthesis of Li_4NH was more reproducible and it was this method that was employed to synthesise Li_4ND for PND investigations that will be discussed later.

4.2.2 Synthesis of Lithium Imide

Lithium imide was synthesised conventionally by decomposing commercial $LiNH_2$ (Sigma-Aldrich, 95%). Approximately 2 g of commercial $LiNH_2$ was loaded into a stainless steel crucible and transferred into a stainless steel reaction vessel (Figure 2-3, Section 2.3.1.1) which was then sealed under a nitrogen atmosphere. On removal from the recirculating glove box, the reaction vessel was placed in a bench furnace and heated to 823 K at 5 K min^{-1}, dwelling at temperature for 2 h before cooling. Decomposing $LiNH_2$ to Li_2NH releases $NH_{3\,(g)}$ therefore the vessel was connected to a vacuum line throughout the reaction to remove the evolved gas. From this synthetic method, the product was a fine white powder and the purity of the sample was determined by PXD and the result is shown in Table 4-4.

Table 4-4: Summary of the reaction conditions employed for the decomposition of $LiNH_2$ to Li_2NH.

Sample number	Temperature (K)	Time (h)	Conditions	Results
17	823	2	Vacuum	Li_2NH, Li_2O

Decomposition of deuterated lithium amide (provided by Dr. D. J. Bull at the University of Salford) to Li_2ND was performed for PND experiments following the method described above. The product was a fine white powder, in agreement with the result obtained for the hydrogenated sample. Determination of the purity of the sample was ascertained by PXD. An overview of the reaction parameters are displayed in Table 4-5.

Table 4-5: Summary of the reaction conditions employed for the decomposition of $LiND_2$ to Li_2ND.

Sample number	Temperature (K)	Time (h)	Conditions	Results
18	823	2	Vacuum	Li_2ND, Li_2O

4.2.3 Synthesis of $Li_{4-2x}N_{1-x}D_{1-x}(ND)_x$

Non-stoichiometric mixtures of Li_4ND and Li_2ND were prepared under an argon atmosphere of a recirculating glove box where x = 0.36, 0.5 and 0.6. The materials were ground together using an agate mortar and pestle before being loaded into a vanadium canister which was sealed with a copper gasket before being removed from the glove box. The vanadium canister was loaded into the furnace and heated to 773 K. Further details are presented in Section 4.2.7 and Table 4-6 summarises the reactions performed on these samples.

4.2.4 Powder X-ray Diffraction (PXD) Experiments

All compounds which were synthesised were initially characterised by PXD using a Bruker D8 diffractometer or a PANalytical X'Pert PRO MPD powder diffractometer, as described in Section 2.4.1.2. Capillaries of the materials were prepared for each PXD measurement. Data were collected from 5-85° 2θ or 10-110° 2θ for 1 h or 12 h respectively, using a step

size of 0.017° 2θ. PXD data collected overnight produced high quality data used for Rietveld refinements.

4.2.5 Thermogravimetric and Differential Thermal Analysis

A Netzsch STA 409 PC was employed to perform TG/DTA experiments. Correction measurements, using an appropriate crucible type, were created typically by setting the temperature to increase at regular intervals until the target temperature was reached. The measurement was held at a specific temperature for a certain period of time before undergoing a controlled cool down. Measurements took place under an argon atmosphere. Before starting the measurement, approximately 0.5-0.6 g of Li_4NH was loaded into the crucible before the sample chamber was closed. The measurement was then set to start when the temperature of the sample chamber reached the initial starting temperature programmed in the correction file. A typical measurement involved heating from room temperature to 773 K at 5 K min^{-1} and holding at temperature for 1 h before undergoing a programmed cooldown.

4.2.6 Coupled Mass Spectrometry; evolved gas analysis

Mass spectrometry was used in conjunction with TG/DTA to give an overview of any gases evolved against time. Each measurement was programmed to detect certain gases depending on the individual experiment. The gases which the measurement was typically programmed to measure were hydrogen, nitrogen and ammonia (refer to Section 2.4.6 for further details).

4.2.7 Powder Neutron Diffraction (PND) Experiments

Powder neutron diffraction studies were performed on the POLARIS instrument at ISIS, Rutherford Appleton Laboratory which is a high intensity, medium resolution diffractometer. [6] It is described more fully in Section 2.4.2.1. Three PND experiments were performed;

1 a variable temperature study of Li_4ND

2 a variable temperature study of Li_2ND

3 a variable temperature study of compounds of the type $Li_{4-2x}N_{1-x}D_{1-x}(ND)_x$ where x = 0.36, 0.5 and 0.6

Initially, PND data were collected for Li_4ND at 323, 523, 673 and 773 K (data collected at 523 and 673 K is presented in the appendix). Approximately 0.6 g of the sample was loaded into a canister and sealed under an argon atmosphere. The canister was then loaded into the furnace and data were collected using the 145° (C), 90° (E) and 35° (A) detector banks. This measurement was followed by the collection of PND data for Li_2ND at 313 and 773 K. The data collection was performed following the same method as for Li_4ND.

The third PND investigation involved a study into the non-stoichiometric mixtures of Li_4ND and Li_2ND. Accurate masses of the each material were weighed out under an argon atmosphere in a recirculating glove box. The materials were hand milled together using an agate mortar and pestle before being transferred into a vanadium canister which was made air-tight using a copper gasket. Three samples were prepared and data were collected at 313 or 323 K for each one before heating to 773 K. A summary of the data collected is presented in Table 4-6.

Table 4-6: Summary of PND data collected for samples of $Li_{4-2x}N_{1-x}D_{1-x}(ND)_x$

Sample	x	Li_{4-2x}	Temperature / K
19	0	Li_4ND	323
20	0	Li_4ND	523
21	0	Li_4ND	673
22	0	Li_4ND	773
23	1	Li_2ND	313
24	1	Li_2ND	773
25	0.36	$Li_{3.28}ND$	313
26	0.36	$Li_{3.28}ND$	773
27	0.5	Li_3ND	323
28	0.5	Li_3ND	773
29	0.6	$Li_{2.8}ND$	313
30	0.6	$Li_{2.8}ND$	773

4.2.8 Rietveld refinement against PND data

The General Structure Analysis System (GSAS) [7] using the EXPGUI interface [8] was employed to carry out Rietveld refinements with the collected PND time of flight data. Data collected from three detector banks; A bank (35^o), E bank (90^o) and C bank (145^o) were fitted consecutively using an appropriate starting model (detailed in subsequent sections) obtained from the online Inorganic Crystal Structure Database (ICSD). Initially, data collected for the backscattering (C) bank was employed followed by the addition of data collected for the E and A banks respectively.

PND data were collected for lithium nitride hydride and lithium imide firstly. For each sample (Table 4-3), background function 1 in GSAS, shifted Chebyschev polynomial, was employed using 8 or 10 coefficients. The background was then refined. The unit cell parameters, peak profile parameters and isotropic temperature factors were then refined followed by the application of an absorption correction. Modelling of the peak shape was carried out using GSAS function 3, a convolution of back-to-back exponentials and pseudo-Voigt combination with Lorentzian broadening. Lastly, the anisotropic temperature factors were refined. Constraints were applied to the thermal parameters of the N and D within Li_4ND since both are located on the 4a and 4b sites with N predominantly occupying the 4a site and D predominantly occupying the 4b site. Constraints were also applied to the thermal parameters of N and D in the 'quasi-imide' phase where both occupy the 4a site in a 50:50 ratio.

4.3 Results and Discussion

4.3.1 Synthesis and PXD characterisation of Lithium Nitride Hydride

The successful synthesis of lithium nitride hydride, using either method of synthesis (conventional synthesis - sample **1** or microwave synthesis – sample **16**), produced a yellow/beige coloured powder. The PXD pattern presented in Figure 4-2 shows that, by conventional methods, a relatively pure sample of Li_4NH can be synthesised, however the presence of a Li_2O impurity was difficult to avoid. The experimental data shown in black fits well with the theoretical pattern shown in red. Indexed reflections are in good agreement with those reported in the literature by Marx. [4] Experimental values were calculated as a = 4.891 (7) Å and c = 9.936 (2) Å where the cell volume was 237.68 (34) $Å^3$. The model used for the calculation, performed by CELREF V3, was obtained from the online Inorganic Crystal Structure Database (ICSD). Powdercell 2.4 was used to obtain a

visual comparison between the experimental and theoretical models. It should be noted that there appears to be a shoulder on two of the peaks (at ~ 31 and 52° 2θ) which will be discussed later.

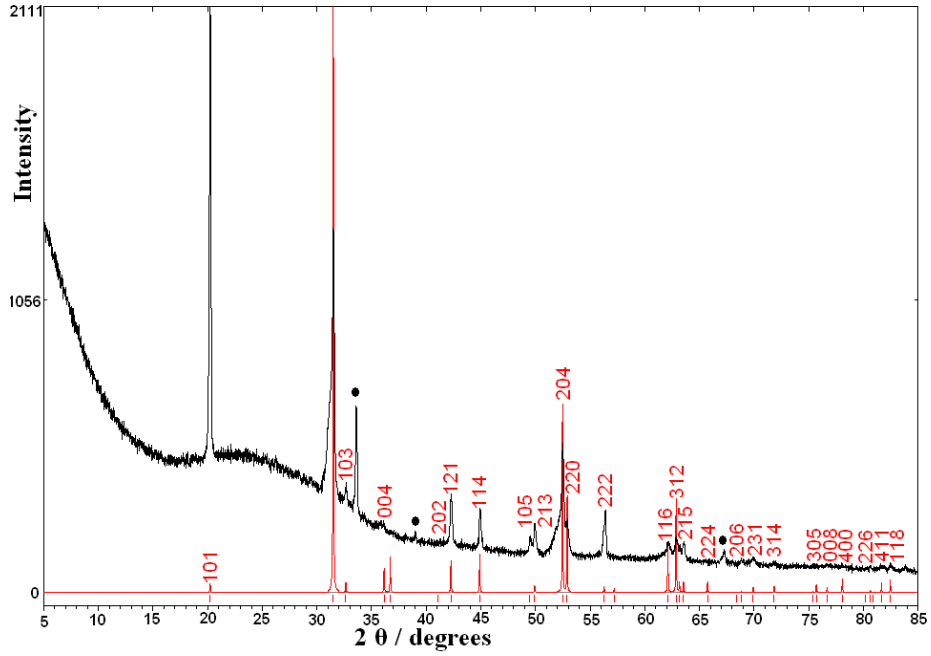

Figure 4-2: PXD analysis showing the experimental (black) and calculated (red) patterns for conventionally synthesised Li_4NH (sample 1).
The black circles indicate reflections from Li_2O impurity.

Figure 4-3 shows the PXD data obtained from sample **2** which was synthesised using a DMO where the starting materials have not fully reacted. In regards to the main phase, Li_4NH, the experimental pattern fits well to that of the theoretical pattern where experimental lattice parameters were refined as a = 4.893 (2) Å and c = 9.936 (8) Å and the cell volume was 237.83 (10) $Å^3$.

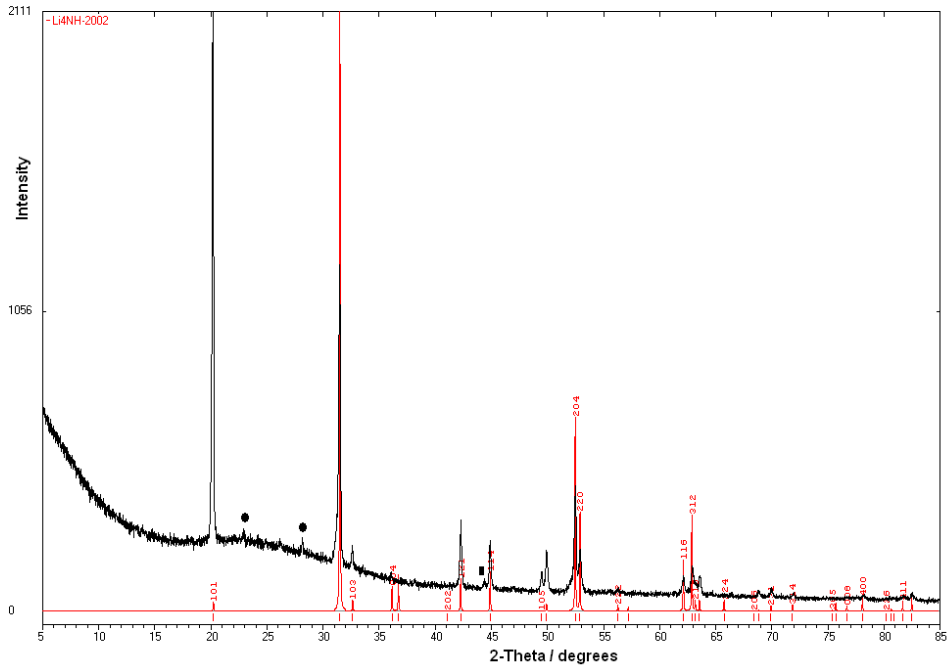

Figure 4-3: PXD analysis showing the experimental (black) and calculated (red) patterns for Li_4NH (sample 2) synthesised using microwave irradiation in a DMO.
The black circles indicate reflections from α-Li_3N and the black square indicates reflection from LiH.

Using a single mode microwave reactor allowed reproducibility in the synthesis of single phase Li_4NH (Figure 4-4). The experimental model (sample **16**) fits well with the theoretical model however indexing yielded cell parameters which vary from the literature values for Li_4NH (a = 4.8918 (1) Å, c = 9.9321 (3) Å). [4] Experimental values obtained were, a = 4.887 (1) Å and c = 9.923 (1) Å and the cell volume was 237.04 (6) $Å^3$. As stated for the conventionally synthesised material, there appears to be a shoulder on two of the peaks (at ~ 31 and 52° 2θ), which will be discussed later.

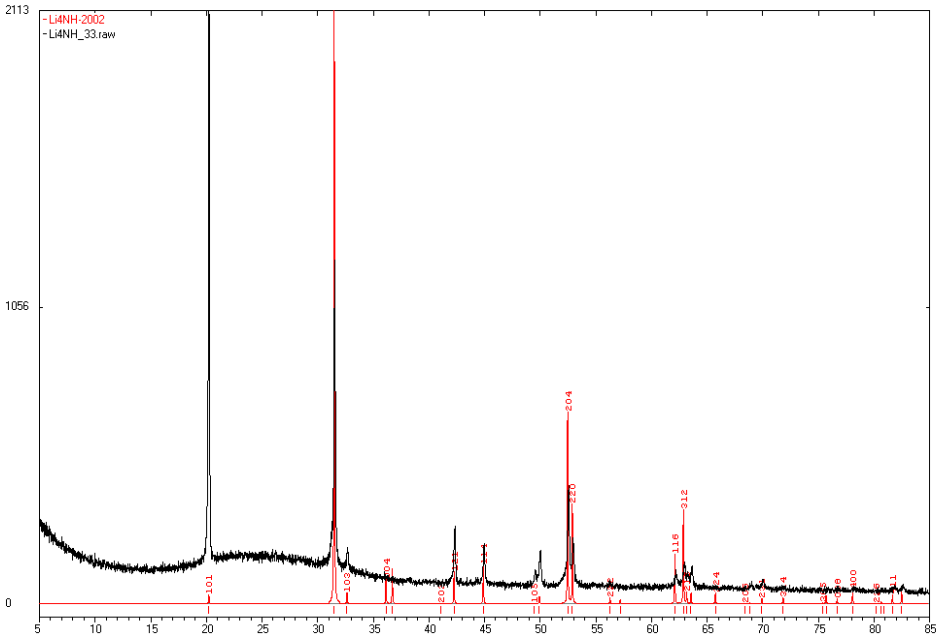

Figure 4-4: PXD analysis showing the experimental (black) and calculated (red) patterns for Li_4NH (sample 16) synthesised using a single mode microwave reactor.

Sample **19** was used for PND experiments and PXD data were collected to determine the purity of the sample (Figure 4-5). Literature values for Li_4ND reported by Marx (a = 4.8868 (1) Å, c = 9.9321 (3) Å) [4] are smaller than those obtained by indexing of the experimental data; a = 4.894 (4) Å, c = 9.945 (2) Å and cell volume = 238.2 (2) Å^3.

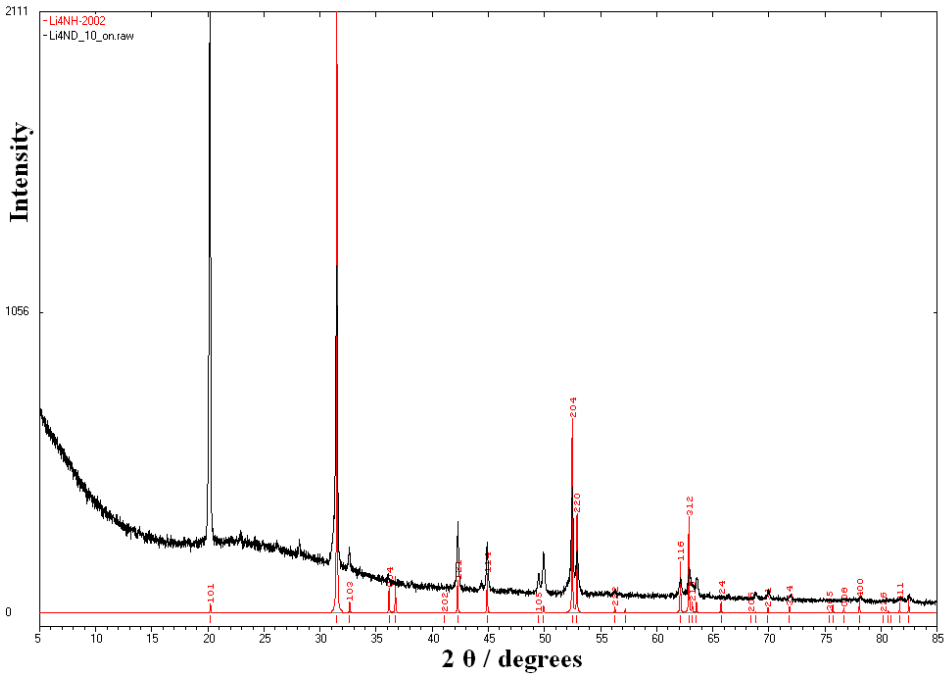

Figure 4-5: PXD analysis showing the experimental (black) and calculated (red) patterns for Li_4ND (sample 19) synthesised using microwave irradiation.

4.3.2 Synthesis and PXD Characterisation of Lithium Imide

Using a conventional method, lithium imide can be successfully synthesised by decomposing lithium amide, resulting in the formation of a white powder. Figure 4.6 highlights the fact that the experimental model fits well to the model proposed by Juza [9] where the experimental cubic *a* lattice parameter was refined as 5.067 (2) Å with a cell volume of 130.10 (5) $Å^3$. The PXD pattern displayed in Figure 4-6 shows the presence of Li_2O as an impurity which is thought to be present from the commercial $LiNH_2$ starting material (PXD data is presented in the appendix).

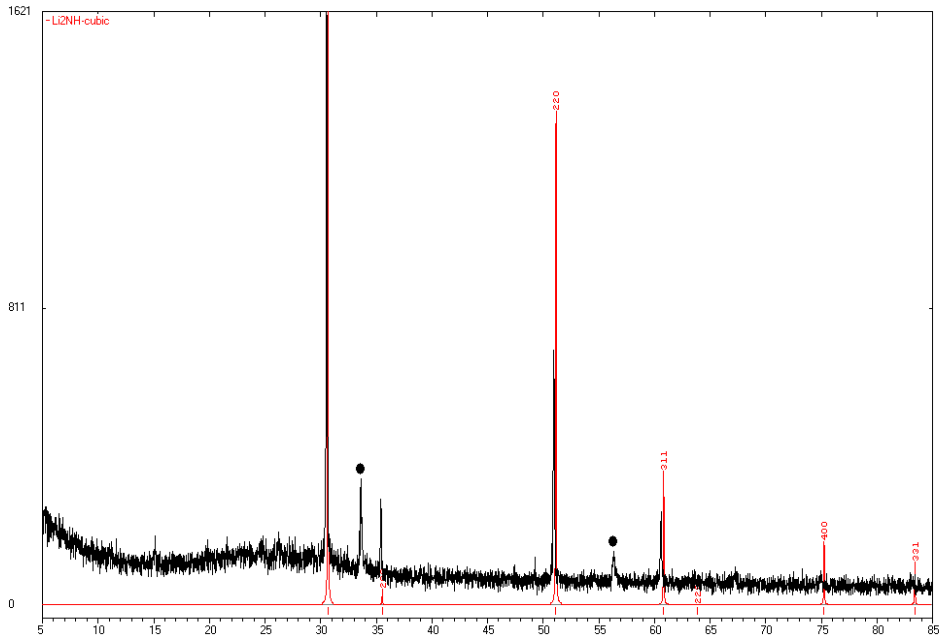

Figure 4-6: PXD analysis showing the experimental (black) and calculated (red) patterns for sample 17, commercial $LiNH_2$ decomposed to Li_2NH.
The black circles indicate the presence of Li_2O.

4.3.3 Thermogravimetric/Differential Thermal Analysis (TG/DTA) and Mass Spectroscopy (MS) of Li_2NH and Li_4NH

4.3.3.1 Decomposition of $LiNH_2$ to Li_2NH

Previous to the synthesis of Li_2NH via the decomposition of $LiNH_2$, a TG/DTA and MS experiment was performed to determine the temperature at which the reaction occurs from lithium amide to lithium imide. Commercial $LiNH_2$ (Sigma Aldrich, 95%) was used for the investigation.

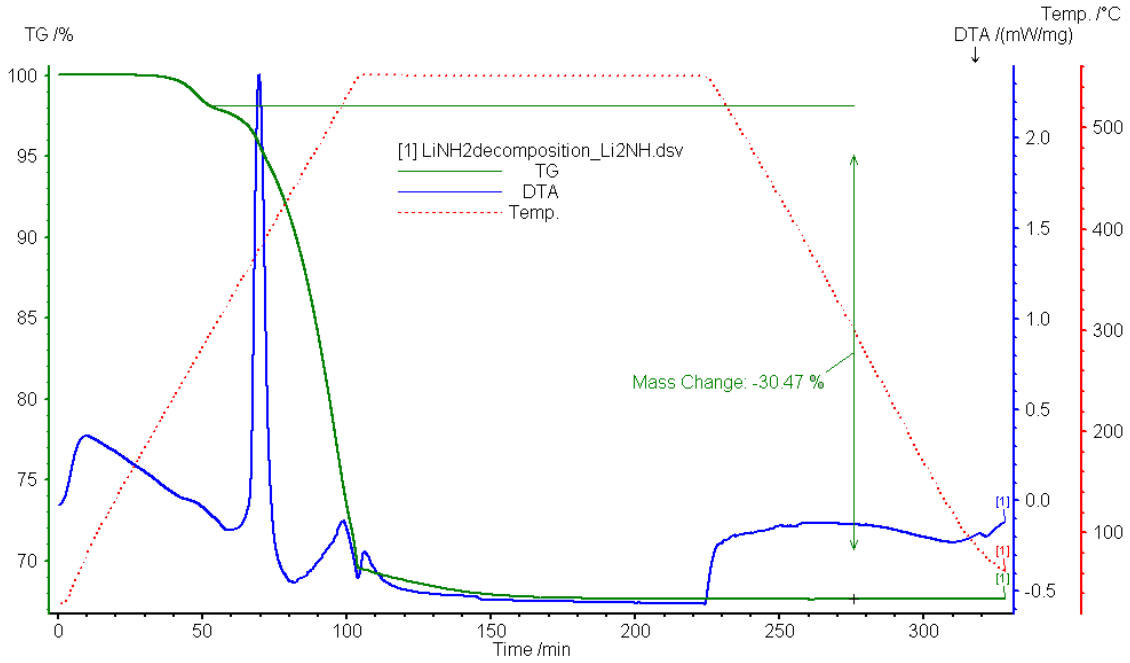

Figure 4-7: Thermogravimetric and differential thermal analysis plot of commercial $LiNH_2$ decomposing to Li_2NH at 550°C.

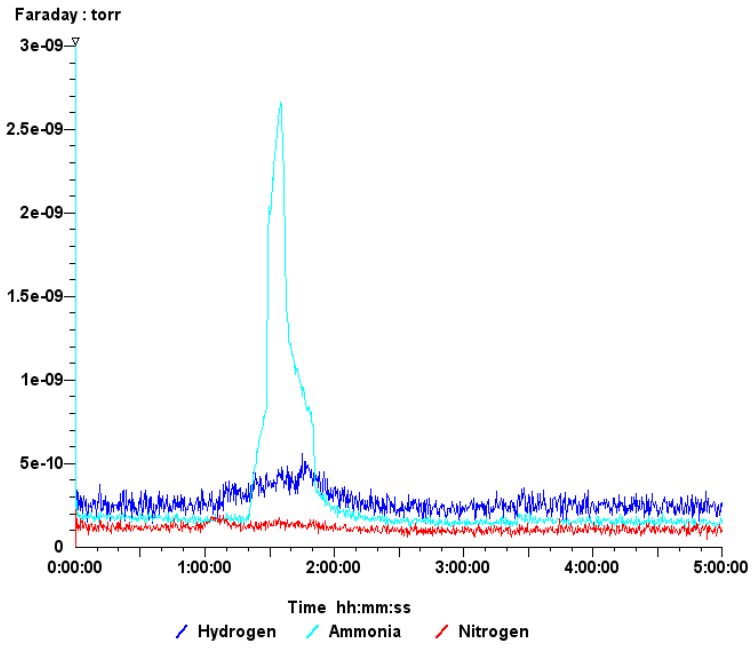

Figure 4-8: Mass spectroscopy analysis of the decomposition of commercial $LiNH_2$ to Li_2NH.

From Figure 4-7, it is clear that an endothermic event occurs after approximately 75 minutes. This interpretation is confirmed by the evolution of $NH_{3(g)}$ shown in Figure 4-8 and also in agreement with the literature [10]

$$2LiNH_2 \rightarrow Li_2NH + NH_3 \quad (5)$$

PXD was used to confirm the composition of the material after TG/DTA analysis, PXD was used. From the results, it was concluded that the product was indeed cubic lithium imide. The experimental model (shown in black) fits well with that of the theoretical model (shown in red) however the PXD pattern revealed the presence of a Li_2O impurity (Figure 4-9).

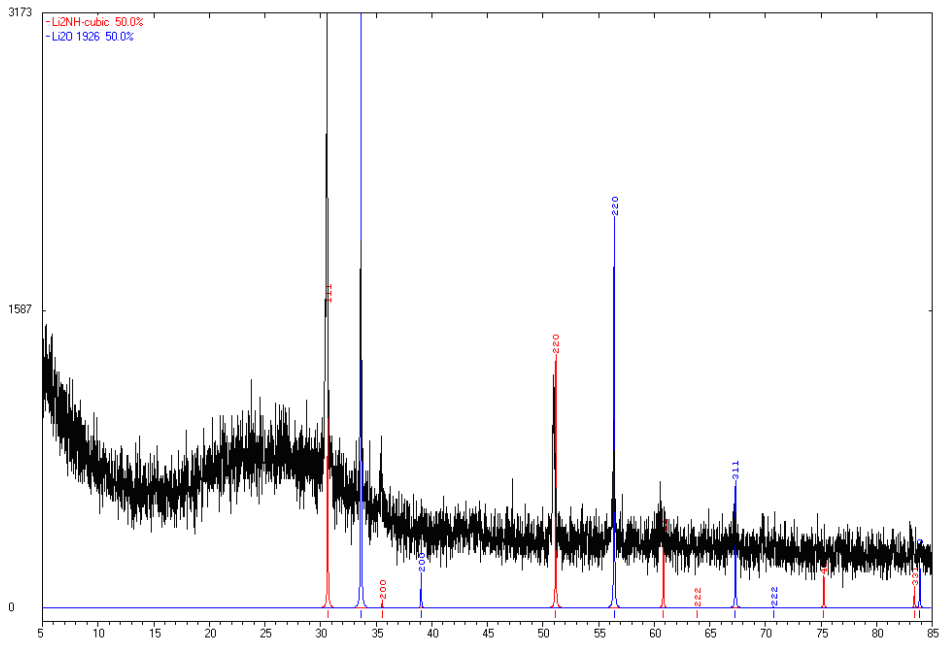

Figure 4-9: PXD analysis showing the experimental (black) and calculated (red) patterns for the decomposition of commercial $LiNH_2$ to Li_2NH.

4.3.3.2 Investigation of the stability of Li_4NH

In order to verify findings by Marx that Li_4NH is stable under an argon atmosphere at 698 K, [4] TG/DTA and MS were performed. The temperature of the experiment was increased to a higher temperature than stated in the literature (773 K) to ascertain if any decomposition would occur. However, it was evident from the TG-DTA (Figure 4-10) and MS (see appendix) data and subsequent PXD (Figure 4-11) that Li_4NH is in fact stable under $Ar_{(g)}$ under these conditions. A high purity sample of Li_4NH (Figure 4-4) was used for the experiment, however it is evident from the post TG-DTA PXD (Figure 4-13) that a small amount of Li_2O was present in the sample post-analysis. This was possibly due to the presence of moisture in the gas under which the reaction was run or may have occurred when moving the sample to another glove box to prepare a capillary for PXD.

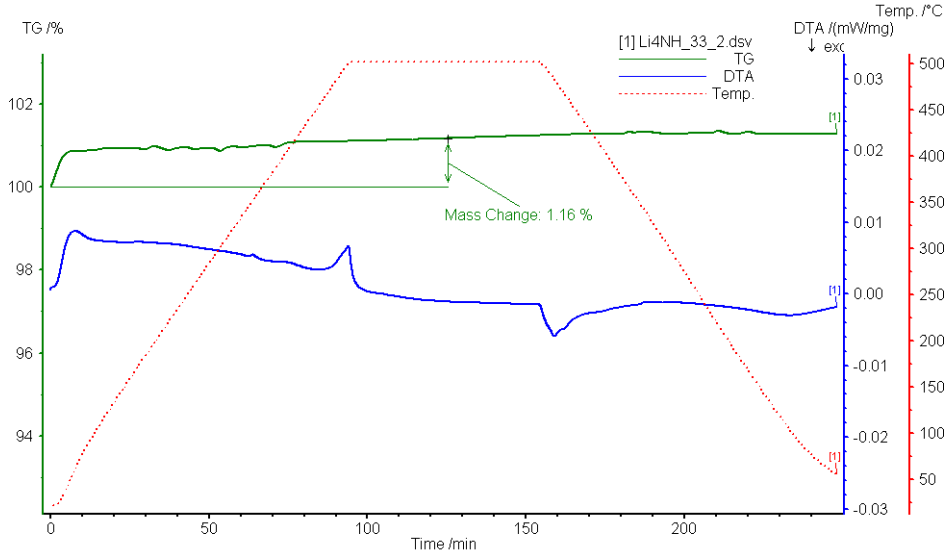

Figure 4-10: Thermogravimetric and differential thermal analysis plot of Li_4NH under $Ar_{(g)}$. The sample was heated to 773 K at 5 K min^{-1}; the sample was held at temperature for 1 h before a programmed cool down.

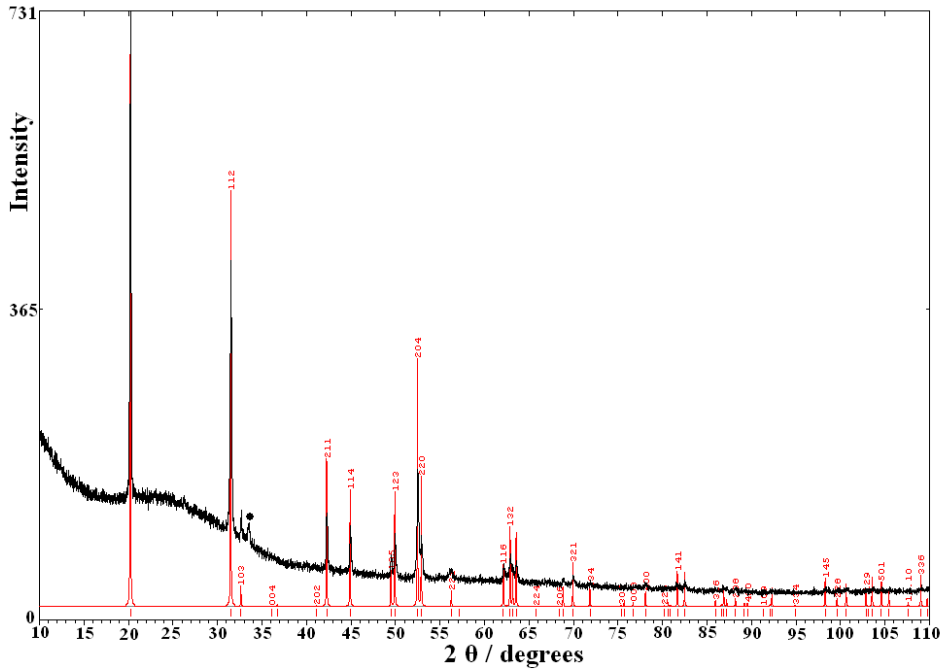

Figure 4-11: PXD analysis showing the experimental (black) and calculated (red) patterns for Li_4NH post TG/DTA.
The black circle indicates a reflection attributed to Li_2O.

It can be concluded from evidence shown in Figure 4-10 that there is no reaction occurring and this is confirmed from PXD analysis (Figure 4-11). The lattice parameters and cell volume values obtained for Li_4NH pre- and post-TG/DTA were calculated by CELREF V3 and are displayed in Table 4-7 below. Although the lattice parameters do not vary within 2σ between pre-and post-reaction, it should be noted that a likely phase transformation is

beginning to occur as shown in the DTA trace on heating and cooling. Since the reaction was cooled slowly, only tetragonal Li_4NH was evident from PXD analysis. The occurrence of a phase transformation is supported by PND experiments as will be discussed later.

Table 4-7: Comparison of lattice parameters of Li_4NH before and after TG/DT analysis.

	Pre-TG/DTA	Post-TG/DTA
***a* lattice parameter / Å**	4.887 (1)	4.891 (2)
***c* lattice parameter / Å**	9.9233 (9)	9.9252 (8)
Cell volume / Å ^{3}	237.04 (6)	237.39 (10)

4.3.4 Powder Neutron Diffraction Experiments

4.3.4.1 Variable temperature study of Li_4ND

The first PND investigation involved studying the effects of heating on the structure of Li_4ND (sample **19**). Selected Rietveld refinement data for sample **19** collected at 323 K are displayed in Table 4-5 and the observed, calculated and difference (OCD) plot for the data obtained is illustrated in Figure 4-12, Figure 4-13 and Figure 4-14 respectively.

The Rietveld refinement of PND data collected for this sample (**19**) revealed the presence of two Li_4ND phases; a low temperature tetragonal Li_4ND phase and a high temperature cubic Li_4ND phase as well as a LiD impurity. The Li_4NH structure proposed by Marx [4] was used as a starting model for the main tetragonal Li_4ND phase. The experimental model fits well to the theoretical model. With regards to LiD, the cubic lattice parameter obtained for the experimental model, a = 4.0756 (3) Å, is slightly larger than the value reported in the literature by Vidal and Vidal-Valat (a = 4.0615 (10) Å). [11] The cubic lattice parameter of Li_4ND (1′) was a = 4.9467 (6) Å. The model used for the refinement of the cubic-Li_4ND phase was based on a Li_2ND type structure proposed by Balogh *et al* which was modified so that both N and D occupy the 4a site. It was initially thought that Li_4ND (1′) was tetragonal (space group *I-4*) with a smaller unit cell however upon analysis using the Rietveld method, it was clear that this proposition was not ideal as the data did not fit well unlike the cubic model.

Table 4-8: Selected Rietveld refinement data from the PND refinement of Li_4ND at 323 K (sample 19).

Empirical Formula	Li_4ND (1)	Li_4ND (1′)	LiD
Collection temperature / K		323	
Crystal system	Tetragonal	Cubic	Cubic
Space Group	*I* $4_1/a$	*Fm-3m*	*Fm-3m*
Lattice parameters / Å	*a* = 4.8843 (1)	*a* = 4.9467 (6)	*a* = 4.0756 (3)
	c = 9.9226 (3)	-	-
V / Å ^{3}	236.72 (1)	121.04 (3)	67.698 (8)
Z	4	2	4
Unit cell formula weight, M_w	175.140	87.570	35.820
Density / (g/cm^3)	1.229	1.201	0.879
wt. %	81.836 (5)	15.040 (5)	3.124 (2)
No. of varied parameters		67	
No. of observations		11745	
R_{wp}		0.0100	
R_p		0.0228	
χ^2		1.120	

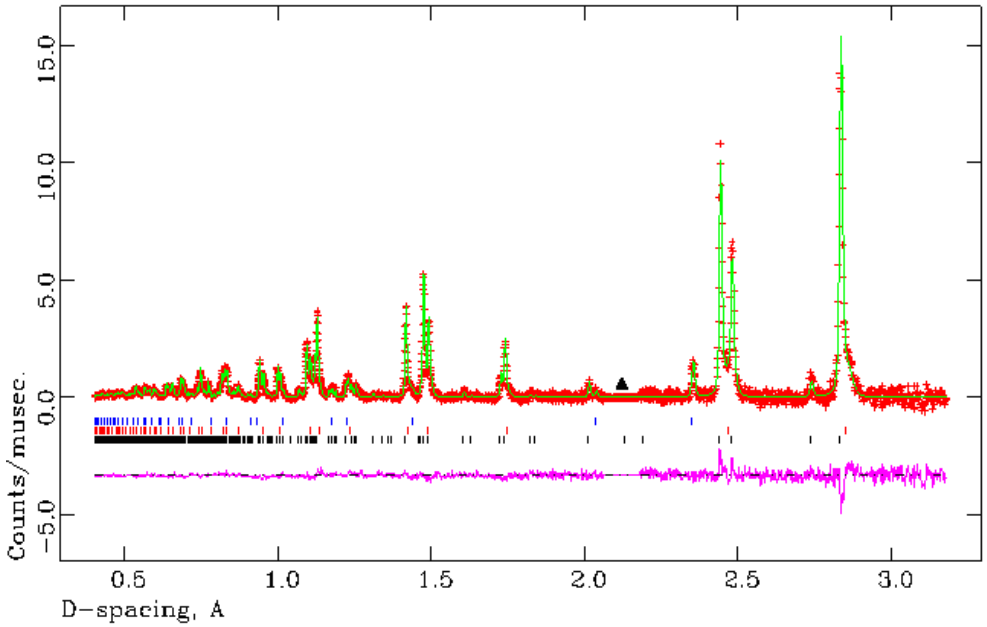

Figure 4-12: Observed, calculated and difference (OCD) plot from the structural refinement of sample 19 (Li_4ND, 323 K) from PND data, 145° (C) bank.

The black tickmarks indicate reflections from Li_4ND (1), the red tickmarks indicate reflections from Li_4ND (1′) and the blue tickmarks indicate reflections LiD. The black triangle represents reflections from the sample environment (i.e. the furnace and the vanadium canister) which have been excluded.

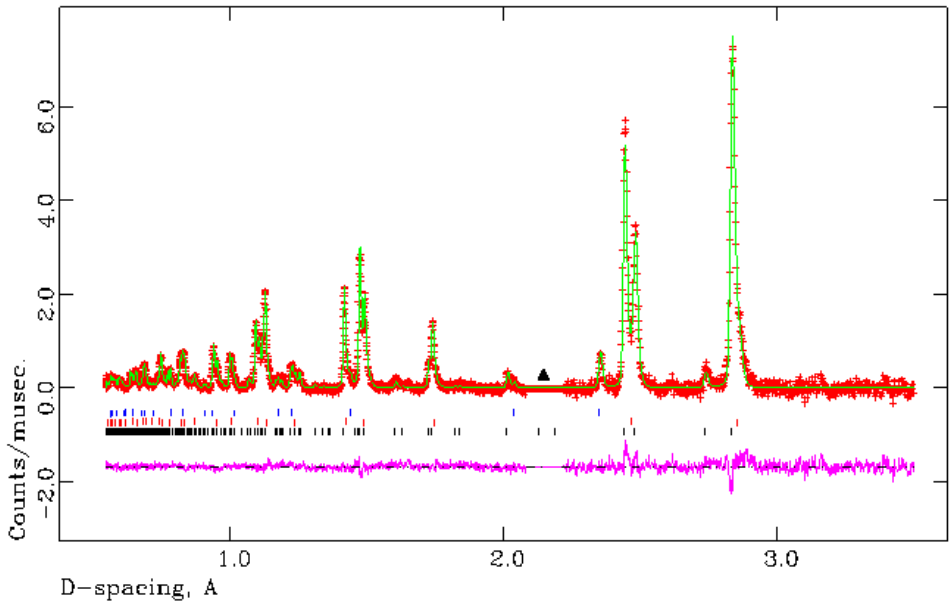

Figure 4-13: Observed, calculated and difference (OCD) plot from the structural refinement of sample 19 (Li_4ND, 323 K) from PND data, 90° (E) bank.

The black tickmarks indicate reflections from Li_4ND (1), the red tickmarks indicate reflections from Li_4ND (1′) and the blue tickmarks indicate reflections LiD. The black triangle represents reflections from the sample environment (i.e. the furnace and the vanadium canister) which have been excluded.

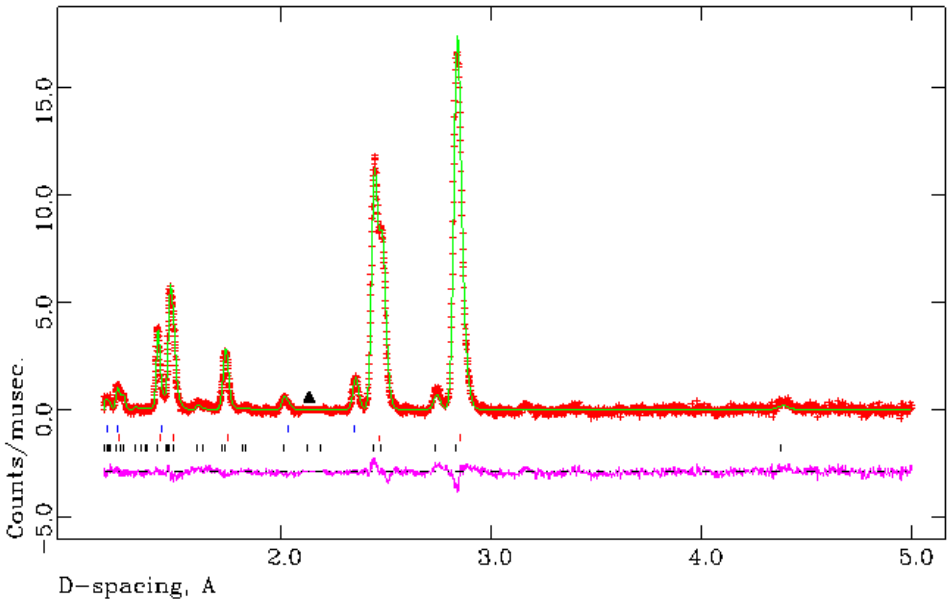

Figure 4-14: Observed, calculated and difference (OCD) plot from the structural refinement of sample 19 (Li_4ND, 323 K) from PND data, 35° (A) bank.
The black tickmarks indicate reflections from Li_4ND (1), the red tickmarks indicate reflections from Li_4ND (1′) and the blue tickmarks indicate reflections LiD. The black triangle represents reflections from the sample environment (i.e. the furnace) which have been excluded.

Atomic positions and anisotropic temperature factors for each phase are presented in Table 4-9, Table 4-10 and Table 4-11. Each atom in the tetragonal Li_4ND phase was refined anisotropically with the exception of Li due to the instability of this atom. Furthermore the occupancies of the N and D atoms, for Li_4ND (1) could not be varied and therefore were fixed at values reported by Marx. [4] With regards to the Li_4ND (1′) and LiD phases, the atoms within these phases were refined isotropically.

Table 4-9: Atom positions and anisotropic temperature factors generated by PND Rietveld refinement for the main Li_4ND phase (1) at 323 K.

Atom	N 1	D 1	N 2	D 2	Li 1
Site	4a	4a	4b	4b	16f
x	0	0	0	0	0.1955 (9)
y	0.25	0.25	0.25	0.25	0.4577 (10)
z	0.125	0.125	0.625	0.625	0.2813 (3)
100 x U_{iso} / Å^2	-	-	-	-	1.87 (5)
100 x U_{11} / Å^2	1.24 (2)	1.24 (2)	2.61 (6)	2.61 (6)	-
100 x U_{22} / Å^2	1.24 (2)	1.24 (2)	2.61 (6)	2.61 (6)	-
100 x U_{33} / Å^2	0.62 (3)	0.62 (3)	3.70 (10)	3.70 (10)	-
100 x U_{12} / Å^2	0	0	0	0	-
100 x U_{13} / Å^2	0	0	0	0	-
100 x U_{23} / Å^2	0	0	0	0	-
Occupancy	0.95	0.05	0.05	0.95	1.00

Table 4-10: Atom positions and isotropic temperature factors generated by PND Rietveld refinement for Li_4ND (1′) at 323 K.

Atom	Li 1	N 1	D 1
Site	8c	4a	4a
x	0.25	0	0
y	0.25	0	0
z	0.25	0	0
100 x U_{iso} / Å^2	3.08 (20)	1.25 (7)	1.25 (7)
Occupancy	1.00	0.50	0.50

Table 4-11: Atom positions and isotropic temperature factors generated by PND Rietveld refinement for LiD at 323 K.

Atom	Li	D
Site	4a	4b
x	0	0.5
y	0	0.5
z	0	0.5
100 x U_{iso} / Å^2	1.6 (3)	2.2 (2)
Occupancy	1.00	1.00

Bond valence calculations for TOF PND data collected at 323 K were performed to confirm if the N/D occupancies on each site was accurate. The calculations were performed using VALENCE and although the calculations are not quantitative, the data collected does indicate that the site occupancies of N1/D1 and N2/D2 as 0.95/0.05 and 0.05/0.95 respectively are sensible.

To determine the bond valence parameters, two expressions are employed to describe the relationship between the bond length and the bond valence: [12]

$$s = (r / r_o)^{-N} \tag{6}$$

and

$$s = \exp[(r_o - r) / B] \tag{7}$$

where r is the bond length, s is the bond valence and r_o, N and B are empirically defined parameters. r_o values for Li-N and Li-D are 1.619 and 1.380 respectively and B is 0.370 which varies only very little from one atom pair to another.

In agreement with the occupancies reported by Marx [4] and in this work, the N1/D1 site is occupied predominantly by N^{3-} anions since the N1-Li1 bond valence sum was calculated as 2.472. Consequently, the N2/D2 site is mainly occupied by D^- anions where a D2-Li1 bond valence sum of 0.849 was obtained. The calculated bond valencies for both N1-Li1 and D2-Li1 offer support to the fact that the occupancies reported by Marx are reasonable. It should be noted that the calculated valence sums do differ from the ideal values (3 for N^{3-} anions and 1 for D^- anions) however this is likely to be due to the fact that this data was

collected at 323 K instead of 293 K and assumes a purely ionic bonding structure in Li_4ND which is unlikely given the tendency of partial covalency in nitrides.

Table 4-12 compares the lattice parameters obtained experimentally in this work and those reported by Marx and by Niewa *et al*. [4, 5] It is evident that the values reported by each author vary however the lattice parameters obtained for Li_4ND (1) from Rietveld refinement in this work were closer to those reported by Marx in comparison to those reported by Niewa *et al*. Furthermore, the temperatures at which the data were collected in this work and in the literature differ by approximately 20 K therefore it is difficult to draw a direct comparison.

Table 4-12: Comparison of lattice parameters and cell volumes for Li_4NH/D between the literature values and those obtained experimentally by PND of sample 19.

	This work Li_4ND (1)	**This work Li_4ND (1′)**	**Marx [4]**	**Niewa et al [5]**
***a* lattice parameter / Å**	4.8843 (1)	4.9467 (6)	4.8868 (1)	4.8765 (3)
***c* lattice parameter / Å**	9.9226 (3)	-	9.9321 (3)	9.8769 (9)
V / Å^3	236.72 (1)	121.04 (3)	237.19	234.88

On increasing the temperature to 673 K (data collected at 523 K and 673 K are reported in the appendix), a transformation from tetragonal Li_4ND to cubic Li_4ND occurred and the weight percentage of this phase increases further at 773 K. An indication of a phase transition was evident from the TG-DTA data presented in Figure 4.10 however it is thought that a rapid cooling rate is the reason for the presence of Li_4ND (1′) therefore since the TG-DTA underwent a programmed cool down, only Li_4ND (1) resulted.

Figure 4-16 indicates the presence of LiD which was present in the material at 323 K and could still be observed in the sample at 673 K. The melting point of LiH/D is 953 K [13] therefore it is not inconceivable that some un-reacted material is still present at 773 K. Selected Rietveld refinement data for sample 22 (773 K) are presented in Table 4-13 and observed, calculated and difference plots are presented in Figure 4-15, Figure 4-16 and Figure 4-17. Atomic positions and isotropic temperature factors for the cubic and tetragonal phases of Li_4ND are presented in Table 4-14 and Table 4-15 respectively.

Table 4-13: Selected Rietveld refinement data from the PND refinement of sample 22 (Li_4ND at 773 K).

Empirical Formula	Li_4ND (1)	Li_4ND (1′)
Collection temperature / K	773	
Crystal system	Tetragonal	Cubic
Space Group	*I* $4_1/a$	*Fm-3m*
Lattice parameters / Å	*a* = 4.9625 (9)	*a* = 5.0542 (2)
	c = 10.059 (4)	-
V / Å ^{3}	247.71 (11)	129.107 (7)
Z	4	2
Unit cell formula weight, M_w	175.140	87.570
Density / (g/cm^3)	1.174	1.124
Wt. %	8.806 (6)	91.194 (6)
No. of varied parameters	53	
No. of observations	11643	
R_{wp}	0.0091	
R_p	0.0233	
χ^2	0.8057	

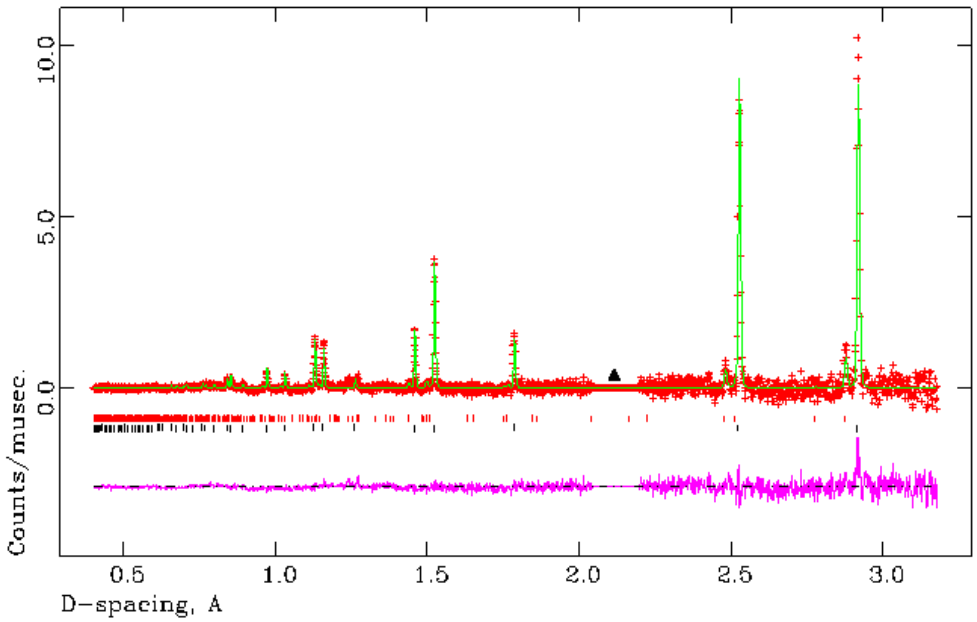

Figure 4-15: Observed, calculated and difference (OCD) plot from structural refinement of sample 22 (Li_4ND at 773 K) from PND data, 145° (C) bank.
The black tickmarks indicate reflections from cubic Li_4ND and the red tickmarks indicate reflections from tetragonal Li_4ND. The black triangle indicates reflections from the sample environment (i.e. the furnace and vanadium canister) which have been excluded.

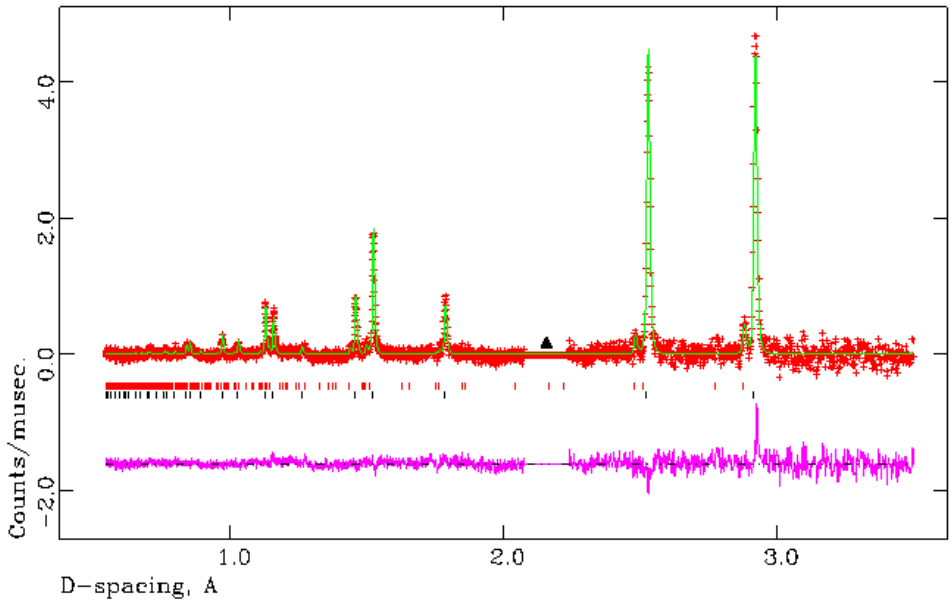

Figure 4-16: Observed, calculated and difference (OCD) plot from structural refinement of sample 22 (Li_4ND at 773 K) from PND data, 90° (E) bank.
The black tickmarks indicate reflections from cubic Li_4ND and the red tickmarks indicate reflections from tetragonal Li_4ND. The black triangle indicates reflections from the sample environment (i.e. the furnace and vanadium canister) which have been excluded.

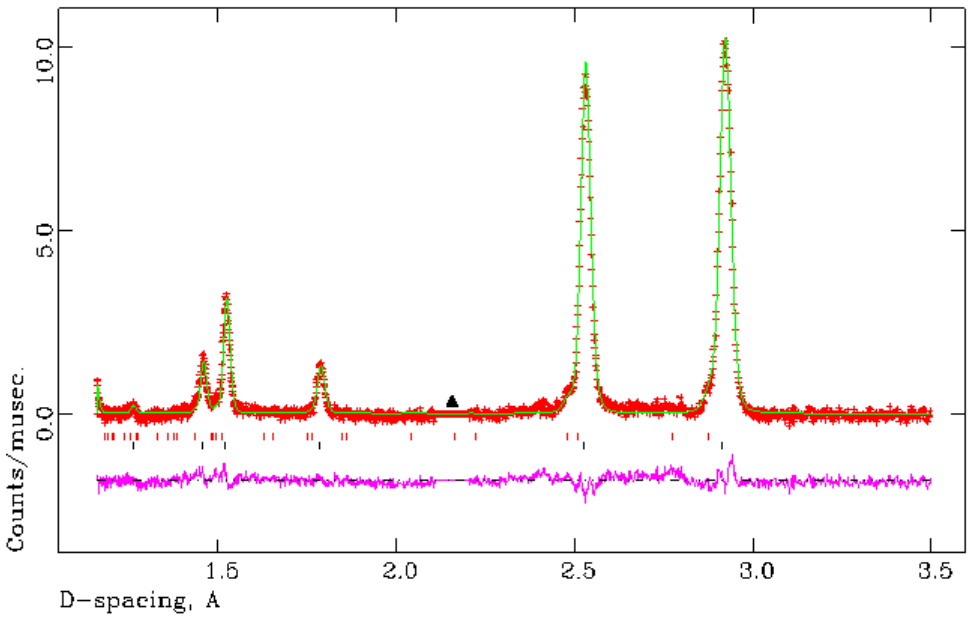

Figure 4-17: Observed, calculated and difference (OCD) plot from structural refinement of sample 22 (Li_4ND at 773 K) from PND data, 35° (A) bank.
The black tickmarks indicate reflections from cubic Li_4ND and the red the tickmarks indicate reflections from tetragonal Li_4ND. The black triangle indicates reflections from the sample environment (i.e. the furnace and vanadium canister) which have been excluded.

Table 4-14: Atom positions and isotropic temperature factors generated by PND Rietveld refinement of cubic Li_4ND at 773 K.

Atom	Li 1	N 1	D 1
Site	8c	4a	4a
x	0.25	0	0
y	0.25	0	0
z	0.25	0	0
100 x U_{iso} / Å^2	9.86 (14)	4.13 (7)	4.13 (7)
Occupancy	1.00	0.50	0.50

Table 4-15: Atom positions and isotropic temperature factors generated by PND Rietveld refinement for tetragonal Li_4ND at 773 K.

Atom	N 1	D 1	N 2	D 2	Li 1
Site	4a	4a	4b	4b	16f
x	0	0	0	0	0.200065
y	0.25	0.25	0.25	0.25	0.454321
z	0.125	0.125	0.625	0.625	0.280127
100 x U_{iso} / Å^2	2.50	2.50	2.50	2.50	2.50
Occupancy	0.95	0.05	0.05	0.95	1.00

Figure 4-18 illustrates the effect that increasing temperature has on the Li_4ND phases within the material during PND experiments. As discussed previously, both tetragonal Li_4ND (1) and cubic Li_4ND (1′) are present in the samples. As the temperature increases, a gradual phase transformation occurs and the cubic phase becomes more apparent at higher temperatures. Data collected at 773 K shows a clear intense peak (magenta) corresponding to a cubic phase. Further confirmation is shown in Figure 4-19. The Rietveld method has also been applied to data collected at 523 K and 673 K and the results obtained are presented in the appendix.

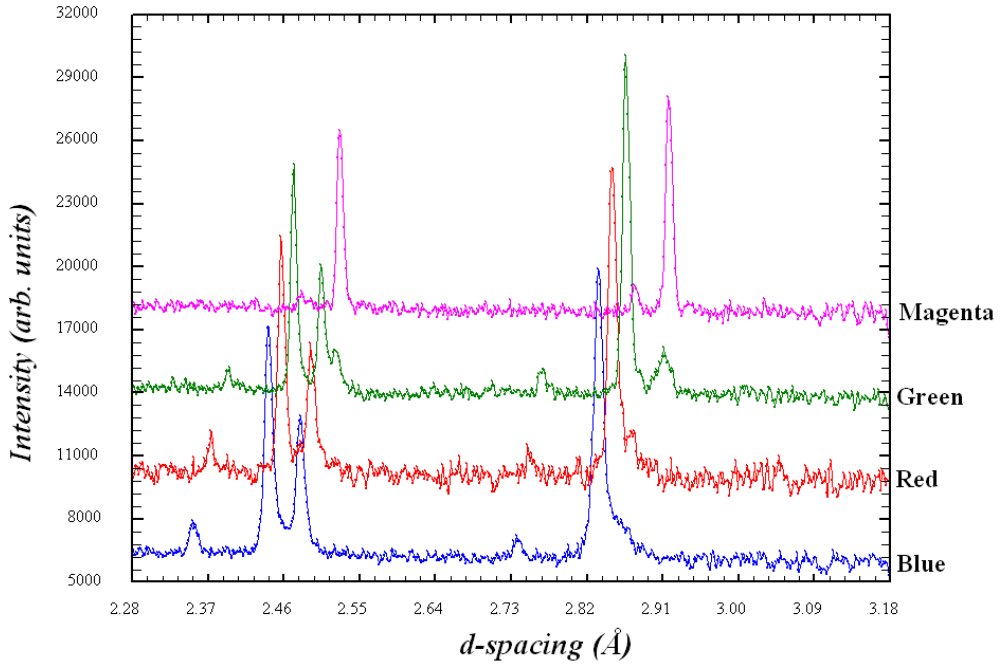

Figure 4-18: Comparison of Li4ND (1) and Li4ND (1′) phases with varying temperatures at high *d*-spacing.

Blue – 323K, red – 523 K, green – 673 K and magneta – 773 K.

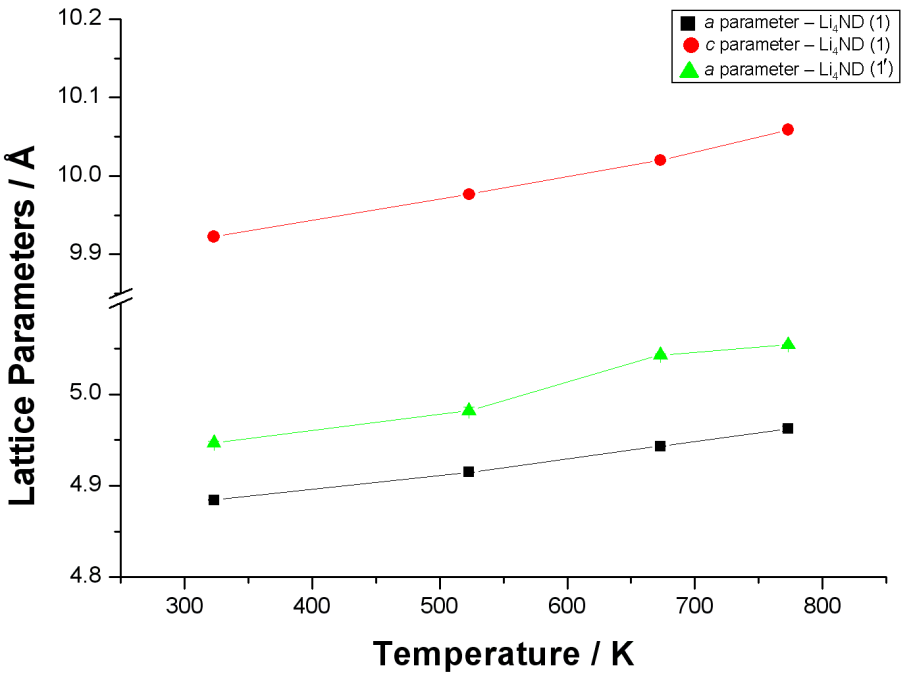

Figure 4-19: Variation of lattice parameters versus temperature of Li_4ND (1) and Li_4ND (1′) with errors of 3-sigma.

Table 4-16 - Table 4-19 show a comparison of interatomic distances and angles obtained from Li_4ND refinements at 323 and 773 K with the values reported in the literature at 293 K. 4, 9, [14] For Li_4ND (1), the values recorded at 323 K deviate slightly from those reported by Marx. The lithium coordination environment within Li_4ND is distorted and illustrated in Figure 4-20. On increasing the temperature to 773 K, the Li-N1/D1 and Li-N2/D2 bonds elongate. This has a subsequent effect on the bond angles which can be recognised from the data presented below. From Table 4-16 and Table 4-17, for the Li-N1/D1 and Li-N2/D2 interatomic distances, the data presented suggests that two effects are present; thermal expansion and a change in the anion distribution from approximate full occupancies of the N1 and D2 sites to one site that is 50% occupied by N and 50 % occupied by D. The literature values employed for comparison for the interatomic distances and bond angles to cubic-Li_4ND phase are based on the Li_2ND type model proposed by Balogh et al. [14]

With regards to Li_4ND (1'), although the interatomic distances are shorter in this work at 323 K and also at 773 K in comparison to those stated in the literature, this is a reflection of the cell size as the lattice parameters are smaller in this work (at 323 K, a = 4.9467 (6) Å, at 773 K, a = 5.0542 (2) Å) than those reported in the literature (at 293 K, a = 5.09187 Å). [14]

A comparison of this system to that of Ba_2NF may be drawn in regards to the distribution of anions (in the latter case nitride and fluoride as opposed to nitride and hydride) within the structure. [15] The low temperature phase exhibits ordering of the anions, i.e. the N site is exclusively occupied by N. At high temperature, a phase transformation occurs resulting in the formation of cubic-Ba_2NF where the cubic phase displays a disordered anion distribution over a single N/F site.

Table 4-16: Comparison of interatomic distances in Li_4ND (1) between the literature values and those obtained from Rietveld refinements of PND data at 323 and 773 K.

Interatomic distance / Å	Li_4ND		
	Literature (Tetragonal) [4]	Tetragonal	Tetragonal
	293 K	323 K	773 K
Li1-N1/D1	4x 2.0717	4x 2.084 (3)	4x 2.1092 (5)
	4x 2.0393	4x 2.026 (6)	4x 2.0382 (3)
Li1-N2/D2	4x 1.9556	4x 1.953 (6)	4x 2.0123 (2)

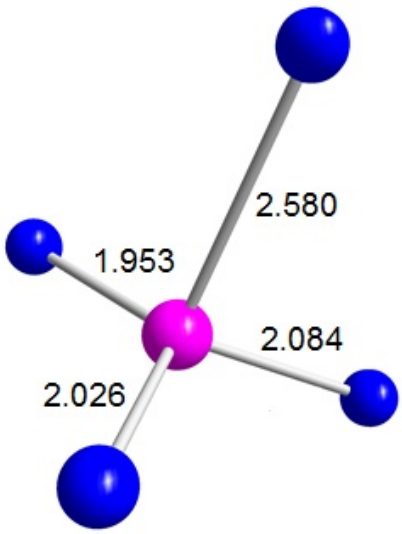

Figure 4-20: Bond coordination environment of the LiN4 tetrahedron in tetragonal Li_4ND based on the interatomic distances obtained from Rietveld refinement of PND data at 323 K (Li^+ - pink, N^{3-} - blue).

Table 4-17: Comparison of interatomic distances in Li_4ND (1′) between the literature valuesand those obtained from Rietveld refinements of PND data at 323 and 773 K.

Interatomic distance / Å	Li_4ND		
	Literature (Cubic) [14]	Cubic	Cubic
	293 K	323 K	773 K
Li1-N1/D1	2.2049	2.1420 (2)	2.18852 (5)

Table 4-18: Comparison of bond angles within Li_4ND (1) obtained from Rietveld refinements of PND data collected at 323 and 773 K.

Bond Angles / °	Li_4ND		
	Literature (Tetragonal) [4]	Tetragonal	Tetragonal
	293 K	323 K	773 K
Li1-N1/D1-Li1	4x 75.482	4x 75.8 (1)	4x 76.18 (2)
	12x 76.017	12x 75.6 (1)	12x 76.01 (2)
	8x 123.665	8x 123.60 (7)	8x 123.18 (1)
	3x 158.192	3x 158.1 (1)	3x 158.689 (1)
	2x 83.762	2x 83.9 (1)	2x 84.57 (2)
	6x 64.144	6x 64.3 (3)	6x 63.192 (9)
	6x 102.282	6x 102.16 (9)	6x 102.664 (8)
Li1-N2/D2-Li1	3x 102.282	3x 103.1 (1)	3x 102.99 (10)
	1x 123.665	1x 123.1 (2)	1x 123.38 (20)

Table 4-19: Comparison of bond angles within Li_4ND (1′) obtained from Rietveld refinements of PND data collected at 323 and 773 K.

Bond Angles / °	Li_4ND		
	Literature (Cubic) [14]	Cubic	Cubic
	293 K	323 K	773 K
Li1-N1/D1-Li1	3x 54.7356 3x 125.2644	3x 54.736 (1) 3x 125.264 (1)	3x 54.736 (1) 3x 125.264 (1)
Li-Li-Li	4x 90.0 (0)	4x 90.0 (0)	4x 90.0 (0)

4.3.4.2 Variable temperature study of Li_2ND

The second PND study involved collecting data at 313 and 773 K to determine the effects of temperature on the structure of Li_2ND. Rietveld refinement of sample **23** (Li_2ND at 313 K) highlighted that the lattice parameters vary from that reported in the literature by Balogh *et al* [14] where a = 5.09187 Å (at 400 K). Selected Rietveld refinement data collected at 313 K are presented in Table 4-20 and the observed, calculated and difference (OCD) plots are shown in Figure 4-21, Figure 4-22 and Figure 4-23. The atomic positions and isotropic temperature factors are presented in Table 4-21.

Table 4-20: Selected Rietveld refinement data from the PND refinement of sample 23 (Li_2ND at 313 K).

Empirical Formula	Li_2ND
Collection temperature / K	313
Crystal system	Cubic
Space Group	*Fm-3m*
Lattice parameters / Å	a = 5.05320 (9)
V / Å ^{3}	129.033 (4)
Z	4
Unit cell formula weight, M_w	119.599
Density / g/cm^3	1.539
No. of varied parameters	52
No. of observations	11798
R_{wp}	0.0148
R_p	0.0360
χ^2	0.9797

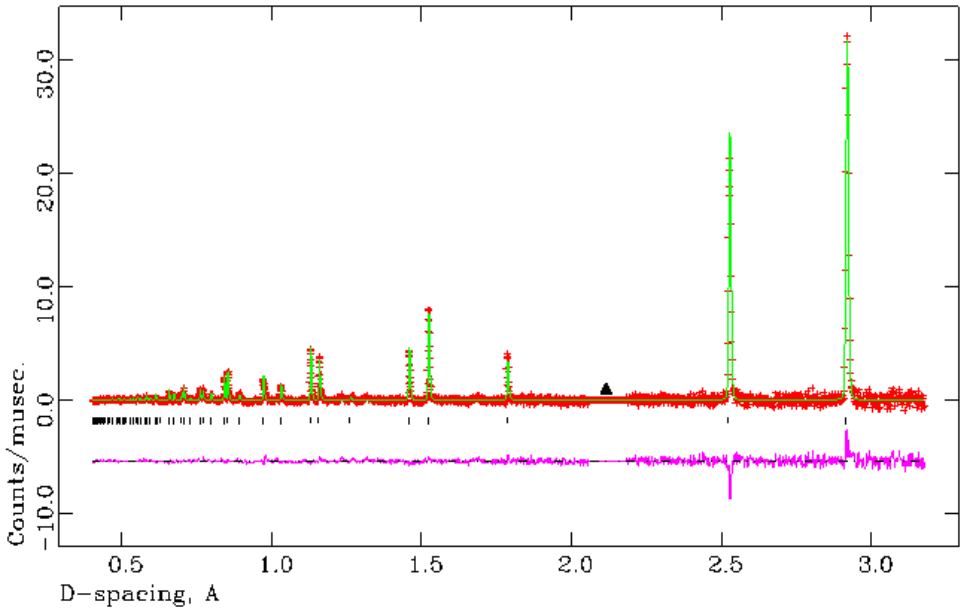

Figure 4-21: Observed, calculated and difference (OCD) plot from structural refinement of sample 23 (Li_2ND at 313 K) from PND data, 145° (C) bank.
The black tickmarks indicate reflections from Li_2ND. The black triangle indicates reflections from the sample environment (i.e. the furnace and vanadium canister), both of which have been excluded.

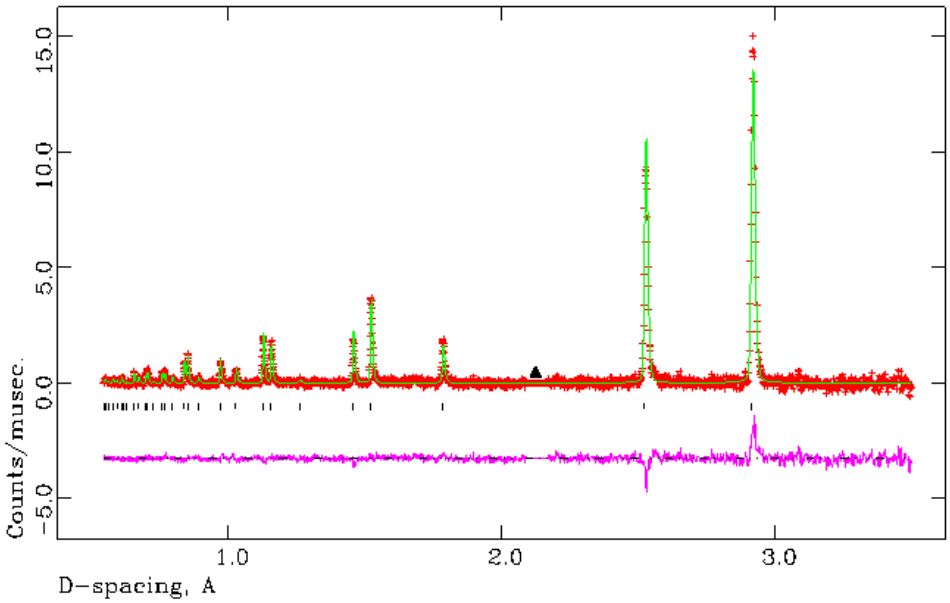

Figure 4-22: Observed, calculated and difference (OCD) plot from structural refinement of sample 23 (Li_2ND at 313 K) from PND data, 90° (E) bank.
The black tickmarks indicate reflections from Li_2ND. The black triangle represents reflections from the sample environment (i.e. the furnace and vanadium canister), which have been excluded.

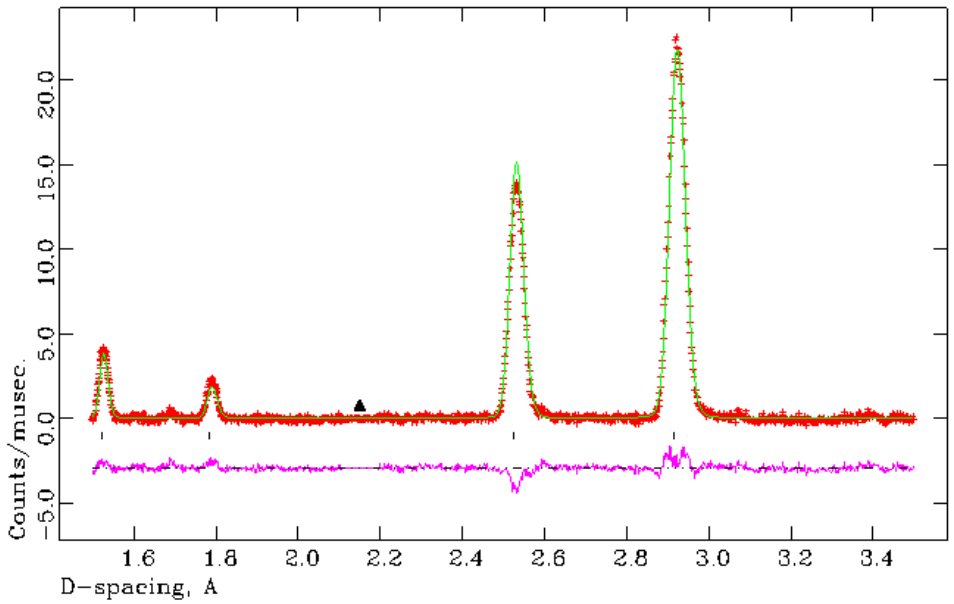

Figure 4-23: Observed, calculated and difference (OCD) plot from structural refinement of sample 23 (Li_2ND at 313 K) from PND data, 35° (A) bank.
The black tickmarks indicate reflections from Li_2ND. The black triangle represents reflections from the sample environment (i.e. the furnace and vanadium canister), which have been excluded.

Table 4-21: Atom positions and isotropic temperature factors generated by PND Rietveld refinement of Li_2ND at 313 K.

Atom	Li 1	N 1	D 2
Site	8c	4a	192l
x	0.25	0	0.1378 (13)
y	0.25	0	0.0957 (14)
z	0.25	0	0.0559 (11)
100 x U_{iso} / Å^2	4.71 (6)	1.98 (2)	3.71 (16)
Occupancy	1.00	1.00	0.0208

In order to determine the stability of cubic Li_2ND and understand the role it plays in experiments with Li_4ND at higher temperature, additional data were collected at 773 K. The observed, calculated and difference plots for data collected at 773 K are presented in Figure 4-24, Figure 4-25 and Figure 4-26. Table 4-22 shows selected Rietveld refinement data collected for sample 24 Li_2ND at 773 K and Table 4-23 displays the atomic positions and isotropic temperature factors.

Table 4-22: Selected Rietveld refinement data from the PND refinement of sample 24 (Li_2ND at 773 K).

Empirical Formula	Li_2ND
Collection temperature / K	773
Crystal system	Cubic
Space Group	*Fm-3m*
Lattice parameters / Å	a = 5.1661 (3)
V / Å ^{3}	137.88 (1)
Z	4
Unit cell formula weight, M_w	119.599
Density / g/cm^3	1.440
No. of varied parameters	45
No. of observations	11962
R_{wp}	0.0200
R_p	0.0655
χ^2	0.6517

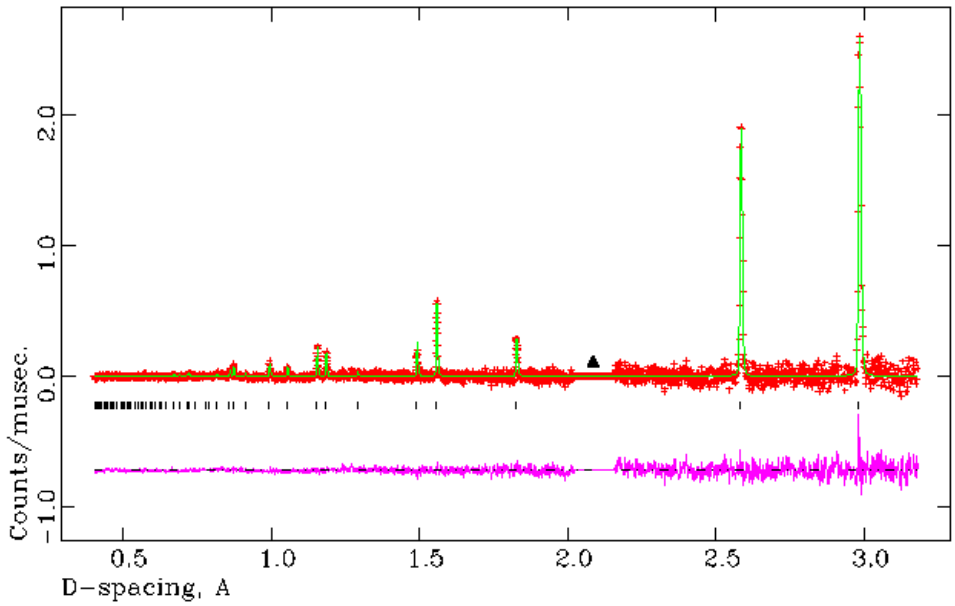

Figure 4-24: Observed, calculated and difference (OCD) plot from structural refinement of sample 24 (Li_2ND at 773 K) from PND data, 145° (C) bank.

The black tickmarks indicate reflections from Li_2ND. The black triangle represents reflections from the sample environment (i.e. the furnace and the vanadium canister) which have been excluded.

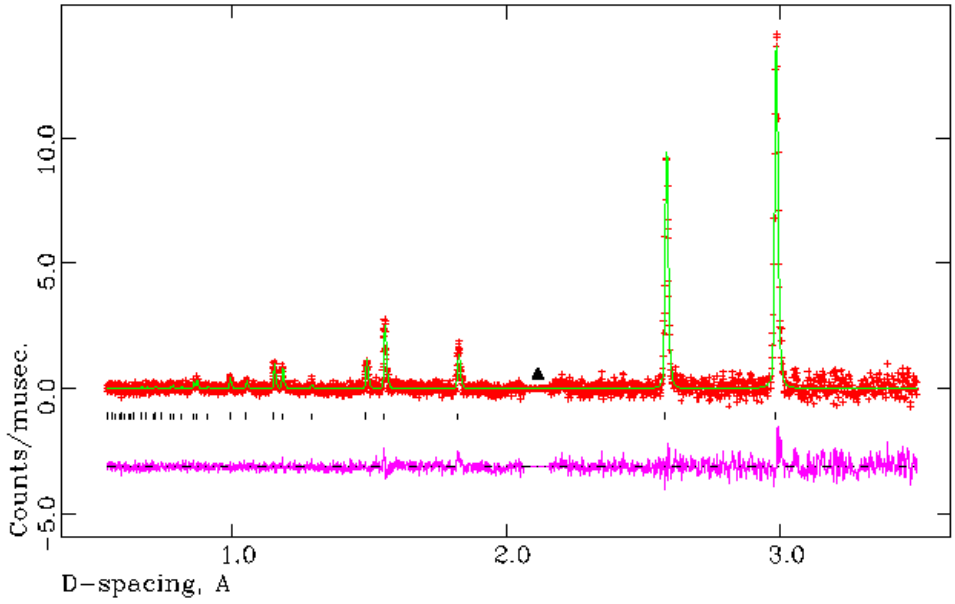

Figure 4-25: Observed, calculated and difference (OCD) plot from structural refinement of sample 24 (Li_2ND at 773 K) from PND data, 90° (E) bank.

The black tickmarks indicate reflections from Li_2ND. The black triangle represents reflections from the sample environment (i.e. the furnace and the vanadium canister) which have been excluded.

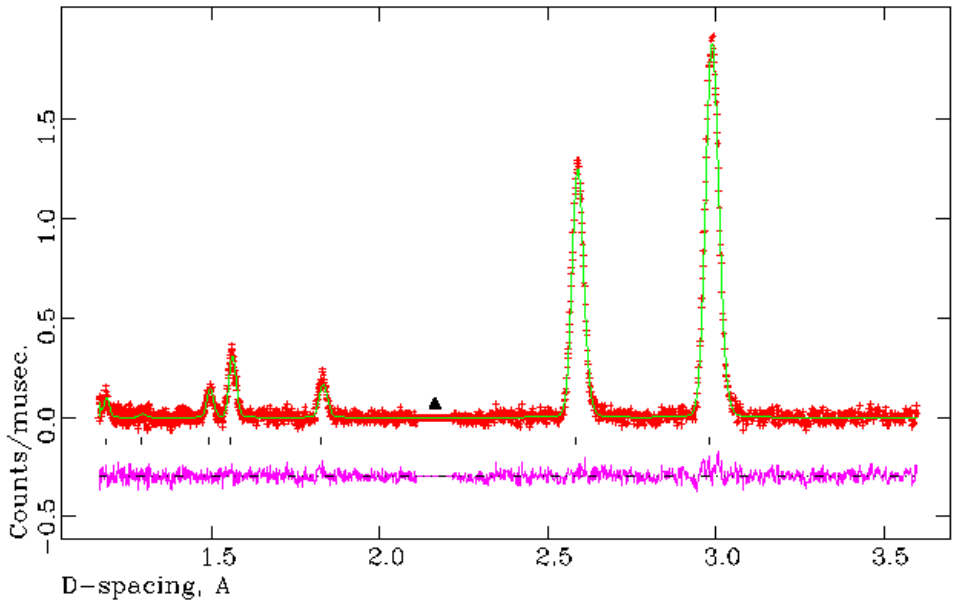

Figure 4-26: Observed, calculated and difference (OCD) plot from structural refinement of sample 24 (Li_2ND at 773 K) from PND data, 35° (A) bank.
The black tickmarks indicate reflections from Li_2ND. The black triangle denotes the sample environment which has been excluded.

Table 4-23: Atom positions and isotropic temperature factors generated by PND Rietveld refinement of Li_2ND at 773 K.

Atom	Li 1	N 1	D 2
Site	8c	4a	192l
x	0.25	0	0.134 (4)
y	0.25	0	0.080 (5)
z	0.25	0	0.054 (6)
100 x U_{iso} / Å^2	4.4 (2)	2.5 (1)	5.6 (7)
Occupancy	1.00	1.00	0.0208

Table 4-24 shows a comparison of interatomic distances obtained from Li_2ND refinements at 313 and 773 K however the values obtained from Rietveld refinements vary from those reported by Balogh *et al*. [14] On increasing temperature, the bond lengths elongate with the exception of N-D which appears to contract on initial inspection. However, it is notable that the error on the N-D bond length at higher temperature is large and therefore within the 3σ distribution, the bond length could vary from 0.79 to 0.91. As a result, it is difficult to state precisely whether the bond length increases or decreases as a function of

temperature. The bond angles generated by Rietveld refinement are presented in the appendix.

Table 4-24: Comparison of interatomic distances in Li_2ND at 313 and 773 K obtained from PND Rietveld refinements.

	Temperature	
Interatomic distance / Å	**313**	**773**
6x N-D	0.894 (5)	0.85 (2)
4x N-Li	2.18810 (3)	2.23700 (8)
6x Li-Li	2.52660 (5)	2.5831 (1)

4.3.4.3 PND study of non-stoichiometric samples of nitride hydride-imides

A third PND experiment was conducted involving an investigation into the ability of non-stoichiometric mixtures of Li_4ND and Li_2ND to form a 'quasi-imide' phase based on Equation 4 below:

$$(1\text{-}x)Li_4ND + xLi_2ND \rightarrow Li_{4-2x}N_{1-x}D_{1-x}(ND)_x \quad (4)$$

where x = 0.36, 0.5 and 0.6 for samples **25**, **27** and **29** at 313 K and samples **26**, **28** and **30** for data collected at 773 K respectively. Data were collected at 313 or 323 K to ensure no impurities of the starting materials were present before heating to 773 K in attempt to synthesise a 'quasi-imide' phase *in-situ*. Since the quality of data collected was relatively poor, the stoichiometric values obtained experimentally by Rietveld refinement may vary from those stated theoretically (Table 4.6). The structural model for the 'quasi-imide' phase is based on a cubic model in the *Fm-3m* space group reported by Balogh *et al*. [14] Information for Table 4.25 which displays theoretical parameters for the quasi-imide model was provided by Dr. D. J. Bull and Dr. R. I. Smith and in order to balance the charge, the lithium lattice must be fully occupied. This enabled values in Table 4.26 to be calculated. According to this model, site occupancies are displayed in Table 4.25 with calculated occupancies from mixtures where x = 0.36, 0.5 and 0.6 (corresponding to samples displayed in Table 4.6).

Table 4-25: Overview of Wyckoff positions, species per unit cell and occupancies for atoms within 'quasi-imide' phase.

Species	Wyckoff position	Species per unit cell	Occupancy
Li^+	8c	2	1
N^{3-}	4a	$\frac{1-x}{2-x}$	$\frac{1-x}{2-x}$
D^-	4a	$\frac{1-x}{2-x}$	$\frac{1-x}{2-x}$
N in ND^{2-}	4a	$\frac{x}{2-x}$	$\frac{x}{2-x}$
D in ND^{2-}	192l	$\frac{x}{2-x}$	$\frac{1}{48}\cdot\frac{x}{2-x}$

An additional D atom was added to the refinement, in comparison to an ideal imide model. The D atom was added on the same site as N as Equation 4 shows that N^{3-}, D^- and $(ND)^{2-}$ atoms are present in the resultant phase. Since N^{3-}, D^- and N of $(ND)^{2-}$ are all located on the same site, the total occupancy must equal 1 (Table 4.26). With regards to the occupancy of the protonic D position for $(ND)^{2-}$, on multiplying the occupancy by the site multiplicity, the average number of imide ions per unit cell results, which is between 0 and 4 (Table 4.25) corresponding to an x value of between 0 and 1.

Table 4-26: Theoretical parameters for the quasi-imide model

Sample	x	Li^+ (8c)	N^{3-} + N of $(ND)^{-2}$ (4a)	D^- (4a)	D of $(ND)^{2-}$ (192l)
26	0.36	1	0.6098	0.3902	0.0046
28	0.5	1	0.6667	0.3333	0.0069
30	0.6	1	0.7143	0.2857	0.0089

4.3.4.3.1 (1-x)Li_4ND + xLi_2ND→ $Li_{4-2x}N_{1-x}D_{1-x}(ND)_x$ (where x = 0.36)

Firstly samples **25** and **26** (where x = 0.36) were investigated at 313 K and then at an elevated temperature of 773 K respectively. Selected Rietveld refinement data, collected at 313 K, are displayed in Table 4.27 and the observed calculated and difference plots for the data are presented in Figures 4.27, 4.28 and 4.29.

Table 4-27: Selected Rietveld refinement data from the PND refinement of sample 25 (where x=0.36) at 313 K.

Empirical Formula	Li_4ND (1)	Li_2ND	Li_4ND (1′)
Collection temperature / K		313	
Crystal system	Tetragonal	Cubic	Cubic
Space Group	*I* $4_1/a$	*Fm-3m*	*Fm-3m*
Lattice parameters / Å	*a* = 4.8858 (1)	*a* = 5.0617 (1)	*a* = 4.9543 (9)
	c = 9.9274 (4)	-	-
V / Å ^{3}	236.97 (1)	129.683 (5)	121.61 (4)
Z	4	4	2
Unit cell formula weight, M_w	175.140	119.599	87.570
Density / (g/cm^3)	1.227	1.531	1.196
wt. %	54.253 (4)	30.016 (4)	15.731 (7)
No. of varied parameters		80	
No. of observations		11523	
R_{wp}		0.0104	
R_p		0.0222	
χ^2		1.457	

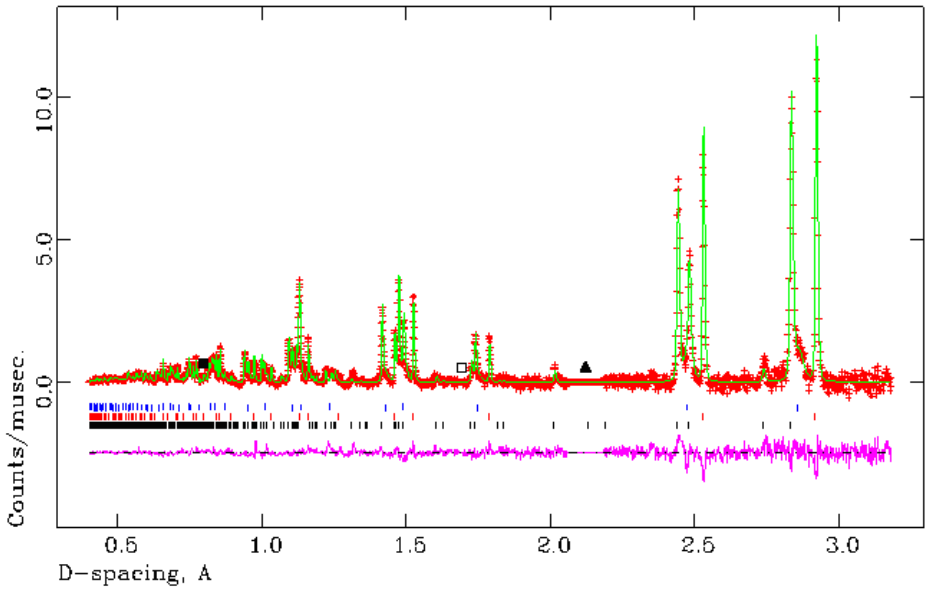

Figure 4-27: Observed, calculated and difference (OCD) plot from structural refinement of data collected from the 145 ^{o} (C) detector bank for sample 25 at 313 K from PND data.
The black tickmarks indicate reflections from tetragonal Li_4ND, the red tickmarks indicate reflections from Li_2ND and the blue tickmarks indicate reflections from cubic Li_4ND. The black square indicates a reflection from LiD, the open square indicates a reflection from $LiND_2$ and the black triangle indicates reflections from the sample environment (i.e. the furnace and the vanadium canister), all of which have been excluded.

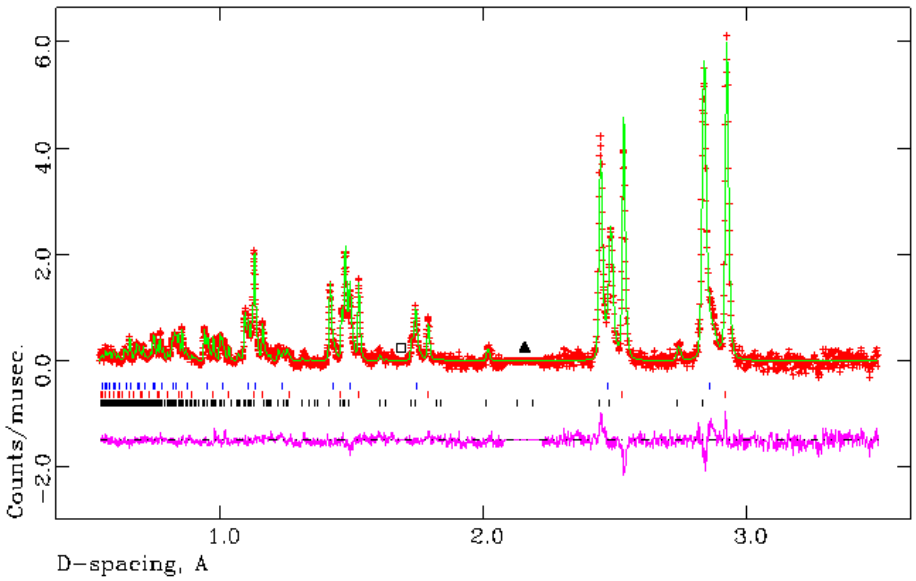

Figure 4-28: Observed, calculated and difference (OCD) plot from structural refinement of data collected from the 90 ^{o} (E) detector bank for sample 25 at 313 K from PND data.
The black tickmarks indicate reflections from tetragonal Li_4ND, the red tickmarks indicate reflections from Li_2ND and the blue tickmarks indicate reflections from cubic Li_4ND. The open square indicates a reflection from $LiND_2$ and the black triangle indicates reflections from the sample environment (i.e. the furnace and the vanadium canister), all of which have been excluded.

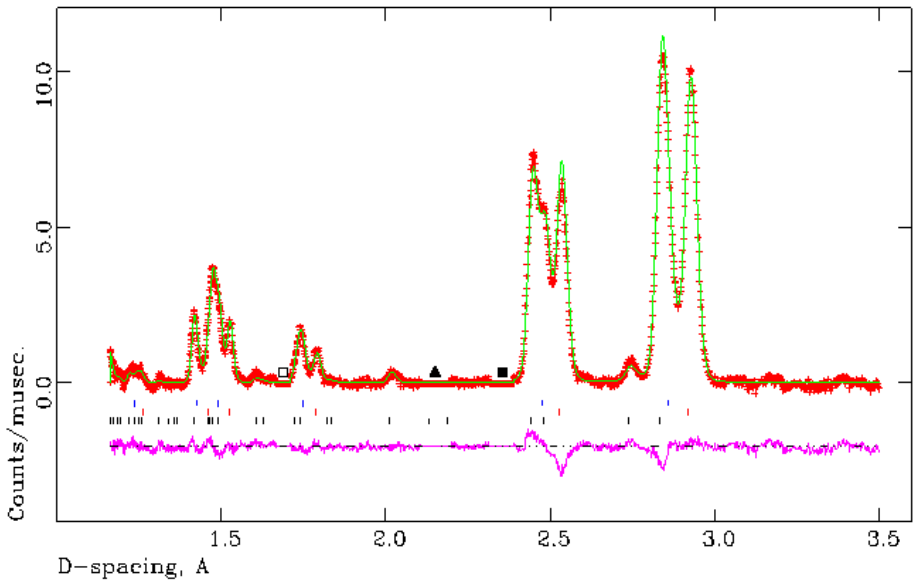

Figure 4-29: Observed, calculated and difference (OCD) plot from structural refinement of data collected from the 35 ° (A) detector bank for sample 25 at 313 K from PND data.
The black tickmarks indicate reflections from tetragonal Li_4ND, the red tickmarks indicate reflections from Li_2ND and the blue tickmarks indicate reflections from cubic Li_4ND. The black square indicates a reflection from LiD, the open square indicates a reflection from $LiND_2$ and the black triangle indicates reflections from the sample environment (i.e. the furnace and the vanadium canister), all of which have been excluded.

Atomic positions and anisotropic temperature factors for Li_4ND (1) are displayed in Table 4.28. With regard to Li_4ND (1), N and D were varied anisotropically and Li was varied isotropically. The fractional occupancies of Li_4ND (1) could not be refined however after a trial and error approach, the occupancies were eventually fixed in agreement with those reported by Marx. [4] Atomic positions and isotropic temperature factors for Li_2ND and Li_4ND (1′) are presented in Tables 4.29 and 4.30 respectively. In terms of the Li_2ND phase, N, D and Li were refined isotropically; the same is true for the atoms within cubic Li_4ND (1′).

Table 4-28: Atom positions and anisotropic temperature factors generated by PND Rietveld refinement for the main Li_4ND (1) phase in sample 25 at 313 K.

Atom	N 1	D 1	N 2	D 2	Li 1
Site	4a	4a	4b	4b	16f
x	0	0	0	0	0.1967 (14)
y	0.25	0.25	0.25	0.25	0.4524 (15)
z	0.125	0.125	0.625	0.625	0.2806 (4)
100 x U_{iso} / Å^2	-	-	-	-	1.33 (6)
100 x U_{11} / Å^2	1.12 (4)	1.12 (4)	2.27 (9)	2.32 (9)	-
100 x U_{22} / Å^2	1.12 (4)	1.12 (4)	2.27 (9)	2.32 (9)	-
100 x U_{33} / Å^2	0.76 (5)	0.76 (5)	4.49 (16)	4.49 (16)	-
100 x U_{12} / Å^2	0	0	0	0	-
100 x U_{13} / Å^2	0	0	0	0	-
100 x U_{23} / Å^2	0	0	0	0	-
Occupancy	0.95	0.05	0.05	0.95	1.00

Table 4-29: Atom positions and isotropic temperature factors generated by PND Rietveld refinement of Li_2ND in sample 25 at 313 K.

Atom	Li 1	N 1	D 2
Site	8c	4a	192l
x	0.25	0	0.138 (2)
y	0.25	0	0.098 (2)
z	0.25	0	0.059 (2)
100 x U_{iso} / Å^2	5.07 (12)	1.87 (3)	3.8 (2)
Occupancy	1.00	1.00	0.0208

Table 4-30: Atom positions and isotropic temperature factors generated by PND Rietveld refinement for the Li_4ND (1′) phase in sample 25 at 313 K.

Atom	Li 1	N 1	D 1
Site	8c	4a	4a
x	0.25	0	0
y	0.25	0	0
z	0.25	0	0
100 x U_{iso} / Å^2	6.2 (4)	1.17 (7)	1.17 (7)
Occupancy	1.00	0.50	0.50

In an attempt to synthesise a quasi-imide, which is based on a cubic *anti*-fluorite structure, the temperature was increased markedly to 773 K (sample **26**). In accordance with the findings of Weidner *et al*, [2] Li_4ND and Li_2ND form a solid solution resulting in the formation of the 'quasi-imide' phase. Simplification of the doubled tetragonal ordered *anti*-fluorite structure of Li_4ND to the disordered simple *anti*-fluorite structure of Li_2ND allows for the formation of a solid solution due to structural similarities in which a modified imide-phase results. Previous to reports based on 'quasi-imides', Marx identified a reaction pathway involving Li_4NH and Li_2NH [4] which was reported to result in the formation of *anti*-fluorite type structures in addition to composition-dependent lattice parameters. These initial reports offer a foundation for the findings of Weidner *et al* [2] and this work.

A modified cubic form of a Li_2ND type [14] was used as a starting model for Rietveld refinement. It should be noted that only data from the 145^o (C) detector bank could be used for analysis for this particular sample at 773 K. Data sets from this detector bank were combined to enable a Rietveld refinement to be performed as data were collected for an insufficient period of time due to problems with the beam. Selected Rietveld refinement data are presented in Table 4.31 and the observed, calculated and difference plot is shown in Figure 4.30.

Table 4-31: Selected Rietveld refinement data from the PND refinement of sample 26 (where x = 0.36) at 773 K.

Empirical Formula	$Li_{4-2x}N_{1-x}D_{1-x}(ND)_x$
Collection temperature / K	773
Crystal system	Cubic
Space Group	*Fm-3m*
Lattice parameters / Å	a = 5.0811 (3)
V / Å ^{3}	131.183 (8)
Unit cell formula weight, M_w	94.616
Density / (g/cm^3)	1.198
No. of varied parameters	20
No. of observations	3851
R_{wp}	0.0055
R_p	0.0124
χ^2	0.9273

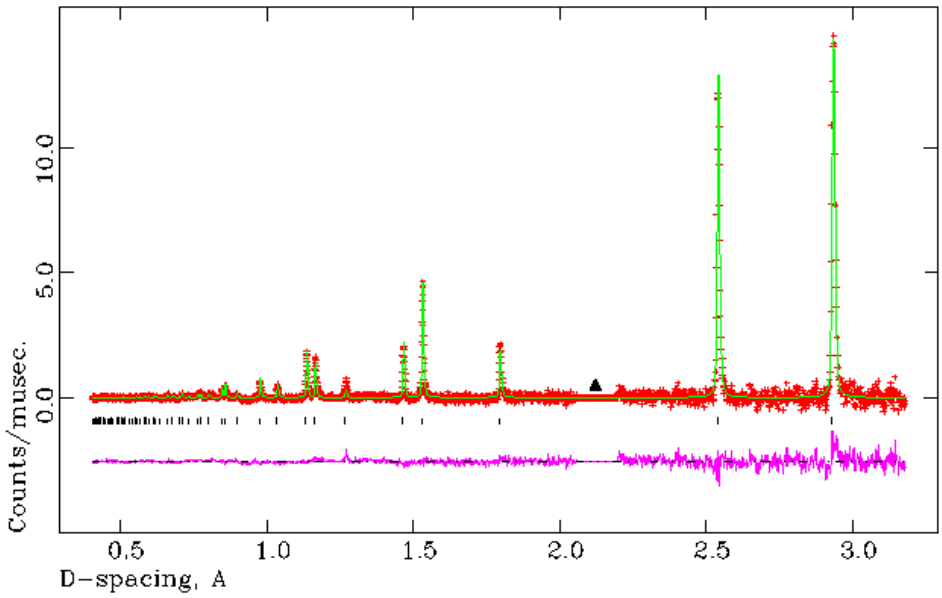

Figure 4-30: Observed, calculated and difference (OCD) plot from structural refinement of data collected from the 145 ° (C) detector bank for sample 26 at 773 K from PND data.
The black tickmarks indicate reflections from the quasi-imide phase. The black triangle indicates reflections from the sample environment (i.e. the furnace and the vanadium canister) which have been excluded.

Atomic positions and isotropic temperature factors are presented in Table 4.32. The thermal parameters for the N and D atoms located on the 4a site were varied isotropically, as were the parameters for the Li atom on the 8c site. Due to the low occupancy of D on site 192l site, the thermal parameter could not be freely refined therefore was fixed at a sensible value in accordance with refined values for Li and N1/D1. Unfortunately, the fractional occupancies could not be varied and therefore were fixed at theoretical values (Table 4.26).

Table 4-32: Atom positions and isotropic temperature factors generated by PND Rietveld refinement of sample 26 at 773 K.

Atom	Li 1	N 1	D1	D 2
Site	8c	4a	4a	192l
x	0.25	0	0	0.139 (10)
y	0.25	0	0	0.092 (12)
z	0.25	0	0	0.055 (11)
100 x U_{iso} / Å^2	8.53 (21)	3.37 (9)	3.37 (9)	5.50
Occupancy	1.00	0.6098	0.3902	0.0046

4.3.4.3.2 (1-x)Li_4ND + xLi_2ND → $Li_{4-2x}N_{1-x}D_{1-x}(ND)_x$ (where x = 0.5)

Samples **27** and **28** (where x = 0.5) were studied at 323 and 773 K respectively to investigate further the effects of stoichiometry and temperature on the formation of a quasi-imide phase. Firstly, a model collected at 323 K was refined against data using the Rietveld method and selected data are presented in Table 4.33. Representations of the observed, calculated and difference plots are shown in Figures 4.31, 4.32 and 4.33. It should be noted that there is a slight LiD impurity present in this sample which has been highlighted in the figures below.

Table 4-33: Selected Rietveld refinement data from the PND refinement of sample 27 (x=0.5) at 323 K.

Empirical Formula	Li_4ND (1)	Li_2ND	Li_4ND (1′)
Collection temperature / K		323	
Crystal system	Tetragonal	Cubic	Cubic
Space Group	*I* $4_1/a$	*Fm-3m*	*Fm-3m*
Lattice parameters / Å	*a* = 4.8892 (2)	*a* = 5.0669 (1)	*a* = 4.9531 (11)
	c = 9.9283 (7)	-	-
V / Å ^{3}	237.33 (2)	130.088 (6)	121.51 (5)
Z	4	4	2
Unit cell formula weight, M_w	175.140	119.599	87.570
Density / (g/cm^3)	1.225	1.527	1.196
Wt. %	35.977 (5)	41.559 (5)	22.464 (8)
No. of varied parameters		77	
No. of observations		11495	
R_{wp}		0.0146	
R_p		0.0344	
χ^2		0.9908	

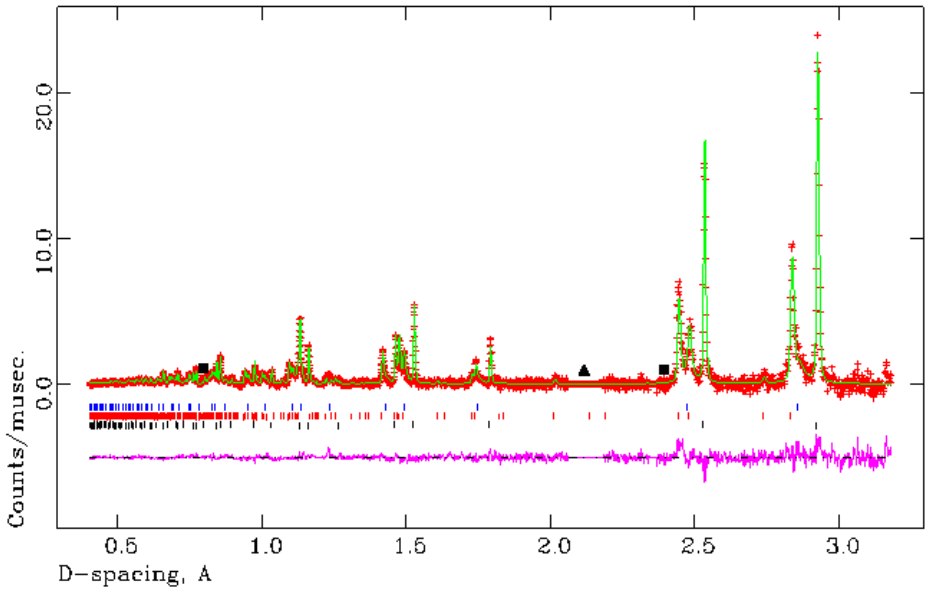

Figure 4-31: Observed, calculated and difference (OCD) plot from structural refinement of data collected from the 145 ° (C) detector bank for sample 27 at 323 K from PND data.
The black tickmarks indicate reflections from Li_2ND, the red tickmarks indicate reflections from Li_4ND (1) and the blue tickmarks indicate reflections from Li_4ND (1′). The black squares indicates reflections from LiD and the black triangle indicate reflections from the sample environment (i.e. the furnace and the vanadium canister), all of which have been excluded.

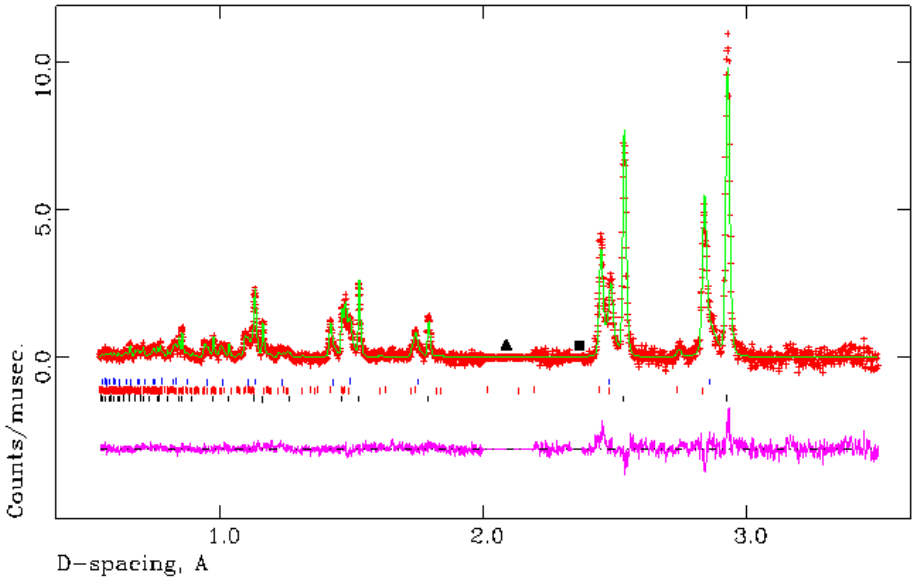

Figure 4-32: Observed, calculated and difference (OCD) plot from structural refinement of data collected from the 90 ° (E) detector bank for sample 27 at 323 K from PND data.
The black tickmarks indicate reflections from Li_2ND, the red tickmarks indicate reflections from Li_4ND (1) and the blue tickmarks indicate reflections from Li_4ND (1′). The black square indicates a reflection from LiD and the black triangle indicate reflections from the sample environment (i.e. the furnace and the vanadium canister), all of which have been excluded.

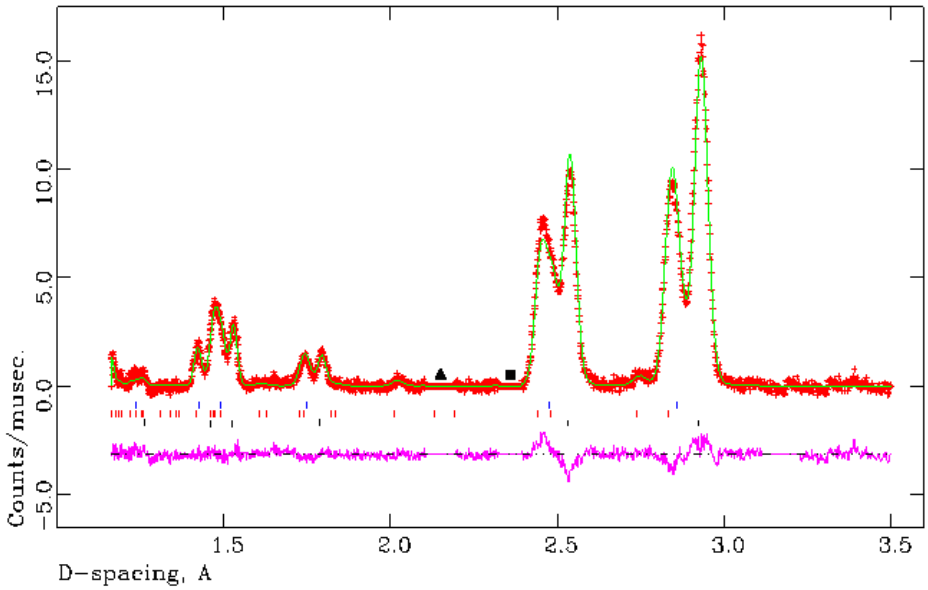

Figure 4-33: Observed, calculated and difference (OCD) plot from structural refinement of data collected from the 35 ° (A) detector bank for sample 27 at 323 K from PND data. The black tickmarks indicate reflections from Li_2ND, the red tickmarks indicate reflections from Li_4ND (1) and the blue tickmarks indicate reflections from Li_4ND (1′). The black squares indicates reflections from LiD and the black triangle indicate reflections from the sample environment (i.e. the furnace and the vanadium canister), all of which have been excluded.

Atomic positions and anisotropic temperature factors for Li_4ND (1) are presented in Table 4-35. The thermal parameters for the N and D atoms of Li_4ND (1) were refined anisotropically. The thermal parameter of Li could only be refined isotropically since when attempting to refine Li anisotropically, the refinement became unstable. The atomic positions and thermal parameters of Li_2ND and Li_4ND (1′) are presented in Table 4-34 and Table 4-36. The thermal parameters of N, D and Li were refined isotropically.

Table 4-34: Atom positions and isotropic temperature factors generated by PND Rietveld refinement of Li_2ND in sample 27 at 323 K.

Atom	Li 1	N 1	D 1
Site	8c	4a	192l
x	0.25	0	0.139 (2)
y	0.25	0	0.094 (2)
z	0.25	0	0.057 (2)
100 x U_{iso} / Å^2	5.6 (1)	2.18 (3)	4.4 (3)
Occupancy	1.00	1.00	0.0208

Table 4-35: Atom positions and anisotropic temperature factors generated by PND Rietveld refinement for Li_4ND (1) in sample 27 at 323 K.

Atom	N 1	D 1	N 2	D 2	Li 1
Site	4a	4a	4b	4b	16f
x	0	0	0	0	0.195 (2)
y	0.25	0.25	0.25	0.25	0.457 (2)
z	0.125	0.125	0.625	0.625	0.2810 (7)
100 x U_{iso} / Å^2	-	-	-	-	1.6 (1)
100 x U_{11} / Å^2	1.25 (6)	1.25 (6)	2.5 (2)	2.5 (2)	-
100 x U_{22} / Å^2	1.25 (6)	1.25 (6)	2.5 (2)	2.5 (2)	-
100 x U_{33} / Å^2	1.2 (1)	1.2 (1)	4.5 (3)	4.5 (3)	-
100 x U_{12} / Å^2	0	0	0	0	-
100 x U_{13} / Å^2	0	0	0	0	-
100 x U_{23} / Å^2	0	0	0	0	-
Occupancy	0.95	0.05	0.05	0.95	1.00

Table 4-36: Atom positions and isotropic temperature factors generated by PND Rietveld refinement for the Li_4ND (1′) phase in sample 27 at 313 K.

Atom	Li 1	N 1	D 1
Site	8c	4a	4a
x	0.25	0	0
y	0.25	0	0
z	0.25	0	0
100 x U_{iso} / Å^2	3.2 (2)	1.57 (9)	1.57 (9)
Occupancy	1.00	0.50	0.50

On heating the sample to 773 K, a new phase was formed (sample **28**). This was modelled on a cubic Li_2ND type phase proposed by Balogh *et al.* [14] Only data from the 145^o (C) detector bank were used for analysis for this particular sample at 773 K. Data sets from this detector bank were combined to enable a Rietveld refinement to be performed as data was

collected for an insufficient period of time due to problems with the beam. Selected Rietveld refinement data is displayed in Table 4-37 and Figure 4.34 is a representation of the observed, calculated and difference plot. Atomic positions and isotropic thermal parameters are displayed in Table 4-38. As previously discussed in Section 4.3.4.3.1, the thermal parameter of D could not be refined.

Table 4-37: Selected Rietveld refinement data from the PND refinement of sample 28 (where x = 0.5) at 773 K.

Empirical Formula	$Li_{4-2x}N_{1-x}D_{1-x}(ND)_x$
Collection temperature / K	773
Crystal system	Cubic
Space Group	*Fm-3m*
Lattice parameters	a = 5.0968 (3)
V / Å ^{3}	132.40 (1)
Unit cell formula weight, M_w	98.235
Density / g/cm^3	1.232
No. of varied parameters	22
No. of observations	3871
R_{wp}	0.0087
R_p	0.0207
χ^2	0.8874

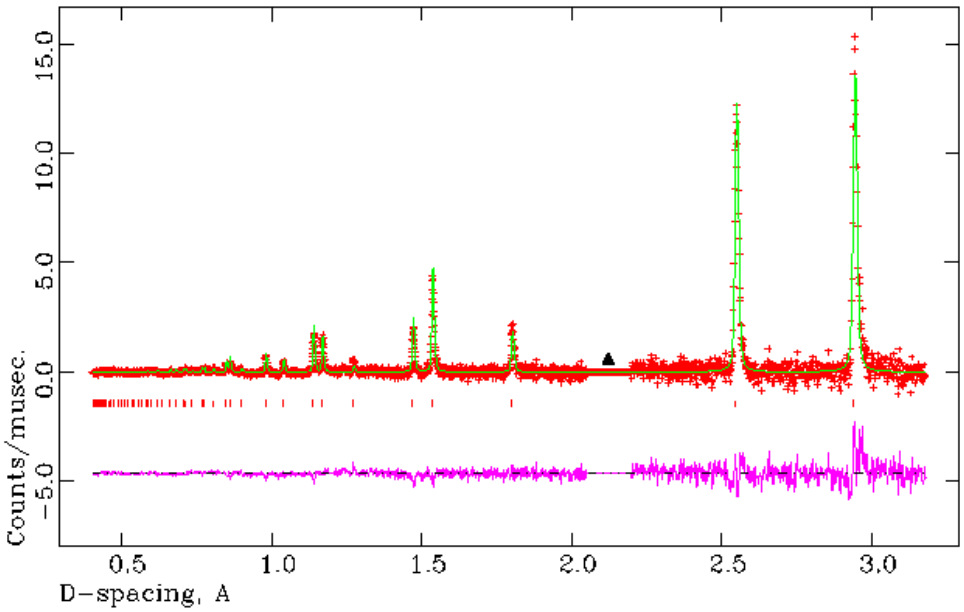

Figure 4-34: Observed, calculated and difference (OCD) plot from structural refinement of data collected from the 145 ° (C) detector bank for sample 28 at 773 K from PND data. The red tickmarks indicate reflections from the quasi-imide phase. The black triangle indicates reflections from the sample environment (i.e the furnace and the vanadium canister) which have been excluded.

Table 4-38: Atom positions and isotropic temperature factors generated by PND Rietveld refinement of sample 28 at 773 K.

Atom	Li 1	N 1	D1	D 2
Site	8c	4a	4a	192l
x	0.25	0	0	0.130 (8)
y	0.25	0	0	0.088 (9)
z	0.25	0	0	0.044 (8)
100 x U_{iso} / Å^2	7.9 (2)	3.79 (8)	3.79 (8)	5.00
Occupancy	1.00	0.6667	0.3333	0.0069

4.3.4.3.3 (1-x)Li_4ND + xLi_2ND → $Li_{4-2x}N_{1-x}D_{1-x}(ND)_x$ (where x = 0.6)

The final samples under investigation were samples **29** and **30** which were based on a mixed sample of non-stoichiometric amounts of Li_4ND and Li_2ND where x = 0.6. PND data were collected at 313 and 773 K. Selected Rietveld refinement data are displayed in Table 4-39 and the observed, calculated and difference plots are shown in Figures 4.35, 4.36 and 4.37. It should be noted that there are two slight impurities in this sample; LiD and $LiND_2$, both of which have been highlighted in the observed, calculated and difference plots below.

Table 4-39: Selected Rietveld refinement data from the PND refinement of sample 29 at 313 K.

Empirical Formula	Li_4ND (1)	Li_2ND	Li_4ND (1′)
Collection temperature / K		313	
Crystal system	Tetragonal	Cubic	Cubic
Space Group	*I* $4_1/a$	*Fm-3m*	*Fm-3m*
Lattice parameters / Å	*a* = 4.8928 (1)	*a* = 5.0696 (1)	*a* = 4.9630 (12)
	c = 9.9360 (8)	-	-
V / Å ^{3}	237.86 (3)	130.294 (6)	122.25 (5)
Z	4	4	2
Unit cell formula weight, M_w	175.140	119.599	87.570
Density / (g/cm^3)	1.223	1.524	1.190
Wt. %	35.947 (5)	51.838 (5)	12.215 (8)
No. of varied parameters		74	
No. of observations		11353	
R_{wp}		0.0180	
R_p		0.0595	
χ^2		0.9895	

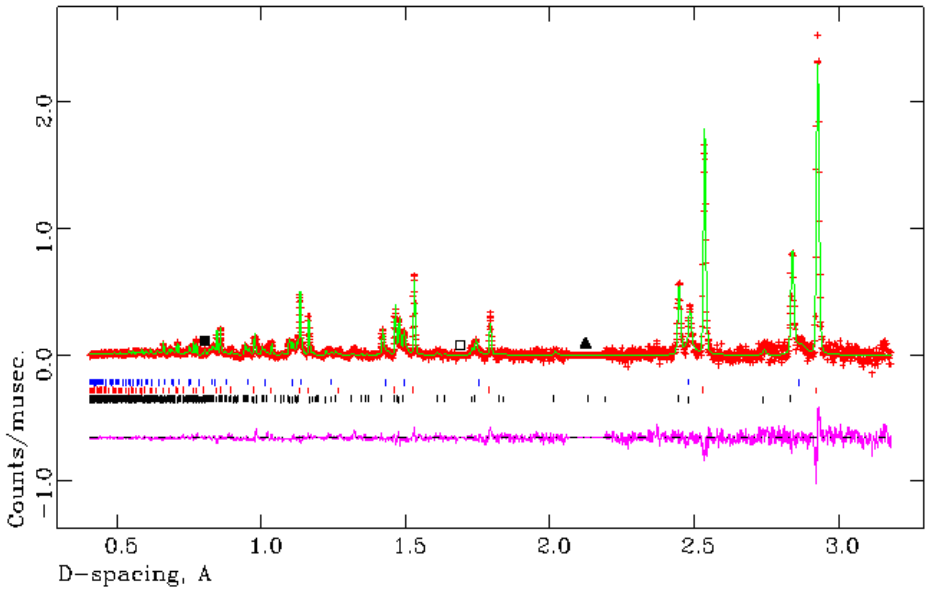

Figure 4-35: Observed, calculated and difference (OCD) plot from structural refinement of data collected from the 145 ^{o} (C) detector bank for sample 29 at 313 K from PND data.
The black tickmarks indicate reflections from Li_4ND (1), the red tickmarks indicate reflections from Li_2ND and the blue tickmarks indicate reflections from Li_4ND (1′). The black square represents a reflection from LiD, the open square indicates a reflection from $LiND_2$ and the black triangle indicates reflections from the sample environment (i.e. the furnace and vanadium canister), all of which have been excluded.

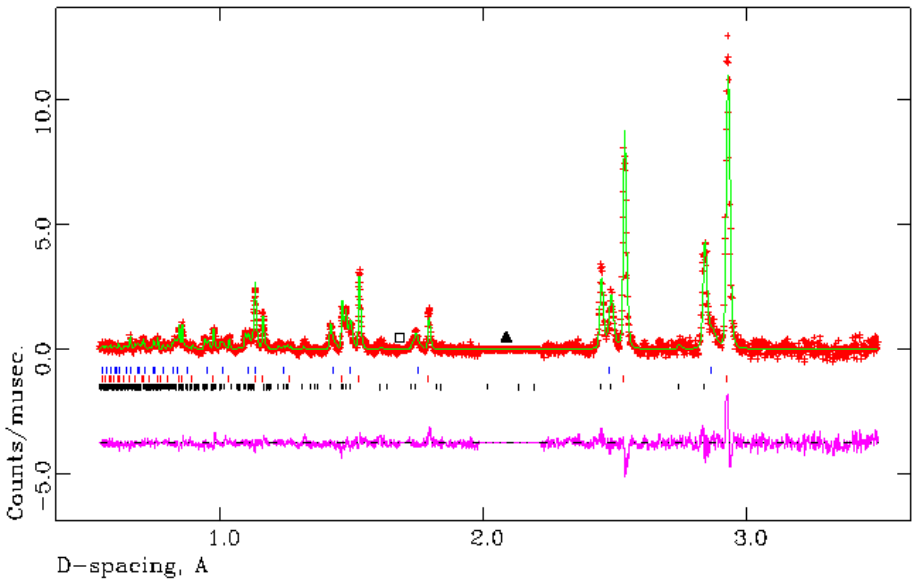

Figure 4-36: Observed, calculated and difference (OCD) plot from structural refinement of data collected from the 90 ^{o} (E) detector bank for sample 29 at 313 K from PND data.
The black tickmarks indicate reflections from Li_4ND (1), the red tickmarks indicate reflections from Li_2ND and the blue tickmarks indicate reflections from Li_4ND (1′). The open square indicates a reflection from $LiND_2$ and the black triangle indicates reflections from the sample environment (i.e. the furnace and vanadium canister), all of which have been excluded.

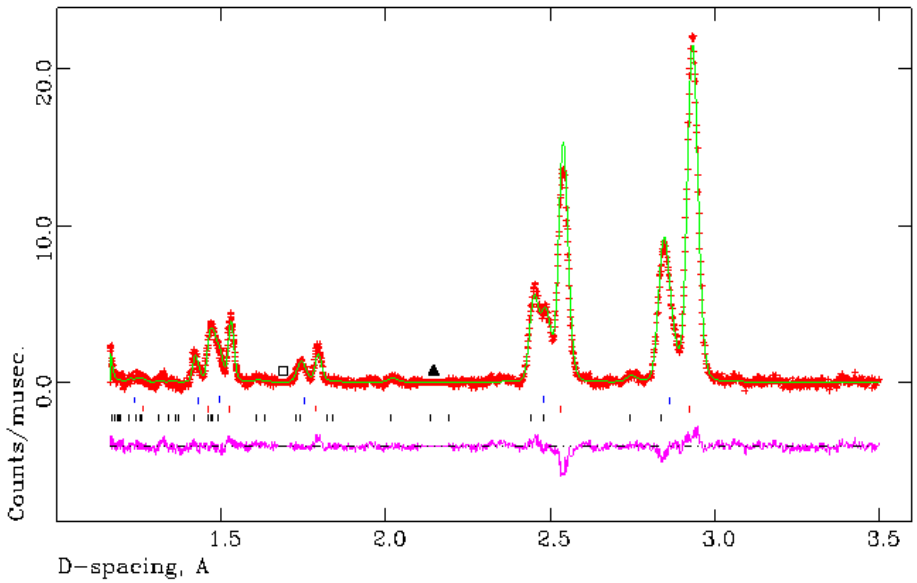

Figure 4-37: Observed, calculated and difference (OCD) plot from structural refinement of data collected from the 35 ° (A) detector bank for sample 29 at 313 K from PND data.
The black tickmarks indicate reflections from Li_4ND (1), the red tickmarks indicate reflections from Li_2ND and the blue tickmarks indicate reflections from Li_4ND (1′). The open square indicates a reflection from $LiND_2$ and the black triangle indicates reflections from the sample environment (i.e. the furnace and vanadium canister), all of which have been excluded.

Atomic positions and anisotropic temperature factors are presented in for each of the three phases in Tables 4.40, 4.41 and 4.42 respectively. Thermal parameters for each of the N and D atoms within Li_4ND (1) was refined anisotropically but the refinement was unstable when varying Li anisotropically. With regard to the Li_2ND and Li_4ND (1′) phases, N, Li and D thermal parameters were refined isotropically.

Table 4-40: Atom positions and anisotropic temperature factors generated by PND Rietveld refinement for Li_4ND (1) in sample 29 at 313 K.

Atom	N 1	D 1	N 2	D 2	Li 1
Site	4a	4a	4b	4b	16f
x	0	0	0	0	0.199 (4)
y	0.250	0.250	0.25	0.25	0.441 (4)
z	0.1250	0.1250	0.625	0.625	0.2771 (9)
100 x U_{iso} / Å^2	-	-	-	-	1.4 (1)
100 x U_{11} / Å^2	1.16 (9)	1.16 (9)	1.9 (2)	1.9 (2)	-
100 x U_{22} / Å^2	1.16 (9)	1.16 (9)	1.9 (2)	1.9 (2)	-
100 x U_{33} / Å^2	0.9 (1)	0.9 (1)	4.8 (4)	4.8 (4)	-
100 x U_{12} / Å^2	0	0	0	0	-
100 x U_{13} / Å^2	0	0	0	0	-
100 x U_{23} / Å^2	0	0	0	0	-
Occupancy	0.95	0.05	0.05	0.95	1.00

Table 4-41: Atom positions and isotropic temperature factors generated by PND Rietveld refinement of Li_2ND in sample 29 at 313 K.

Atom	Li 1	N 1	D 1
Site	8c	4a	192l
x	0.25	0	0.139 (2)
y	0.25	0	0.095 (2)
z	0.25	0	0.054 (2)
100 x U_{iso} / Å^2	5.4 (1)	1.96 (3)	3.6 (2)
Occupancy	1.00	1.00	0.0208

Table 4-42: Atom positions and isotropic temperature factors generated by PND Rietveld refinement for Li_4ND (1′) in sample 29 at 313 K.

Atom	Li 1	N 1	D 1
Site	8c	4a	4a
x	0.25	0	0
y	0.25	0	0
z	0.25	0	0
100 x U_{iso} / Å^2	6.4 (7)	1.3 (1)	1.3 (1)
Occupancy	1.00	0.50	0.50

Subsequent data were collected for this sample at 773 K and selected Rietveld refinement data are presented in Table 4.43 and observed, calculated and difference plots from the 145^o (C), 90^o (E) and 35^o (A) detector banks are displayed in Figures 4.38, 4.39 and 4.40. Atomic positions and anisotropic temperature factors are shown in Table 4.44. The thermal displacement parameters for the N1 and D1 atoms were refined isotropically as were those for Li. The thermal parameter for D on the 192l site could not be varied.

Table 4-43: Selected Rietveld refinement data from the PND refinement of sample 30 (where x = 0.6) at 773 K.

Empirical Formula	$Li_{4-2x}N_{1-x}D_{1-x}(ND)_x$
Collection temperature / K	773
Crystal system	Cubic
Space Group	*Fm-3m*
Lattice parameters	a = 5.1188 (3)
V / Å ^{3}	134.12 (1)
Unit cell formula weight, M_w	101.292
Density / g/cm^3	1.254
No. of varied parameters	43
No. of observations	11669
R_{wp}	0.0169
R_p	0.0576
χ^2	0.6127

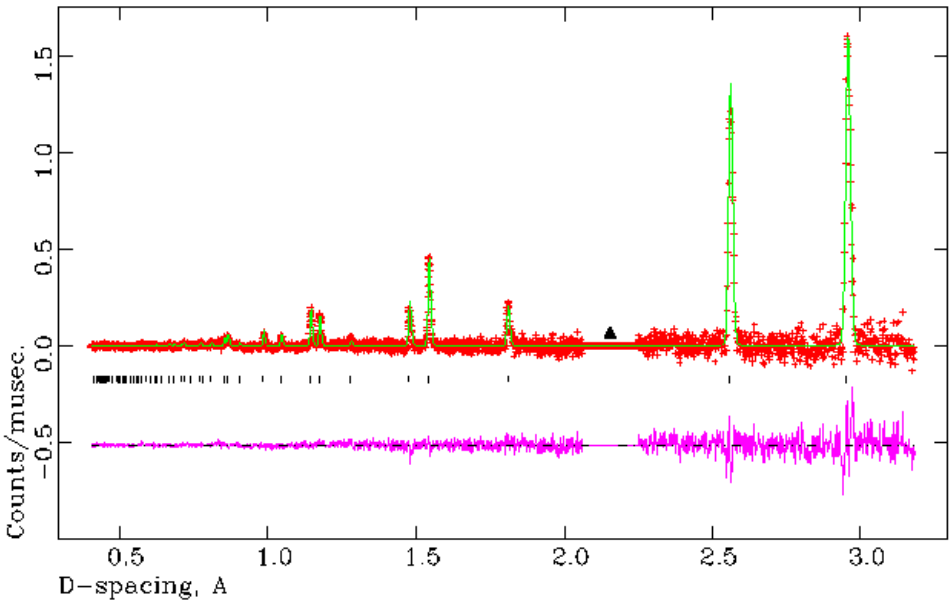

Figure 4-38: Observed, calculated and difference (OCD) plot from structural refinement of data collected from the 145 ° (C) detector bank for sample 30 at 773 K from PND data.
The black tickmarks indicate reflections from the quasi-imide phase. The black triangle indicates reflections from the sample environment (i.e. the furnace and the vanadium canister) which have been excluded.

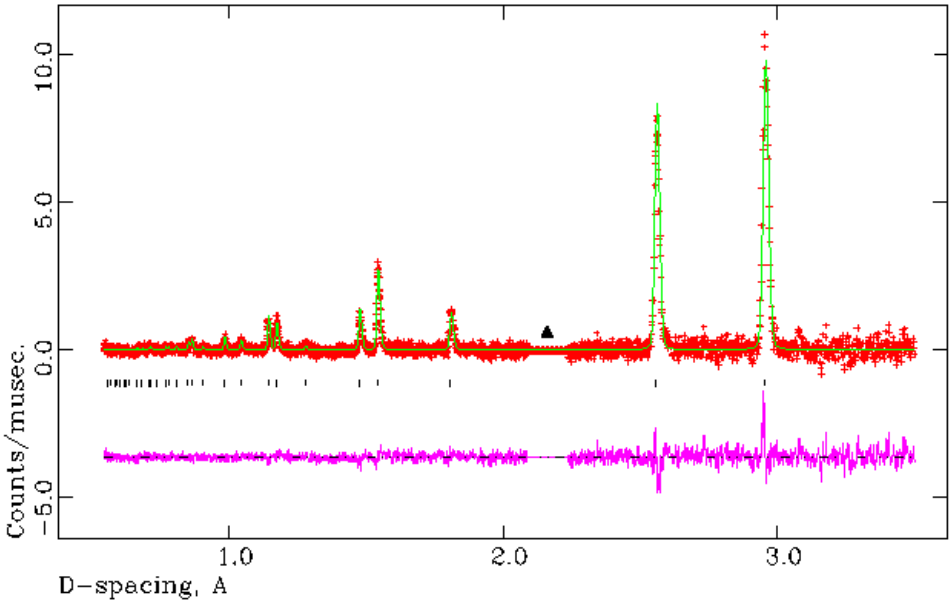

Figure 4-39: Observed, calculated and difference (OCD) plot from structural refinement of data collected from the 90 ° (E) detector bank for sample 30 at 773 K from PND data.
The black tickmarks indicate reflections from the quasi-imide phase. The black triangle indicates reflections from the sample environment (i.e. the furnace and the vanadium canister) which have been excluded.

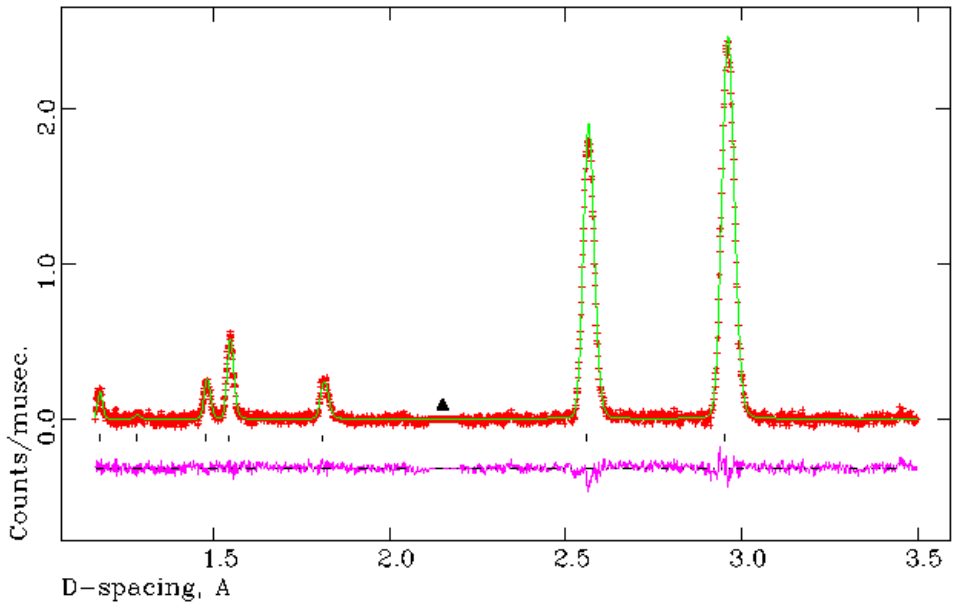

Figure 4-40: Observed, calculated and difference (OCD) plot from structural refinement of data collected from the 35 ° (A) detector bank for sample 30 at 773 K from PND data.
The black tickmarks indicate reflections from the quasi-imide phase. The black triangle indicates reflections from the sample environment (i.e. the furnace and the vanadium canister) which have been excluded.

Table 4-44: Atom positions and isotropic temperature factors generated by PND Rietveld refinement of sample 30 at 773 K.

Atom	Li 1	N 1	D1	D 2
Site	8c	4a	4a	192l
x	0.25	0	0	0.144 (5)
y	0.25	0	0	0.11 (9)
z	0.25	0	0	0.04 (9)
100 x U_{iso} / Å^2	8.5 (2)	3.4 (1)	3.4 (1)	5.50
Occupancy	1.00	0.7143	0.0089	0.2857

From Rietveld analysis of PND data collected for samples **22**, **24**, **26**, **28** and **30**, it is evident that as the value of x increases, the *a* lattice parameter of the new quasi-imide increases therefore the lattice parameter is composition dependent and this trend was also reported by Weidner *et al*. [2] The increase in size of the unit cell is shown clearly in Table 4-45 and Figure 4.41 is a representation of the structure.

Interatomic distances were also generated from Rietveld refinement of the PND data and are presented in Table 4.46. Considering the cubic symmetry of the structure where the N

and Li atoms are located on special positions and the distances obtained, the elongation of the Li-N bonds as x increases are responsible for the increase in lattice parameter value.

Table 4-45: Overview of lattice parameters obtained from Rietveld refinement of PND data at 773 K for varying values of x in samples of $Li_{4-2x}N_{1-x}D_{1-x}(ND)_x$.

x	*a* lattice parameter / Å
0.0	5.0542 (2)
0.36	5.0811 (2)
0.5	5.0968 (3)
0.6	5.1188 (3)
1.0	5.1661 (3)

Table 4-46: Overview of the interatomic distances obtained from Rietveld refinement of PND data at 773 K for varying values of x in samples of $Li_{4-2x}N_{1-x}D_{1-x}(ND)_x$.

	Interatomic Distances / Å		
x	**4x Li-N**	**6x N-D**	**6x Li-Li**
0.0	2.1852 (5)	0.89756 (2)	2.4733 (3)
0.36	2.20019 (6)	0.89 (4)	2.54056 (9)
0.5	2.20699 (10)	0.83 (4)	2.5484 (2)
0.6	2.21650 (9)	0.9 (2)	2.5594 (1)
1.0	2.23700 (8)	0.85 (2)	2.5831 (1)

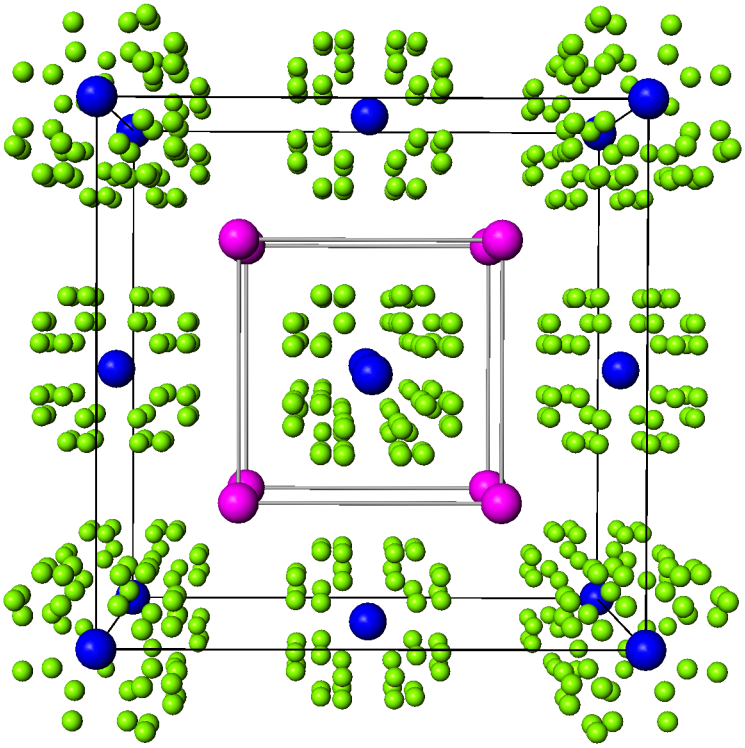

Figure 4-41: Illustration of a cubic 'quasi-imide' phase.
The lithium and nitrogen are on fixed sites. The hydrogen atoms represent all possible sites which may be occupied around the nitrogen atoms, as in the imide, expect rotational disorder of N-D (Li^+ - pink, N^{3-} - blue, H^+ - green).

Another feature of the quasi-imide phase which results as x increases is an increase in cell volume, calculated unit cell formula weight and cell density. The increase in calculated unit cell formula weight implies a change in the stoichiometry of $Li_{4-2x}N_{1-x}D_{1-x}(ND)_x$. As the value of x increases, an increase in the amount of the larger $(ND)_x$ leads to an increase in the calculated unit cell formula weight. Although the cell volume increases with increasing x, the correlation deviates slightly from linear behaviour. A representation of this is shown in Figure 4.42.

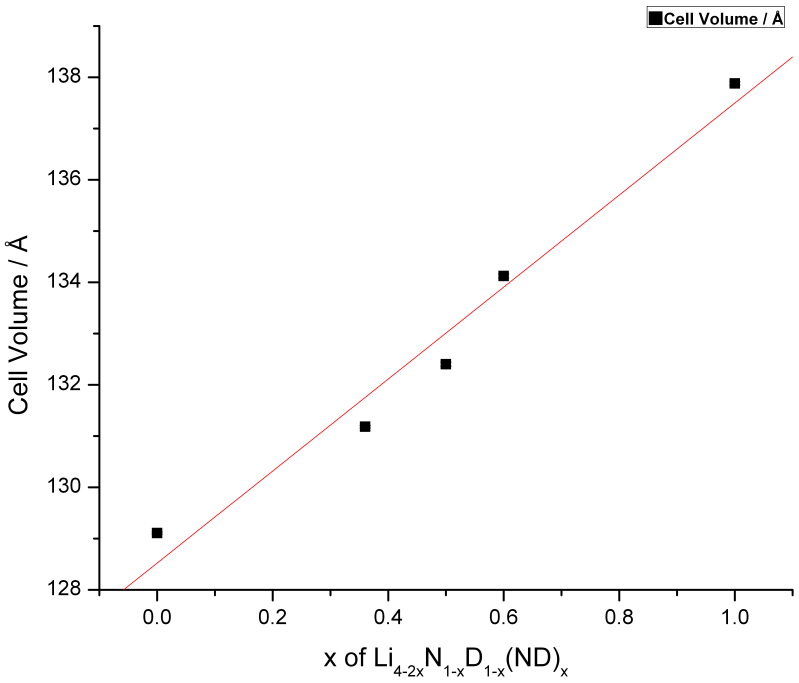

Figure 4-42: Comparison of cell volume obtained from Rietveld refinement of PND data at 773 K versus value of x.

The reaction pathway adopted by the 'quasi-imide' model suggested in this work and previously, [2, 3] differs from that suggested by Chen *et al* and David *et al* with regards to charge balance. [16 17] Firstly, Chen *et al* reported the formation of a Li-rich imide phase (Li_xNH_{3-x} where $x > 2$) as a result of the thermal desorption of a 1:2 mixture of $LiNH_2$ and LiH. [16] However, Chen *et al* stated that further investigations were required to verify the structure. Subsequently, during the investigation of the decomposition product of hydrogenated Li_3N, David *et al* reported a series of non-stoichiometric compounds ($Li_{2-x}NH_{1+x}$). [17] The aforementioned authors propose that charge balance is maintained via an exchange of Li^+ for H^+ however the 'quasi-imide' model suggested in this work and by Weidner *et al* [2] indicate that the inclusion of both H^+ and H^- (D^+ and D^-) is the reason that charge balance is maintained. Formation of the solid solutions between the imide-amide or the nitride-hydride-imide and associated mechanisms are dependent on different reaction conditions, e.g. high and low H_2 pressure respectively. It is believed that when the H_2 partial pressure is low, Li_3N reacts with LiH resulting in the formation of Li_4NH which subsequently reacts with Li_2NH to form the 'quasi-imide'.

4.4 Conclusions

Significant advances in the synthesis of Li_4ND using microwave radiation have been presented in this chapter. Using this novel synthetic method instead of a conventional method is advantageous in many regards including rapid heating and ultrafast cooling rates. As a consequence of rapid heating one disadvantage transpires; the temperature at which the reaction takes place cannot be monitored accurately. Fortunately, after employing a trial and error approach using various reaction parameters, including reaction time, power and atmosphere under which the reactions were run, optimum conditions emerged therefore the reaction temperature was not as critical as it may have been under conventional conditions. Furthermore, by employing the novel microwave synthesis, encouragingly the results are easily reproduced.

A PND study of Li_4ND over a variable temperature range resulted in the conclusion that at temperatures of 673 K and above, Li_4ND transforms from a tetragonal structure to a cubic structure. With regards to the tetragonal structure, the 4a and 4b sites are occupied by both N and D with the 4a site being predominantly occupied by N (approximately 95%) whereas the 4b site is predominantly occupied by D (approximately 95%). This was supported by bond valence calculations. Rietveld analysis confirmed the presence of a second Li_4ND phase in the sample at 313/323 K. This second phase is thought to be cubic Li_4ND and the structure is based on a modified Li_2ND type suggested by Balogh *et al* [14] however it should be noted that there are no previous reports of cubic-Li_4ND in the literature. On formation of the cubic structure, there is a change in anion distribution from approximately fully N and D occupied sites to one site that is occupied in a 50:50 ratio.

A PND investigation of Li_2ND was also conducted and data was collected at 313 and 773 K. The main purpose of collecting data at 313 K was to ensure that there were no impurity phases present in the starting material and to establish that Li_2ND was stoichiometric. With regards to the structure, Rietveld refinement of the data collected at 773 K shows that the lattice parameters increased which is consistent with thermal expansion.

As identified by Marx, a reaction involving Li_4NH and Li_2NH results in the formation of a cubic 'quasi-imide' phase ($Li_{4-2x}N_{1-x}D_{1-x}(ND)_x$) in which N^{3-}, D^- and $(ND)^{2-}$ are disordered across the *anti*-fluorite anion sites. This work revealed that the temperature at which the quasi-imide phases formed was 773 K. Various non-stoichiometric mixtures of Li_4ND and Li_2ND were analysed using the Rietveld method and by modifying the cubic structure proposed for Li_2ND by Balogh *et al*, [14] this allowed the cubic quasi-imide phase to be refined. Although the data obtained were relatively poor (either due to poorly crystalline samples or insufficient data collection times) and the structure is a complex one, a general

trend in the data was apparent; as the value of x was increased, an expansion of *a* resulted and the cell volume (and density) increased. Furthermore, as the value of x increases (0.36, 0.5, 0.6), the anion distribution changes; the occupancy of imide N in $(ND)^{2-}$ on the 4a site increases as does the occupancy of protonic D of $(ND)^{2-}$ on the 192l site. Furthermore, the Li-N and Li-Li bonds elongate with x.

4.5 References

[1] P. Chen, Z. Xiong, J. Luo, J. Lin and K. L. Tan, *Nature*, 2001, **420**, 302

[2] E. Weidner, D. J. Bull, I. L. Shabalin, S. G. Keens, M. T. F. Telling and D. K. Ross, *Chemical Physical Letters*, 2007, **444**, 76

[3] D. J. Bull, E. Weidner, I. L. Shabalin, M. T. F. Telling, C. M. Jewell, D. H. Gregory and D. K. Ross, *Physical Chemistry Chemical Physics*, 2010, **12**, 2089

[4] R. Marx, *Zeitschrift für anorganische und allgemeine Chemie*, 1997, **623**, 1912

[5] R. Niewa and D. A. Zherebtsov*, Zeitschrift fuer Kristallographie - New Crystal Structures*, 2002, **217**, 317

[6] R. I. Smith and S. Hull, *User Guide for the POLARIS Powder Diffractometer at ISIS Rutherford Appleton Laboratory Report*, 1997, RAL-TR-97-038

[7] A.C. Larson and R.B. Von Dreele, Generalized Structure Analysis System, 1990, MS-H805, Los Alamos, NM 87545

[8] B. H. Toby, *Journal of Applied Crystallography*, 2001, **34**, 210

[9] R. Juza and R. Opp, *Zeitschrift für Anorganische und Allgemeine Chemie*, 1951, **266**, 325

[10] Y. H. Hu and E. Ruckenstein, *Journal of Physical Chemistry A*, 2003, **107**, 9737

[11] J. P. Vidal and G. Vidal-Valat, *Acta Crystallographica B*, 1986, **42**, 131

[12] I. D. Brown and D. Altermatt, *Acta Crystallographica B*, 1985, **41**, 244

[13] CRC Handbook of Chemistry and Physics, 61st Edition, 1980-81, Edited by R. C. Weast and M. J. Astle, *CRC Press*

[14] M. P. Balogh, C. Y. Jones, J. F. Herbst, L. G. Hector, M. Kundrat Jr., *Journal of Alloys Compounds*, 2006, **420**, 326

[15] A. S. Bailey, R. W. Hughes, P. Hubberstey, C. Ritter, R. I. Smith and D. H. Gregory, *Inorganic Chemistry*, in press, DOI 10.1021/IC201264U

[16] P. Chen, Z. Xiong, J. Luo, J. Lin and K. L. Tan, *Journal of Physical Chemistry B*, 2003, **107**, 10967

[17] W. I. F. David, M. O. Jones, D. H. Gregory, C. M. Jewell, S. R. Johnson, A. Walton and P. P. Edwards, *Journal of the American Chemical Society*, 2007, **129**, 1594

5 The Li-Ca-N System

5.1 Introduction

Of the alkali metals, only lithium is known to form ternary nitrides with group 2 elements with Li-Mg-N being the most well studied of these systems. [1] Although closely related to LiMgN, in which stoichiometric LiMgN as well as Mg and Li rich phases are known, [2] to date, only one ternary nitride is known for the Li-Ca-N system; LiCaN. [3] Other ternary nitrides containing lithium and a group 2 element, other than LiMgN, include LiBeN, LiSrN and LiBaN. [4 5 6] A Li-rich phase for the Li-Sr-N system was also reported by Cordier *et al*; Li_4SrN_2. [3]

To date, there is only one previous report of the crystal structure of LiCaN determined by X-ray diffraction. [3] The nitride adopts a distorted orthorhombic structure based on an *anti*-fluorite in which half the tetrahedral holes are occupied by Ca atoms and Li atoms are displaced from the remaining tetrahedral positions of the approximately cubic close-packed matrix. Lithium atoms are coordinated to three nitrogen atoms in a trigonal planar geometry, as in Li_3N, although in LiCaN the triangle is distorted as is shown in Figure 5.1. Each calcium atom is tetrahedrally coordinated to a nitrogen atom, comparable to the coordination in α-Ca_3N_2. Each nitrogen forms pentagonal bipyramids with four calcium atoms (two axial, two equatorial) and three lithium atoms (equatorial).

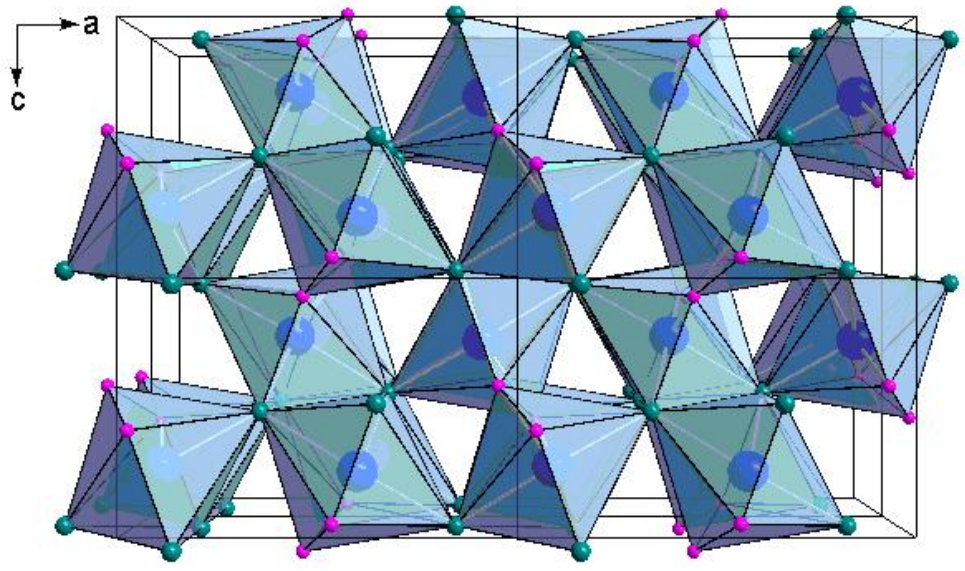

Figure 5-1: Distorted orthorhombic structure adopted by LiCaN.
(Li^+ - pink, N^{3-} - blue, Ca^{2+} - teal)

The ternary nitride, LiCaN can be synthesised by a solid state reaction using stoichiometric amounts of calcium metal and lithium nitride at a temperature of 873 K under an $N_{2(g)}$ pressure of 2 bar. [7] Furthermore, reacting Li_3N and Ca_3N_2 at 973 K under a nitrogen atmosphere also results in the formation of LiCaN. [8]

In relation to work by performed initially by Yamane *et al* [1] and subsequently by Bailey *et al* [2] involving PXD and PND studies respectively, results concluded that defect structures within the Li-Mg-N system were present. Therefore, as well as stoichiometric LiMgN, this system also contains Mg-rich and Li-rich compounds. [2] Due to the reports of the Mg-rich and Li-rich phases within the Li-Mg-N system together with the lack of structural data reported on the Li-Ca-N system, attempts were made to synthesise non-stoichiometric LiCaN. A subsequent PND study was conducted to investigate if the Li-Ca-N systems behaves in a similar way to that of the Li-Mg-N system.

This chapter describes the synthesis of lithium calcium nitride both conventionally and by a novel synthesis using microwaves. An initial study of the structure was performed by PXD and subsequently by PND. A PND study was essential in order to derive accurate Li positions, provide information on thermal displacements and ascertain if the material is perfectly stoichiometric as proposed. Based on the findings of the defect structures within the Li-Mg-N system by Yamane *et al* [1] and Bailey *et al*, [2] a further PND study was conducted to investigate non-stoichiometric LiCaN. The sample selected was influenced by the opportunity to introduce defects (essentially Li^+ vacancies) in $Li_{3-x}Ca_xN_{1-x/3}$ (by analogy to the Li-Mg-N system).

5.2 Experimental

5.2.1 Synthesis of Ca_3N_2

Synthesis of Ca_3N_2 (sample **1**) was carried out by a direct reaction between calcium metal and nitrogen gas. A piece of calcium (~ 6 g) was cut from a larger ingot (Alfa Aesar, 97%) and cleaned, under an argon-filled atmosphere in a recirculating glove box, to remove any oxides present on the surface of the material. The metal piece was then placed inside a stainless steel crucible which was then transferred into a stainless steel reaction vessel which was sealed under nitrogen (Section 2.3.1.1, Figure 2.5) before being removed from the glove box. The reaction vessel was evacuated before being purged with nitrogen and heated to 993 K for 24 h.

On cooling, the reaction vessel was opened in a recirculating glove box under a nitrogen atmosphere. The material was ground using an agate mortar and pestle before preparing a capillary for PXD.

5.2.2 Synthesis of Li-Ca-N materials

5.2.2.1 Synthesis of LiCaN

Lithium calcium nitride was synthesised using two different methods. Initially, LiCaN was synthesised coventionally by reacting Li_3N and Ca_3N_2 in a stainless steel reaction vessel under a static nitrogen atmosphere, using a 25 wt. % excess of Li_3N. The reactants were ground together using an agate mortar and pestle before pelletising the material using a 13 mm pellet die (samples **3**-**22**). The pellet was transferred into a stainless steel crucible which was then placed inside a stainless steel reaction vessel (Section 2.3.2.1, Figure 2.8). This was sealed before being removed from the glove box. The reaction vessel was heated to 923 K for 24 h. Upon completion of the reaction and subsequent cooling, the reaction vessel was opened in a recirculating glove box under a nitrogen atmosphere. The material was then ground using an agate mortar and pestle before preparing a capillary for PXD. An overview of the reaction conditions that were varied in order to synthesise single phase LiCaN using conventional methods are discussed in Table 5.1. For conventional syntheses, all material was pelletised unless stated otherwise.

Table 5-1: Summary of Li_3N + Ca_3N_2 reactions using a conventional method

Sample	Excess of Li_3N (%)	Time (h)	Temp (K)	Reaction Conditions	Results
2	-	48	923	$N_{2(g)}$ atmosphere, non-pelletised	LiCaN, CaO
3	-	48	973	$N_{2(g)}$ atmosphere	LiCaN, CaO
4	-	48	923	$N_{2(g)}$ atmosphere	LiCaN, CaO
5	10	48	923	$N_{2(g)}$ atmosphere	LiCaN, CaO
6	10	48	823	$N_{2(g)}$ atmosphere	LiCaN, CaO
7	15	48	923	$N_{2(g)}$ atmosphere	LiCaN, CaO
8	15	24	923	$N_{2(g)}$ atmosphere	LiCaN, CaO
9	15	24	823	$N_{2(g)}$ atmosphere	LiCaN, CaO
10	15	24	973	$N_{2(g)}$ atmosphere	LiCaN, CaO
11	25	48	923	$N_{2(g)}$ atmosphere	LiCaN, CaO
12	25	48	823	$N_{2(g)}$ atmosphere	LiCaN, CaO
13	25	48	973	$N_{2(g)}$ atmosphere	LiCaN, CaO
14	25	24	923	$N_{2(g)}$ atmosphere	LiCaN, CaO
15	25	24	973	$N_{2(g)}$ atmosphere	LiCaN, CaO
16	25	24	823	$N_{2(g)}$ atmosphere	LiCaN, CaO
17	25	48	923	$N_{2(g)}$ atmosphere	LiCaN, CaO
18	25	24	923	$N_{2(g)}$ atmosphere	LiCaN, CaO
19	2:1	48	973	$N_{2(g)}$ atmosphere	LiCaN, CaO
20	2:1	24	973	$N_{2(g)}$ atmosphere	LiCaN, CaO
21	2:1	48	923	$N_{2(g)}$ atmosphere	LiCaN, CaO
22	4:1	24	973	$N_{2(g)}$ atmosphere	LiCaN, CaO, α-Li_3N

In addition to the conventional route of synthesis, this ternary nitride can be prepared using a novel method via microwave synthesis. Using the same stiochiometries of reactants, the material was loaded into a silica glass tube which was sealed either under vacuum or by using a septum cap. Two types of microwave apparatus were employed; a multi-mode reactor and a single mode reactor, both of which facilitate plasma generation. In the case of

LiCaN synthesis, the plasma is cerise in colour before becoming lilac; this is true for reactions using both types of microwave reactors. When an orange glow was observed and the lilac glow ceased, this indicated that the reaction had reached completion.

Using a domestic microwave oven (Panasonic 4697 NN-TS53W) (Section 2.3.2.1, Figure 2.10), the vacuum-sealed tube was reacted at medium power (approximately 400 w) for 600 seconds to obtain the desired product. Using a single mode microwave reactor, CEM Discover, (where the microwaves are focussed directly on the sample) (Section 2.3.2.1, Figure 2.11), the reaction took place under a nitrogen or argon atmosphere at 300 w and the reaction time was reduced to 150 seconds. Conditions for both MW syntheses were optimised after varying numerous parameters outlined in Tables 5.2 and 5.3. It should be noted that the times stated in Tables 5.2 and 5.3 were not continuous and therefore periods of cooling were introduced for two main reasons. The first and most simplistic factor for the introduction of cooling periods was to avoid cracking of the silica glass tube. Secondly, Houmes and zur Loye reported that extremely rapid heating can lead to the evaporation of Li_3N ultimately resulting in the incomplete formation of the desired product [9] therefore cooling periods enabled this problem to be avoided. It was also vital that the reaction was monitored closely to ensure that thermal runaway did not occur which would have led to melting of the material as this has been reported elsewhere within solid state chemistry. [10]

Table 5-2: Summary of Li_3N + Ca_3N_2 reactions using a domestic microwave oven

Sample	Excess of Li_3N (%)	Time (secs)	Power	Reaction Conditions	Results
23	25	420	'Med/High'	$N_{2\,(g)}$ atmosphere	α-Li_3N, β-Li_3N, Ca_3N_2
24	25	900	'High'	$N_{2\,(g)}$ atmosphere, Fe susceptor	α-Li_3N, Ca_3N_2, LiCaN, CaO
25	25	600	'Med/High'	Vacuum	LiCaN, CaO

Table 5-3: Summary of Li_3N + Ca_3N_2 reactions using a single mode microwave reactor

Sample	Excess of Li_3N (%)	Time (secs)	Power (watts)	Reaction Conditions	Results
26	25	120	300	$N_{2(g)}$ atmosphere	LiCaN, CaO
27	25	150	300	$N_{2(g)}$ atmosphere	LiCaN, CaO
28	-	150	300	$N_{2(g)}$ atmosphere	LiCaN, CaO
29	25	150	300	$N_{2(g)}$ atmosphere	LiCaN, CaO
30	50	150	300	$N_{2(g)}$ atmosphere	LiCaN, CaO, Ca_3N_2

Despite varying numerous parameters using each of the synthetic methods described, it was impossible to obtain single phase LiCaN; a slight CaO impurity was present regardless. Both starting materials and each sample were analysed by PXD to determine the purity of each. In regards to the starting materials used for each synthesis, data collected from PXD revealed that both Li_3N (Alfa Aesar, 99.4 %) (see appendix) and Ca_3N_2 (laboratory synthesised) did not have any oxide impurities present (Figure 5.2).

5.2.2.2 Synthesis of non-stoichiometric LiCaN

In attempts to make $Li_{3-x}Ca_xN_{1+(x/3)}$ (x = 1.6) for a PND study, the same method of synthesis, using a single mode microwave reactor, was followed. It should be noted that an excess of Li_3N continued to be used throughout these reactions also. A summary of the reactions performed in order to ascertain the most appropriate reaction conditions are is detailed in Table 5.4.

Table 5-4: Summary of $Li_{3-x}Ca_xN_{1+(x/3)}$ (x = 1.6) reactions using a single mode microwave reactor

Sample	Excess of Li_3N (%)	Time (secs)	Power (watts)	Reaction Conditions	Results
35	25	120	300	$N_{2(g)}$ atmosphere	LiCaN, CaO, Ca_3N_2
36	25	150	300	$N_{2(g)}$ atmosphere	LiCaN, CaO

5.2.3 Scanning Electron Microscopy

A small amount of sample (conventionally and MW synthesised material) was deposited onto an aluminium stub using adhesive carbon tabs. All preparations were carried out under a nitrogen atmosphere in a recirculating glove box due to the air sensitive nature of the material. Each tab was placed inside a glass vial which was sealed before removal from the glove box.

The sample was subsequently transferred quickly from the glass vial into the vacuum column of the microscope, once again so as to minimise exposure to the air. Each sample was examined by J. Gallagher on a Hitachi S-4700 SEM with an applied accelerating voltage of 5 kV and a working distance of 12.5 mm.

5.2.4 Powder X-ray Diffraction (PXD) Experiments

All compounds which were synthesised were initially characterised by PXD using a Bruker D8 or a PANalytical X'Pert PRO MPD powder diffractometer, as described in Section 2.4.1.1. Capillaries of the materials were prepared for each PXD measurement. Data were collected from 5-85° 2θ or 10-110° 2θ for 1 h or 12 h respectively, using a step size of 0.017° 2θ. PXD data collected overnight produced high quality data which were used for Rietveld refinements.

5.2.5 Rietveld refinement against PXD data

The structure of LiCaN, synthesised both conventionally and by microwave reaction, was refined using the General Structure Analysis System (GSAS) [11] via the EXPGUI interface. [12] The background of both samples was successfully modelled using GSAS background function 1 (shifted Chebyschev function), using 12 or 14 coefficients. This was followed by refinement of the cell parameters. Subsequently, peak profiles (using GSAS function 3, a convolution of back-to-back exponentials and pseudo-Voigt combination with Lorentzian broadening) and atomic positions were refined as well as isotropic temperature factors. Lastly, anisotropic temperature factors were refined.

5.2.6 Powder Neutron Diffraction (PND) Experiments

Powder neutron diffraction studies on the Li-Ca-N system were performed at ISIS, Rutherford Appleton Laboratory. The diffraction experiments were carried out on POLARIS which is a high intensity, medium resolution diffractometer [13] and described more fully in Section 2.4.2.1. Data were collected for three samples within the Li-Ca-N system and are detailed below (Table 5.5).

Table 5-5: Summary of the PND experiments performed on POLARIS.

Sample	Composition	Temperature (K)
37	LiCaN	300
38	LiCaN	400
39	$Li_{3-x}Ca_xN_{1+(x/3)}$ where x = 1.6	300
40	$Li_{3-x}Ca_xN_{1+(x/3)}$ where x = 1.6	400

Approximately 1 g of each sample was loaded into a 8 mm vanadium canister in a glove box under an argon atmosphere. The canister was made air-tight by using a copper gasket which was placed between the lid and the canister. Measurements were carried out in a furnace at 300 and 400 K for approximately 2 h each and data were collected at the 145^o (C), 90^o (E) and 35^o (A) detector banks.

5.2.7 Rietveld refinement against PND data

The General Structure Analysis System (GSAS) [11] via the EXPGUI interface [12] was employed to carry out Rietveld refinements of the collected PND time of flight data. Data were employed from three detector banks; A bank (35^o), E bank (90^o) and C bank (145^o) and an appropriate starting model based on the known structure of LiCaN [3] was used in each refinement. For sample **37**, the data were fitted to the LiCaN phase and an additional CaO impurity phase. In the case of the $LiNH_2$ impurity phase, the signal to noise ratio was poor therefore it was difficult to achieve a good fit of this phase. The LiCaN phase was refined to the orthorhombic structure proposed by Cordier *et al* [3] in the space group *Pnma*. The impurity phase of CaO, which crystallises in the space group *Fm-3m*, was modelled against the standard rock salt structure [14] and $LiNH_2$ was modelled against a tetragonal starting model suggested by Jacobs and Juza [15] in space group *I-4*.

Initially data collected from the 145^{o} (C) bank for samples **37** and **38** at 300 K and 400 K respectively were used in refinements. In both cases background function 1, shifted Chebyschev (in GSAS) was employed using 10 coefficients and was refined. This was followed by refinement of the unit cell and an absorption correction was applied. The peak profiles (using GSAS function 3, a convolution of back-to-back exponentials and pseudo-Voigt combination with Lorentzian broadening), atomic positions and isotropic temperature factors were then subsequently refined. Impurity phases were then added once the refinement of the main phase was near completion. Lastly, the anisotropic temperature factors were refined for the main phase. Prior to completing the refinement, as many parameters as possible were simultaneously refined for each data set to obtain the best possible fit with the optimum number of varied parameters.

The same procedure as described above was followed for samples **39** and **40**, although the number of coefficients used for obtaining a good fit of the background was increased (14 coefficients were used).

5.3 Results and Discussion

5.3.1 Synthesis of Ca_3N_2

Successful laboratory synthesis of α-Ca_3N_2 resulted in a material which was a dark red colour. Figure 5.2 shows the PXD pattern obtained and highlights the fact that the experimental pattern shown in black fits well to the theoretical pattern input using PowderCell 2.4 (in red). Furthermore, the PXD pattern shown below confirms the fact that no impurities were present within the sample. The cubic cell parameters (a = 11.468 (6) Å) are in good agreement with that reported in the literature by Laurent *et al* [16] (a = 11.473 (1) Å).

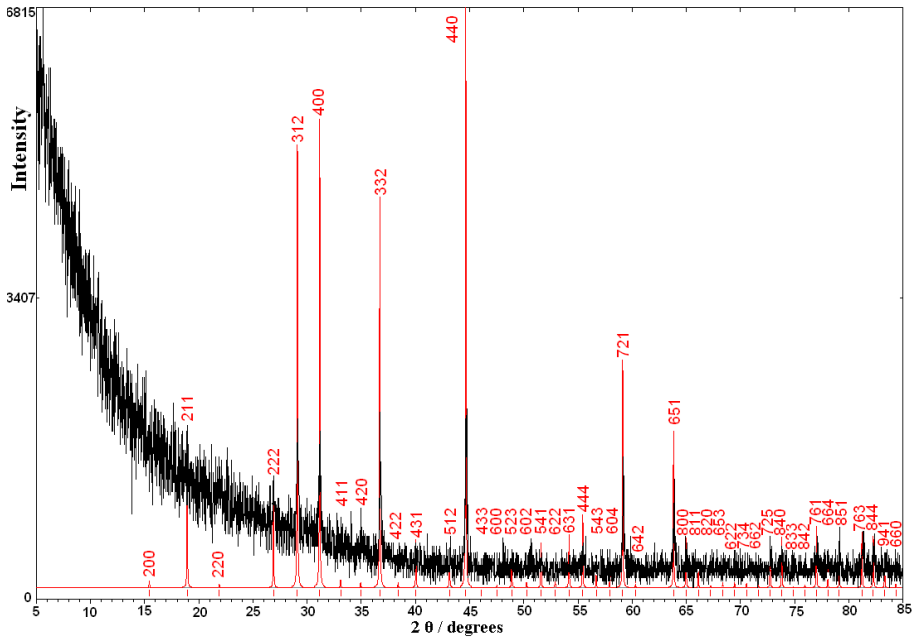

Figure 5-2: Powder pattern obtained for lab-synthesised Ca_3N_2 (indicated in red).

5.3.2 Synthesis of LiCaN

Lithium calcium nitride was successfully synthesised using two different methods and both yielded a product which had a slight CaO impurity. Both the conventionally synthesised LiCaN and the material synthesised by the employment of microwaves gave rise to a bright orange coloured product. Rietveld refinements were performed using the LiCaN model structure proposed by Cordier *et al* in 1989 (in orthorhombic space group *Pnma)*. [3] The structures for materials obtained from both synthetic methods resulted in good agreement to the theoretical model and χ^2 values of 1.953 and 1.284 were obtained for the conventional and novel microwave synthesis methods respectively. Selected Rietveld refinement data is shown in Table 5.6. Figure 5.3 illustrates the observed, calculated and difference (OCD) plot for conventionally synthesised LiCaN. Atomic positions and anisotropic temperature factors for the LiCaN phase are displayed in Table 5.7. It should be noted that the atomic position for the Li atom could not be varied due to the instability of the refinement but the atomic positions (x, z) of Ca and N were varied (Table 5.7).

Table 5-6: Selected Rietveld refinement data from the PXD refinement of sample 16 at 293 K.

Empirical Formula	LiCaN	CaO
Collection Temperature / K	293	
Crystal system	Orthorhombic	Cubic
Space Group	*Pnma*	*Fm-3m*
Lattice parameters / Å	a = 8.4502 (5)	a = 4.7956 (3)
	b = 3.6639 (2)	-
	c = 5.5254(4)	-
V / Å ^{3}	171.070 (18)	110.286 (13)
Unit cell formula weight, M_w	244.112	224.316
Density (g/cm^3)	2.370	3.378
Wt. %	92.318 (1)	7.682 (6)
No. of varied parameters	31	
No. of observations	11812	
R_{wp}	0.1406	
R_p	0.0887	
χ^2	1.953	

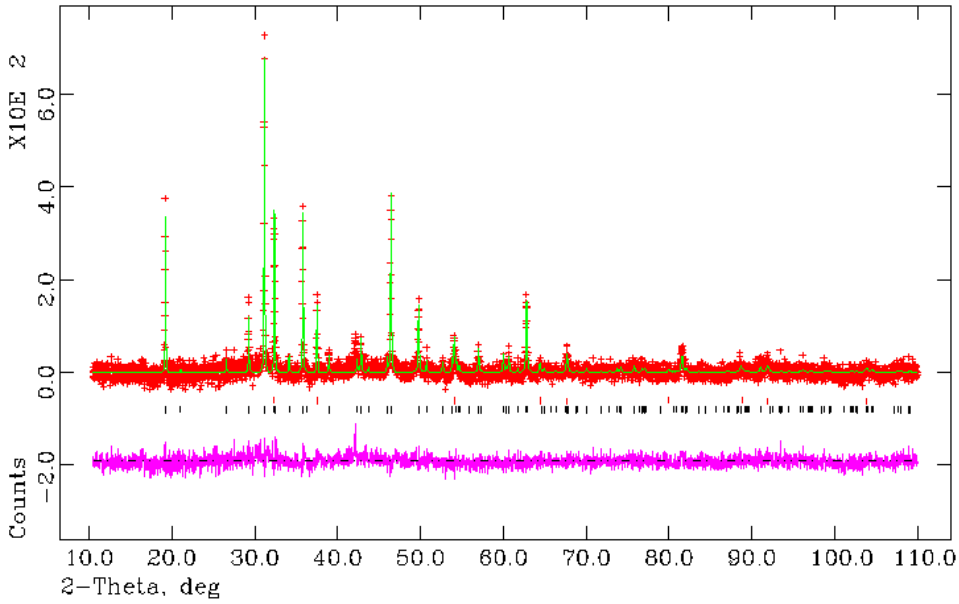

Figure 5-3: Observed, calculated and difference (OCD) plot obtained for sample 16 refined against PXD data.
The black tickmarks indicate the LiCaN phase and the red tickmarks indicate the impurity phase, CaO.

Table 5-7: Atom positions and anisotropic temperature factors for the LiCaN phase in sample 16 generated from the Rietveld refinement of PXD data.

Atom	Li	Ca	N
Site	4c	4c	4c
x	0.047610	0.1527 (8)	0.408 (3)
y	0.25	0.25	0.25
z	0.574490	0.025 (1)	0.2344 (3)
100 x U_{11} / Å^2	0.7 (26)	9.6 (5)	8.6 (20)
100 x U_{22} / Å^2	7.2 (29)	8.1 (4)	7.0 (16)
100 x U_{33} / Å^2	8.6 (30)	9.2 (5)	9.6 (18)
100 x U_{12} / Å^2	0	0	0
100 x U_{13} / Å^2	1.8 (22)	-2.1 (7)	2.7 (12)
100 x U_{23} / Å^2	0.00	0.00	0.00
Occupancy	1.00	1.00	1.00

A Rietveld refinement was performed on sample **26** in order to compare LiCaN prepared via conventional heating versus that produced by microwave synthesis. Figure 5.4 shows the observed, calculated and difference (OCD) plot for this material which was synthesised using microwaves. Selected Rietveld refinement data is shown in Table 5.8. Atomic positions were varied for all atoms in the main phase and data is displayed in Table 5.9 along with anisotropic temperature factors.

Table 5-8: Selected Rietveld refinement data generated from the PXD refinement of sample 26 at 293 K.

Empirical Formula	LiCaN	CaO
Collection Temperature / K	293	
Crystal System	Orthorhombic	Cubic
Space Group	*Pnma*	*Fm-3m*
Lattice parameters / Å	a = 8.4775 (3)	a = 4.814 (3)
	b = 3.6794 (2)	-
	c = 5.5440 (2)	-
V / Å ^{3}	172.930 (11)	112.554 (13)
Z	4	4
Unit cell formula weight, M_w	244.112	224.316
Density (g/cm^3)	2.344	3.309
Wt. %	87.979 (2)	12.021 (7)
No. of varied parameters	42	
No. of observations	4786	
R_{wp}	0.0502	
R_p	0.0352	
χ^2	1.284	

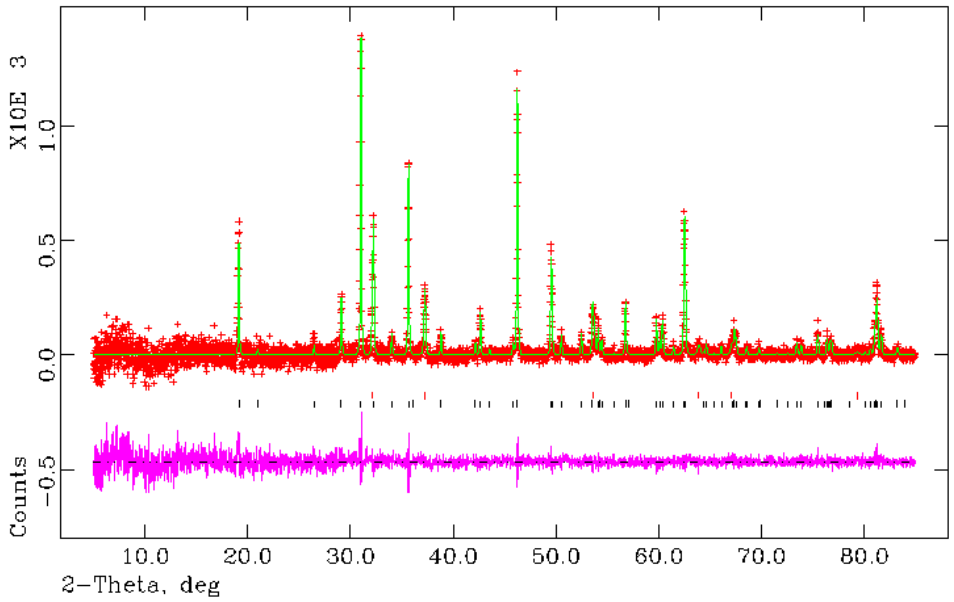

Figure 5-4: Observed, calculated and difference (OCD) plot obtained for sample 26. The black tickmarks indicate the LiCaN phase and the red tickmarks indicate the impurity phase, CaO.

Table 5-9: Atom positions and anisotropic temperature factors for LiCaN generated by Rietveld refinement of PXD data.

Atom	**Li**	**Ca**	**N**
Site	4c	4c	4c
x	0.038 (4)	0.1557 (4)	0.4051 (16)
y	0.25	0.25	0.25
z	0.569 (5)	0.0272 (5)	0.2401 (18)
100 x U_{iso} / Å^2	8.5 (10)	-	-
100 x U_{11} / Å^2	-	4.37 (20)	6.9 (10)
100 x U_{22} / Å^2	-	3.86 (18)	3.5 (8)
100 x U_{33} / Å^2	-	3.93 (20)	4.2 (7)
100 x U_{12} / Å^2	-	0	0
100 x U_{13} / Å^2	-	0.81 (27)	0.5 (6)
100 x U_{23} / Å^2	-	0	0
Occupancy	1.00	1.00	1.00

In terms of lattice parameters, those reported for the microwave synthesis are in good agreement with those stated in the literature however there is a difference in the lattice parameters obtained for the conventional synthesis (Table 5.10). The unit cell parameters for the conventionally synthesised material are smaller than that of both reported in the literature and for the microwave synthesis. It should be noted that Cordier *et al* synthesised the LiCaN material at 1123 K [3] and in this work, the conventional synthesis was carried out at 823 K. It is difficult to reach a final conclusion with regards to the LiCaN material synthesised via microwaves, since the temperature cannot be monitored using this synthetic method. There was an attempt to refine the occupancies in order to ascertain if a non-stoichiometric phase was present, but the occupancies did not vary from 1.

Table 5-10: Comparison of lattice parameters for different synthetic methods in relation to literature values. [3]

Lattice Parameter	Literature	Conventional Synthesis (Sample 16)	Microwave Synthesis (Sample 26)
a **/ Å**	8.471 (3)	8.4502 (2)	8.4775 (3)
b **/ Å**	3.676 (2)	3.6639 (2)	3.6794 (2)
c **/ Å**	5.537 (3)	5.5254 (4)	5.5440 (2)

5.3.3 Scanning Electron Microscopy

The morphology of LiCaN samples synthesised both conventionally and by irradiating with microwaves are not well defined. From Figures 5.5 (a-b) and 5.6 (a-b), it is evident that there are smaller particles present on the surface of larger agglomerations. These agglomerations are present almost certainly due to the high temperature at which the reactions were performed and in both cases indicates an onset of sintering. It can be observed from Figures 5.6 (a-b) and 5.7 (a-b) that the method of synthesis employed has very little effect on the overall particle size or morphology of LiCaN.

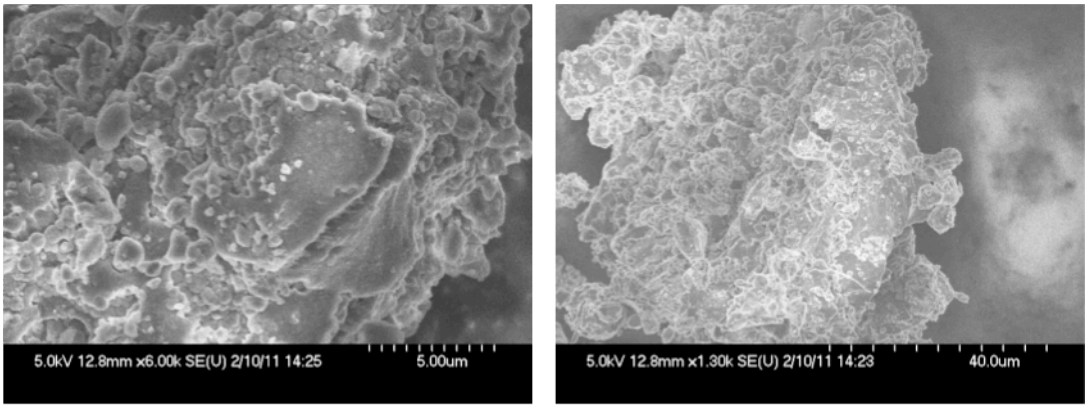

Figure 5-5:SEM micrographs of conventionally synthesised LiCaN (sample 16) at (a) 5 µm and (b) 40 µm.

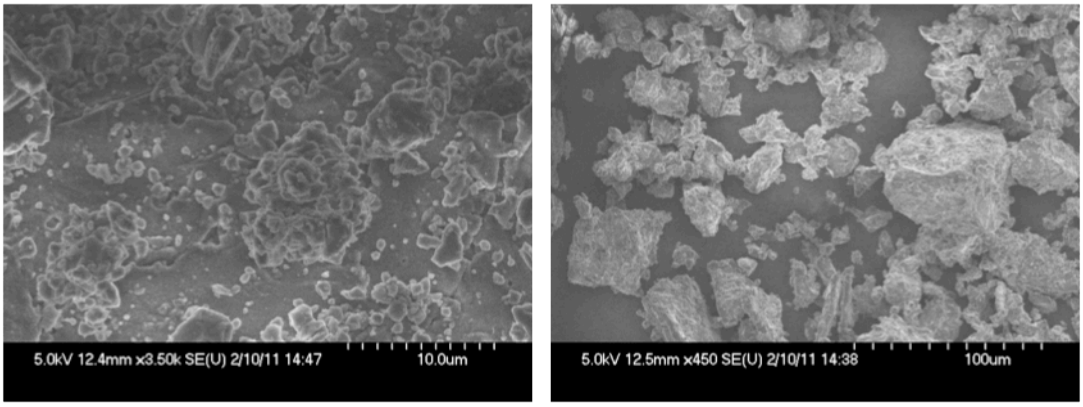

Figure 5-6:SEM micrographs of LiCaN (sample 26) synthesised by microwave reaction at (a) 10 µm and (b) 100 µm.

5.3.4 Powder Neutron Diffraction (PND) Experiments

Powder neutron diffraction experiments were performed on POLARIS at ISIS at the Rutherford Appleton Laboratory. Two different experiments were conducted; the first involved the investigation of laboratory synthesised LiCaN. The second experiment was a study into the compound $Li_{3-x}Ca_xN_{1+x/3}$ (where x = 1.6). The choice of sample for the second PND experiment was influenced by the opportunity to introduce defects (essentially Li^+ vacancies) by analogy to the Li-Mg-N system. [1 2] The temperatures at which the experiments were conducted at were chosen carefully, considering conditions when materials would not be "in service" (ambient) and conditions where they would be expected to be in operation as hydrogen stores (373 – 473 K). For each experiment, data were collected at 300 and 400 K.

5.3.4.1 PND study of stoichiometric LiCaN at 300 and 400 K

The initial PND experiment was conducted in order to obtain a definitive structural model of lithium calcium nitride from powder neutron diffraction which is an important first step towards a systematic study of the process and mechanism of hydrogenation in this system. Selected Rietveld refinement data is presented in Table 5.11 and Figures 5.7, 5.8 and 5.9 show the observed, calculated and difference (OCD) plots for data collected at 300 K for sample **37** at the 145^{o} (C), 90^{o} (E) and 35^{o} (E) detector banks respectively. It should be noted that the starting material was not single phase lithium calcium nitride. Powder X-ray diffraction patterns obtained for the material used for the PND experiment highlighted the presence of a calcium oxide impurity. However PXD failed to draw attention to the presence of a lithium amide impurity, a calcium nitride impurity and a very slight α-Li_3N impurity. The impurity phases of CaO and $LiNH_2$ were refined and the main phase, LiCaN, was fitted to the model proposed by Cordier *et al*, [3] however the third and fourth impurity phases of Ca_3N_2 and α-Li_3N could not be refined due to the relatively low intensities of these phases. It is unexpected that $LiNH_2$ should be present as an impurity however if the vanadium canister used for the PND experiment was not fully dry then the moisture could have reacted with the LiCaN to form a $LiNH_2$ impurity. The poor fit of the data can be attributed to a peak shape issue that can be clearly seen at higher *d* spacing (3.072 Å) and is also highlighted in the difference plot. A trial and error approach, in regards to the varying of Gaussian and Lorentzian peak profile functions, was employed to obtain the best fit of the data. Atomic positions and anisotropic temperature factors were obtained for each atom in this phase and the values are reported in Table 5.12.

Table 5-11: Selected Rietveld refinement data from the PND refinement of sample 37 (300 K).

Empirical Formula	LiCaN	CaO	$LiNH_2$
Collection Temperature / K		300	
Crystal system	Orthorhombic	Cubic	Tetragonal
Space Group	*Pnma*	*Fm-3m*	*I-4*
Lattice parameters / Å	a = 8.4964 (2)	a = 4.8337 (2)	a = 5.111 (1)
	b = 3.6874 (10)	-	-
	c = 5.5575 (1)	-	c = 10.150 (6)
V / Å ^{3}	174.12 (1)	112.93 (1)	265.11 (20)
Z	4	4	8
Unit cell formula weight, M_w	244.112	224.316	183.712
Density (g/cm^3)	2.328	3.298	1.151
wt. %	84.893 (2)	12.296 (2)	2.811 (1)
No. of varied parameters		76	
No. of observations		11833	
R_{wp}		0.0136	
R_p		0.0282	
χ^2		2.133	

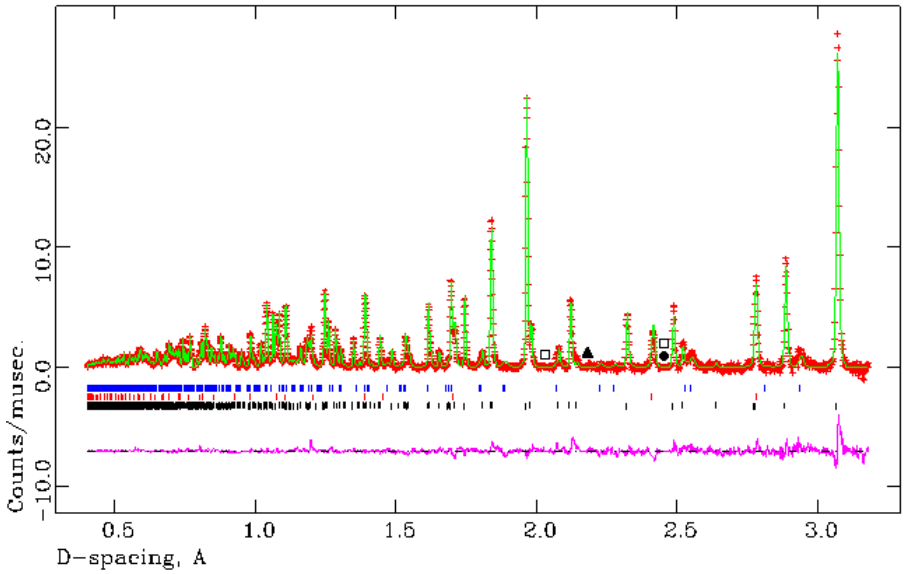

Figure 5-7: Observed, calculated and difference (OCD) plot from the structural refinement of sample 37 (300 K), 145° (C) bank.

The black tickmarks indicate reflections from LiCaN, the red tickmarks indicate reflections from CaO and the blue tickmarks represent reflections from $LiNH_2$. The white square indicates reflections from Ca_3N_2, the black triangle represents a reflection from the sample environment (i.e. the furnace) and the black circle represents a reflection from α-Li_3N, all of which have been excluded.

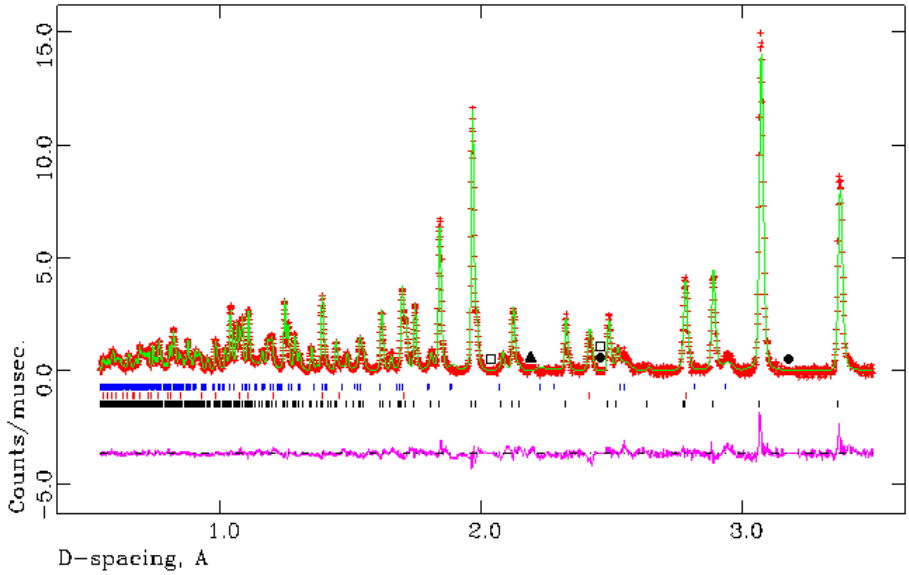

Figure 5-8: Observed, calculated and difference (OCD) plot from the structural refinement of sample 37 (300 K), 90° (E) bank.

The black tickmarks indicate reflections from LiCaN, the red tickmarks indicate reflections from CaO and the blue tickmarks represent reflections from $LiNH_2$. The white square represents reflections from Ca_3N_2, the black triangle represents reflections from the sample environment (i.e. the furnace) and the black circle represents a reflection from α-Li_3N, all of which have been excluded.

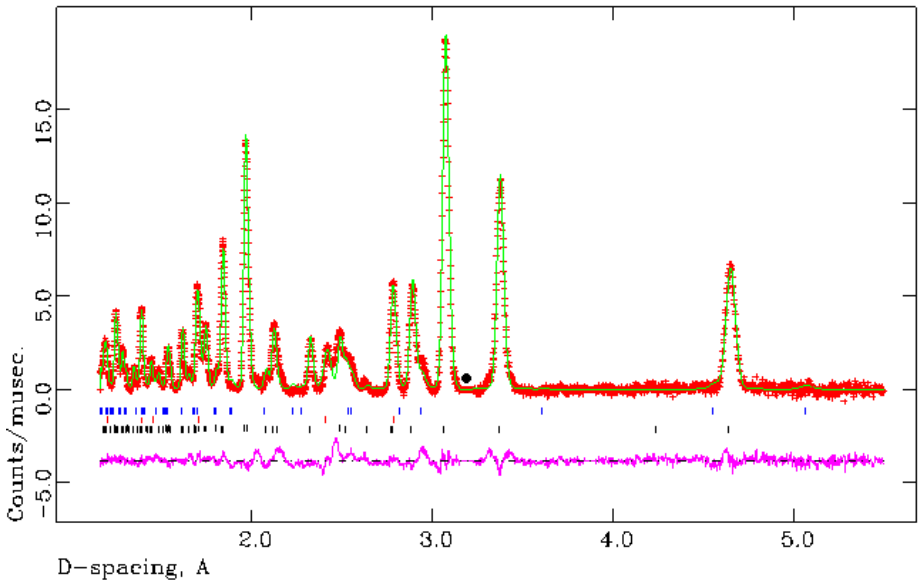

Figure 5-9: Observed, calculated and difference (OCD) plot from the structural refinement of sample 37 (300 K), 35° (A) bank.
The black tickmarks indicate reflections from LiCaN, the red tickmarks indicate reflections from CaO and the blue tickmarks represent reflections from $LiNH_2$. The black circle represents a reflection from α-Li_3N which has been excluded.

Table 5-12: Atom positions and anisotropic temperature factors for the LiCaN phase of sample 37 at 300 K generated by PND Rietveld refinement.

Atom	Li	Ca	N
Site	4c	4c	4c
x	0.0463 (4)	0.1566 (2)	0.40614 (7)
y	0.25	0.25	0.25
z	0.5725 (5)	0.0260 (2)	0.2409 (2)
100 x U_{11} / Å^2	1.95 (13)	0.78 (4)	1.63 (2)
100 x U_{22} / Å^2	0.69 (11)	1.04 (4)	1.16 (2)
100 x U_{33} / Å^2	2.23 (16)	1.11 (4)	1.40 (2)
100 x U_{12} / Å^2	0	0	0
100 x U_{13} / Å^2	-0.10 (11)	-0.24 (4)	-0.14 (3)
100 x U_{23} / Å^2	0	0	0
Occupancy	1.00	1.00	1.00

With regard to lattice parameters obtained from Rietveld refinement of sample **37**, it is evident from the data presented in Table 5.13 that there is a difference (outwith 3σ) in the values obtained by X-ray diffraction and by PND. The lattice parameters obtained from Rietveld analysis of the PND data revealed that *a*, *b* and *c* are larger than initially reported by Cordier *et al* (*a* = 8.471 (3) Å, *b* = 3.676 (2) Å, *c* = 5.537 (3) Å). [3]

Table 5-13: Comparison of lattice parameters reported in the literature (single crystal X-ray diffraction) [3] and this work (PXD and PND) of LiCaN between 293 and 300 K.

Lattice parameter	Literature Single crystal XRD	This work PXD	This work PND
a **/ Å**	8.471 (3)	8.4775 (3)	8.4964 (2)
b **/ Å**	3.676 (2)	3.6794 (2)	3.6874 (1)
c **/ Å**	5.537 (3)	5.5440 (2)	5.5575 (1)

Further PND data were collected at a higher temperature, at 400 K (sample **38**). As the temperature increases from 300 K to 400 K, the lattice parameters obtained from the experimental data are consistent with thermal expansion. Selected Rietveld refinement data are presented in Table 5.14 and Figures 5.10, 5.11 and 5.12 show the observed, calculated and difference (OCD) plot for sample **38**. Data were collected at the 145^{o} (C), 90^{o} (E) and 35^{o} (A) detector banks. Atomic positions and anisotropic temperature factors for sample **38** are displayed in Table 5.15.

Table 5-14: Selected Rietveld refinement data from the PND refinement of sample 38 at 400 K.

Empirical Formula	LiCaN	CaO	$LiNH_2$
Collection Temperature / K		400	
Crystal system	Orthorhombic	Cubic	Tetragonal
Space Group	*Pnma*	*Fm-3m*	*I-4*
Lattice parameters / Å	a = 8.5067 (2)	a = 4.8391 (4)	a = 5.110 (2)
	b = 3.6947 (10)	-	-
	c = 5.5663 (1)	-	c = 10.273 (7)
V / Å ^{3}	174.95 (1)	113.39 (1)	268.24 (23)
Z	4	4	8
Unit cell formula weight, M_w	244.112	224.316	183.712
Density (g/cm^3)	2.317	3.285	1.137
wt. %	84.291 (2)	10.844 (2)	2.865 (1)
No. of varied parameters		77	
No. of observations		11797	
R_{wp}		0.0131	
R_p		0.0273	
χ^2		1.740	

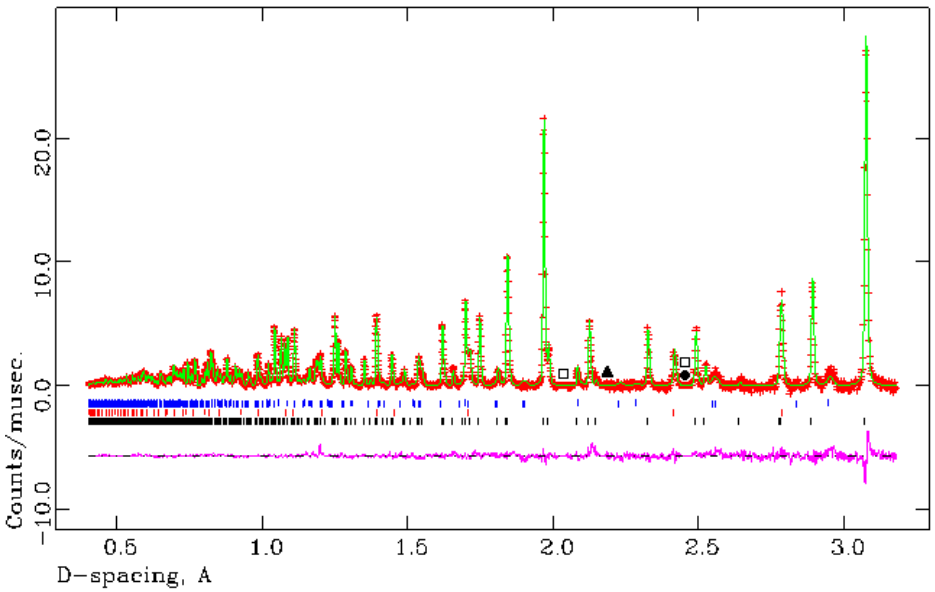

Figure 5-10: Observed, calculated and difference (OCD) plot from the structural refinement of sample 38 at 400 K, 145° (C) bank.

The black tickmarks indicate reflections from LiCaN, the red tickmarks indicate reflections from CaO and the blue tickmarks indicate reflections from $LiNH_2$. The white square represents reflections from Ca_3N_2, the black triangle represents reflections from the sample environment (i.e. the furnace) and the black circle represents a reflection from α-Li_3N, all of which have been excluded.

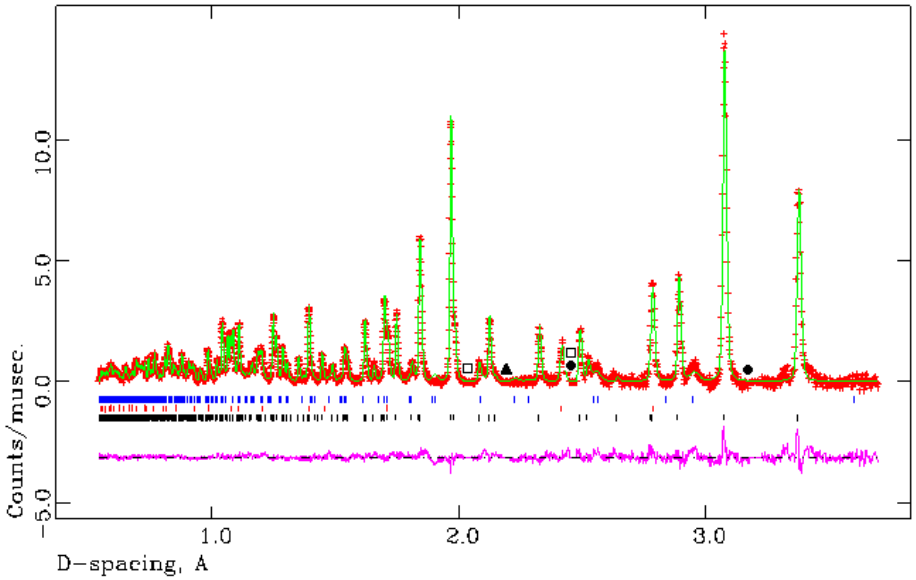

Figure 5-11: Observed, calculated and difference (OCD) plot from the structural refinement of sample 38 at 400 K, 90° (E) bank.

The black tickmarks indicate reflections from LiCaN, the red tickmarks indicate reflections from CaO and the blue tickmarks indicate reflections from $LiNH_2$. The white square represents reflections from Ca_3N_2, the black triangle represents reflections from the sample environment (i.e. the furnace) and the black circles represent reflections from α-Li_3N, all of which have been excluded.

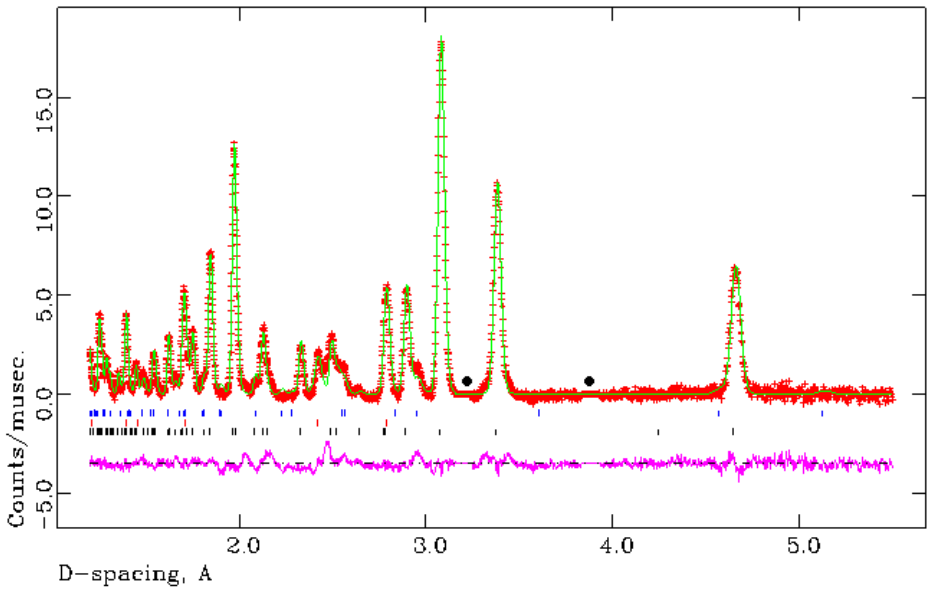

Figure 5-12: Observed, calculated and difference (OCD) plot from the structural refinement of sample 38 at 400 K, 35° (A) bank.
The black tickmarks indicate reflections from LiCaN, the red tickmarks indicate reflections from CaO and the blue tickmarks indicate reflections from $LiNH_2$. The black circles indicate reflections from α-Li_3N which have been excluded.

Table 5-15: Atom positions and anisotropic temperature factors for the LiCaN phase of sample 38 at 400 K generated by PND Rietveld refinement.

Atom	Li	Ca	N
Site	4c	4c	4c
x	0.0463 (4)	0.1561 (2)	0.40588 (7)
y	0.25	0.25	0.25
z	0.5702 (6)	0.0261 (2)	0.2413 (2)
100 x U_{11} / Å^2	1.5 (1)	0.64 (4)	1.35 (2)
100 x U_{22} / Å^2	0.5 (1)	0.96 (5)	1.00 (2)
100 x U_{33} / Å^2	2.1 (2)	0.95 (5)	1.12 (3)
100 x U_{12} / Å^2	0	0	0
100 x U_{13} / Å^2	-0.4 (1)	0.01 (4)	-0.12 (3)
100 x U_{23} / Å^2	0	0	0
Occupancy	1.00	1.00	1.00

As expected, the bond lengths expand as the temperature increases. Although the interatomic distances do not differ greatly from sample **37** to sample **38** (300 K to 400 K), a subtle thermal expansion result is evident from the values generated by Rietveld refinements. A comparison of the interatomic distances by employment of PND at 300 K and 400 K is shown in Table 5.16. The bond angles obtained Rietveld refinement of samples **37** and **38** are displayed in Table 5.17 however the increase in temperature from 300 K to 400 K had little effect.

Table 5-16: Comparison of interatomic distances of LiCaN obtained by Rietveld analysis of PND data of samples 37 and 38 collected at 300 and 400 K respectively.

Interatomic Distance / Å	Temperature / K	
	300	**400**
2x Li1-Li1	2.160 (3)	2.155 (3)
1x Li1-Ca1	2.689 (3)	2.704 (3)
3x Li1-N1	2.107 (2), 2x 2.110 (3)	2.118 (2), 2x 2.106 (3)
4x Ca1-N1	2.434 (2), 2x 2.4887 (8), 2.491 (2)	2.440 (2), 2x 2.4906 (8), 2.491 (2)

Table 5-17: Comparison of bond angles within LiCaN obtained by Rietveld analysis of PND data of samples 37 and 38 collected at 300 and 400 K respectively.

Bond Angle / ^{o}	Temperature / K	
	300	**400**
1x Li1-Li1-Li1	117.2 (3)	118.0 (3)
2x Li1-Li1-Ca1	118.5 (2)	117.8 (2)
3x Li1-Li1-N1	59.25 (7), 169.3 (2), 59.1 (1)	59.04 (8), 168.8 (3), 59.6 (2)
3x N1-Li1-N1	122.1 (2), 2x 118.36 (8)	121.5 (2), 2x 118.63 (8)
6x N1-Ca1-N1	2x 119.94 (4), 119.27 (3), 95.61 (4), 2x 98.52 (4)	2x 119.77 (4), 119.27 (4), 95.76 (4), 2x 98.63 (4)

5.3.4.2 PND study of $Li_{3-x}Ca_xN_{1+x/3}$ at 300 and 400 K

The second PND experiment was based on $Li_{3-x}Ca_xN_{1+x/3}$ (x = 1.6). Since an excess of Li_3N was used to synthesise stoichiometric LiCaN (refer to Section 5.3.4.1), a 25 wt. % increase of Li_3N was also used for these reactions (samples **39** and **40**) to ensure a true comparison could be drawn from the results obtained for both sets of samples (**37** and **38** versus **39** and **40**). However, it should be noted that since such a high excess of Li_3N was used in the reactions, controlling the stoichiometry proved problematic. The aim of this part of the study was to try and introduce defects (essentially Li^+ vacancies) into the material and obtain further structural information. Furthermore, the study aimed to investigate a possible link between the Li-Ca-N and Li-Mg-N systems as a consequence of the defect structures existing within the Li-Mg-N system as reported by Yamane *et al* and Bailey *et al*. [1, 2]

Selected refinement data are shown in Table 5.18 and Figures 5.13, 5.14 and 5.15 show the observed, calculated and difference (OCD) plots for data collected at 300 K at the 145^o (C), 90^o (E) and 35^o (E) detector banks. As in samples **37** and **38** above, it should be noted that the sample was not single phase. PXD measurements had failed to highlight the presence of Ca_3N_2 in these particular samples. In accordance with the previous sample, the main phase was fitted to a model based on the structure of LiCaN proposed by Cordier *et al*. [3] The impurity phases of CaO [14] and Ca_3N_2 [16] were also fitted to theoretical models relatively well. Atomic positions and anisotropic temperature factors for the main phase of sample **39**, LiCaN, are displayed in Table 5.19.

Table 5-18: Selected Rietveld refinement data from the PND refinement of sample 39 at 300 K.

Empirical Formula	LiCaN	CaO	Ca_3N_2
Collection Temperature / K		300	
Crystal system	Orthorhombic	Cubic	Cubic
Space Group	*Pnma*	*Fm-3m*	*I 21/a-3*
Lattice parameters / Å	a = 8.4839 (1)	a = 4.8219 (3)	a = 11.469 (1)
	b = 3.6823 (10)	-	-
	c = 5.5499 (10)	-	-
V / Å ^{3}	173.371 (4)	112.11 (1)	1508.62 (24)
Z	4	4	16
Unit cell formula weight, M_w	244.112	224.316	2374.064
Density (g/cm^3)	2.338	3.323	2.611
wt. %	88.873 (2)	4.452 (2)	4.675 (2)
No. of varied parameters		82	
No. of observations		11976	
R_{wp}		0.0125	
R_p		0.0270	
χ^2		1.836	

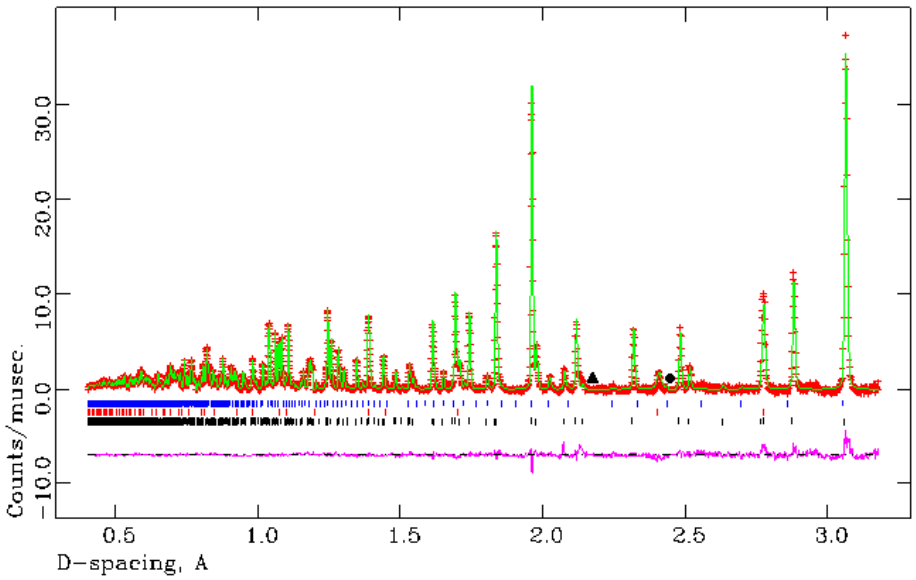

Figure 5-13: Observed, calculated and difference (OCD) plot from the structural refinement of sample 39 at 300 K, 145° (C) bank.

The black tickmarks indicate reflections from LiCaN, the red tickmarks indicate reflections from CaO and the blue tickmarks indicate reflections from Ca_3N_2. The black triangle indicates a reflection from the sample environment (i.e. the furnace) and the black circle indicates a reflection from α-Li_3N, both of which have been excluded.

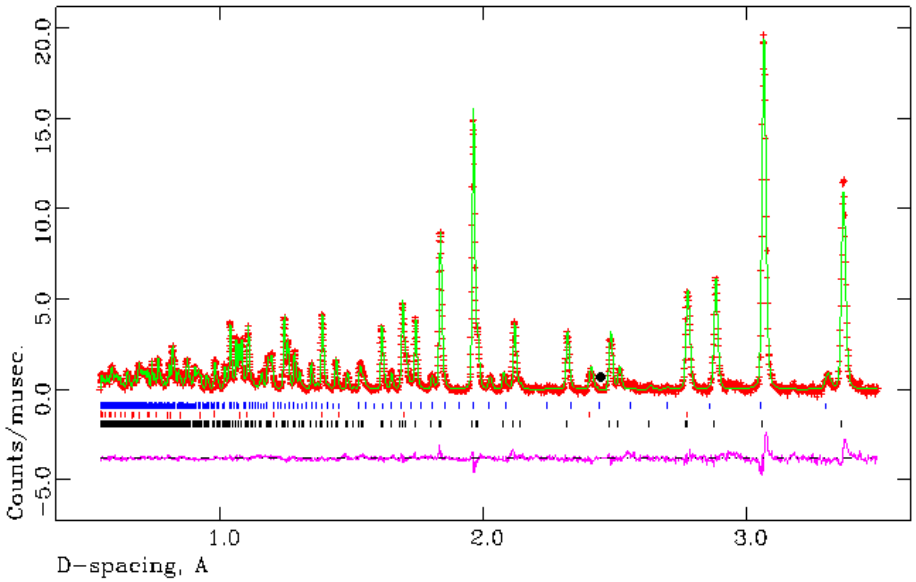

Figure 5-14: Observed, calculated and difference (OCD) plot from the structural refinement of sample 39 at 300 K, 90° (E) bank.

The black tickmarks indicate reflections from LiCaN, the red tickmarks indicate reflections from CaO and the blue tickmarks indicate reflections from Ca_3N_2. The black circle indicates a reflection from α-Li_3N which has been excluded.

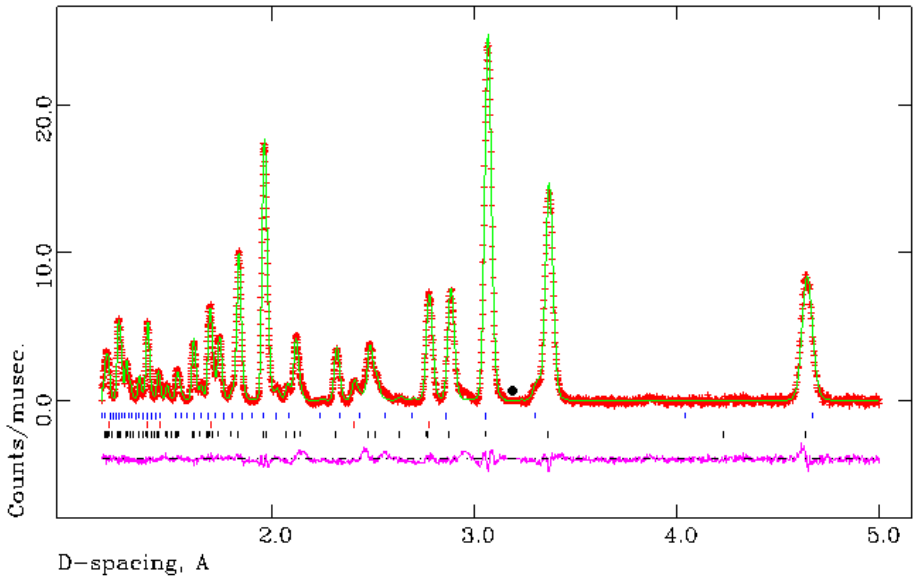

Figure 5-15: Observed, calculated and difference (OCD) plot from the structural refinement of sample 39 at 300 K, 35° (A) bank.
The black tickmarks indicate reflections from LiCaN, the red tickmarks indicate reflections from CaO and the blue tickmarks indicate reflections from Ca_3N_2. The black circle indicates a reflection from α-Li_3N which has been excluded.

Table 5-19: Atom positions and anisotropic temperature factors for the LiCaN phase of sample 39 generated by PND Rietveld refinement at 300 K.

Atom	Li	Ca	N
Site	4c	4c	4c
x	0.0473 (2)	0.1562 (1)	0.40639 (5)
y	0.25	0.25	0.25
z	0.5718 (4)	0.0261 (1)	0.2411 (1)
100 x U_{11} / Å^2	1.49 (8)	0.38 (3)	0.94 (1)
100 x U_{22} / Å^2	0.27 (7)	0.86 (3)	0.67 (1)
100 x U_{33} / Å^2	1.40 (10)	0.52 (3)	0.75 (2)
100 x U_{12} / Å^2	0	0	0
100 x U_{13} / Å^2	-0.64 (7)	0.04 (2)	-0.05 (2)
100 x U_{23} / Å^2	0	0	0
Occupancy	1.00	1.00	1.00

From the information obtained from Rietveld refinement, it is evident that the lattice parameters in sample **39** differ from those reported in the literature [3] which may be indicative of a subtle change in composition. However, on varying the Li and N occupancies, a value of greater than 1 was obtained which does not make chemical sense and when attempting to vary the Ca occupancy, it only varied by 0.01. Bailey *et al* stated that the defect structures reported within the Li-Mg-N system were controlled by composition and temperature. [2] Furthermore, Stoeva *et al* reported that reaction conditions such as reaction duration and temperature can have an effect on the levels of vacancies within the structure of nitridometallates. [17] It is therefore possible that if the parameters used during the synthesis of LiCaN were altered then this may offer a route by which vacancies can be induced and controlled.

The LiCaN phase of sample **39** was also refined against a cubic model in attempt to compare this system to the Li-Mg-N system as described by Bailey *et al*, [2] however attempts were unsuccessful and the best model for LiCaN in this work is most certainly an orthorhombic model (space group *Pnma*).

Further PND data were collected at 400 K. Selected Rietveld refinement data for sample **40** are shown in Table 5.20 and Figures 5.16, 5.17 and 5.18 show the observed, calculated and difference (OCD) plots for data collected at this temperature at the 145^{o} (C), 90^{o} (E) and 35^{o} (E) detector banks. In accordance with the previous sample, the main phase was fitted to the theoretical model proposed by Cordier *et al*. [3] The impurity phases of CaO [14] and Ca_3N_2 [16] were also fitted to theoretical models relatively well. As expected, an increase in lattice parameters was evident which is consistent with thermal expansion. Atomic positions and anisotropic temperature factors for sample **40** are displayed in Table 5.21.

Table 5-20: Selected Rietveld refinement data from the PND refinement of sample 40 at 400 K.

Empirical Formula	LiCaN	CaO	Ca_3N_2
Collection temperature / K		400	
Crystal system	Orthorhombic	Cubic	Cubic
Space Group	*Pnma*	*Fm-3m*	*I 21/a-3*
Lattice parameters / Å	a = 8.4929 (1)	a = 4.8279 (4)	a = 11.4837 (9)
	b = 3.6886 (10)	-	-
	c = 5.5574 (10)	-	-
V / Å ^{3}	174.096 (4)	112.53 (1)	1514.40 (21)
Z	4	4	16
Unit cell formula weight, M_w	244.112	224.316	2372.064
Density (g/cm^3)	2.340	3.327	2.614
wt. %	89.944 (2)	5.786 (2)	4.270 (2)
No. of varied parameters		83	
No. of observations		11864	
R_{wp}		0.0121	
R_p		0.0249	
χ^2		2.260	

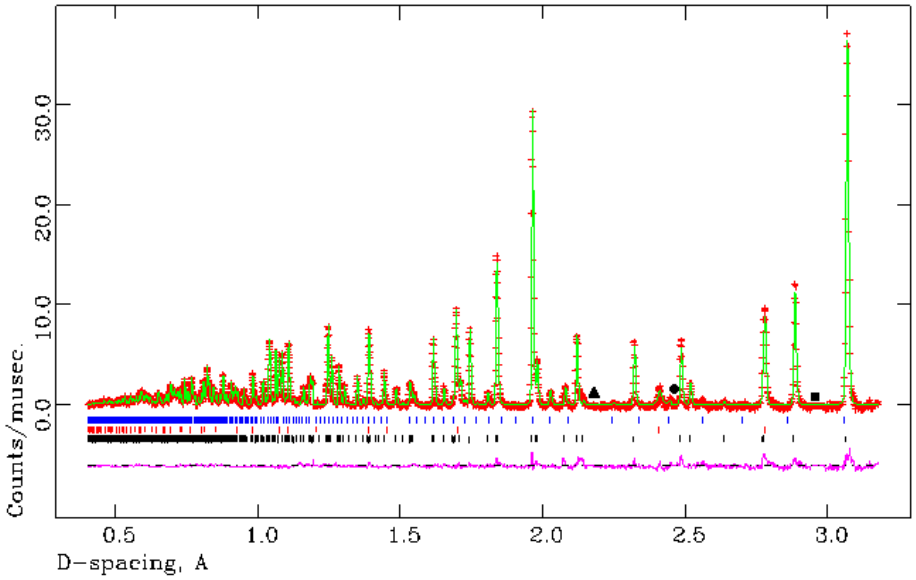

Figure 5-16: Observed, calculated and difference (OCD) plot from structural refinement of sample 40 at 400 K, 145° (C) bank.

The black tickmarks indicate reflections from LiCaN, the red tickmarks indicate reflections from CaO and the blue tickmarks indicate reflections from Ca_3N_2. The black triangle indicates a reflection from the sample environment (i.e. the furnace), the black circle indicates a reflection from α-Li_3N and the black square indicates a reflection from $LiNH_2$, all of which have been excluded.

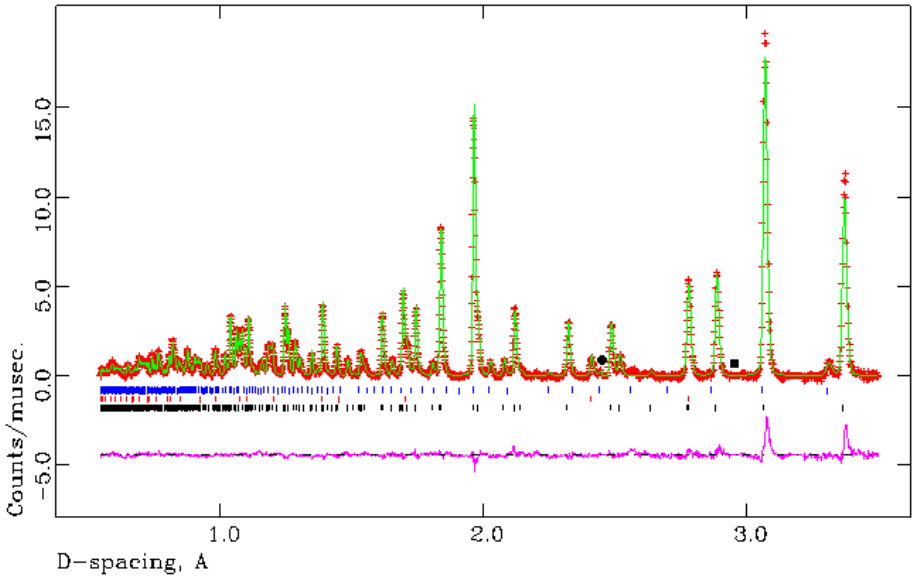

Figure 5-17: Observed, calculated and difference (OCD) plot from structural refinement of sample 40 at 400 K, 90° (E) bank.

The black tickmarks indicate reflections from LiCaN, the red tickmarks indicate reflections from CaO and the blue tickmarks indicate reflections from Ca_3N_2. The black circle indicates a reflection from α-Li_3N and the black square indicates a reflection from $LiNH_2$, both of which have been excluded.

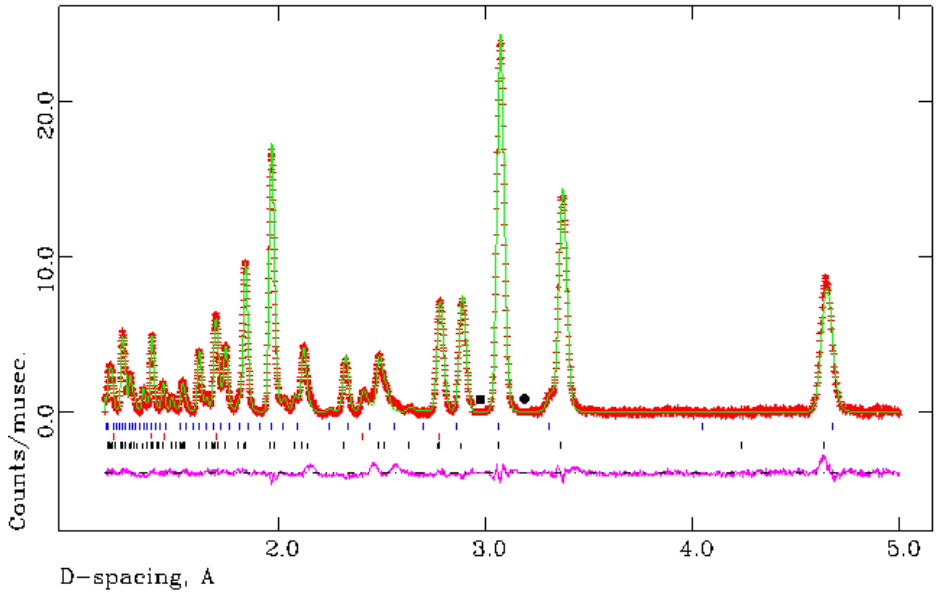

Figure 5-18: Observed, calculated and difference (OCD) plot from structural refinement of sample 40 at 400 K, 35° (A) bank.

The black tickmarks indicate reflections from LiCaN, the red tickmarks indicate reflections from CaO and the blue tickmarks indicate reflections from Ca_3N_2. The black circle indicates a reflection from α-Li_3N and the black square indicates a reflection from $LiNH_2$, both of which have been excluded.

Table 5-21: Atom positions and anisotropic temperature factors for the LiCaN phase of sample 40 generated by PND Rietveld refinement at 400 K.

Atom	Li	Ca	N
Site	4c	4c	4c
x	0.0476 (3)	0.1561 (1)	0.40615 (2)
y	0.25	0.25	0.25
z	0.5712 (4)	0.0263 (1)	0.2413 (1)
100 x U_{11} / Å^2	2.04 (9)	1.17 (3)	1.76 (2)
100 x U_{22} / Å^2	1.01 (9)	1.54 (3)	1.48 (2)
100 x U_{33} / Å^2	2.59 (13)	1.31 (3)	1.56 (2)
100 x U_{12} / Å^2	0	0	0
100 x U_{13} / Å^2	-0.73 (8)	0.12 (3)	-0.06 (2)
100 x U_{23} / Å^2	0	0	0
Occupancy	1.00	1.00	1.00

Interatomic distances and bond angles obtained from Rietveld analysis of TOF PND data for sample **40** are displayed in Tables 5.22 and 5.23 respectively. In agreement with the previous findings for sample **37** and **38**, there is only a subtle difference of the interatomic distances between samples **39** and **40**. With regard to the bond angles, the temperature increase has little effect which is evident from the values displayed in Table 5.23.

Table 5-22: Comparison of interatomic distances of LiCaN obtained by Rietveld analysis of PND data of samples 39 and 40 collected at 300 and 400 K respectively.

Interatomic Distance / Å	Temperature / K	
	300	**400**
2x Li1-Li1	2.161 (2)	2.163 (2)
1x Li1-Ca1	2.685 (2)	2.692 (2)
3x Li1-N1	2x 2.104 (1), 2.108 (2)	2x 2.109 (1), 2.111 (2)
4x Ca1-N1	2.435 (1), 2x 2.485 (5), 2.482 (1)	2.437 (1), 2x 2.4879 (6), 2.485 (1)

Table 5-23: Comparison of bond angles within LiCaN obtained by Rietveld analysis of PND data of samples 39 and 40 collected at 300 and 400 K respectively.

Bond Angle / ^{o}	Temperature / K	
	300	**400**
1x Li1-Li1-Li1	116.8 (2)	117.0 (2)
2x Li1-Li1-Ca1	118.3 (1)	118.1 (1)
3x Li1-Li1-N1	59.23 (5), 168.4 (2), 59.04 (9)	59.21 (5), 168.2 (2), 59.13 (10)
3x N1-Li1-N1	121.11 (10), 2x 118.27 (5)	121.93 (11), 2x 118.33 (5)
6x N1-Ca1-N1	2x 119.87 (2), 119.29 (2), 95.64 (3), 2x 98.57 (3)	2x 119.82 (3), 119.32 (2), 95.69 (3), 2x 98.59 (3)

5.4 Conclusions

Significant developments have been made in regards to the synthesis of lithium calcium nitride. Although previous works have shown that this ternary nitride can be made conventionally, [7, 8] the novel approach using microwave technology has many advantages as outlined in Chapter 4. The microwave process is appealing due to its ability to dramatically reduce reaction times however in order to obtain the desired product, a specific set of reaction conditions must be followed. It is at this optimisation stage that the process is time consuming since each reaction parameter must be carefully investigated to ensure that the product can be ultimately synthesised quickly and easily. Using Li_3N as a starting material for microwave reactions is attractive since it is an ionic conductor and therefore heats well on exposure to microwaves. [9] As stated previously, cooling periods were employed to ensure that evaporation of Li_3N did not occur as this was reported by Houmes and zur Loye as a result of extremely rapid heating and therefore leading to the subsequent formation of incomplete products. Although reacting two nitrides, Li_3N and Ca_3N_2 in this case, starts off relatively slowly (i.e. no reaction can be observed for the first 30 seconds), rapid heating occurs and the reaction reaches completion in the remaining 90 seconds (sample **26**). When using a single mode microwave reactor, it is unknown how important the atmosphere under which the reaction is run since reactions have only been conducted under a $N_{2(g)}$ atmosphere. Although the nitrogen content of Li_3N and Ca_3N_2 should be sufficient to drive the reaction resulting in the formation of LiCaN, performing the reaction under another inert gas such as $Ar_{(g)}$ may not yield the same products. If this is the case then it would be obvious that the $N_{2(g)}$ atmosphere must play a role in the formation of the desired products and that the N content of the two starting materials is insufficient.

Until now, the structural information available on LiCaN was limited to data collected during a single crystal X-ray diffraction experiment conducted by Cordier *et al*. [3] The work in this thesis has reported detailed structural information obtained by PND at both ambient and elevated temperatures from which we have been able to report accurate Li positions and anisotropic temperature factors. Furthermore, the lattice parameters obtained from Rietveld refinement of data collected for sample **37** indicate a subtle change in composition of LiCaN. The data which was collected for sample **38** yielded lattice parameters consistent with thermal expansion, as expected. Since the elements within LiCaN, with the exception of Ca, are lighter and have a lower electron density, Li and N do not scatter well when interacting with X-rays however both interact better with neutrons.

Therefore the data collected from PND, i.e. the lattice parameters, is likely to be much more accurate for lighter elements than in comparison to PXD.

In order to compare the Li-Ca-N system with that of Li-Mg-N, a further PND study was performed which involved attempting to synthesise and characterise non-stoichiometric phases within the Li-Ca-N system. Due to the interest surrounding the Li-Mg-N system, i.e. its ability to reversibly store hydrogen and the fact that the non-stoichiometric defect structures form a compositional band (both Mg-rich and Li-rich phases) around the 1:1 LiMgN which was previously considered a line phase, the Li-Ca-N system was investigated to determine if there were any similarities within the systems. In relation to the Li-Mg-N system, by altering the stoichiometries of the starting materials, the idea was to try and introduce defects (essentially Li^+ vacancies) into the structure however at this point, only a subtle change in composition resulted, indicated by a change in lattice parameters. Furthermore, a result of thermal expansion is evident as the temperature increased from 300 K to 400 K, in agreement with the findings for samples **37** and **38**.

Table 5-24: Overview of lattice parameters for LiCaN samples 37 - 40

Lattice Parameters		PND samples			
	Literature [3]	37	38	39	40
	293 K	300 K	400 K	300 K	400 K
a **/ Å**	8.471 (3)	8.4964 (2)	8.5067 (2)	8.4839 (1)	8.4929 (1)
b **/ Å**	3.676 (2)	3.6874 (10)	3.6947 (10)	3.6823 (10)	3.6886 (10)
c **/ Å**	5.537 (3)	5.5575 (1)	5.5663 (1)	5.5496 (1)	5.5574 (10)

Furthermore, attempts were made to vary the occupancies of Li, Ca and N within the LiCaN phase however the resultant occupancies did not vary much from 1. Additionally, attempts to fit the data using an alternative model such a simple cubic structure (as reported in the Li-Mg-N system for $Li_{1.11}Mg_{0.89}N_{0.96}$, space group *Fm-3m*) proved unsuccessful proving that the orthorhombic LiCaN model [3] proposed by Cordier *et al* was the most appropriate model. Due to the fact that the stoichiometry could not be strictly controlled due to the excess 25 wt. % of Li_3N required, it is possible that this has had an adverse effect and the stoichiometry chosen to induce defects was not correct. By analogy to the Li-Mg-N system, the opportunity to introduce defects into $Li_{3-x}Ca_xN_{1+x/3}$ should lie between $1.5<x<<3$ however using a value of x = 1.6, resulted in only a subtle change in composition of the LiCaN phase.

5.5 References

[1] H. Yamane, T. H. Okabe, O. Ishiyama, Y. Waseda, M. Shimada, *Journal of Alloys and Compounds*, 2001, **319**, 124

[2] A. S. Bailey, P. Hubberstey, R. W. Hughes, C. Ritter and D. H. Gregory, *Chemistry of Materials*, 2010, **22**, 3174

[3] G. Cordier, A. Gudat, R. Kniep and A. Rabenau, *Angewante Chemie International Edition in English*, 1989, **28**, 1702

[4] J. F. Brice, J. P. Motte and R. Streiff, *Comptes Rendus de L'Académie des Sciences Paris*, 1969, **C269**, 910

[5] J. F. Brice and J. Aubry, *Comptes Rendus de L'Académie des Sciences Paris*, 1970, **C270**, 1658

[6] J. F. Brice and J. Aubry, *Comptes Rendus de L'Académie des Sciences Paris*, 1970, **C271**, 825

[7] W. X. Yuan, J. Li, G. Wang, A. G. Cheng, X. Zhao, *Journal of Crystal Growth*, 2006, **290**, 621

[8] D. J. Siddons, *PhD thesis*, University of Nottingham, 1997

[9] J. D. Houmes and H.-C zur Loye, *Journal of Solid State Chemistry*, 1997, **130**, 266

[10] M. Gasgnier, A. Loupy, A. Petit and H. Jullien, *Journal of Alloys and Compounds*, 1994, **204**, 165

[11] A.C. Larson and R.B. Von Dreele, Generalized Structure Analysis System, 1990, MS-H805, Los Alamos, NM 87545

[12] B. H. Toby, *Journal of Applied Crystallography*, 2001, **34**, 210

[13] R. I. Smith and S. Hull, User Guide for the Polaris Powder Diffractometer at ISIS Rutherford Appleton Laboratory Report, 1997, RAL-TR-97-038

[14] I. Oftedal, *Zeitschrift für Physikalische Chemie*, 1927, **128**, 154

[15] H. Jacobs and R. Juza, *Zeitschrift für anorganische und allgemeine Chemie*, 1972, **391**, 271

[16] Y. Laurent, J. Lang, M. T. le Bihan, *Acta Crystallographica B*, 1968, **24**, 494

[17] Z. Stoeva, R. I. Smith, and D. H. Gregory, *Chemistry of Materials*, 2006, **18**, 313

6 Conclusions and Future Work

This thesis describes the synthesis and characterisation of group I and II nitrides as potential hydrogen storage materials. Both conventional and novel methods were employed to synthesise binary and ternary nitrides. The main characterisation techniques employed for the work presented in this thesis are powder X-ray diffraction and powder neutron diffraction.

Lithium nitride is a material that has fascinated solid state scientists for decades due to its unique structure and stability, which is an unusual trait for binary nitrides of the alkali metals. Lithium nitride consists of three polymorphs; alpha, beta and gamma, with the latter being the least well documented. Alpha-Li_3N was reported to crystallise in space group *P6/mmm* and the beta polymorph in space group *$P6_3/mmc$*. Single phase α-Li_3N was synthesised using by flowing $N_{2(g)}$ over a Na/Li alloy which was followed by sodium distillation. PXD yielded lattice parameters of a = 3.659 (2) Å and c 3.879 (1) = Å, which is in good agreement with the literature. Applying pressure induces a phase transition from α-Li_3N to β-Li_3N and this was conducted by either use of a multi-anvil high pressure procedure (experiments were performed by Dr. Gunter Heymann and Prof. Hubert Huppertz at the Leopold-Franzens-Universität, Innsbruck, Austria) or by ball milling. With regard to the multi-anvil high pressure procedure, it was evident from the results obtained that pressure alone was not sufficient to convert α-Li_3N to β-Li_3N; heating of the sample was required to aid conversion.

Considering the second method for synthesising β-Li_3N, by employment of ball milling for 25 h, an unknown pressure was applied to form β-Li_3N (a = 3.5660 (6) Å, c = 6.356 (2) Å - PXD). It should be noted that after milling commercial Li_3N for 5 h, the sample was composed of ~98 wt. % β-Li_3N however samples were milled for 25 h in attempt to synthesise a sample which was 100 % β-Li_3N. The same trend emerged when using laboratory synthesised α-Li_3N - after ball milling for 5 h, the sample was composed of ~98 wt. % β-Li_3N. In addition to PXD, PND was employed to investigate further the structure of β-Li_3N enabling the attainment of more accurate lattice parameters and thermal displacement parameters over a variable temperature range. By employment of PND, an initial study of the structure of β-Li_3N over a variable temperature range (4.2 – 600 K) was conducted. At temperatures below 50 K, negative thermal expansion of the a parameter occurred and on subsequent increase of temperature the structure exhibited a positive thermal expansion coefficient. At 500 K, a temperature induced phase transformation occurred from β-Li_3N to α-Li_3N and on reaching 600 K, the percentage weight fractions were 60 wt. % and 40 wt. % for the beta and alpha phases respectively.

Lithium nitride has shown potential as a hydrogen storage medium however studies into the effect of the beta polymorph of Li_3N on hydrogen uptake potential of Li_3N have never been conducted. This gap in the literature led to the investigation of the interaction of β-Li_3N with D_2. At temperatures below 50 K, negative thermal expansion was observed and solid D_2 was evident in the PND patterns. Due to the fact that this study was investigated under a pressure of approximately 10 bar, it is not unexpected for $D_{2(g)}$ to liquefy then solidify at such low temperatures. On increasing the temperature above 50 K stepwise to 400 K, positive thermal expansion resulted. Formation of $LiND_2$ and LiD occurred at 500 K and on reaching 600 K, the material was composed solely of these two phases. It should be noted that at no point during the process was Li_2ND observed. It is likely that the temperature increment from 400 K to 500 K was too large and therefore if data had been collected at temperatures within this region then the presence of Li_2ND would have been detected.

The presence of $D_{2(g)}$ would appear to inhibit expansion of the bonds within β-Li_3N and therefore has a subsequent effect on the lattice parameters. In order to reach a definitive conclusion regarding the effect of $D_{2(g)}$ on the structure of β-Li_3N, repeating the experiment using an inert gas, such as $Ar_{(g)}$, instead of $D_{2(g)}$ would possibly indicate whether the likely inhibition of lattice expansion is only a function of pressure or if the $D_{2(g)}$ is in some other way affecting the structure. Furthermore, conducting hydrogen uptake measurements (i.e. PCT measurements) using single phase α-Li_3N, β-Li_3N and then commercial Li_3N would indicate the importance and/or role of each polymorph with regards to hydrogen storage.

Further work involving the hydrogen storage mechanism of Li_3N was conducted by focusing on Li_4NH, a minority phase which has been reported to form during a proposed reaction pathway involving the decomposition of Li_3N. Li_4NH/D was synthesised using both conventional and novel means. The novel synthesis involved the employment of microwaves to facilitate the reaction between Li_3N and LiH/to form Li_4ND. A systematic study of varying reaction parameters enabled optimization of the process in order to obtain single phase Li_4NH/D. The use of microwave technology in the synthesis of ternary nitrides has offered an alternative to conventional synthetic methods and is advantageous in many regards: rapid heating and cooling rates, and selective heating. Plasma generation was an important factor in determining if the materials are still reacting or not. When plasma formation ceases, this is generally indicative of the fact that the reaction has reached completion. Although rapid heating is advantageous, it is a hindrance that the temperature cannot be controlled. A trial and error approach was employed to ascertain favourable reaction conditions which included reaction time, power and the atmosphere under which the reactions were run. Determining the

aforementioned parameters ensured that the temperature at which the reaction was conducted was not as critical as it may have been under conventional conditions.

A PND investigation of Li_4ND revealed the presence of tetragonal Li_4ND (a = 4.8843 (1) Å, c = 9.226 (3) Å) at 323 K. To ensure that the occupancies of the 4a and 4b sites were correct, i.e. the 4a site was predominantly occupied by N and the 4b site was predominantly occupied by D, bond valence calculations were performed. These calculations confirmed that the occupancies reported by Marx [1] and in this work are sensible where the anion distribution on the 4a site is 0.95/0.05 N/D and the 4b site is 0.05/0.95 N/D. When performing Rietveld analysis of Li_4ND at 323 K, a second Li_4ND phase was evident and refined as a new cubic phase (a = 4.9467 (6) Å) in which N^{3-} and D^- ions which are disordered across the *anti*-fluorite anion sites. The cubic Li_4ND phase was refined against a modified cubic *anti*-fluorite Li_2ND model proposed by Balogh *et al* [2] in which the N position is partly occupied by D. An increase in temperature to 773 K induces a phase transition resulting in cubic Li_4ND being the dominant phase.

A further PND investigation was conducted in order to obtain a further understanding of the mechanisms within the Li-N-H system; this involved an *in-situ* experiment between (1-x)Li_4ND and xLi_2ND using varying values of x (0.36, 0.5 and 0.6). After heating to 773 K, the resultant product was a cubic 'quasi-imide' phase ($Li_{4-2x}N_{1-x}D_{1-x}(ND)_x$). The various non-stoichiometric mixtures of Li_4ND and Li_2ND were analysed by using the Rietveld method and the resultant 'quasi-imide' phase was fitted to a model of cubic Li_2ND which was modified resulting in a 4a site which was occupied by both N and D. Although the data obtained were relatively poor due to the poor crystallinity of the samples or due to the insufficient data collection time, and considering the fact that the structure is a complex one, a general trend in the data emerged; as the value of x was increased, an expansion of a resulted and the cell volume (and density) increased. It should also be noted that as the value of x increases (0.36, 0.5, 0.6), the anion distribution changes; the occupancy of N^{3-} and N of $(ND)^{2-}$ on the 4a site increases as does the occupancy of protonic D of $(ND)^{2-}$ on the 192l site. Therefore, this work has demonstrated that N^{3-}, D^- and $(ND)^{2-}$ can be simultaneously accommodated within the same structure and the inclusion of both D^- and D^+ maintains the charge balance within the structure. In addition to the research performed by Weidner *et al* and Bull *et al*, [3, 4] this work confirms the likelihood of the 'quasi-imide' phase playing an important role in offering an alternative pathway with regards to hydrogen storage within the Li-N-H system.

In order to synthesise the 'quasi-imide' *in-situ*, a temperature of 773 K was employed however this temperature may be higher than required therefore TG-DTA experiments combined with mass spectrometry may give an indication of the temperature at which the phase transition occurs.

With regard to Li_2ND, in order to ascertain that no impurity phases were present in the starting material, a PND experiment was conducted on Li_2ND at 313 K and further data were then collected at 773 K before the *in-situ* 'quasi-imide' experiment was conducted. Rietveld refinement of both data sets highlighted the fact that *a* increased with temperature which is therefore consistent with positive thermal expansion.

Another focus of the research presented in this thesis was the synthesis and characterisation of LiCaN. The ternary nitride can be synthesised both conventionally and by a novel means using microwaves. Both syntheses were investigated in great depth to optimise the synthesis and attempt to obtain single phase LiCaN. Unfortunately, it was apparent from both PXD and PND data that the resultant product, by either the conventional or microwave method, had a CaO impurity. Although both synthetic methods produced a material composed of LiCaN with a CaO impurity, the novel method offered many advantages over synthesis by conventional means which has been discussed previously.

Preliminary structural investigations into the Li-Ca-N were performed in order to obtain definitive structures and information of the thermal displacement parameters at ambient and elevated temperatures. The LiCaN phase was refined to the orthorhombic structure proposed by Cordier *et al* [5] in the space group *Pnma* and by employment of the Rietveld method, lattice parameters of a = 8.4870 (5) Å, b = 3.6842 (2) and c = 5.5526 (3) Å were obtained at 300 K. Based on the work performed on the Li-Mg-N system and the desire to ascertain whether the same structural defects (essentially Li^+ vacancies) were present in the Li-Ca-N system, a further PND study was performed of $Li_{3-x}Ca_xN_{1+x/3}$ (x = 1.6) however no such defects were apparent. In order to induce defects, alternating the synthetic method may enable non-stoichiometric phases to form, i.e. longer duration times or higher temperatures may be required. [6]

Since we have ascertained accurate atomic positions and thermal parameters for LiCaN, these experiments have formed a foundation for future *in-situ* experiments to study the interaction of LiCaN with $D_{2\,(g)}$.

6.1 References

[1] R. Marx, *Zeitschrift für anorganische und allgemeine Chemie*, 1997, **623**, 1912

[2] M. P. Balogh, C. Y. Jones, J. F. Herbst, L. G. Hector, M. Kundrat Jr., *Journal of Alloys Compounds*, 2006, **420**, 326

[3] E. Weidner, D. J. Bull, I. L. Shabalin, S. G. Keens, M. T. F. Telling and D. K. Ross, *Chemical Physical Letters*, 2007, **444**, 76

[4] D. J. Bull, E. Weidner, I. L. Shabalin, M. T. F. Telling, C. M. Jewell, D. H. Gregory and D. K. Ross, *Physical Chemistry Chemical Physics*, 2010, **12**, 2089

[5] G. Cordier, A. Gudat, R. Kniep and A. Rabenau, *Angewante Chemie International Edition in English*, 1989, **28**, 1702

[6] Z. Stoeva, R. I. Smith, and D. H. Gregory, *Chemistry of Materials*, 2006, **18**, 313

7 Appendix

7.1 Chapter 3

7.1.1 A.3.1 Interatomic distances and bond angles - β-Li_3N, PXD data

Table A.3.1. Comparison of interatomic distances within α-Li_3N in un-milled and milled commercial Li_3N.

	Ball Milling Duration		
Interatomic Distance / Å	**0 h (Sample 1)**	**5 h (Sample 2)**	**25 h (Sample 6)**
2x Li1-N1	1.9355 (3)	-	-
6x Li2-N1	2.1043 (2)	-	-
Li1-Li2	2.8591 (2)	-	-

Table A.3.2. Comparison of bond angles within α-Li_3N in un-milled and milled commercial Li_3N.

	Ball Milling Duration		
Bond Angle / °	**0 h (Sample 1)**	**5 h (Sample 2)**	**25 h (Sample 6)**
N1-Li1-N1	4x 180.0 (0)	-	-
Li1-N1-Li2	4x 90.0 (0)	-	-
Li2-N1-Li2	4x 0.0 (0)	-	-

Table A.3.3. Comparison of interatomic distances within β-Li_3N in un-milled and milled commercial Li_3N.

	Ball Milling Duration		
Interatomic Distance / Å	**0 h (Sample 1)**	**5 h (Sample 2)**	**25 h (Sample 6)**
2x Li1-N1	2.0596 (2)	2.0518 (3)	2.0590 (3)
3x Li2-N1	(6x) 2.330 (5)	2.338 (2)	2.334 (5)
Li1-Li2	2.928 (8)	2.897 (3)	2.925 (7)

Table A.3.4. Comparison of bond angles within β-Li_3N in un-milled and milled commercial Li_3N.

Bond Angle / °	**Ball Milling Duration**		
	0 h (Sample 1)	**5 h (Sample 2)**	**25 h (Sample 6)**
N1-Li1-N1	2x120.00 (0) 2x119.99 (0)	2x120.00 (0) 2x119.99 (0)	2x120.00 (0) 2x119.99 (0)
Li1-N1-Li2	2x 89.991 (0) 4x 63.77 (7) 4x 63.76 (7)	2x 89.991 (0) 4x 63.98 (2) 4x 63.97 (2)	2x 89.992 (0) 4x 63.47 (9) 4x 63.47 (9)
Li2-N1-Li2	2x 117.87 (3) 2x 62.13 (3)	2x 118.67 (7) 2x 61.33 (7)	2x 116.7 (4) 2x 63.3 (4)

Table A.3.5. Comparison of interatomic distances within α-Li_3N in un-milled and milled laboratory synthesised α-Li_3N.

	Ball Milling Duration		
Interatomic Distance / Å	**0 h (Sample 7)**	**5 h (Sample 8)**	**25 h (Sample 11)**
2x Li1-N1	1.93689 (3)	-	-
6x Li2-N1	2.10609 (2)	-	-
Li1-Li2	2.86155 (2)	-	-

Table A.3.6. Comparison of bond angles within α-Li_3N in un-milled and milled laboratory synthesised α-Li_3N.

	Ball Milling Duration		
Bond Angle / °	**0 h (Sample 7)**	**5 h (Sample 8)**	**25 h (Sample 11)**
N1-Li1-N1	4x 180.0 (0)	-	-
Li1-N1-Li2	4x 90.0 (0)	-	-
Li2-N1-Li2	4x 60.0 (0)	-	-

Table A.3.7. Comparison of interatomic distances within β-Li_3N in un-milled and milled laboratory synthesised α-Li_3N.

	Ball Milling Duration		
Interatomic Distance / Å	**0 h (Sample 7)**	**5 h (Sample 8)**	**25 h (Sample 11)**
2x Li1-N1	-	2.0580 (1)	2.0568 (4)
3x Li2-N1	-	2.3391 (12)	2.365 (4)
Li1-Li2	-	2.9095 (18)	2.870 (6)

Table A.3.8. Comparison of bond angles within β-Li_3N in un-milled and milled laboratory synthesised α-Li_3N.

Bond Angle / °	Ball Milling Duration		
	0 h (Sample 7)	**5 h (Sample 8)**	**25 h (Sample 11)**
N1-Li1-N1	-	2x120.00 (0) 2x119.99 (0)	2x120.00 (0) 2x119.99 (0)
Li1-N1-Li2	-	2x 90.00 (0) 4x 63.91 (1) 4x 63.90 (1)	2x 90.00 (0) 4x 63.95 (5) 4x 63.94 (5)
Li2-N1-Li2	-	2x 118.39 (5) 2x 61.61 (5)	2x 118.6 (2) 2x 63.4 (2)

7.1.2 A.3.2 PND variable temperature measurements on β-Li_3N

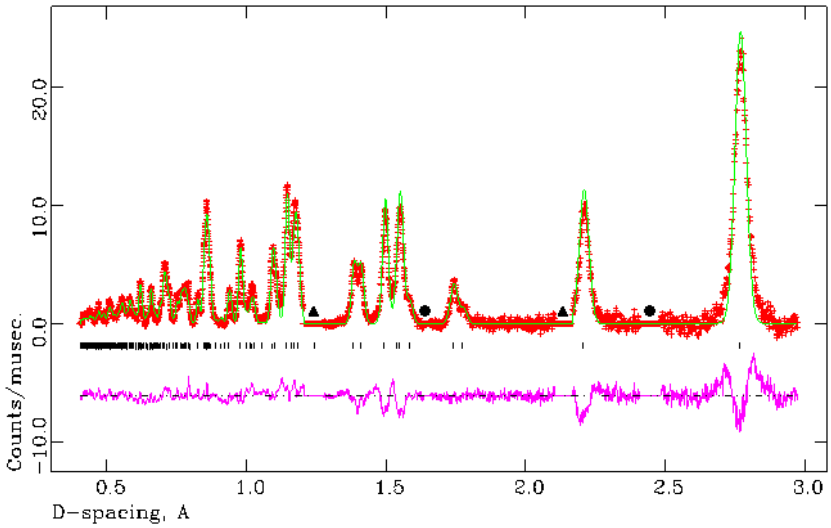

Figure A.3.1 Observed, calculated and difference (OCD) plot from the structural refinement of sample 20 (β-Li_3N at 15 K) from PND data, 145° (C) bank.
The black tickmarks indicate reflections from β-Li_3N. The black triangles represent reflections from the sample environment and the black circle represents a reflection from α-Li_3N, both of which have been excluded.

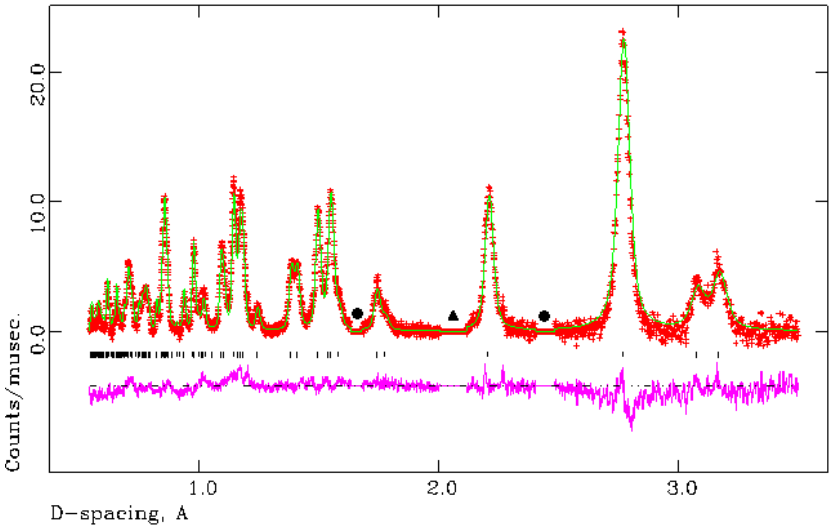

Figure A.3.2 Observed, calculated and difference (OCD) plot from the structural refinement of sample 20 (β-Li_3N at 15 K) from PND data, 90° (E) bank.
The black tickmarks indicate reflections from β-Li_3N. The black triangles represent reflections from the sample environment and the black circle represents a reflection from α-Li_3N, both of which have been excluded.

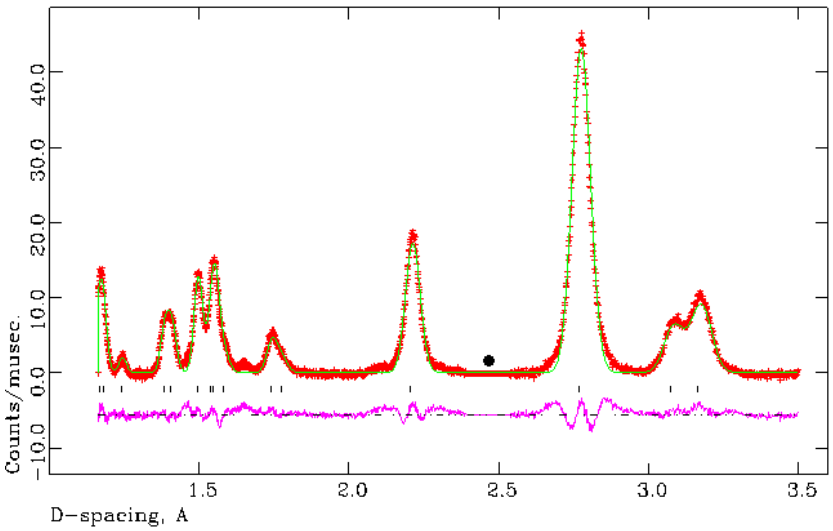

Figure A.3.3 Observed, calculated and difference (OCD) plot from the structural refinement of sample 20 (β-Li_3N at 15 K) from PND data, 35° (A) bank.
The black tickmarks indicate reflections from β-Li_3N. The black circle represents a reflection from α-Li_3N which has been excluded.

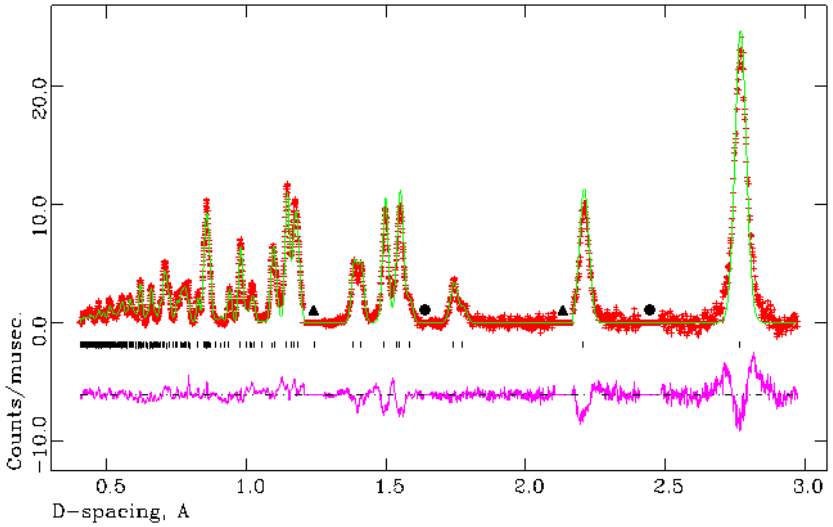

Figure A.3.4 Observed, calculated and difference (OCD) plot from the structural refinement of sample 21 (β-Li_3N at 50 K) from PND data, 145° (C) bank.
The black tickmarks indicate reflections from β-Li_3N. The black triangles represent reflections from the sample environment and the black circle represents a reflection from α-Li_3N, both of which have been excluded.

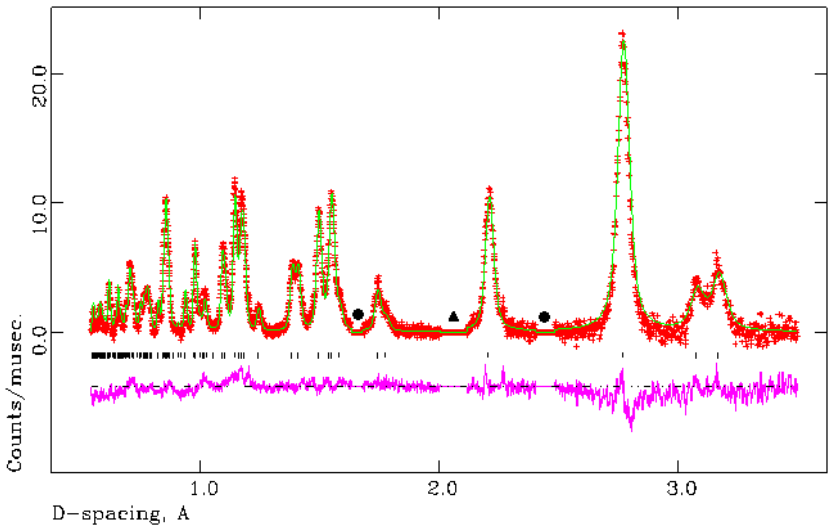

Figure A.3.5 Observed, calculated and difference (OCD) plot from the structural refinement of sample 21 (β-Li_3N at 50 K) from PND data, 90° (C) bank.
The black tickmarks indicate reflections from β-Li_3N. The black triangles represent reflections from the sample environment and the black circle represents a reflection from α-Li_3N, both of which have been excluded.

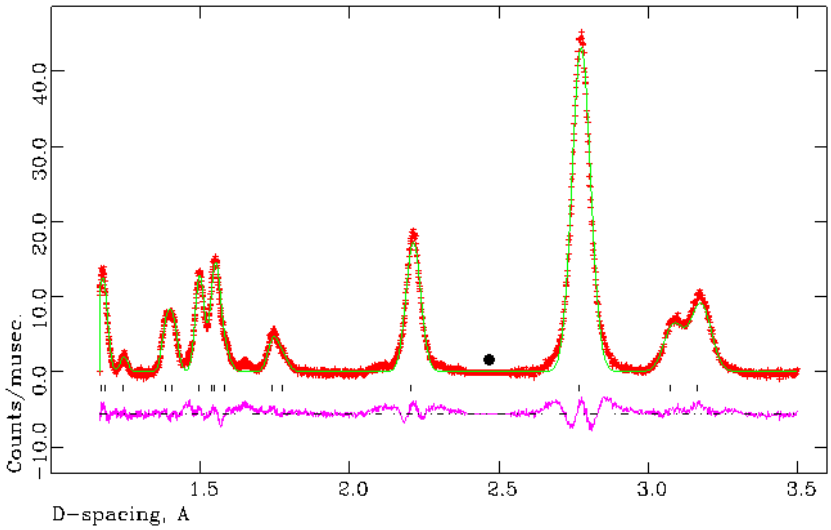

Figure A.3.6 Observed, calculated and difference (OCD) plot from the structural refinement of sample 21 (β-Li_3N at 50 K) from PND data, 35° (A) bank.
The black tickmarks indicate reflections from β-Li_3N. The black circle represents a reflection from α-Li_3N which has been excluded.

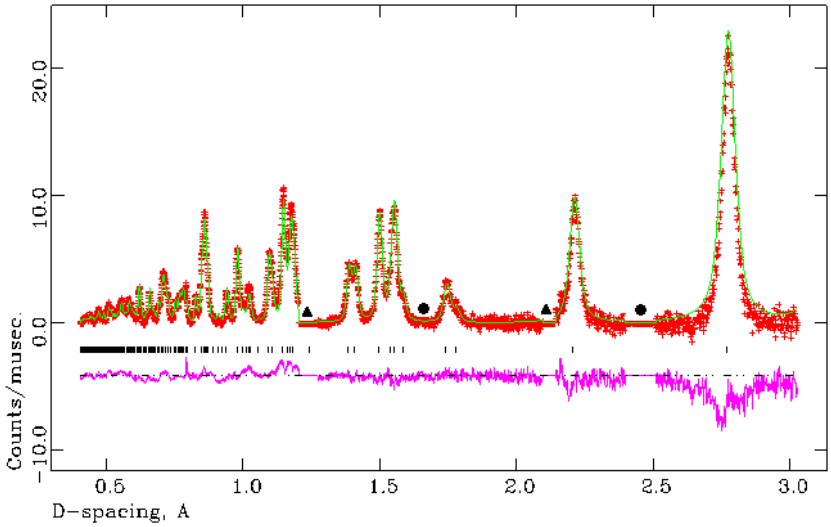

Figure A.3.7 Observed, calculated and difference (OCD) plot from the structural refinement of sample 23 (β-Li_3N at 193 K) from PND data, 145° (C) bank.
The black tickmarks indicate reflections from β-Li_3N. The black triangles represent reflections from the sample environment and the black circle represents a reflection from α-Li_3N, both of which have been excluded.

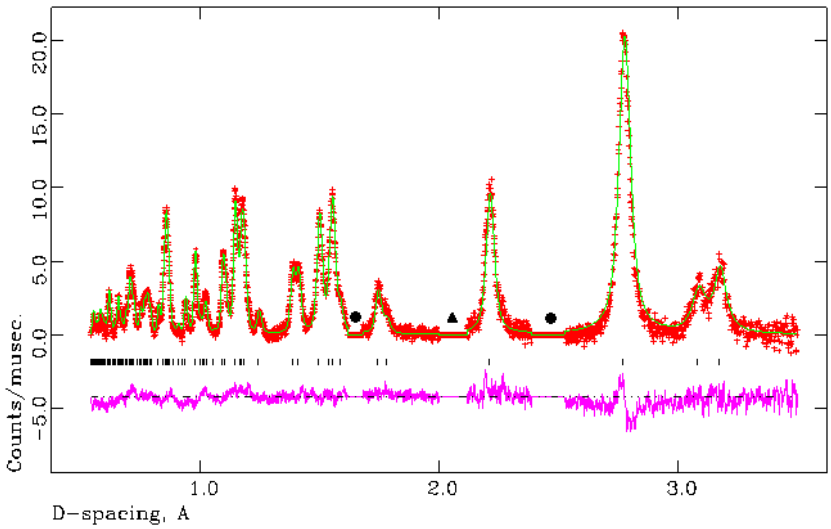

Figure A.3.8 Observed, calculated and difference (OCD) plot from structural refinement of sample 23 (β-Li_3N at 193 K) from PND data, 90° (E) bank.
The black triangle represents a reflection from the sample environment and the black circle represents a reflection from α-Li_3N, both of which have been excluded.

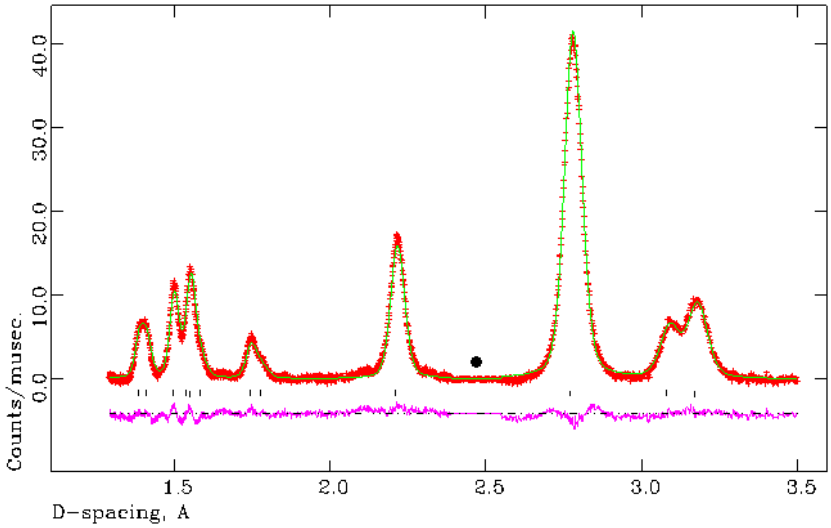

Figure A.3.9 Observed, calculated and difference (OCD) plot from structural refinement of sample 23 (β-Li_3N at 193 K) from PND data, 35° (A) bank.
The black tickmarks indicate reflections from β-Li_3N. The black circle represents a reflection from α-Li_3N which has been excluded.

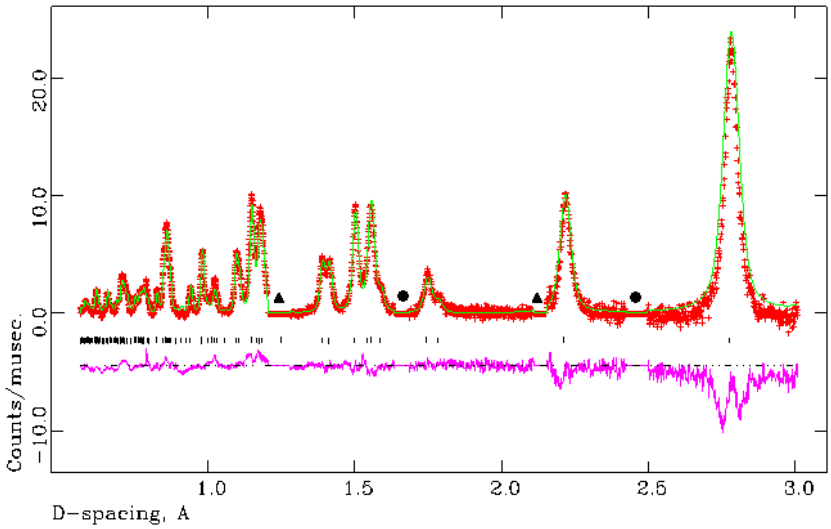

Figure A.3.10 Observed, calculated and difference (OCD) plot from the structural refinement of sample 24 (β-Li_3N at 293 K) from PND data, 145° (C) bank.
The black tickmarks indicate reflections from β-Li_3N. The black triangles represent reflections from the sample environment and the black circle represents a reflection from α-Li_3N, both of which have been excluded.

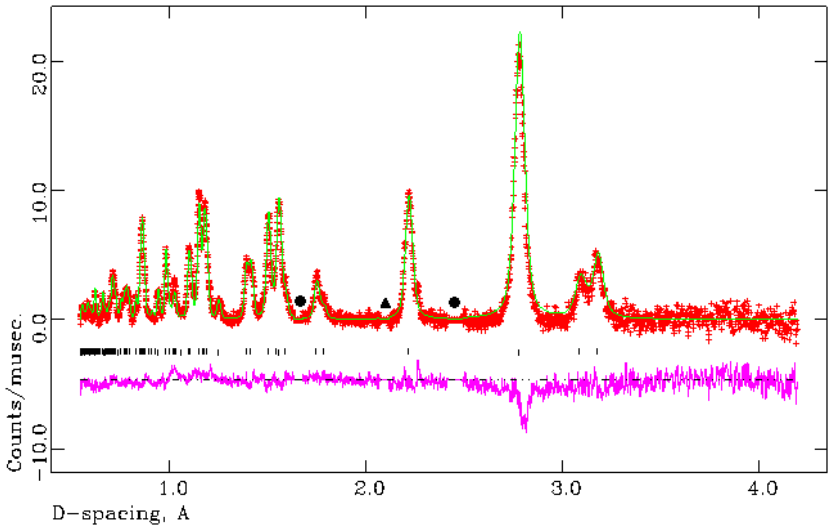

Figure A.3.11 Observed, calculated and difference (OCD) plot from structural refinement of sample 24 (β-Li_3N at 293 K) from PND data, 90° (E) bank.
The black tickmarks indicate reflections from β-Li_3N. The black triangle represents a reflection from the sample environment and the black circle represents a reflection from α-Li_3N, both of which have been excluded.

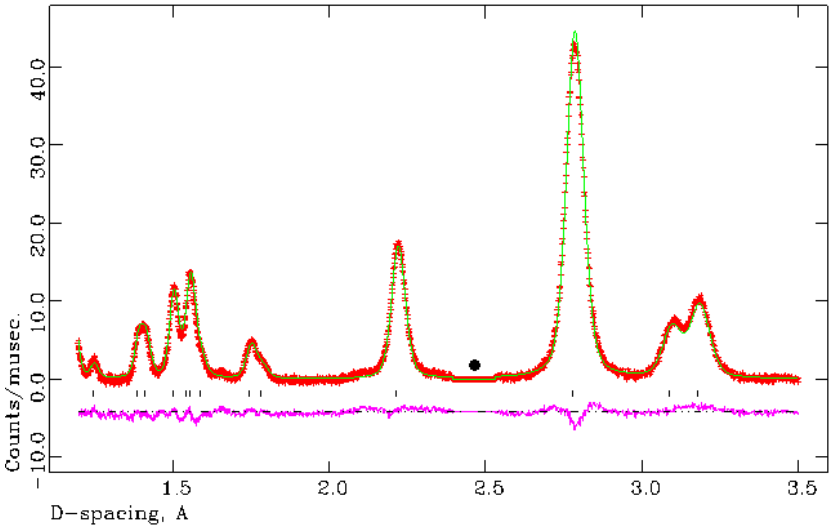

Figure A.3.12 Observed, calculated and difference (OCD) plot from structural refinement of sample 24 (β-Li_3N at 293 K) from PND data, 35° (A) bank.
The black tickmarks indicate reflections from β-Li_3N. The black circle represents a reflection from α-Li_3N which has been excluded.

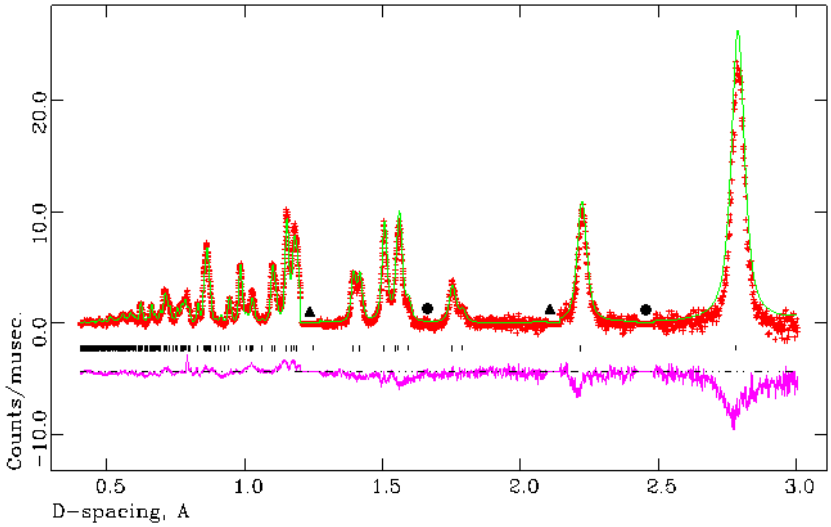

Figure A.3.13 Observed, calculated and difference (OCD) plot from the structural refinement of sample 25 (β-Li_3N at 400 K) from PND data, 145° (C) bank.
The black tickmarks indicate reflections from β-Li_3N. The black triangles represent reflections from the sample environment and the black circle represents a reflection from α-Li_3N, both of which have been excluded.

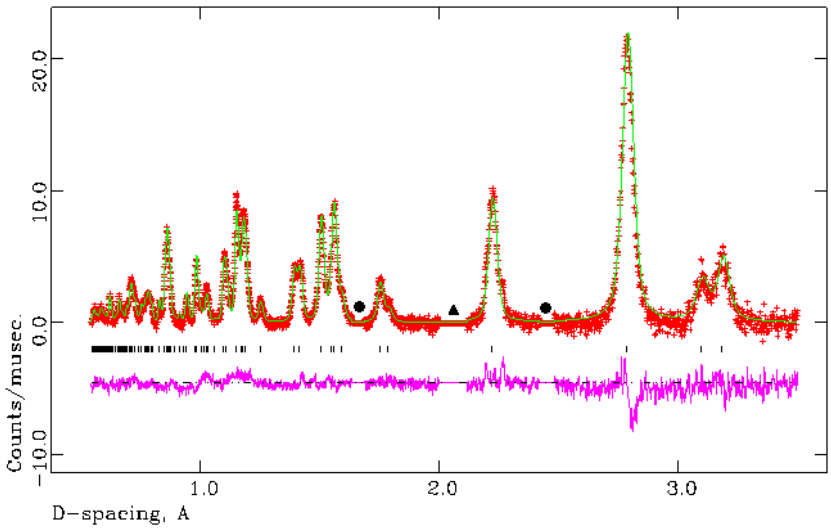

Figure A.3.14 Observed, calculated and difference (OCD) plot from structural refinement of sample 25 (β-Li_3N at 400 K) from PND data, 90° (E) bank.
The black tickmarks indicate reflections from β-Li_3N. The black triangle represents a reflection from the sample environment and the black circle represents a reflection from α-Li_3N, both of which have been excluded.

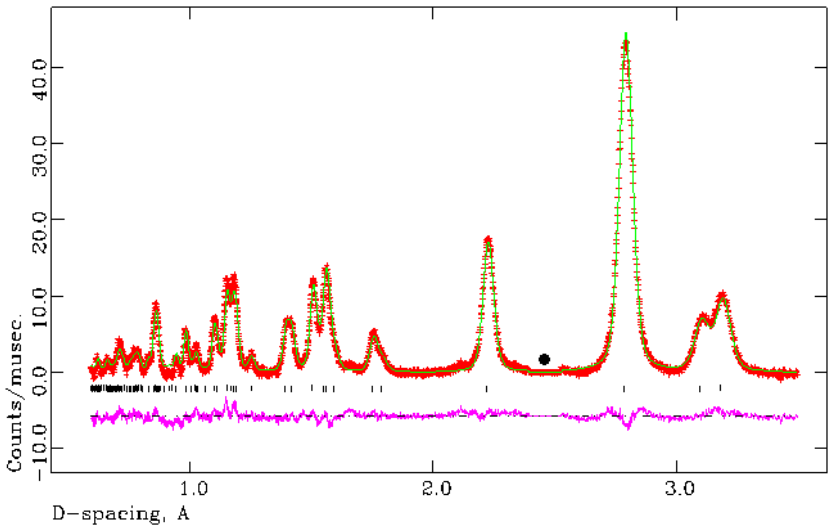

Figure A.3.15 Observed, calculated and difference (OCD) plot from structural refinement of sample 25 (β-Li_3N at 400 K) from PND data, 35° (A) bank.
The black tickmarks indicate reflections from β-Li_3N. The black circle represents a reflection from α-Li_3N which has been excluded.

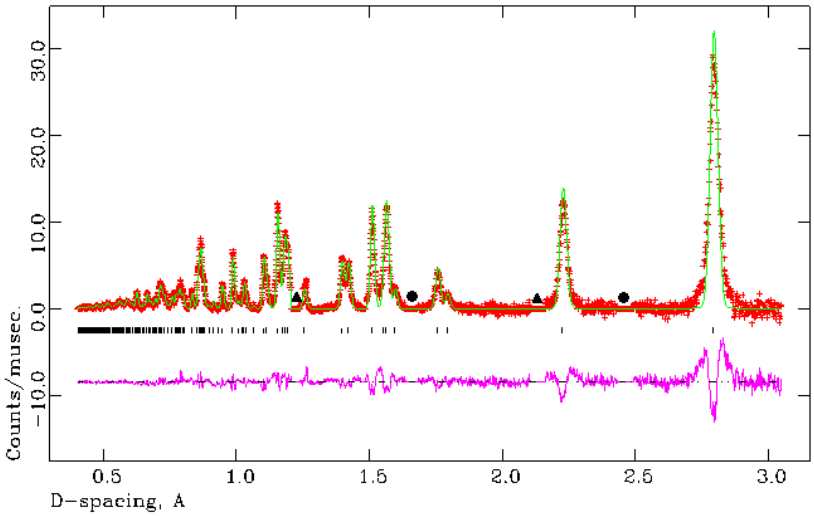

Figure A.3.16 Observed, calculated and difference (OCD) plot from the structural refinement of sample 26 (β-Li_3N at 513 K) from PND data, 145° (C) bank.
The black tickmarks indicate reflections from β-Li_3N. The black triangles represent reflections from the sample environment and the black circles represent reflections from α-Li_3N, both of which have been excluded.

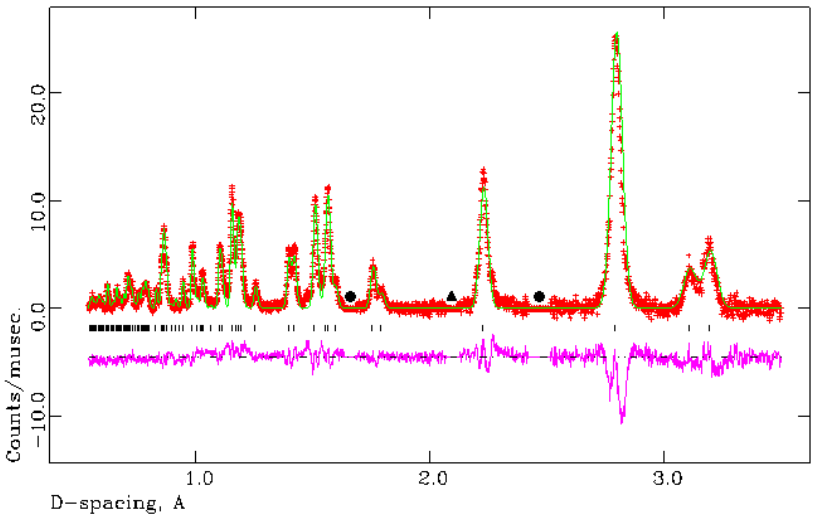

Figure A.3.17 Observed, calculated and difference (OCD) plot from structural refinement of sample 26 (β-Li_3N at 513 K) from PND data, 90° (E) bank.
The black tickmarks indicate reflections from β-Li_3N. The black triangle represents a reflection from the sample environment and the black circles represent reflections from α-Li_3N, both of which have been excluded.

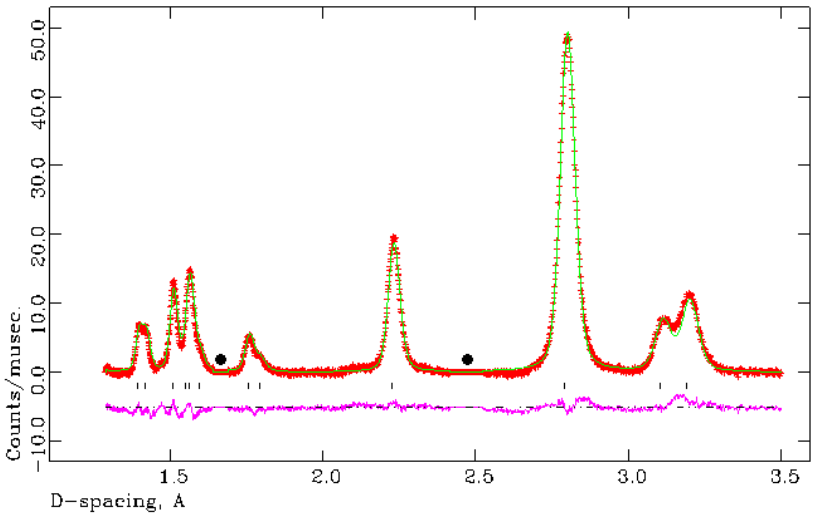

Figure A.3.18 Observed, calculated and difference (OCD) plot from structural refinement of sample 26 (β-Li_3N at 513 K) from PND data, 35° (A) bank.
The black tickmarks indicate reflections from β-Li_3N. The black circles represent reflections from α-Li_3N which have been excluded.

7.1.3 A.3.3 In-situ variable temperature measurements of β-Li_3N under D_2

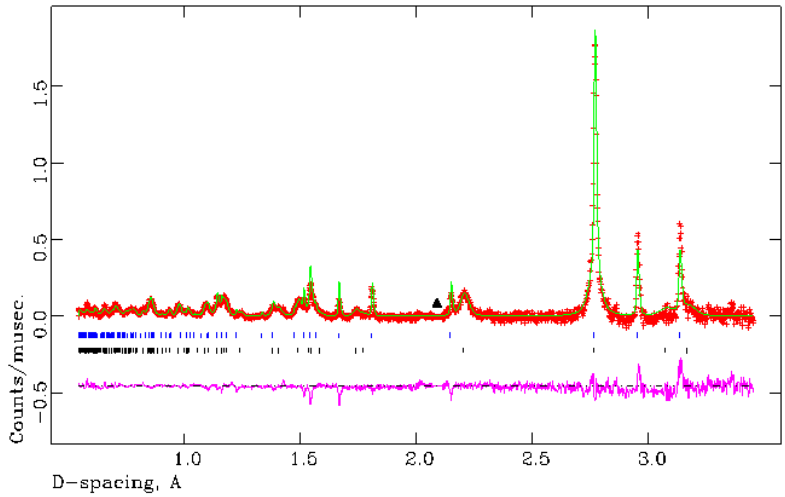

Figure A.3.19 Observed, calculated and difference (OCD) plot from structural refinement of sample 29 (β-Li_3N/D_2 at 15 K) from PND data, 90° (E) bank.
The black tickmarks indicate reflections from β-Li_3N. The black triangle represents a reflection from the sample environment.

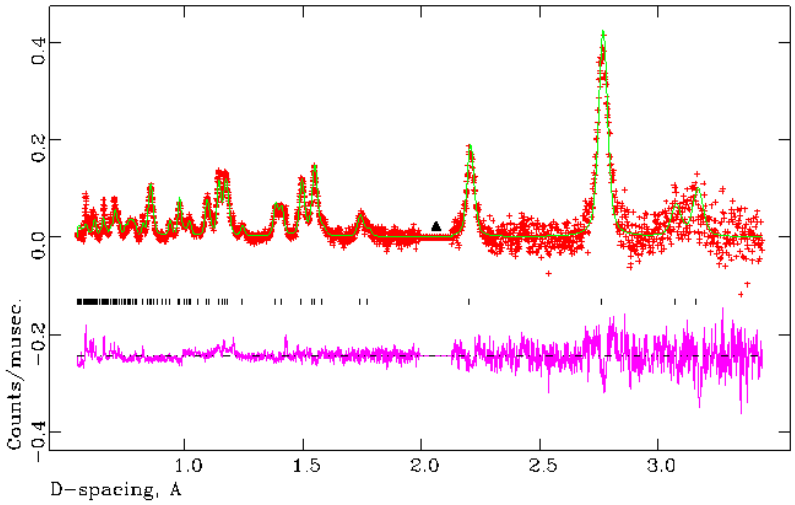

Figure A.3.20 Observed, calculated and difference (OCD) plot from structural refinement of sample 30 (β-Li_3N/D_2 at 50 K) from PND data, 90° (E) bank.
The black tickmarks indicate reflections from β-Li_3N. The black triangle represents a reflection from the sample environment.

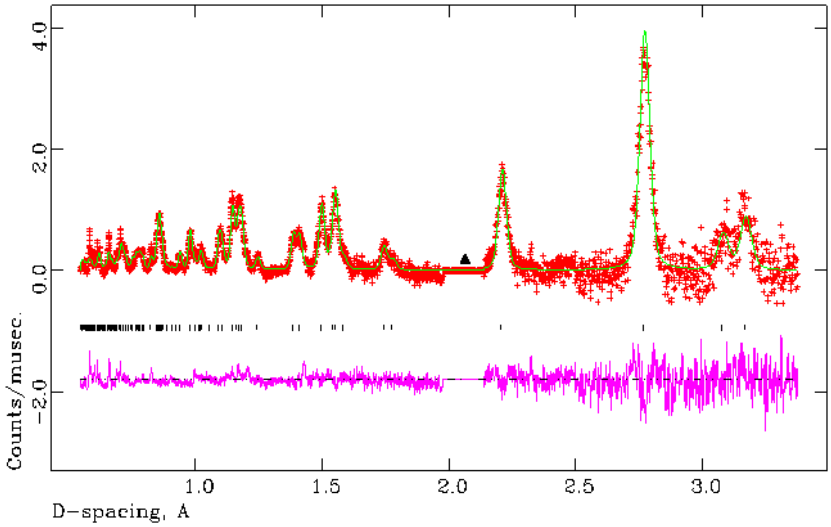

Figure A.3.21 Observed, calculated and difference (OCD) plot from structural refinement of sample 32 (β-Li_3N/D_2 at 200 K) from PND data, 90° (E) bank.
The black tickmarks indicate reflections from β-Li_3N. The black triangle represents a reflection from the sample environment.

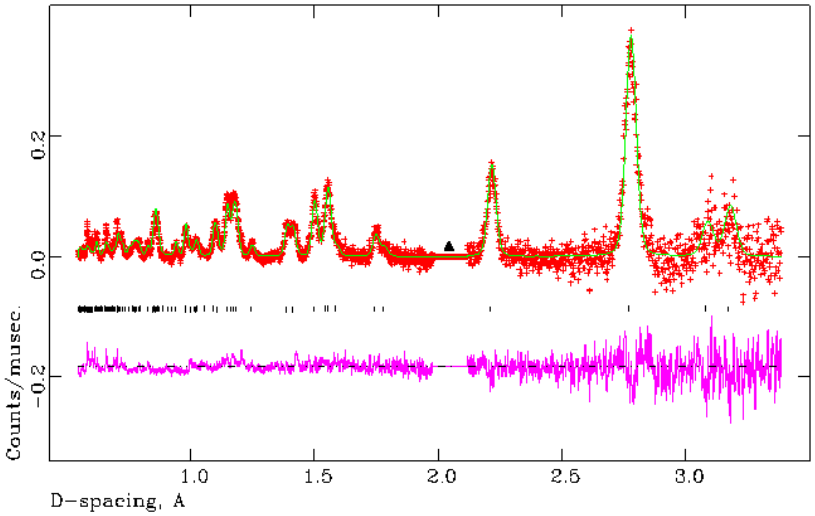

Figure A.3.22 Observed, calculated and difference (OCD) plot from structural refinement of sample 33 (β-Li_3N/D_2 at 300 K) from PND data, 90° (E) bank.
The black tickmarks indicate reflections from β-Li_3N. The black triangle represents a reflection from the sample environment.

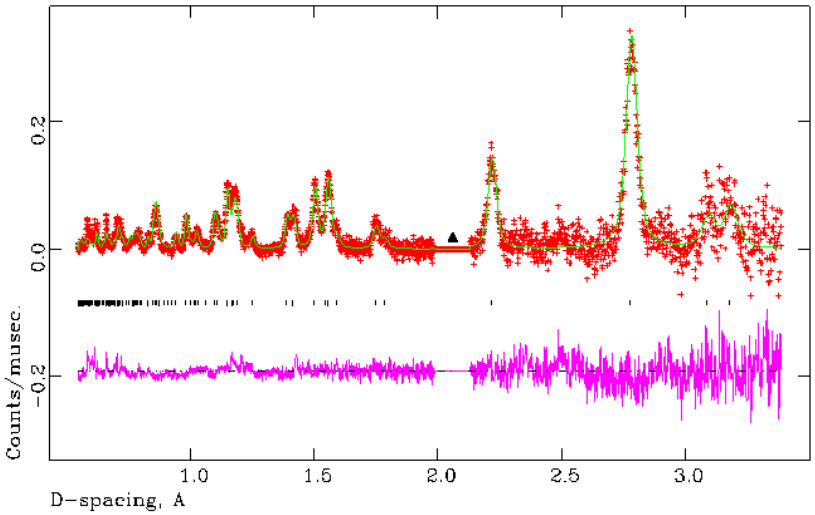

Figure A.3.23 Observed, calculated and difference (OCD) plot from structural refinement of sample 34 (β-Li_3N/D_2 at 400 K) from PND data, 90° (E) bank.
The black tickmarks indicate reflections from β-Li_3N. The black triangle represents a reflection from the sample environment.

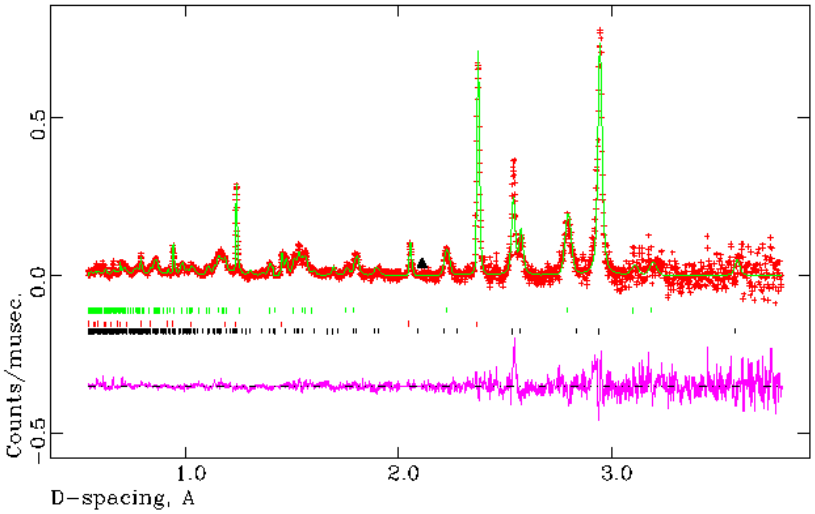

Figure A.3.24 Observed, calculated and difference (OCD) plot from structural refinement of sample 35 (β-Li_3N/D_2 at 500 K) from PND data, 90° (E) bank.
The black tickmarks indicate reflections from $LiND_2$, the red tickmarks indicate reflections from LiD and the green tickmarks indicate reflections from β-Li_3N. The black triangle represents a reflection from the sample environment.

Table A.3.9 Comparison of the interatomic distances generated by Rietveld refinement for β-Li_3N in the absence of $D_{2(g)}$.

Sample	Temperature / K	β-Li_3N		
		Li(1)-N(1)	Li(2)-N(1)	Li(1)-Li(2)
19	**4.2**	2.0526 (2)	2.080 (18)	2.9225 (13)
20	**15**	2.0523 (1)	2.0842 (18)	2.9249 (13)
21	**50**	2.0527 (2)	2.0882 (18)	2.9282 (13)
22	**100**	2.0527 (1)	2.0893 (15)	2.9287 (10)
23	**200**	2.0558 (1)	2.09113 (16)	2.93220 (15)
24	**300**	2.0603 (1)	2.0979 (19)	2.9404 (13)
25	**400**	2.0662 (1)	2.0976 (18)	2.9443 (13)
26	**500**	2.0720 (1)	2.1059 (21)	2.9540 (15)
27	**600**	2.07776 (9)	2.1118 (26)	2.9623 (19)

Table A.3.10 Comparison of the interatomic distances generated by Rietveld refinement for β-Li_3N under $D_{2(g)}$.

Sample	Temperature / K	β-Li_3N/D_2		
		Li(1)-N(1)	Li(2)-N(1)	Li(1)-Li(2)
28	**4.2**	2.0481 (4)	2.016 (8)	2.874 (6)
29	**15**	2.0483 (3)	2.023 (9)	2.879 (7)
30	**50**	2.0491 (5)	2.015 (7)	2.874 (5)
31	**100**	2.0497 (4)	2.0265 (6)	2.8821 (5)
32	**193**	2.0528 (5)	2.052 (7)	2.902 (5)
33	**293**	2.0574 (5)	2.049 (8)	2.904 (6)
34	**400**	2.0611 (5)	2.080 (9)	2.928 (6)
35	**500**	2.0712 (5)	2.12 (2)	2.955 (16)

Table A.3.11 Comparison of lattice parameters of β-Li_3N in the absence and presence of D_2.

Temperature / K	β-Li_3N		β-Li_3N/D_2	
	a / Å	c / Å	a / Å	c / Å
4.2	3.5550 (3)	6.3356 (6)	3.5477 (7)	6.3452 (20)
15	3.5546 (3)	6.3385 (7)	3.5476 (5)	6.3334 (18)
50	3.5552 (3)	6.3389 (6)	3.5490 (9)	6.3312 (21)
100	3.5552 (2)	6.3395 (5)	5.5499 (8)	6.3319 (19)
193	3.5605 (2)	6.3445 (5)	3.5554 (8)	6.3369 (20)
293	3.5683 (3)	6.3569 (6)	3.5633 (9)	6.3545 (23)
400	3.5785 (2)	6.3744 (5)	3.5697 (9)	6.3649 (24)
500	3.5886 (2)	6.3902 (5)	3.5872 (8)	6.3875 (32)
600	3.5986 (2)	6.4000 (4)	-	-

Further information can be found on the accompanying CD.

7.1.4 A.3.4 Variable temperature PND refinements – β-Li_3N

53376_Li_3N_15K_nongas_5_c_excluded.dis
53376_Li_3N_15K_nongas_5_c_excluded.tbl

53377_Li_3N_50K_nongas_excluded_4_c.dis
53377_Li_3N_50K_nongas_excluded_4_c.tbl

53379_Li_3N_nongas_193K_nongas_4.dis
53379_Li_3N_nongas_193K_nongas_4.tbl

53380_Li_3N_293K_3.dis
53380_Li_3N_293K_3.tbl

53381_Li_3N_400K_nongas_4.dis
53381_Li_3N_400K_nongas_4.tbl

53382_Li_3N_513K_nongas_A_3.dis
53382_Li_3N_513K_nongas_A_3.tbl

7.1.5 A.3.5 Variable temperature PND refinements – β-Li_3N/D_2

E52745_Li_3N_15K_corrected_4_C.dis
E52745_Li_3N_15K_corrected_4_C.tbl

E52747_Li_3N_50K_corrected_2.dis
E52747_Li_3N_50K_corrected_2.tbl

E52751_Li_3N_200K_corrected_2.dis
E52751_Li_3N_200K_corrected_2.tbl

E52753_Li_3N_300K_corrected_2.dis
E52753_Li_3N_300K_corrected_2.tbl

E52755_Li_3N_400K_corrected_2.dis
E52755_Li_3N_400K_corrected_2.tbl

E52757_Li_3N_500K_corrected_2.dis
E52757_Li_3N_500K_corrected_2.tbl

7.2 Chapter 4

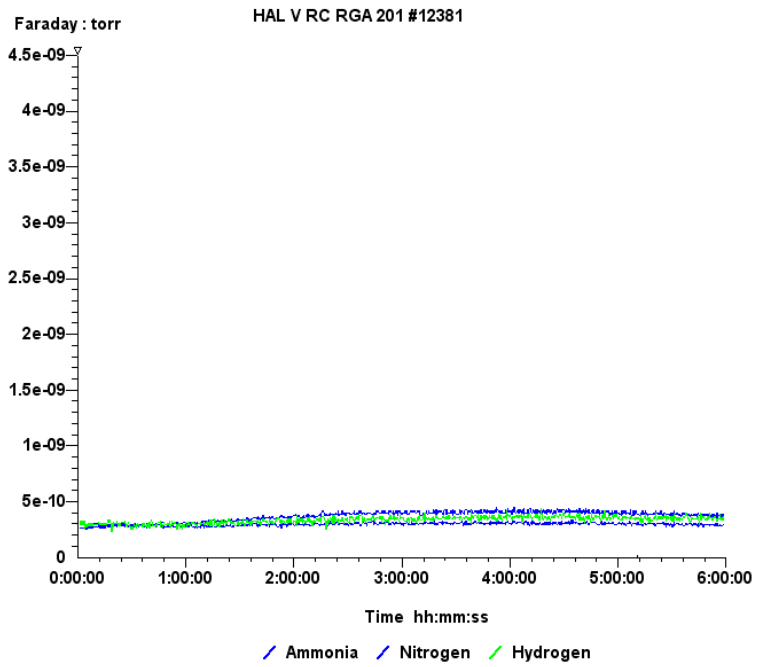

Figure A. 4.1. Mass spectrometry analysis of Li_4NH under $Ar_{(g)}$. ($NH_{3(g)}$ is shown as the top line and $N_{2(g)}$ is the bottom blue line).

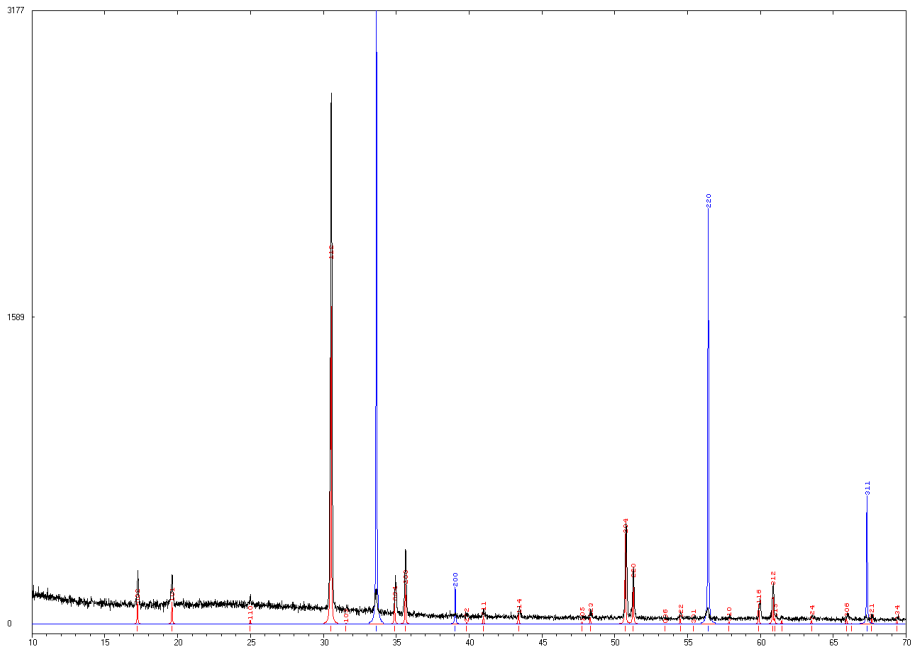

Figure A.4.2 PXD analysis of commercial $LiNH_2$ showing the experimental (black) and calculated (red – $LiNH_2$ and blue – Li_2O).

7.2.1 A.4.1 Variable temperature study of Li_4ND

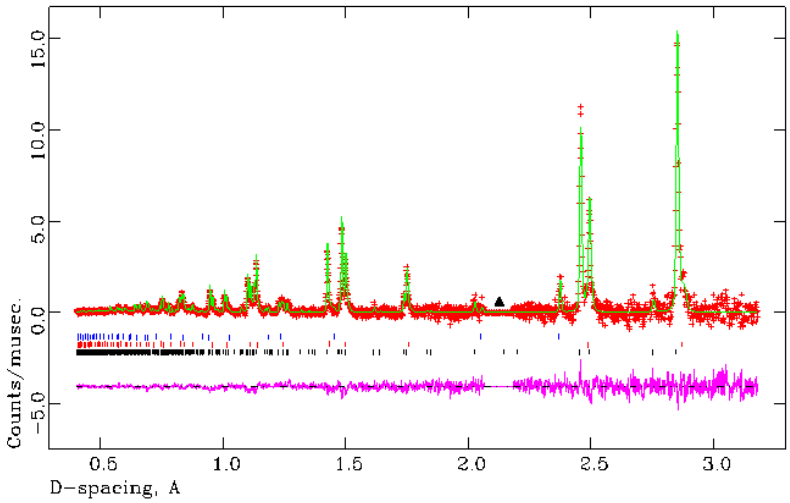

Figure A.4.3 Observed, calculated and difference (OCD) plot from structural refinement of Li_4ND at 523 K from PND data, 145° (C) bank.

The black tickmarks indicate reflections from tetragonal Li_4ND (1), the red tickmarks indicate reflections from cubic Li_4ND (1′) and the blue tickmarks indicate reflections from LiD. The black triangle represents reflections from the sample environment (i.e. the furnace and the vanadium canister) which have been excluded.

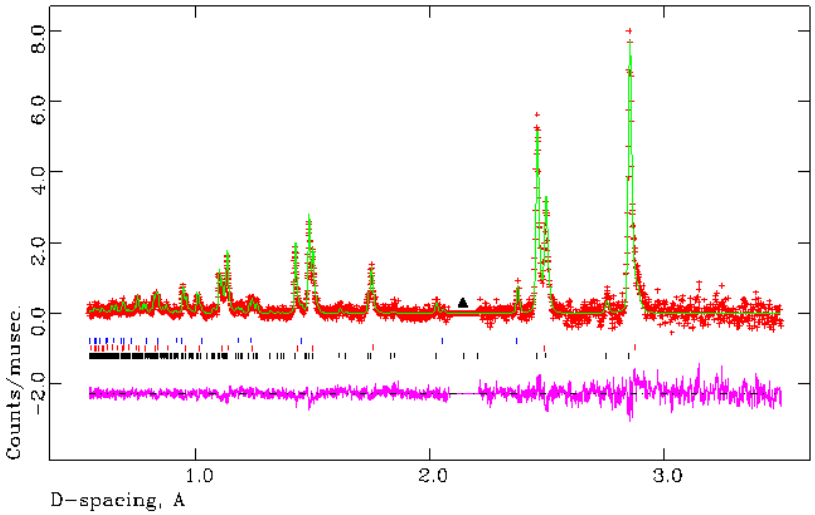

Figure A.4.5 Observed, calculated and difference (OCD) plot from structural refinement of Li_4ND at 523 K from PND data, 90° (E) bank.

The black tickmarks indicate reflections from tetragonal Li_4ND, the red tickmarks indicate reflections from cubic Li_4ND and the blue tickmarks indicate reflections from LiD. The black triangle represents reflections from the sample environment (i.e. the furnace and the vanadium canister) which have been excluded.

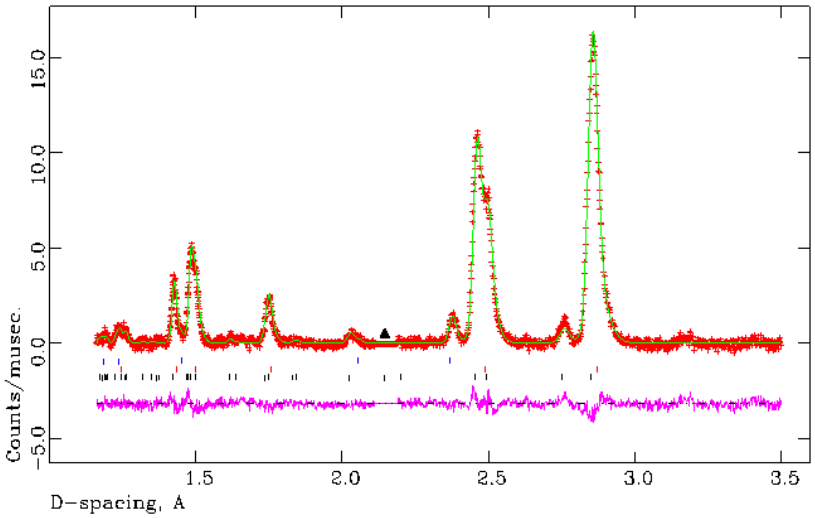

Figure A.4.6 Observed, calculated and difference (OCD) plot from structural refinement of Li_4ND at 523 K from PND data, 35° (A) bank.

The black tickmarks indicate reflections from tetragonal Li_4ND, the red tickmarks indicate reflections from cubic Li_4ND and the blue tickmarks indicate reflections from LiD. The black triangle represents reflections from the sample environment (i.e. the furnace and the vanadium canister) which have been excluded.

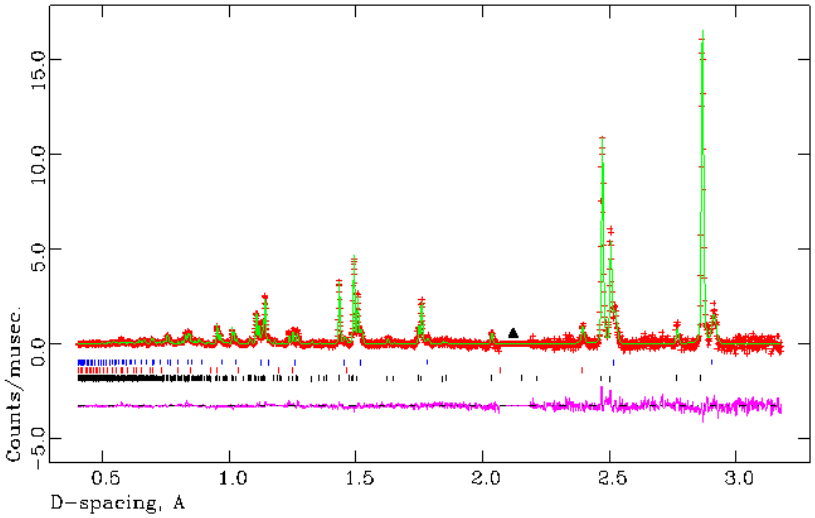

Figure A.4.7 Observed, calculated and difference (OCD) plot from structural refinement of Li_4ND at 673 K from PND data, 145° (C) bank.

The black tickmarks indicate reflections from tetragonal Li_4ND, the red tickmarks indicate reflections from LiD and the blue tickmarks indicate reflections from cubic Li_4ND. The black triangle represents reflections from the sample environment (i.e. the furnace and the vanadium canister) which have been excluded.

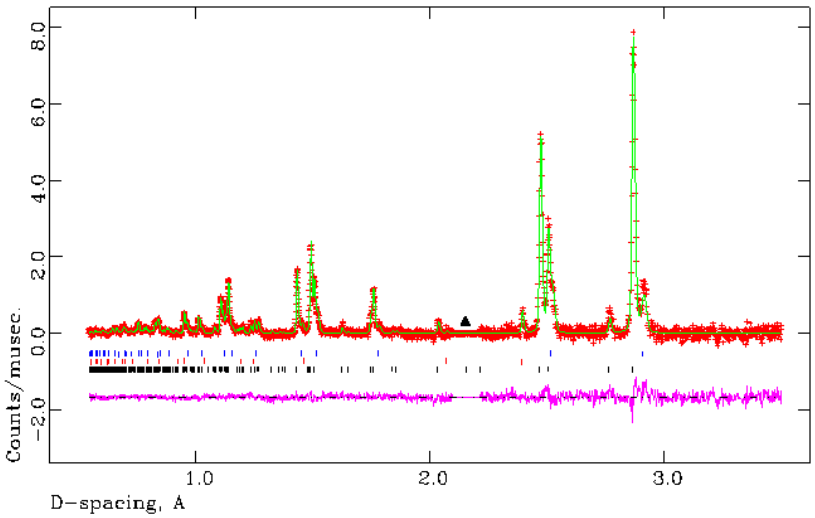

Figure A.4.8 Observed, calculated and difference (OCD) plot from structural refinement of Li_4ND at 673 K from PND data, 90° (E) bank.

The black tickmarks indicate reflections from tetragonal Li_4ND, the red tickmarks indicate reflections from LiD and the blue tickmarks indicate reflections from cubic Li_4ND. The black triangle represents reflections from the sample environment (i.e. the furnace and the vanadium canister) which have been excluded.

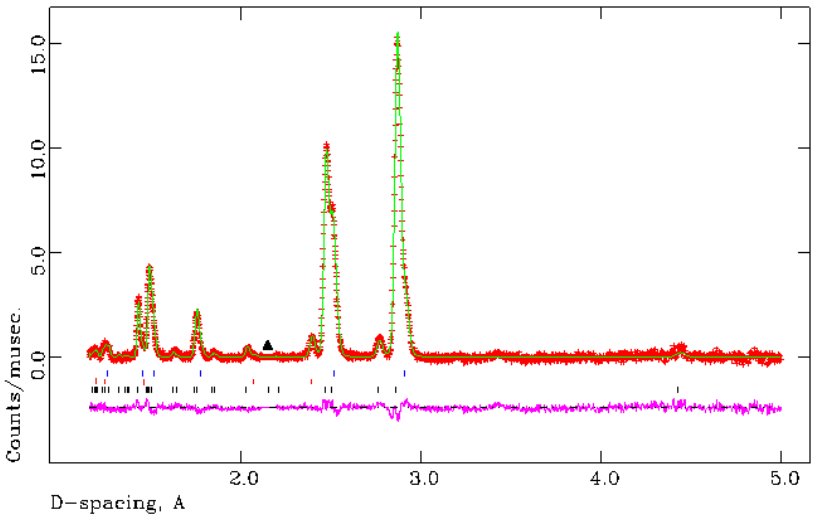

Figure A.4.9 Observed, calculated and difference (OCD) plot from structural refinement of Li_4ND at 673 K from PND data, 35° (A) bank.

The black tickmarks indicate reflections from tetragonal Li_4ND, the red tickmarks indicate reflections from LiD and the blue tickmarks indicate reflections from cubic Li_4ND. The black triangle represents reflections from the sample environment (i.e. the furnace and the vanadium canister) which have been excluded.

7.2.2 A.4.2 PND study of non-stoichiometric nitride-hydride-imide samples

313 K 57281_sample26_313K_8_D_excluded.dis
773 K 57283-98_sample26_773K_7_C_exlcuded.dis

313 K 57475_sample27_313K_16_excluded.dis
773 K 57669-80_sample27_773K_5_NS_3_exlcuded.dis

313 K 57315_sample28_313K_8_G_excluded.dis
773 K 57337_sample28_773K_9_exlcuded.dis

7.3 Chapter 5 Appendix

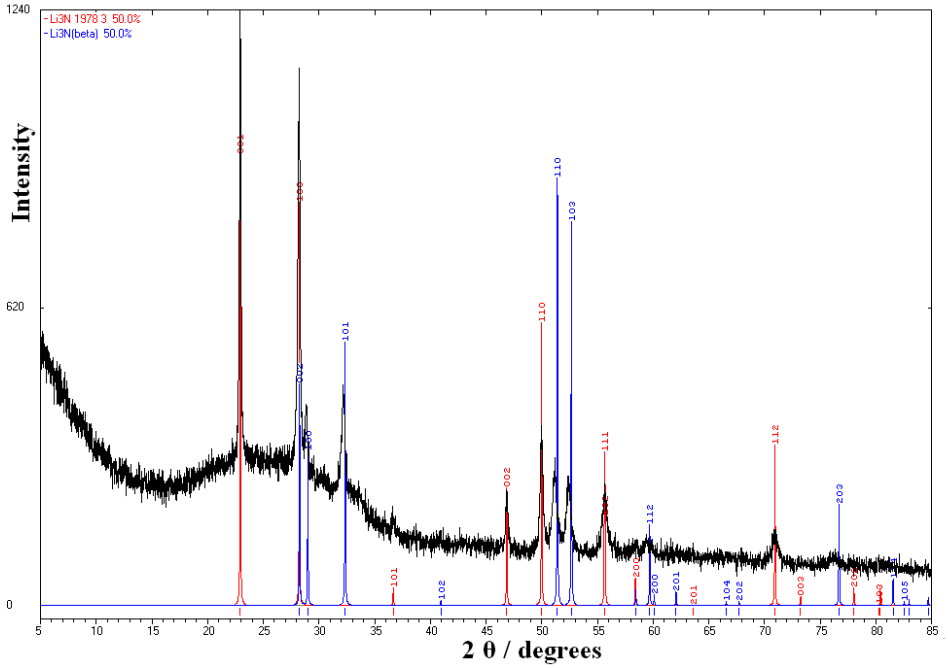

Figure A.5.1 Powder pattern obtained for commercial Li_3N (α-Li_3N indicated in red and β-Li_3N indicated in blue).

7.3.1 A.5.1 LiCaN – PXD data

Please find the following files on the accompanying CD.

Sample16_LiCaN.dis

Sample26_LiCaN.dis